An integrated modal approach to surface and volume scattering in ocean acoustic waveguides

by

Brian H. Tracey

B. A., Physics Kalamazoo College (1988)

M. S., Oceanographic Engineering
M.I.T. / Woods Hole Oceanographic Institution (1992)

Submitted in partial fulfillment of the
requirements for the degree of

DOCTOR OF PHILOSOPHY IN OCEANOGRAPHIC ENGINEERING

at the

MASSACHUSETTS INSTITUTE OF TECHNOLOGY

and the

WOODS HOLE OCEANOGRAPHIC INSTITUTION

January 1996

Signature of Author ....
Department of Ocean Engineering, MIT and the
MIT/WHOI Joint Program in Oceanographic Engineering

Certified by ....
Professor Henrik Schmidt
Professor of Ocean Engineering, Massachusetts Institute of Technology
Thesis Supervisor

Accepted by ....
Professor Henrik Schmidt
Acting Chairman, Joint Committee for Oceanographic Engineering
Massachusetts Institute of Technology-Woods Hole Oceanographic Institution

An integrated modal approach to surface and volume scattering in ocean acoustic waveguides

Brian H. Tracey

Submitted to the Massachusetts Institute of Technology and the Woods Hole Oceanographic Institution in partial fulfillment of the requirements for the degree of Doctor of Philosophy.

Abstract

Acoustic propagation in the ocean can be strongly affected by small random variations in ocean properties, including rough surfaces and volume fluctuations in the ocean or seabed. Such inhomogeneities scatter part of the incident acoustic field, stripping energy from the coherent part of the field. This scattered energy, or reverberation, propagates further in the modes of the ocean waveguide. The distribution of energy among modes is changed and the coherence of the acoustic field is reduced.

This thesis introduces several models which describe scattering of low-frequency sound. First, the rough surface scattering theory of Kuperman and Schmidt is reformulated in terms of normal modes. Scattering from rough fluid-fluid interfaces and rough elastic halfspaces is modeled, and statistics of the acoustic field are calculated. Numerical results show the modal formulation agrees well with Kuperman and Schmidt's model, while reducing computation times by several orders of magnitude for the scenarios considered.

Next, a perturbation theory describing scattering from sound speed and density fluctuations in acoustic media is developed. The theory is used to find the scattered field generated by volume fluctuations in sediment bottoms. Modal attenuations due to sediment volume scattering are calculated, and agreement is demonstrated with previous work.

The surface and volume scattering theories are implemented in a unified modal reverberation code and used to study bottom scattering in shallow water. Numerical examples are used to demonstrate the relationship between volume and surface scattering. Energy distribution among scattered field modes is found to be a complicated function of the scattering mechanism, the scatterer statistics, and the acoustic environment. In particular, the bottom properties strongly influence the coherence of the acoustic field. Examples show that excitation of fluid-elastic interface waves is a potentially important scattering path. Cross-modal coherences are calculated and used to study the loss of signal coherence with range.

Finally, earlier work on scattering from the Arctic ice sheet is extended. Simulations of long-range transmissions are compared with data from the April 1994 trans-Arctic propagation test. The results show modal attenuations and group speeds can be predicted reasonably well, indicating that acoustic monitoring of Arctic climate is feasible.

Thesis supervisor : Prof. Henrik Schmidt
Professor of Ocean Engineering

Acknowledgments

I am extremely grateful for the financial support of the Office of Naval Research, under contracts N00014-92-J-1282 and N00014-95-1-0307, which made it possible for me to carry out this work.

In deciding to work in acoustics, I was influenced by Dr. Wayne Wright at Kalamazoo College and by Dr. Richard Coulter at Argonne National Laboratory. Dr. Wright's classes gave me my first introduction to wave propagation and stimulated my interest in this branch of physics. My internship with Dr. Coulter (another Kalamazoo alum) gave me my first taste of hands-on acoustics, strengthening my sense that this was the field for me.

At MIT I have been fortunate to have Henrik Schmidt as an advisor. Henrik has excellent physical insight, which I relied on to keep me moving forward at several points in the thesis. I have benefited from his management style, which gives his students both independence and support, and the obvious enjoyment Henrik gets from his work helps remind me why I went into research in the first place.

I am also very grateful for the suggestions of my other committee members, Art Baggeroer and Jim Lynch. Art's input was especially important for the work on Arctic propagation, and Jim's suggestions prompted me to look more carefully at the numerical examples shown and at modal modeling issues. I would also like to thank Dajun Tang for chairing the defense and for his many suggestions and comments on the volume scattering work. My contributions are strongly influenced by D.J.'s work, as shown by the number of times I reference him.

My fellow-students, past and present, have helped me greatly. Ken Rolt helped me develop a better physical understanding of acoustics early in graduate school, and helped me out this fall by proof-reading this thesis. Kevin LePage has been generous with his Arctic scattering code and feedback about modeling. My conversations with Hua He, Rama Rao, Brian Sperry, Qing Wang, and many others have given me a broader understanding of acoustics and vibration. Special thanks go to Dan Li, for his comments on volume scattering, and J.T. Goh, for his insight on practically all aspects of acoustics and computation. I value the friendships I have formed in graduate school, and I'm looking forward to keeping in touch as the years go by.

My family - my parents Alice and Don, my brother Bruce, and my wife Laura - have been encouraging and comforting, as always. They have helped me keep a sense of perspective even while finishing this thesis. I want to especially thank Laura. With her love and support I can face each new phase of life with confidence.

Contents

List of Figures

Chapter 1

Introduction

1.1 Motivation and problems considered

The field of underwater acoustics has seen large changes in the past decade or so. Some of these changes are driven by technological advances. The ability to store and process large amounts of data has led to more ambitious experiments, ranging from basin-scale ocean temperature measurements to the tracking of ocean fronts using tomographic arrays. Advances in computing speed have allowed modelers to consider more realistic models of the ocean. The effects of range dependence, elastic media, and random variations in the ocean's properties can be studied and numerical results obtained in a reasonable amount of time. The decreased time needed to run forward acoustic models also makes inversion for environmental parameters easier, leading to interest in matched field processing and tomography.

Perhaps more important than the technological advances have been the changes in the types of problems which ocean acousticians are asked to solve. The end of the Cold War has brought a decrease in naval interest in deep-water and Arctic Ocean environments. At the same time the interest in anti-submarine warfare in shallower coastal waters such as the Persian Gulf has grown. There is also general scientific interest in coastal oceans, and several experiments are being mounted to use acoustics as a sensing tool for learning about coastal ocean processes. Better knowledge of these processes is important for understanding the effects of human activities on the marine environment, and the knowledge gained can be used to further improve acoustic models. On a global scale, increasing concern about climate change has led to several international acoustics experiments designed to measure ocean temperature, including the Heard Island/ATOC program and the trans-Arctic propagation

(TAP) experiment carried out in April 1994.

These new areas of interest bring with them new challenges for the ocean acoustics modeler. Acoustic prediction in shallow water is quite difficult for several reasons. Shallow water propagation is strongly affected by sea bottom properties, which are often difficult to measure. Coastal environments will in general have range-dependent bathymetry, and random variations of the seabed, both within the seabed and at the water-bottom interface, will act to scatter sound. Shallow water oceanography is also quite complicated, and motions such as internal waves have been shown to have a large effect on sound transmission. This sensitivity to the bottom parameters and oceanography raises the possibility of inverting for ocean properties from acoustic data, if the propagation and scattering physics can be understood well enough.

In long-range acoustic thermometry experiments bottom interaction is usually less significant, but oceanographic variability causes travel time and amplitude fluctuations in the signal. Since ocean temperature is determined from travel time, the ocean's variability may limit our ability to measure temperature. In the Arctic, the ocean is believed to be fairly calm, but the upward-refracting nature of the environment means that long range transmissions will interact many times with the ice cover. The scattering from rough ice causes the acoustic field to become less coherent with range, and introduces time travel perturbations. For any long-range transmission, whether in the Arctic or temperate oceans, it is very important to model the range dependence of the ocean. In the Arctic several very distinct water masses are present.

The work presented here is part of the overall effort to develop computationally efficient acoustic modeling tools to meet the needs outlined above. New methods for treating range dependent environments are being developed at MIT and elsewhere [69]. In this thesis we instead focus on the effects of small random variations in ocean properties. These random fluctuations scatter a fraction of the energy incoherently. Scattering has two main effects we would like to capture. First, energy lost to scattering causes attenuation of the coherent part of the acoustic field. Second, the scattered energy propagates further in the waveguide, affecting the coherence of the total sound field. This propagating scattered field is also known as the *reverberation*.

The acoustic pressure can be expressed as a sum of normal modes, or resonances of the waveguide. This modal approach is appealing because low-frequency sound fields can often be described using a relatively small number of modes, resulting in efficient calculations. The modes can be thought of as vertical standing waves, and arise from constructive interference

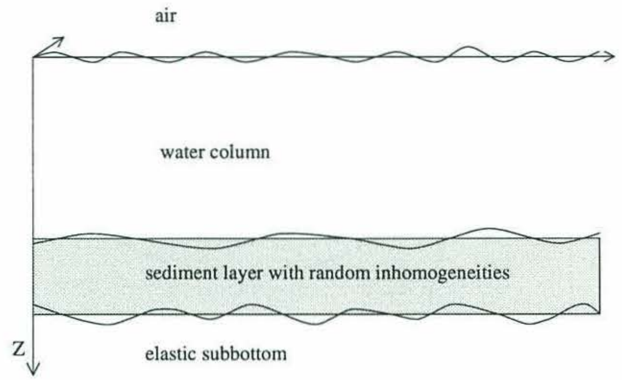

Figure 1-1: General shallow water scenario. Roughness exists between different layers, and volume fluctuations exist in the sediment.

of up- and down-going plane waves.

The basic scenarios considered in this thesis are illustrated in Figs. 1.1 and 1.2. Figure 1.1 shows a shallow water environment, with the water column overlying a sediment bottom layer and an elastic halfspace subbottom. The air/water, water/sediment, and sediment/subbottom interfaces are all rough. A random scattering layer may be present within the sediment. In addition, internal waves will be present in the water column, though scattering from these fluctuations is not modeled in this thesis. While this picture is somewhat idealized, it is realistic in including many different types of scattering with different characteristic length scales. One of the main contributions of this thesis is that the integrated nature of the computer code lets us study these different mechanisms for scattering together or separately. Figure 1.2 shows the scenario used in modeling transmission for the TAP Arctic acoustic thermometry experiments. The sound field interacts with the ice cover, both sides of which may be rough.

In the following chapters an earlier reverberation model developed for use with the wavenumber integration model OASES [45] is reformulated in terms of modes and used to study scattering from rough interfaces between waveguide layers. Rough fluid-fluid, fluid-elastic, and impenetrable interfaces are modeled. A new scattering model is presented which describes the effects of random variations in density and sound speed of a fluid. These results are used to study scattering from shallow water sediment bottoms containing randomly fluctuating layers. These different scattering models are combined into one computer code. Finally, a parameter study is presented showing the effects of ice scattering on the coherent portion of the acoustic field. This work is an extension of work done earlier by LePage and Schmidt [47].

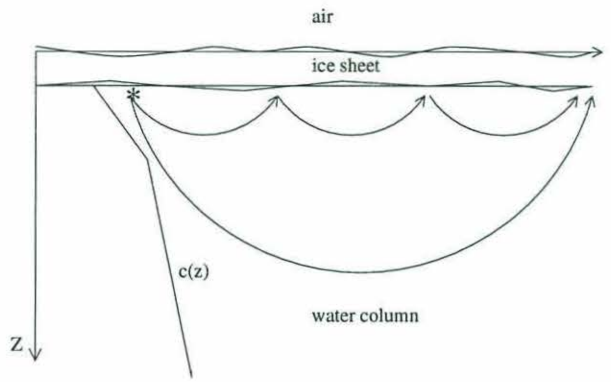

Figure 1-2: Arctic propagation environment. Upward refraction causes repeated interaction with the rough ice

1.2 Overview of Relevant Literature

The modeling of scattering from both rough interfaces and volume fluctuations has been an active research area for many years, and the related literature is vast. Much of the literature deals with scattering without considering the effects of locating the scatterer in a waveguide. We will briefly overview the main approaches before moving on to consider scattering and reverberation in waveguides, the main subject of this thesis.

In rough surface scattering theory the basic problem is the description of the effects of roughness on an interface separating two halfspaces. Oglilvy [59] has published an excellent review of publications up to 1986. An exact solution for the scattered field can be written using the Helmholtz integral theorem, giving the field in a volume in terms of the values of the field on the surface of the volume. The integral equation can be solved numerically to calculate scattering from a particular realization of a rough surface, and the relationship between roughness statistics and scattered field statistics can then be studied using a Monte Carlo approach. This method is computationally intensive, though useful for providing a reference solution for comparison with other solutions [80]. As a result the scattered field is generally found using an approximate method. The two most frequently used approximations are the Kirchoff (or tangent plane) approximation and the perturbation approximation. In the Kirchoff approximation the curvature of the slope at each point on the rough surface is assumed to be small compared to a wavelength. Mathematically the requirement is $ka \cos\theta >> 1$, where k is the acoustic wavenumber, a is the radius of curvature of the surface, and θ is the grazing angle. The surface is considered to be locally flat, so an incident wave is scattered in the specular direction. The reflection coefficient calculated for a flat interface is used, with the angle of incidence adjusted by the slope of the interface. One attractive feature of the Kirchoff approximation is that there is no restriction on surface height or slope, as long as the slope changes slowly.

The scattering problem can also be solved using the method of small perturbations (MSP). In this approach the rough surface slope is assumed small, allowing the boundary conditions at each point on the surface to be written in a linearly shifted and rotated local coordinate system. The acoustic field is decomposed into coherent and scattered parts, and the boundary conditions on the surface are then expanded in a Taylor series around the mean interface, with the roughness height as the small parameter. If the roughness height is small compared to an acoustic wavelength only the first-order small terms are retained. The resulting expressions can be solved to find the scattered field and the loss from the coherent field due to scattering. Early work of Bass and Fuks [2] on perturbation scattering theories has been extended by Kuperman [43] and Kuperman and Schmidt [44, 45, 68]. The Kuperman-Schmidt theory (abbreviated KS) forms the basis for the work in this thesis.

Work by Bass and Fuks on scattering from a rough boundary described by an impedance boundary condition also provides the basis for several articles by Kudryashov, Kryazhev, *et al.* [41, 40, 42]. In these papers the impedance boundary condition is perturbed, assuming the roughness is small and gently sloping. Expressions for the scattered field in a waveguide are found. This theory has been applied to studying scattering from a rough ice cover, including the effects of elasticity. The main drawback of this approach is that the impedance boundary condition is only a *single* boundary condition, and cannot satisfy continuity on the surface [12, p. 87]. The impedance scattering theory is compared with the KS theory in Chapter 5, and in more detail in Appendix C. The comparison shows that the two theories agree in situations where only one boundary condition must be satisfied (pressure-release or rigid boundaries), but that the impedance scattering theory gives unphysical results in other cases.

A number of other rough surface scattering theories are available. In analysis of field data Lambert's law is often invoked. Lambert's law is really an empirical fit to scattering data, expected to be valid for extremely rough surfaces. It predicts that the scattering pattern is sinusoidal, with the maximum scattering normal to the surface. Lambert's law seems to fail when low grazing angles or near-specular scattering is considered [19]. Rough facet models have also been developed, in which the rough surface is considered to consist of an distribution of flat facets with known reflection properties. Twersky [82] has published a number of papers modeling scattering from a distribution of 'bosses' on an otherwise smooth surface. These bosses may be of arbitrary shape, and the scattering from each individual boss is known. This theory allows consideration of multiple scattering between bosses on the rough surface. Tolstoy [81] has developed a similar approach, modeling scattering from a distribution of hemispheres located on a fluid-fluid interface. His results show the existence of a roughness boundary wave, not predicted by other theories. This boundary wave has been observed in scale model studies of outdoor sound propagation [1]. One disadvantage of boss scattering theories is that the surfaces modeled may not be physically realistic.

In volume scattering the canonical problem is modeling propagation through unbounded random media. Chernov [11] and Ishimaru [33] have published well-known books treating this problem. Different approaches are appropriate depending on the scale of fluctuations in the medium. If the variations in medium properties are small, a perturbation solution can be sought. Chernov developed a perturbation solution for an acoustic medium with small random variations in density and sound speed. He showed that the density scattering term has a maximum in the backscatter direction, an effect we will see in Chapter 3. Citing data taken by Beranek, Chernov argued that density fluctuations are generally small in the ocean and can be ignored.

The next level of complexity in volume scattering theory is to consider sound incident from the water column on a sediment bottom containing random layers. Waveguide effects are neglected; this is justifiable if the receivers in an ocean scattering experiment are fairly far from the ocean surface. Volumetric scattering from within the bottom has been modeled by assuming the scattering sources are uncorrelated uniform spheres [72, 37]. Perturbation approaches based on Chernov's work have been developed by Ivakin and Lysanov [35] and Hines [31]. Ivakin and Lysanov used a plane wave approach which did not include contributions from lateral waves, while Hines used the method of steepest descent to capture lateral as well as refracted wave contributions. D.J. Tang [75] developed a self-consistent perturbation theory to model scattering from sound speed fluctuations in the sediment. He was able to calculate a coherent field reflection coefficient which included loss due to scattering [78]. His results are used in Chapter 3 for comparison with the self-consistent perturbation theory developed in this thesis, which includes both density and volume fluctuations.

Gilbert [24] has used a Born-approximation scattering technique to estimate plane wave backscatter from stochastically described near-surface bubble layers. Gilbert's approach gives a reasonably good fit to experimental data.

So far all the scattering theories described treat either rough surface scattering or volume scattering, but not both together. In the real ocean both interface roughness and volume fluctuations exist. Ivakin and Lysanov [36] have considered both effects at the same time, and found the volume and surface scattering effects are not additive. At low grazing angles for fast bottoms the presence of roughness enhances penetration of sound into the bottom, generating more volume scattering. In this thesis we will ignore cross-effects between the scattering mechanisms for simplicity.

1.2.1 Relationship between surface and volume scattering

Most theoretical developments treat surface and volume scattering as completely different problems. Recently, however, several authors have begun to view the problems as related. Ivakin [34] views rough surfaces as special cases of volume fluctuations. Any material from the lower medium present above the mean interface can be viewed as a volume fluctuation of the upper medium's properties, and vice versa (see Fig. 1.3). There are also situations in which ocean randomness can be equally well described in terms of volume or surface variations. The sediment bottom shown in Figure 1.4, which shows sediment structure for a site near the mid-Atlantic ridge as imaged by a bottom-penetrating sonar, gives one example [48]. The sediment is seen to be deposited in layers, most of which are fairly flat. At around 20 m. and 60 m., regions of rapid variation in the sediment are seen. These regions could be viewed as layers in which sediment volume properties change randomly, or as stacks of rough interfaces. Tang [77] has shown analytically that both descriptions give identical scattering results.

In this thesis perturbation approaches to scattering are used. This leads us to classify problems as surface or volume scattering problems based on mathematical convenience. This is illustrated by considering two scenarios- first, scattering from an irregular basalt-water interface, and second, scattering from random variations in the sediment. In the first case differences in sound speed and density between the water and basalt are quite large, while the height and slope of the variations may not be. The scattering is best described by a rough surface scattering theory, which takes height and slope as the small parameters. In the sediment case the sound speed and density variations will generally be quite small, but bottom properties may fluctuate rapidly in the horizontal. A perturbation theory taking sound speed and density fluctuations as the small parameters will be less restrictive.

It is worth stressing again that the classification of a problem as volume or surface scattering is often more a matter of mathematical convenience than physics. The numerical results in Chapter 4 show no striking differences in the type of scattering generated by surface and volume scattering. Much larger changes are seen when effects of bottom elasticity are included.

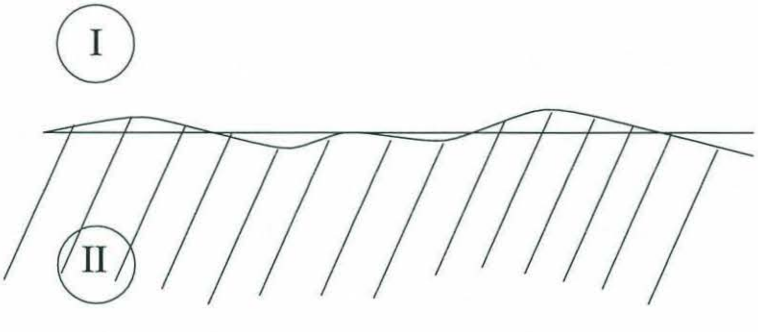

Figure 1-3: Two-halfspace problem. Randomness can be viewed either as surface roughness or as volume fluctuations of material properties near the mean interface.

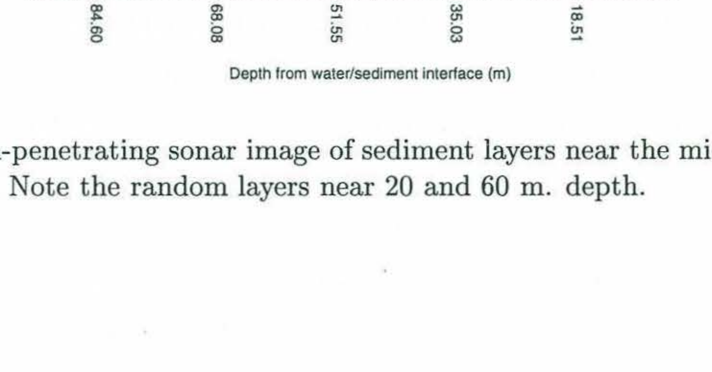

Figure 1-4: Bottom-penetrating sonar image of sediment layers near the mid-Atlantic ridge (plotted sideways). Note the random layers near 20 and 60 m. depth.

Next we review previous work which considers waveguide propagation effects on the scattered field. These can generally be grouped according to the type of propagation model used. Since this thesis focuses on modal propagation we pay particular attention to modal reverberation models.

1.2.2 Non-modal reverberation models

Ray-tracing is the oldest numerical modeling technique for ocean acoustics, and has been used to model the effects of ocean non-uniformity. Baxter and Orr [3] used a ray tracing code to study the effects of internal waves on the thermocline in shallow water. A stochastic ray tracing model was developed by Schneider [70] which simulated ocean randomness by perturbing ray angles at different points along the ray path. Lynch *et al.* developed the HARPO 3-D raytracing code, used to study the effect of large scale ocean inhomogeneities such as eddy fields[50]. Ray codes such as HARPO and ARTIST [49] can handle arbitrary bathymetry and can be used to model scattering from large features. However, the ray equations are a high-frequency approximation, and the resulting problems with turning points and caustics are well known. In addition the equations are nonlinear. It has been suggested that ray solutions may be chaotic at long ranges [60], though it is not clear whether ray chaos is a problem in practice.

The parabolic equation method can be used to study the effect of sound speed profile variations. Scheer and Baggeroer [67] used Collin's FEPE code to propagate through realizations of a random ocean. The PE result was sampled at different ranges and decomposed into modes, showing leakage of energy between modes due to the non-adiabatic nature of the propagation. Peregrym [62] used the parabolic equation to model scattering from solitary waves in the thermocline in shallow water. The parabolic equation method has not been applied as much for scattering from rough surfaces, since the mathematical formulation is not completely resolved [38, p. 344].

Boundary element methods have been used to model scattering from large-scale features [23, 19]. These methods could also be used to model scattering from smaller scale surface roughness, but the calculation would be extremely computationally intensive. Finite difference methods are also available [13] but are also very computationally intensive.

Finally, Kuperman and Schmidt have extended the self-consistent rough surface scattering theory [44, 45] to consider general scattering in stratified acoustic and elastic media. A reverberation code based on the SAFARI wavenumber integration approach has been developed [68] which takes into account the effects of the waveguide on scattered field propagation. Both individual realizations and ensemble statistics of the scattered field can be calculated. This approach will be discussed in much greater detail below. The method has been extended by LePage [46] and Fan [19] to consider 3D scattering from a roughness patch of limited extent. Fan includes waveguide effects, and excitation of waveguide modes can be seen in his realization results.

1.2.3 Mode coupling theories

If the ocean depth is constant and the sound speed profile is independent of range, modal solutions of the wave equation can be sought using separation of variables. If the ocean depth changes, either due to large-scale bathymetry or interface roughness, or the sound speed varies with range, the problem is no longer separable. In these cases a coupled mode solution can be sought. The acoustic pressure can be expanded either in terms of local modes, which satisfy the boundary conditions at a given range, or ideal modes, which are the eigensolutions for the average sound speed profile (assuming the water depth is constant). Expansion in terms of local modes works best when the ocean depth is changing, for example when the bottom is sloping. When modeling coupling due to interface roughness and/or small scale oceanographic variability, the ideal mode approach is preferable [51] and is used by most authors.

At long ranges coupling will cause the modal amplitudes to reach a stable distribution, which represents a balance between coupling and attenuation. Generally energy from the low order modes is coupled into the higher order modes, which are attenuated more rapidly. If there is no attenuation the energy will eventually be equally partitioned among all modes.

Suzanne McDaniel has used coupled mode theory to study a number of effects, including volume scattering, changes in waveguide depth, and the effects of scattering from a rough bottom. In her first paper on rough surface scattering [53] she follows the coupled mode theory of Pierce [64]. The coupling coefficients are found to be dependent on the wavenumber difference $k_n - k_m$ as well as the rms slope of the rough interface. The change in power in mode power due to coupling is calculated. Power loss to the continuous spectrum is shown to be important for modes close to cutoff. A follow-up article rederived the results, allowing for a density discontinuity at the ocean bottom [52]. Some examples of comparison with experimental data are shown. McDaniel and McCammon [55] have used mode coupling theory to estimate coupling caused by depth variations of stratified sediment layers. The sediment variations are described by a power law spectrum. This paper includes a calculation of the horizontal self-modal coherence - i.e. coherence of a mode evaluated at two points (x, y_1, z) and (x, y_2, z). One example shows that total coherence can actually increase with range, as higher order modes decay.

McDaniel [54] has also carried out a comparison of her coupled-mode theory with the self-consistent scattering theory developed in Kuperman and Ingenito. In this paper she extends her earlier work to look at scattering from a rough sea surface. Her main conclusion is that the modal attenuation predicted by Kuperman and Ingenito is exactly the same as that predicted by her second-order approach to coupled mode theory. The mode coupling estimates show only energy scattered out of each mode, not energy scattered back into the mode from other modes. Kirchoff scattering theory does not agree as well.

James Miller analyzed mode coupling due to scattering from the rough sea surface in his Ph.D. thesis [58]. In the limit of small wave height he uses adiabatic mode theory to estimate travel time and phase biases introduced by surface roughness. For larger wave heights where coupling is important, the field is divided into adiabatic and coupled parts. The Lippman-Schwinger equation is used to write the full Green's function in terms of the Green's function for the adiabatic case. The coupling potential term in this equation is identified with the mode coupling coefficient, and McDaniel's results for the single-scatter coupling coefficient for the rough interface are used. Thus energy travels in an adiabatic mode to the sea surface, undergoes a single-scattering process and travels away in an adiabatic mode.

Kennett [39] has published theoretical results for mode coupling due to elastic inclusions in waveguides. His work is mainly treating the seismic problem of propagation at very low frequencies (1 Hz. or less). In addition, the inclusions he treats are large deterministic blocks, not interface roughness or volume fluctuations. Still, it might be possible to extend his work to deal with mode coupling in elastic waveguides.

Boyles [7] has found an exact coupled mode solution for a cylindrically symmetric ocean with a time varying sea surface and horizontal changes in the sound speed. He finds two coupling terms, one of which is proportional to the values of the incident and scattered modes on the boundary, and the other to the derivatives of the modes on the rough boundary. Boyles' article includes an excellent bibliography.

Dozier and Tappert [16] published a well-known paper which uses a fiber optic waveguide theory to estimate energy transfer between modes caused by scattering from small sound-speed variations due to internal waves. A spectral modal of internal wave variability is developed which is consistent with the Garrett-Munk spectrum. This paper assumes that the cross-modal coherences are zero, which will not be true for shorter ranges. The "master equation" for the evolution of modal intensities is derived, and its behavior at long ranges is analyzed, showing the modal energy eventually is repartitioned into a configuration independent of initial mode excitations. A similar approach was used by Bellis and Tappert [4] to analyze multiple rough surface scattering. The results predict that coupling between modes depends mostly on the second derivative of the rough boundary.

Gorskaya and Raevskii [26] study mode coupling due to a rough pressure-release surface using a multiple scattering method. The boundary conditions are expanded in a Taylor series, and linear terms are retained. Expressions for the decay of the coherent field and the modal coherence are derived. It is argued that the cross-modal coherences are small and can be neglected. In some limiting cases the intensity equation can be rewritten in terms of a diffusion equation. In a later paper the authors [27] extend this technique to scattering from a rough fluid bottom.

1.2.4 Modal scattering theories

A number of authors have combined rough surface or volume scattering theories with modal descriptions of the pressure field. The work in this thesis falls into this class. Scattering causes energy transfer between modes, as in coupled mode theory, but multiple scattering is generally neglected. Phenomena such as modal equipartition cannot be modeled using a single-scatter theory, since the scattered energy is not allowed to redistribute itself among the modes. Neglect of multiple scattering means the results may not be accurate at long ranges. Jackson *et al.* [37]have argued that the single scatter approximation is valid if attenuation is mostly due to absorption rather than scattering, the idea being that if scattered energy is attenuated rapidly it will not have a chance to rescatter. Thus the validity of the approximation will depend on the scenario considered.

Ingenito [32] derived the scattered field from an object located in an isovelocity water column overlying a layered bottom. Scattering from a rigid sphere is examined in detail. The acoustic field in the water is written as a sum of modes, and each mode shape is expressed as a sum of up- and down-going plane waves. The scattering of plane waves corresponding to each mode is described through the sphere's plane wave scattering coefficient. Scattering from each incident mode into every other mode is considered, meaning the scattering coefficient is evaluated at a discrete sets of incident and scattered angles corresponding to mode propagation.

This approach has been extended by a number of authors. Yang [87] decomposed the normal modes into plane waves using the WKB approximation, allowing nonconstant sound speed profiles. Rough boundary scattering was modeled by finding the plane-wave scattering functions for hemispheres located on pressure-release and rigid surfaces. The portion of the incident mode propagating toward the rough surface scatters into the out-going parts of other modes via a plane-wave scattering coefficient. Dale Ellis [17] has recently published another description of a normal mode reverberation theory which proceeds along the same lines, decomposing the normal modes into up- and down-going plane waves and invoking the ray-mode analogy to describe the scattering process. Ellis used Lambert's law to give a plane wave scattering coefficient for his calculations. Earlier work by Zhang and Jin [88] uses the same general method.

This approach to rough surface scattering in these papers is physically intuitive and is quite general, allowing for the use of a variety of scattering theories to calculate the scattering coefficient. However, we notice that only the up-going part of the scattered field is taken into account (for bottom scattering); the down-going portion of the field is neglected. In effect the Rayleigh assumption is made - the scattered field is assumed to consist only of waves traveling away from the rough interface. This assumption may seem problematic, since Ogilvy [59] notes that the scattered field boundary conditions cannot be satisfied exactly under the Rayleigh approximation.

The more rigorously derived KS theory can be used as a check on this assumption. The decomposition assumed in the wavenumber integration approach shows clearly that both up- and down-going plane waves are needed to satisfy the scattered field boundary conditions. Furthermore, in reverberation problems it is clear that there will be both up- and down-going scattered waves traveling in the waveguide. Thus it seems clear that heuristic approaches based on the ray/mode analogy are not formally consistent with MSP scattering theory. The more important question is whether the extra assumption made by Ellis and others will have a large effect on the results. Kuperman and Schmidt have argued [45] that using the Rayleigh hypothesis is often valid. If the horizontal cycle length of a ray is much longer than the roughness correlation length, energy scattered at a rough bottom into a ray will be incoherent with the roughness when it next interacts with the bottom. Since the energy is incoherent it will have little effect on the boundary conditions, so this down-going scattered energy can be ignored. On the other hand, if the waveguide is shallow compared to the roughness length scales (as in an Arctic ice sheet), the down-going scattered field component must be included.

A number of articles published have used perturbation theories to describe scattering in a modal environment. Shang [71] has published a result for long-range reverberation due to a rough fluid bottom. This approach is quite similar to that developed in Chapter 2, though it is limited to an isovelocity water column and isovelocity fluid bottom, and cross-coherences between the scattered field modes are assumed to be zero. The scattered field is written using the Helmholtz integral theorem. A result for the reverberation intensity is calculated which involves the second moment of the roughness profile. The second moment is expressed, through the Fourier transform, in terms of the roughness power spectrum. The final result shows that the intensity is a sum over modes with the summation kernel weighted by values of the roughness spectrum evaluated at differences between the mode eigenvalues.

Harper and Labianca [30] use a perturbation theory to study scattering from a time-varying rough ocean surface. The pressure field is written in a series expansion, with zeroth order corresponding to the unperturbed modes. First and second order terms are calculated for 2D and 3D cases. The time-varying nature of the surface causes a spreading of the signal bandwidth. In general the carrier signal is shown to be reduced in amplitude, and the spectrum of the ocean surface is mapped onto signal sidebands on either side of the carrier. If the integral expression Labianca and Harper derive for the scattered field is evaluated using contour integration (not done in their paper) the result can be shown to be exactly equivalent to that derived in Chapter 2 for scattering from a rough pressure-release surface.

There have also been a number of approaches which treat reverberation caused by volume scattering. D.J. Tang [76] has used first-order perturbation theory to model scattering by sound speed and density fluctuations in sediment bottoms. The scattered field propagates modally, and the expected intensity of the scattered field is found from a double integral over the scattering volumes, using the spatial correlation function to describe the volume fluctuations. A Gaussian form of the spatial fluctuation is assumed and used to simplify the spatial integrals. Scattering into the continuous spectrum is neglected.

Modal theories have also been developed to model scattering by sound speed variations in the water column, from internal waves or other oceanographic disturbances. Sutton and McCoy have examined both single- and multiple-scattering from inhomogeneities. Their single-scatter theory [73], which has similarities to the work presented here, uses a first order perturbation, Born approximation approach to calculate the scattered field. The average intensity is calculated for each mode as a function of range, and the effects of various length scales for the inhomogeneities are examined. Their multiple-scatter theory [74] assumes the ocean is divided into range steps Δr which are small enough that the scattering within each can be described using a single-scatter theory like that in [73]. The self-coherences of the modes are calculated at a fixed range r, and the coherences are marched out in range in steps Δr. This work neglects scattering from the discrete modes into the continuous spectrum, and assumes, as do Dozier & Tappert, that cross-modal coherences can be ignored. Beran and Frankenthal [6] have generalized this work by calculating the cross-modal coherence functions. This work is quite interesting and is useful for examining the validity of the "random phases" argument made in Dozier and Tappert. It is subject to several restrictions, namely 1) a parabolic equation approach is used to solve for the modal amplitudes, limiting the approach to small grazing angles, and 2) the coherence is calculated in range steps Δr which are constrained to be large compared to the acoustic wavelength and correlation lengths of the sound speed fluctuations. This latter restriction means, for example, that their theory could not be used to estimate the spatial correlation of the field along a horizontal line array. However their work is extremely interesting as it provides a method for extending single-scatter results to consider multiple scattering.

1.2.5 Summary of the state-of-the-art

At this point the most general and widely applicable rough interface reverberation theory is probably that developed by Kuperman and Schmidt. The theory as implemented in Schmidt's scattering code (OASS) [68] can model scattering from both fluid and elastic interfaces, and the backscattered field is implicitly included in the solution. One drawback of the KS formulation is that is appears to be difficult to include the effects of correlation between roughness on different interfaces when calculating ensemble statistics of the scattering.

As detailed above, a large number of modal reverberation and coupling models have been developed. The advantages of the modal approach are that computations can be quite fast, and that the intermediate analytic results often give useful physical insight. However, very little work has been done on mode coupling or scattering due to rough elastic interfaces. The one exception of which the author is aware is the impedance scattering theory of Kudryashov and Krysazhev [40]. As discussed in Chapter 5, the impedance scattering theory used only seems to be valid for high-impedance boundaries.

One common assumption made in most modal approaches to either surface or volume scattering is that the cross-modal coherences are zero. Since the field in the absence of scattering is totally coherent, this assumption can only be expected to be true at long ranges after the field has been thoroughly "randomized" by scattering. It is often argued that the cross-modal terms can be neglected because they are expected to contribute little to the overall reverberant field intensity. This may be true, but for many signal processing applications the coherence loss due to scattering may be of more interest than the scattered field intensity. Beran and Frankenthal [6] have made good progress toward retaining the cross-modal information. Still, there are several restrictions on their approach, as discussed previously.

In volume scattering, several Born approximation theories have been developed which model scattering from both sound speed and density fluctuations, and Tang has developed a self-consistent theory for scattering from sound speed fluctuations only [75]. A self-consistent theory including both scattering mechanisms would be helpful, since density fluctuations have been shown to be important [86] and mean field attenuation will affect total field correlation statistics.

1.3 Contributions of thesis

This thesis makes several contributions to scattering and reverberation theory. These are summarized by area:

Rough surface scattering and reverberation:

- The Kuperman-Schmidt theory is reformulated in terms of normal modes. Scattering from rough fluid and impenetrable interfaces and rough elastic halfspaces is considered.
- The relationship of the Helmholtz integral theorem to the reverberation problem is clarified.
- The results are implemented numerically and compared with OASS results. Good agreement is shown, and computation time is reduced by several orders of magnitude.
- The reverberation code is used to develop a better understanding of the effects of the roughness statistics, acoustic environment, and scattering mechanism on the scattered field.

Volume scattering and reverberation:

- A new self-consistent perturbation theory is derived which accounts for scattering from both sound speed and density fluctuations in a fluid.
- The theory is applied to find modal attenuation due to scattering from a random layer in the seabed. Agreement with Tang's results is shown.

- The expected spectral distribution of scattered energy is calculated and used to develop physical insight. Three-dimensional effects and the relative importance of sound speed and density fluctuations are examined.
- Reverberation in a 2D ocean is modeled and implemented.
- Surface and volume scattering for different ocean scenarios are compared directly. The mechanisms are shown to be equivalent when describing randomness within the sediment.

Scattering and propagation in the Arctic:

- Parameters of the rough ice sheet which have the largest effect on modal attenuation and group speed are identified.
- Long-range propagation is simulated and compared to experimental data.
- The scattering theory of Kudryashov *et al.* is compared with the KS theory, and theoretical differences are noted. Examination of both theories applied to scattering from a rough ice sheet suggests that more work remains to be done on this important problem.

1.4 Overview of thesis

Chapter 2 begins by reviewing normal mode theory and the KS scattering theory. A wavenumber domain-based modal formulation of the KS approach is developed using the Helmholtz integral theorem. Results are presented for a number of kinds of rough interfaces, and for (x, z) and (r, z) oceans. Both the forward-scattered and back-scattered field are found. The statistics used to describe the reverberant field are defined and calculated.

In Chapter 3 a new self-consistent theory for scattering due to sound speed and density fluctuations is derived. Numerical results for the scattered field power spectral density are presented and discussed. Modal attenuations due to scattering are calculated for a 3D ocean. Expressions for reverberation in a 2D ocean are then found.

Chapter 4 presents numerical results for the two reverberation theories. First, rough surface scattering results are compared to predictions from Schmidt's OASS, and good agreement is demonstrated. Scattering generated by rough surfaces and volume fluctuations is compared. With both scattering mechanisms the spatial correlation statistics of the scattered field are shown to be shaped by waveguide propagation effects. The backscattered intensity vs. time is found for a number of scenarios, showing the roles played by the continuous spectrum modes and elastic interface waves.

Chapter 5 presents a parameter study of the effects of ice sheet properties on scattering loss in long-range Arctic transmission, using a modified version of LePage's [47] earlier work. Data from the April '94 trans-Arctic propagation experiment are compared to simulation results using historical data to describe the environment. The results show that some parts of the Arctic were warmer than the historical databases indicate.

Chapter 6 summarizes the physical insights gained from the modeling, and suggests directions for future work.

Chapter 2

Scattering from rough surfaces

The scattering theory developed by Kuperman and Schmidt [44] has been coupled with the OASES propagation model and used to study reverberation in both shallow water and Arctic ocean waveguides. This implementation is quite versatile and can model a variety of fluid and elastic interfaces. Unfortunately the calculations involved in finding the scattered field are very computationally intensive. Since many ocean waveguides are well described in terms of modal propagation, it is natural to think of reformulating the KS scattering theory using a modal expansion of the pressure field. This reformulation is presented in this chapter. The numerical results shown in Chapter 4 show that the scattering physics are described well while computation time is reduced by several orders of magnitude.

The formulation is developed starting with the Helmholtz integral theorem, which states that the pressure field in a volume can be written in terms of the values of the pressure field and its derivatives on the boundaries of the volume. Below we show that this means the scattered field in the waveguide can be written in terms its boundary conditions at the rough interface. The KS scattering theory directly gives the necessary boundary conditions for the scattered field.

This chapter begins by reviewing the normal mode solution for an ocean with no roughness. Notation is introduced and the modal form of the Green's function is reviewed. The KS scattering theory is then discussed. In the third section the Helmholtz integral theorem is used to develop the the scattering formulation for a two-dimensional ocean. The problems of rough fluid-fluid boundaries, impenetrable boundaries, and a rough elastic halfspace are treated. The resulting expressions for rough pressure-release and rough fluid-fluid boundaries are closely related to results shown in the literature; no comparable previous result is known for the rough elastic interface. Statistical measures of the reverberant field, including the cross-modal coherence and spatial correlation of the field, are introduced.

2.1 Solution to unperturbed problem

The linear wave equation in a fluid is derived from the hydrodynamic equations describing particle motion, in the limit of small amplitude disturbances. If the motion is assumed to be periodic with time dependence $e^{i\omega t}$, where ω is the radial frequency, then the acoustic pressure obeys the Helmholtz equation:

$$\left[\nabla^2 + k_0^2(\vec{r}, z)\right] p(\vec{r}, z) = 0. \tag{2.1}$$

where the wavenumber is defined as $k_0 = \frac{2\pi f}{c}$. In general in the ocean the sound speed depends much more strongly on depth than on the horizontal coordinates. If we assume c to be a function of depth only, and restrict ourselves to considering an (x, z) Cartesian geometry, the Helmholtz equation becomes

$$\left[\frac{\partial^2}{\partial z^2} + \frac{\partial^2}{\partial x^2} + k_0^2(z)\right] p(x, z) = 0. \tag{2.2}$$

The pressure field must also satisfy the boundary conditions at the top and bottom of the water column. If the ocean depth is constant, the boundary conditions do not depend on x. Since k also is independent of range, the Helmholtz equation can be solved through separation of variables. Here we use a Fourier transform method instead. Using the transform defined as

$$\begin{aligned} f(x, z) &= \int_{-\infty}^{\infty} dk\, \tilde{f}(k, z) e^{-ikx} \\ \tilde{f}(k, z) &= \frac{1}{2\pi} \int_{-\infty}^{\infty} dx\, f(x, z) e^{ikx} \end{aligned} \tag{2.3}$$

the Helmholtz equation is reduced to

$$\left[\frac{\partial^2}{\partial z^2} + k_0^2(z) - k^2\right] \tilde{p}(k, z) = 0. \tag{2.4}$$

This ordinary differential equation is known as the depth-separated wave equation. Together with the boundary conditions it constitutes an eigenvalue problem. If the boundary conditions are of several basic types (Dirichlet, Neumann, or Robin - see DeSanto [12, Chap. 2] for details) then the problem falls into the Sturm-Liouville class, meaning the solutions will have certain properties. Here we will only note that the solution consists of a series of n eigenvalues k_n and eigenvectors, or mode shapes, ψ_n. The mode shapes are orthogonal, and are normalized over the ocean depth such that:

$$\int_0^D \frac{\psi_m(z)\psi_n(z)}{\rho(z)} dz = \delta_{nm} \tag{2.5}$$

For some simple cases these eigenvalues and mode shapes can be found analytically, but in general numerical methods are required. For a Sturm-Liouville problem these modes form a complete set, meaning that any solution to the depth-separated wave equation can be found as a weighted sum of modes.

The completeness property of the modes can be used to find a solution for the Green's function. The depth-dependent Green's function is defined as the transformed pressure field generated by a source of unit amplitude; mathematically it solves

$$\left[\frac{\partial^2}{\partial z^2} + k_0^2(z) - k^2\right] G_\omega(k, z) = -\frac{\delta(z - z_s)}{2\pi} \tag{2.6}$$

where the sound source is located at $(x = 0, z = z_s)$. Since the modes form a complete set, the Green's function can be written as a sum of modes. If $\delta(z - z_s)$ is also expanded as a sum of modes, the mode orthogonality can be used to find the coefficients a_m for the Green's function, giving [38, p. 277-278]

$$G_\omega(k, z, z_s) = \frac{1}{2\pi\rho(z_s)} \sum_m \frac{\psi_m(z_s)\psi_m(z)}{k^2 - k_m^2} \tag{2.7}$$

The Green's function can be thought of a transfer function for the acoustic waveguide. Since the waveguide is assumed to be a linear system, the sound field caused by multiple sources can be found by convolving the source distribution with the Green's function.

The pressure field in the spatial domain is found by inverse transforming the wavenumber domain solution. If the acoustic source is of unit strength the spatial pressure field is simply the transformed Green's function. From the form of the Green's function given above we can see there are simple poles at $k = \pm k_m$, the modal eigenvalues. These poles are shown in Fig. 2.1. Physically the poles are resonances of the waveguide. Up- and down-going plane waves propagating at the modal angles interfere constructively, while waves propagating at other angles do not. The poles near the positive k axis correspond to waves traveling in the positive x direction, while the negative poles travel towards in the negative x direction. Attenuation with range is accounted for by having a complex eigenvalue, displacing the poles from the real axis. For positive k the imaginary part must be negative: $(k = Re(k) - \alpha, \alpha > 0)$, so $e^{-ikx} = e^{-iRe(k)x}e^{-\alpha x}$ showing the field will attenuate as $x \to \infty$. From similar arguments negative-traveling waves attenuate if $Im(k) > 0$ for $k < 0$.

The wavenumber integral is evaluated by using simple contour integration. We calculate the field traveling towards $x \to \infty$ by replacing the line integral in Eq. 2.8 with the contour integral shown in Fig. 2.1. This contour extends along the real axis and is closed in the lower half-plane by a semi-circle C of radius R. Any contribution from C will be exponentially attenuated for positive x since $Im(k)$ is large and negative along C. Thus the contour along C will give a negligible contribution compared to the line integral we are interested in evaluating. By Cauchy's theorem the integral around a contour is a sum of the residues of all poles inside the contour. Using the standard methods for evaluating the residues, the acoustic field is given by

$$p(x,z) = \frac{i}{\rho}\sum_m \frac{\psi_m(z_s)\psi_m(z)}{2k_m} e^{-ik_m x} \tag{2.8}$$

In underwater acoustics the pressure is usually normalized by the strength of the field at one meter. The normalized pressure field is [38, p. 276]:

$$p(x,z) = \frac{\sqrt{2\pi k_0}}{\rho(z_s)} e^{i(k_0 - \pi/4)} \sum_m \frac{\psi_m(z_s)\psi_m(z)}{k_m} e^{-ik_m x} \tag{2.9}$$

A similar form for the left-traveling modes can be found by enclosing those poles with a contour in the upper half-plane and going through the same steps.

The discussion so far has considered only a two-dimensional (x, z) ocean with a line source. The same basic steps can be followed to find the pressure field for other geometries. For a three dimensional Cartesian (x, y, z) ocean the Helmholtz equation is changed by using the differential operator $\nabla^2 = \frac{\partial^2}{\partial x^2} + \frac{\partial^2}{\partial y^2} + \frac{\partial^2}{\partial z^2}$. Using the two-dimensional Fourier transform defined as

$$\begin{aligned} f(\vec{r}, z) &= \frac{1}{2\pi}\int_{-\infty}^{\infty} d^2\vec{k}\, \tilde{f}(\vec{k}, z) e^{-i\vec{k}\cdot\vec{x}} \\ \tilde{f}(\vec{k}, z) &= \frac{1}{2\pi}\int_{-\infty}^{\infty} d^2\vec{r}\, f(\vec{r}, z) e^{i\vec{k}\cdot\vec{x}}, \end{aligned} \tag{2.10}$$

where $\vec{r} = (x, y)$ and $\vec{k} = (k_x, k_y)$, the depth-separated wave equation is found:

$$\left[\frac{\partial^2}{\partial z^2} + k_0^2(z) - \vec{k}^{\,2}\right] \tilde{p}(\vec{k}, z) = 0. \tag{2.11}$$

This equation is used to find the eigenvectors and mode shapes. Since the horizontal wavenumber in the equation is squared, the eigenvalues found will specify the *magnitude* of $\vec{k}$, but not the direction. Physically this corresponds to the fact that the vertical angle of the mode is set by the resonances of the waveguide, but the mode can travel at any horizontal angle. The normal modes again form a complete set, and an expansion of the Green's function as a sum of modes can be carried out, giving

$$G_\omega(\vec{k}, z, z_s) = \frac{1}{2\pi\rho(z_s)} \sum_m \frac{\psi_m(z_s)\psi_m(z)}{\vec{k}^{\,2} - k_m^2} \tag{2.12}$$

The pressure field in the spatial domain for a source, strength S_ω, at $(\vec{r} = 0, z = z_s)$ is given by

$$p(\vec{r}, z) = \frac{S_\omega}{2\pi} \int_{-\infty}^{\infty} d^2\vec{k}\, G(\vec{k}, z) e^{-i\vec{k}\cdot\vec{r}}. \tag{2.13}$$

For a point source and an ocean of constant depth, both the field and the environment are cylindrically symmetric. We use this fact to simplify the integral. We switch from Cartesian to polar coordinates, giving $\vec{k} = (k_x, k_y) \rightarrow (kcos\theta, ksin\theta)$, where k is the radial part of the wavenumber and θ is the angle of horizontal propagation. For a receiver along the x axis $\vec{r} = (r\cos\theta, 0)$, and the integral becomes

$$p(\vec{r}, z) = \frac{S_\omega}{2\pi} \int_0^{\infty} dk\, k \int_0^{2\pi} d\theta G(\vec{k}, z, z_s) e^{-ikcos\theta x} \tag{2.14}$$

Since G is not a function of angle the θ integration can be carried out separately, giving a Bessel function of the first kind. The integral over k is carried out using contour integration techniques, exactly as in the 2D case, and gives a sum over the residues of the poles $k = \pm k_m$. Combining these results and using the far-field asymptotic form of the Bessel function, we find

$$p(r, z) \approx \frac{i}{\rho(z_s)\sqrt{8\pi r}} e^{-i\pi/4} \sum_m \psi_m(z_s)\psi_m(z) \frac{e^{-ik_m r}}{\sqrt{k_m}} \tag{2.15}$$

This agrees with results given in standard texts. Normalizing the field to the pressure at 1 meter gives

$$p(r, z) \approx \frac{1}{\rho(z_s)} \sqrt{\frac{2\pi}{r}} e^{i(k_0 - \pi/4)} \sum_m \psi_m(z_s)\psi_m(z) \frac{e^{-ik_m r}}{\sqrt{k_m}} \tag{2.16}$$

So far we have assumed the boundary conditions are of the simple types which give a

Sturm-Liouville problem. Unfortunately realistic boundary conditions for ocean bottoms are often not of this type. For example, the boundary conditions are often specified by giving the impedance of the boundary. In this case the eigenvalue problem is not Sturm-Liouville. The solution then consists of two parts: a discrete spectrum, which is a sum over modes, and a continuous spectrum. Physically, the continuous spectrum describes propagation at steeper grazing angles. If the sound is incident on the ocean bottom at angles larger than the critical angle, some energy is transmitted into the bottom. Because of the energy loss true resonances cannot exist, though damped resonances (sometimes termed pseudo-resonances or leaky modes) do exist. These leaky modes are seen in the complex plane as poles with large imaginary parts. In contrast, at grazing angles shallower than the critical angle, no transmission into the bottom occurs. Reflected waves do not lose energy, and proper resonances exist. These resonances are the normal modes (also called proper modes) we have discussed above.

The continuous spectrum can only be exactly modeled using a wavenumber integration approach, but there are several ways to approximate its contribution. The simplest is the 'false-bottom' method, in which a pressure release (Neumann) boundary is inserted deep in the ocean bottom. If there is attenuation in the bottom and the false bottom is deep enough, any reflections from this unphysical boundary will be attenuated and will not affect the solution. The pressure-release boundary converts the problem into a Sturm-Liouville problem. Generally a large number of false-bottom modes are found in addition to the proper modes. Summing these false bottom modes approximates the integral over the continuous spectrum.

A more compact representation can be obtained by including the leaky modes in the complex plane. We note that the propagation of waves in the bottom is described by the vertical wavenumber k_z, which is found from the horizontal wavenumber k through the square root function: $k_z = \sqrt{k_b^2 - k^2}$, where k_b is the medium wavenumber. Since the square root is a multi-valued function, it is necessary to chose a branch cut in the complex plane to get unique solutions. The Pekeris branch cut, which defines

$$\begin{aligned} k_z &= \sqrt{k_b^2 - k^2}, k < k_b \\ &= -i\sqrt{k^2 - k_b^2}, k > k_b \end{aligned} \tag{2.17}$$

is shown in Figure 2.1. This choice of branch cut reveals the leaky modes, seen as poles with large imaginary parts. The contour integration shown in Figure 2.1 now encloses these

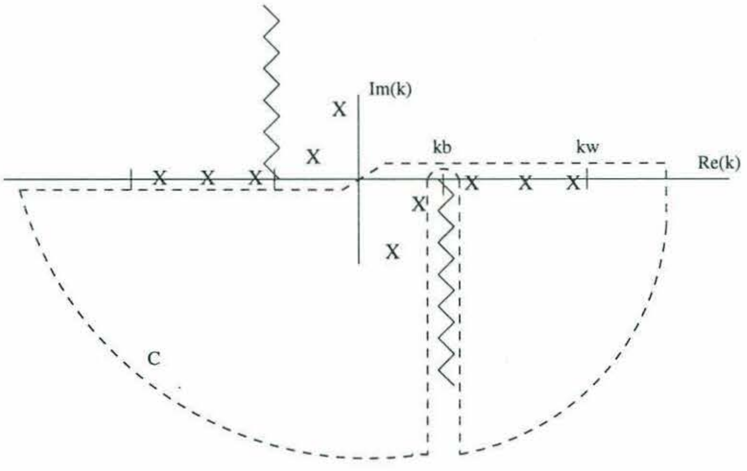

Figure 2-1: Contour integration in the complex plane, fast fluid bottom example. Proper modes are located close to the real axis between k_b and k_w; Pekeris branch cut is shown at $k = k_b$; leaky poles are exposed for $k < k_b$.

modes as well. The contributions to the contour integral from the two vertical cuts around the branch cut are in general small. The total field is then approximated as a sum of proper modes and leaky modes.

For many problems the leaky mode sum can be used to give a good representation of the continuous spectrum. Problems can be encountered because the complex root finders used to find these poles are not always reliable. In addition, for the branch cut defined, the leaky mode amplitudes grow exponentially in the bottom. This means they cannot be used to represent the field in the bottom itself, though their amplitudes are bounded in the water column. Both leaky mode and false bottom approximations of the continuous spectrum will be used in this thesis. A more detailed mathematical discussion of the continuous spectrum contribution can be found in DeSanto [12].

2.2 Kuperman/Schmidt scattering theory

The KS scattering theory has been presented in a number of publications [44, 45, 68], so only a brief overview is given here. Their work is a self-consistent perturbation scattering theory based on the pioneering work of Bass and Fuks [2]. The attenuation of the mean field due to scattering can be calculated, as well as the scattered field itself. One of the most important contributions made by Kuperman and Schmidt is the development of a compact boundary operator notation. This notation makes treatment of complicated elastic interfaces much more manageable, and is readily incorporated into the OASES wavenumber integration code. The boundary operator contains the boundary conditions for the problem, written in a matrix form. For example, for a fluid-fluid boundary, the conditions of continuity of pressure and velocity can be written

$$B\vec{p} = 0 \tag{2.18}$$

where the boundary operator is

$$B = \begin{bmatrix} 1 & -1 \\ \frac{1}{\rho_1}\frac{\partial}{\partial z} & -\frac{1}{\rho_2}\frac{\partial}{\partial z} \end{bmatrix} \tag{2.19}$$

The top row of B enforces continuity of pressure at the interface, and the bottom row enforces velocity continuity. The vector of acoustic amplitudes is

$$\vec{p} = \begin{bmatrix} \tilde{p}_1 \\ \tilde{p}_2 \end{bmatrix} \tag{2.20}$$

where $\tilde{p}_1$ is the acoustic pressure field above the interface and $\tilde{p}_2$ is the field below. If there are isovelocity layers above and below the interface then the acoustic fields will be in the form of exponentials. The boundary operator then simplifies considerably, as $\frac{\partial}{\partial z} \to -ik_z$, reducing the boundary conditions to algebraic equations.

The boundary conditions must also be satisfied at a rough interface. Here we consider a one-dimensionally rough surface in a two-dimensional ocean, but the full 3D case gives results of the same form [45]. The deviation from the mean interface is written as $\gamma(x)$, which by definition is zero-mean. We assume the statistics to be homogeneous, described by some correlation function

$$N(x'') = < \gamma(x)\gamma(x') > \tag{2.21}$$

where $x'' = x - x'$. The correlation function is related to the roughness power spectrum through the Fourier transform:

$$< \gamma^2 > P(p) = \frac{1}{2\pi}\int_{-\infty}^{\infty} dx'' N(x'') e^{ipx''} \tag{2.22}$$

where $< \gamma^2 >$ is the mean-squared roughness height. The boundary conditions on the rough interface must be satisfied at each point, using the local normal to the surface. If the slopes are small ($\gamma' << 1$) then these rotated boundary conditions can be written as

$$B^{*}\vec{p} = B\vec{p} + \gamma' \cdot b\vec{p} \tag{2.23}$$

where b is a rotation operator accounting for the effect of the slopes γ'.

The total acoustic field is then written as a sum of mean-field (coherent) and scattered field (incoherent) components. For an acoustic field this is written as

$$p(x,z) = < p(x,z) > + s(x,z); \tag{2.24}$$

elastic displacement fields are written similarly. The rotated boundary conditions are then expanded in a Taylor series to second order, assuming the roughness parameter γ is small. Since higher-order terms are neglected, multiple scattering is not included in the theory. The expansion results in two coupled equations, one for the mean field and the other for the scattered field. After some algebra the mean field equation is found to be

$$\left(\tilde{B}(k) + \frac{<\gamma^2>}{2}\frac{\partial^2}{\partial z^2}\tilde{B}(k) + I_1(k) + I_2(k)\right) < \tilde{p}(k) >= 0 \tag{2.25}$$

where the scattering integrals are

$$\begin{aligned} I_1(k) &= -\frac{<\gamma^2>}{2\pi}\int_{-\infty}^{\infty} dqP(q-k)\frac{\partial \tilde{B}(q)}{\partial z}\tilde{T}(k,q) \\ I_2(k) &= -\frac{<\gamma^2>}{2\pi}\int_{-\infty}^{\infty} dqP(q-k)[i(q-k)\cdot\tilde{b}(q)]\tilde{T}(k,q) \end{aligned} \tag{2.26}$$

and $\tilde{T}(k,q)$ is the transfer matrix from incident mean-field wavenumber k to the scattered field component q:

$$\tilde{T}(k,q) = \tilde{B}^{-1}(q)\left(\frac{\partial \tilde{B}(k)}{\partial z} - i(q-k)\cdot\tilde{b}(k)\right). \tag{2.27}$$

The mean field equation describes the loss of energy from the mean field due to the perturbed boundary conditions at the interface. Note that if the roughness parameter $\gamma = 0$ this equation gives the unperturbed problem.

The scattered field in turn is forced by the mean field:

$$\tilde{B}(q)\tilde{s}(q) = -\frac{1}{2\pi}\int_{-\infty}^{\infty} dk\tilde{\gamma}(q-k)\left[\frac{\partial \tilde{B}(k)}{\partial z} - i(q-k)\tilde{b}(k)\right] < \tilde{p}(k,z) > \tag{2.28}$$

where the right-hand side (RHS) is a forcing term describing the interaction of the mean field with the rough boundary. The RHS plays the same role as the physical source does for the unperturbed problem. The scattered field can be thought of as being generated by a distribution of "virtual sources" located at the rough surface.

An equation of the form above can be implemented in the OASES code. However, for the normal mode approach the boundary operator is not used directly. The connection between the scattered field equation and the normal mode formulation is the subject of the next section.

To make the use of the KS theory more clear, we consider the simple case of scattering from a rough interface separating two fluid halfspaces. This was the scenario studied by Kuperman [43] in his original paper. At the boundary between two fluids continuity of pressure and normal velocity are required. At the interface the continuity conditions are

$$\begin{aligned} p_1 &= p_2 \\ \frac{1}{\rho_1}\frac{\partial p_1}{\partial z} &= \frac{1}{\rho_2}\frac{\partial p_2}{\partial z} \end{aligned} \tag{2.29}$$

The boundary conditions are expanded to include rotation terms, and the scattering matrices are identified as:

$$\tilde{B}(q) = \begin{bmatrix} 1 & -1 \\ \frac{1}{\rho_1}\frac{\partial}{\partial z} & -\frac{1}{\rho_2}\frac{\partial}{\partial z} \end{bmatrix} \tag{2.30}$$

and

$$\tilde{b}(q) = \begin{bmatrix} 0 & 0 \\ \frac{ik}{\rho_1} & \frac{-ik}{\rho_2} \end{bmatrix} \tag{2.31}$$

(for more detail see the original article by Kuperman). The perturbation equations are then written

$$\tilde{s_1}(q,z') - \tilde{s_2}(q,z') = \frac{-1}{2\pi}\int_{-\infty}^{\infty} dk\tilde{\gamma}(q-k)\left[\frac{\partial\!<\tilde{p}_1(k,z')>}{\partial z} - \frac{\partial\!<\tilde{p}_2(k,z')>}{\partial z}\right] \tag{2.32}$$

$$\begin{aligned} \frac{\partial\tilde{s_1}(q,z')}{\partial z} - \frac{\rho_1}{\rho_2}\frac{\partial\tilde{s_2}(q,z')}{\partial z} &= \frac{-1}{2\pi}\int_{-\infty}^{\infty} dk\tilde{\gamma}(q-k)[\frac{\partial^2\!<\tilde{p}_1(k,z')>}{\partial z^2} - \frac{\rho_1}{\rho_2}\frac{\partial^2\!<\tilde{p}_2(k,z')>}{\partial z^2} \\ &+ (q-k)\cdot k\left(<\tilde{p}_1(k,z')> - \frac{\rho_1}{\rho_2}<\tilde{p}_2(k,z')>\right)] \end{aligned} \tag{2.33}$$

These terms can be evaluated if the mean field and the transform of the interface roughness are known. The scattering is seen to be modulated by the transformed surface roughness at the difference wavenumber. This type of Bragg scattering result is seen in many developments of scattering theory.

2.3 Modal formulation for two-dimensional waveguide

In this section the basic scattering formulation is developed for a two-dimensional waveguide with a rough fluid-fluid boundary. Pressure-release or rigid boundaries can be treated as limiting cases of the fluid-fluid boundary. The formulation for waveguides with rough fluid-elastic boundaries is more complicated, and is shown in detail in Sect. 2.3.3, but the general form of the solution is the same as for the fluid-fluid case.

The Helmholtz integral theorem states that the pressure field in some volume can be found in terms of an integral over the surface of the volume, given the values of the field and its derivatives on the surface. Mathematically, for a two-dimensional, Cartesian coordinate system and a sound wave of angular frequency ω,

$$\begin{aligned} p(x,z) &= \int_{S'} dS' [p(x',z') \frac{\partial G_\omega(x,z \mid x',z')}{\partial n'} - \frac{\partial p(x',z')}{\partial n'} G_\omega(x,z \mid x',z')] \\ &+ \int_V dV(source) \end{aligned} \tag{2.34}$$

where (x',z') denotes coordinates on the surface S', $\frac{\partial}{\partial n'}$ is the derivative normal to the surface, and $G_\omega(x,z \mid x',z')$ is the Green's function evaluated at (x,z) for a source at (x',z'). As before we separate the acoustic field into coherent (mean) and incoherently scattered parts, giving

$$p(x,z) = < p(x,z) > + s(x,z) \tag{2.35}$$

Substituting this into the Helmholtz integral formula shows that both the mean and scattered field must satisfy the integral equation separately. Since the source terms in the volume integral are all first-order, they will appear as sources to the mean field only. The scattered field satisfies the source-free Helmholtz integral and can be written

$$s(x,z) = \int_{S'} dS' [s(x',z') \frac{\partial G_\omega(x,z \mid x',z')}{\partial n'} - \frac{\partial s(x',z')}{\partial n'} G_\omega(x,z \mid x',z')] \tag{2.36}$$

This integral is valid provided the Green's function is the solution of the wave equation everywhere inside the surface integral. Thus it is valid in both the water column and bottom, and across all smooth interfaces, since the Green's function satisfies the continuity boundary conditions. It will *not* be valid at rough interfaces, however, since the Green's function is found assuming all interfaces are smooth. To avoid this problem the surface integral must be deformed to run around any rough interfaces.

As an example, Figure 2.2 shows a waveguide with a smooth surface and a rough fluid-fluid bottom interface. From the radiation condition the pressure at $x = \pm\infty$ goes to zero, so the vertical parts of the surface integral will disappear. There is therefore no difficulty deforming the integral to cross the rough surface and run back along the other side as shown. Since the direction of the surface normal changes, the integrand will change sign across the interface. The integral also disappears along all smooth interfaces, since the Green's function and the mean field are proportional. The scattered field can then be written in terms of the two line integrals back and forth along the rough surface. Written out with an explicit notation, this is

$$\begin{aligned} s(x,z) &= \int_{-\infty}^{\infty} dx'[s_1(x',z')\frac{\partial G_1^{(1)}(x,z \mid x',z')}{\partial z'} - \frac{\partial s_1(x',z')}{\partial z'} G_1^{(1)}(x,z \mid x',z')] \\ &- \int_{-\infty}^{\infty} dx'[s_2(x',z')\frac{\partial G_2^{(2)}(x,z \mid x',z')}{\partial z'} - \frac{\partial s_2(x',z')}{\partial z'} G_2^{(2)}(x,z \mid x',z')] \quad (2.37) \end{aligned}$$

The notation used here is that s_1 is the scattered field in the water (medium 1) and s_2 is the scattered field evaluated in the bottom. The subscript on the Green's function indicates the medium in which the field is sampled, while the superscript denotes the medium in which the source is located. Depth derivatives are assumed to be taken from the appropriate direction - in other words $\frac{\partial s_1}{\partial z}$ is the derivative of the scattered field in medium 1, taken approaching the interface from above, while $\frac{\partial s_2}{\partial z}$ is the derivative taken in the sediment approaching the interface from below.

This integral can be simplified using the reciprocity theorem and continuity conditions for the Green's function. Since we are usually interested in the scattered field in the water, the integral is rewritten in terms of mode shapes and sources in the water. The continuity conditions across the interface for the field generated by a source in the lower medium give

$$G_1^{(2)} \mid z' = G_2^{(2)} \mid z' \quad (2.38)$$

$$\frac{1}{\rho_1}\frac{\partial G_1^{(2)}}{\partial z} \mid z' = \frac{1}{\rho_2}\frac{\partial G_2^{(2)}}{\partial z} \mid z' \quad (2.39)$$

while the reciprocity theorem for exchanging the source location between medium 1 and

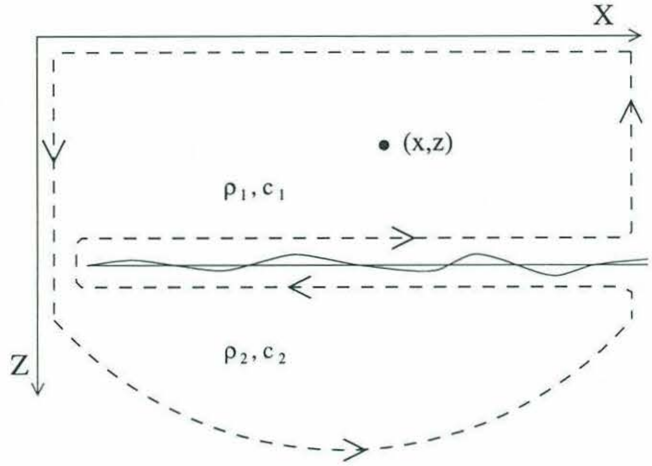

Figure 2-2: Helmholtz integral theorem for penetrable bottom. The surface integral is deformed to run along both sides of the rough surface

medium 2 gives [38, App 2A]

$$\rho_1 G^{(1)} = \rho_2 G^{(2)} \tag{2.40}$$

The terms coming from the integration below the interface can be rewritten using the continuity relations and reciprocity. Reverting to the earlier notation and writing $G_\omega = G_1^{(1)}$, the scattered field is given by

$$\begin{aligned} s(x,z) &= \int_{-\infty}^{\infty} dx'[(s_1(x',z') - s_2(x',z'))\frac{\partial G_\omega(x,z \mid x',z')}{\partial z'} \\ &- (\frac{\partial s_1(x',z')}{\partial z'} - \frac{\rho_1}{\rho_2}\frac{\partial s_2(x',z')}{\partial z'})G_\omega(x,z \mid x',z')]. \end{aligned} \tag{2.41}$$

This intermediate result shows that the scattered field is forced by the discontinuities in the boundary conditions at the rough interface. As the previous section showed, these discontinuities fall out of the KS perturbation theory in a natural way. Before the KS results can be applied, the Helmholtz integral must be transformed to the wavenumber domain. Carrying out the transform gives (see App. A.1)

$$\begin{aligned} \tilde{s}(q,z) &= 2\pi[(\tilde{s}_1(q,z') - \tilde{s}_2(q,z'))\frac{\partial G_\omega(q,z,z')}{\partial z'} \\ &- (\frac{\partial \tilde{s}_1(q,z')}{\partial z'} - \frac{\rho_1}{\rho_2}\frac{\partial \tilde{s}_2(q,z')}{\partial z'})G_\omega(q,z,z')] \end{aligned} \tag{2.42}$$

The discontinuities in the scattered field and its derivative at the rough interface, found from the KS theory, act as forcing terms for the scattered field.

The discussion so far has dealt with fluid-fluid rough interfaces only. For scattering problems involving elastic layers there will be 3 or more boundary conditions. The integral equation is more complicated, involving shear and compressional potentials in the bottom. In general, though, the scattered field equations are of the form

$$\tilde{s}(q,z) = 2\pi[\Delta_1(q)\frac{\partial G_\omega(q,z,z')}{\partial z'} - \Delta_2(q)G_\omega(q,z,z')], \tag{2.43}$$

where Δ_1 is the discontinuity in the scattered field across the rough interface, and Δ_2 represents the discontinuity in momentum.

The remaining steps are to use the KS theory to find the forcing terms Δ_1 and Δ_2, and to write the Green's function and the incident pressure field as modal sums. Section 2.3.2 shows these steps for fluid and impenetrable boundaries, and section 2.3.3 shows the results for a rough elastic halfspace. In both cases the transformed scattered field can be written in the general form:

$$\tilde{s}(q,z) = \frac{1}{(2\pi)^2}\int_{-\infty}^{\infty} dk \sum_{n,m} \tilde{\gamma}(q-k)\psi_n(z)\frac{a_{nm}(q,k)}{(k^2-k_m^2)(q^2-q_n^2)} \tag{2.44}$$

where

$$a_{nm}(q,k) = \frac{-NM}{\rho(z')\rho(z_s)}\left[\Delta_m^{(1)}(q,k)\frac{\partial\psi_n(z')}{\partial z'} + \Delta_m^{(2)}(q,k)\psi_n(z')\right] \tag{2.45}$$

Here NM is the normalization to the field at 1 m., and comes from the normalized incident field. The poles at $k = \pm k_m$ and $q = \pm q_n$ show that both the mean and scattered fields travel in the resonant modes of the waveguide. The terms inside the k-integral represent the transfer from incident k to scattered wavenumber q.

2.3.1 Spatial domain solution

The scattered field in the spatial domain is found by inverse transforming the result for $\tilde{s}$ above. Since $\tilde{\gamma}$ is a Fourier transform, we can write it explicitly. The scattered field is then given by

$$\begin{aligned} s(x,z) &= \frac{1}{(2\pi)^2}\int_{-\infty}^{\infty} dq\, \tilde{s}(q,z)e^{-iqx} \\ &= \frac{1}{(2\pi)^3}\int_{-\infty}^{\infty}\int_{-\infty}^{\infty}\int_{-\infty}^{\infty} dq\, dk\, dx' \sum_{n,m} \gamma(x')e^{i(q-k)x'}\psi_n(z) \end{aligned}$$

$$\frac{a_{nm}(q,k)}{(k^2-k_m^2)(q^2-q_n^2)}e^{-iqx}. \tag{2.46}$$

The integrand has simple poles at $q = \pm q_n$ and $k = \pm k_m$, where the positive poles correspond to forward-propagating waves (bounded as $x \to \infty$), and the negative poles correspond to back-propagating modes (bounded as $x \to -\infty$). The integrals over q and k can be evaluated as a sum of residues using Cauchy's theorem. In doing so, we must be careful to pick the correct poles for the physical situation we are considering.

We begin by first considering scattering from the mean field traveling out from the source to the right, then use symmetry to include scattering from the left side of the source as well. The poles at $k = k_m$ correspond to the right-going waves. The equation above shows that, for $x' > 0$, we can close the contour in the lower half-plane. Evaluating the integral as a sum of modes gives:

$$s(x,z) = \frac{i}{(2\pi)^2}\int_{-\infty}^{\infty} dq \int_0^{\infty} dx' \sum_{n,m} \gamma(x')e^{-ik_m x'}\psi_n(z)\frac{a_{nm}(q,k_m)}{2k_m(q^2-q_n^2)}e^{-iq(x-x')}. \tag{2.47}$$

The outgoing field can scatter either forward or backward:

Forward scatter

We first examine a bistatic geometry, with the receiver located some distance away from the source. Sound interacting with the rough bottom at ranges $x' < x$ can scatter forward to the receiver. These contributions are found by enclosing the positive q_n poles, giving

$$s_f(x,z) = \frac{-1}{2\pi}\sum_{n,m}\int_0^x dx'[\gamma(x')e^{i(q_n-k_m)x'}]\psi_n(z)\frac{a_{nm}(q_n,k_m)}{4k_m q_n}e^{-iq_n x}. \tag{2.48}$$

To simplify the notation, we define the forward-scattering coefficient f_{nm} to be

$$f_{nm} = \frac{a_{nm}(q_n,k_m)}{4k_m q_n} \tag{2.49}$$

Writing the complex eigenvalues as $k_m = \bar{k}_m - i\alpha_m$, etc., helps make the effect of mode attenuation more clear:

$$s_f(x,z) = \frac{-1}{2\pi}\sum_{n,m}\int_0^x dx'[\gamma(x')e^{-(\alpha_m-\alpha_n)x'}e^{i(\bar{q}_n-\bar{k}_m)x'}]\psi_n(z)f_{nm}e^{-\alpha_n x}e^{-i\bar{q}_n x}. \tag{2.50}$$

This expression models propagation of mode m forward to a scattering point x', and then further forward propagation in mode n to the receiver. The different attenuation rates of the two modes are accounted for by the $e^{-(\alpha_m-\alpha_n)x'}$ term.

Backward scatter

In a bistatic experiment rough surfaces at ranges beyond the receiver ($x' > x$) can scatter backwards to the receiver. These waves are found by enclosing the negative q poles, giving

$$s_b(x,z) = \frac{-1}{2\pi}\sum_{n,m}\int_x^\infty dx'[\gamma(x')e^{i(-q_n-k_m)x'}]\psi_n(z)\frac{a_{nm}(-q_n,k_m)}{-4k_m q_n}e^{iq_n x}. \tag{2.51}$$

The notation is simplified by defining the backscattering coefficient as

$$b_{nm} = \frac{a_{nm}(-q_n,k_m)}{4k_m q_n} \tag{2.52}$$

If the attenuations are again written explicitly, we have

$$s_b(x,z) = \frac{1}{2\pi}\sum_{n,m}\int_x^\infty dx'[\gamma(x')e^{-\alpha_n(x'-x)}e^{-\alpha_m x'}]e^{i(-\bar{q}_n-\bar{k}_m)x'}]\psi_n(z)b_{nm}e^{i\bar{q}_n x}. \tag{2.53}$$

We will show in Chapter 4 that, for rough surface scattering, the forward-scattered field is nearly always much stronger than the backscattered field. For a bistatic experiment this means that backscattered energy from beyond the receiver can often be neglected.

Backscattering is measured directly in monostatic experiments, with the source and receiver located at the same range. For monostatic backscatter we need to include scattering from $x' < 0$. From physical arguments the backscattering should be symmetric about $x' = 0$. Mathematically, we will see from the sections below that the scattering coefficients obey the symmetry relation: $a_{nm}(-q,k) = a_{nm}(q,-k)$. The total backscattered energy is then

$$s_b(0,z) = \frac{1}{2\pi}\sum_{n,m}\int_{-\infty}^\infty [\gamma(x')e^{-(\alpha_n+\alpha_m)|x'|}e^{i(-\bar{q}_n-\bar{k}_m)x'}]\psi_n(z)b_{nm} \tag{2.54}$$

Mode m travels away from the source, attenuating as it travels, until it back-scatters at some range x' into the backward going mode n. Mode n then attenuates as it travels back to the receiver, giving the total attenuation shown. Since the attenuation *sum* rather than difference is what is important here, we expect attenuation to have a much stronger effect. Attenuation must be included in the system in order to avoid unphysical results. If there is no attenuation in the system, scattering from rough patches infinitely far away will propagate to the receiver, causing the scattered field to diverge.

So far all the calculations presented have been for a two-dimensional (x, z) ocean. Scattering in a fully three-dimensional ocean is a much harder problem, but could be approached in the same way. As an intermediate case we consider the scenario in which both the environment and the roughness are axisymmetric, so there is no out-of-plane scattering. As shown by Schmidt *et al.* [69] and detailed in Appendix A.7, the solution of the Helmholtz equation in cylindrical geometries can be related very simply to the 2D Cartesian solution. To a good approximation, the effects of the cylindrical geometry can thus be taken into account by multiplying the 2D Cartesian result by a factor of $\sqrt{2/\pi r}$.

2.3.2 Scattering terms for rough fluid and impenetrable boundaries

In section 2.2, the results of the KS theory for a rough fluid-fluid interface were shown. The forcing term shown there can be expressed in terms of normal modes by using the modal expansion for the mean field and the Green's function.

The Δ_1 term is simply the jump in scattered field pressure across the rough interface. If the mean field is given as a sum of modes, and the result from section 2.2 is simplified by using the fact that the mode derivatives above and below the interface are related by the ratio of densities, the Δ_1 term becomes

$$\begin{aligned}\Delta_1(q) &= \frac{-NM}{(2\pi)^2\rho_1}\int_{-\infty}^{\infty} dk \sum_m \tilde{\gamma}(q-k_m)\frac{\psi_m(z_s)\frac{\partial\psi_m(z')}{\partial z}(1-\frac{\rho_2}{\rho_1})}{k^2-k_m^2} \\ &\equiv \frac{-NM}{(2\pi)^2\rho(z_s)}\int_{-\infty}^{\infty} dk \sum_m \tilde{\gamma}(q-k_m)\frac{\Delta_m^{(1)}(q,k)}{k^2-k_m^2} \qquad (2.55)\end{aligned}$$

The Δ_2 term is the jump in the derivative of the scattered field. It is simplified by rewriting the second derivative using the Helmholtz equation, and by using $<\tilde{p}_1>=<\tilde{p}_2>$. The result is

$$\begin{aligned}\Delta_2(q) &= \frac{NM}{(2\pi)^2\rho_1}\int_{-\infty}^{\infty} dk \sum_m \tilde{\gamma}(q-k)\left[k_1^2-\frac{\rho_1}{\rho_2}k_2^2-qk_m(1-\frac{\rho_1}{\rho_2})\right]\frac{\psi_m(z_s)\psi_m(z')}{k^2-k_m^2} \\ &\equiv \frac{NM}{(2\pi)^2\rho(z_s)}\int_{-\infty}^{\infty} dk \sum_m \tilde{\gamma}(q-k)\frac{\Delta_m^{(2)}(q,k)}{k^2-k_m^2} \qquad (2.56)\end{aligned}$$

These forcing terms are used to find the reverberant field as outlined above.

Many authors have developed scattering theories for simple impenetrable boundaries, such as rigid or pressure release surfaces [30, 26]. These boundaries are limiting cases of the fluid-fluid boundary. The results for a rough pressure release surface are found by taking the limits as $\rho_2 \to 0, <\tilde{p}(z')> \to 0$. The transformed scattered field in the water column is then given by:

$$\tilde{s}(q,z) = \frac{-NM}{(2\pi)^2\rho(z_s)} \int_{-\infty}^{\infty} dk \sum_{n,m} \tilde{\gamma}(q-k) \frac{\psi_m(z_s)\psi_m'(0)}{k^2 - k_m^2} \frac{\psi_n(z_s)\psi_n'(0)}{q^2 - q_n^2} \tag{2.57}$$

Thus the scattered field depends only on the *derivatives* of the field at the rough surface. This result can be shown to be exactly equal to that derived by Harper & Labianca [30] in their paper on mode coupling due to a rough pressure-release surface.

Similarly the results for the rigid boundary can be obtained by letting $\rho_2 \to \infty$ and $\frac{\partial <\tilde{p}>}{\partial z} |_{z'} \to 0$. The resulting scattered field is

$$\begin{aligned} \tilde{s}(q,z') &= \frac{-1}{2\pi} \int_{-\infty}^{\infty} dk \tilde{\gamma}(q-k) \left(\frac{\partial^2}{\partial z^2} + (q-k)k \right) < \tilde{p}(k,z') > \\ &= \frac{-NM}{(2\pi)^2\rho(z_s)} \int_{-\infty}^{\infty} dk \sum_{n,m} \tilde{\gamma}(q-k)[k_0^2(z) - kq] \frac{\psi_m(z_s)\psi_m(z')}{k^2 - k_m^2} \frac{\psi_n(z_s)\psi_n(z')}{q^2 - q_n^2} \end{aligned} \tag{2.58}$$

The field now depends on the values of the modes at the rough interface. It is interesting to note that the term introduced by the rough surface slopes is proportional to $q - k$. As the slopes increase this term will become more important, and backscattering can be expected to grow.

The simple case of an ideal waveguide, an isovelocity ocean with a pressure release top and bottom boundary conditions, is treated in Appendix A.3. The top boundary is assumed to be rough. The scattered field calculated using the modal scattering theory is shown analytically to agree with the results of the wavenumber- domain based KS approach.

2.3.3 Scattering terms for a rough elastic halfspace

In this section the scattering theory is extended to deal with a rough elastic ocean bottom. Because of the added complexity of the fluid-elastic boundary, we limit ourselves here to considering scattering from an elastic halfspace. This simplification reduces the calculations needed considerably.

The fluid-elastic boundary conditions are formulated starting with the equations of motion for the elastic medium. The equations of motion, stress-strain relationships, and Hooke's law for isotropic elastic media are presented by many authors, for example Doyle [14, p. 158], and are summarized in Appendix A.4 For the two-dimensional case we make the two assumptions that there is only in-plane strain (i.e. all out-of-plane derivatives are zero) and that there is no out-of-plane motion.

In the elastic halfspace we have only down-going waves, since the source is in the water column. If the fluid-elastic interface is at z_i, the transformed compressional potential $\tilde{\phi}$ and shear potential $\tilde{\psi}$ are given by

$$\begin{aligned} \tilde{\phi}(k,z) &= Ce^{-\gamma_p(z-z_i)} \\ \tilde{\psi}(k,z) &= De^{-\gamma_s(z-z_i)} \end{aligned} \tag{2.59}$$

where $\gamma_p = \sqrt{k^2 - k_p^2}$ and $\gamma_s = \sqrt{k^2 - k_s^2}$.

At the fluid-elastic interface three boundary conditions must be satisfied. The first is the continuity of normal stress (negative of pressure); second is continuity of displacement; and third, the tangential shear σ_{xz} must be zero at the interface, since water cannot support a shear force. To set up these boundary conditions we must write the stresses and displacements in the elastic bottom in terms of the velocity potentials. From Hooke's law and the stress-strain relation σ_{zz} and σ_{xz} are found, as shown in Appendix A.4. The boundary conditions for the unperturbed problem are then gathered together in matrix form. If the field is expressed in terms of modes, the boundary conditions become

$$\tilde{B}(k_m) \begin{bmatrix} \psi_m(z_i) \\ C_m \\ D_m \end{bmatrix} = 0 \tag{2.60}$$

where $\tilde{B}(k)$ is a 3×3 matrix, shown in the Appendix. Here $\psi_m(z_i)$ is the value of the mode shape at the fluid-elastic interface, C_m is the amplitude of the down-going compressional plane wave, and D_m is the amplitude of the down-going shear plane wave.

KRAKEN [66] does not give mode shapes inside the elastic bottom, but from the mode shape in the water we can find ψ_n and $\psi_n^{'}$ at the fluid-elastic interface z_i. These boundary conditions are used to solve for the unknowns C_m and D_m in terms of the mode shape in the water, as shown in Appendix A.4. To account for attenuation in the bottom, we include an imaginary part of the bottom shear and compressional wavenumbers:

$$\begin{aligned} \tilde{k_p} &= k_p(1 - i\delta_p) \\ \tilde{k_s} &= k_s(1 - i\delta_s) \end{aligned} \tag{2.61}$$

The imaginary parts δ are found by dividing the shear and compressional attenuations given in units of dB/λ by a conversion factor (approximately 54.58) [38, Chap. 2]. Thus, to find the incident field strength, the eigenvalues and mode shapes in the water are found numerically and are used to estimate C_m and D_m. The complex medium wavenumbers are used to find the plane wave attenuations.

The scattered field forcing terms can now be calculated. The boundary operators $\frac{\partial \tilde{B}(k)}{\partial z}$ and $\tilde{b}(k)$ are found by expanding the boundary conditions, and the forcing terms for the KS theory can be calculated. The resulting terms do not add much physical insight, and are given in the Appendix.

When studying rough fluid-fluid interfaces, we used reciprocity to rewrite the Helmholtz integral theorem in a form which directly gave the scattered field in the waveguide. Such an approach is possible for the fluid-elastic interface, but the fluid-elastic reciprocity relationship is quite complicated. To avoid this difficulty an impedance method used earlier by Kudryashov [42] is modified for use here.

The scattered field equation is a set of three coupled equations, representing the three boundary conditions. These equations can be manipulated into an impedance form, giving

$$\tilde{s}(q, z_i) - Z_0(q)\frac{\partial \tilde{s}(q, z_i)}{\partial z} = G_s(q). \tag{2.62}$$

$\tilde{s}(q, z_i)$ is the scattered field in the water, evaluated at the fluid-elastic interface z_i. The forcing term for the scattered field is

$$G_s(q) = \frac{-NM}{(2\pi)^2 \rho(z_s)} \int_0^\infty dk \sum_m \tilde{\gamma}(q-k) \frac{\Delta_m^{(1)}(q,k) + \Delta_m^{(2)}(q,k) Z_0(q)}{k^2 - k_m^2} \tag{2.63}$$

The exact forms of $\Delta_m^{(1)}$, $\Delta_m^{(2)}$, and the boundary impedance $Z_0(q)$ are shown in Appendix A.4. A solution to this equation can be written down by inspection, following Kudryashov:

$$\tilde{s}(q, z) = \frac{G_s(q)\psi(z, q)}{\pi(q)} \tag{2.64}$$

where

$$\pi(q) = \tilde{s}(q, z_i) - Z_0(q)\frac{\partial \tilde{s}(q, z_i)}{\partial z}. \tag{2.65}$$

Here $\psi(z, q)$ is the solution to the homogeneous depth-separated wave equation, and satisfies and the boundary conditions at all smooth interfaces (e.g. the ocean surface when bottom scattering is considered). As a check, the solution for $\tilde{s}$ results in an identity when inserted in the scattered field boundary condition and evaluated for $z = z_i$. Finally we transform $\tilde{s}(q)$

to find the scattered field in space. The function $\pi(q)$ is basically the impedance boundary condition for the mean field, and is zero at the wavenumbers $q = \pm q_n$ of the unperturbed solution. At these wavenumbers $\psi(z,q)$ becomes by definition the unperturbed mode shape $\psi_n(z)$. Summing the residues, the forward scattered field is found to be (see App. A.4)

$$
\begin{aligned}
s_f(x,z) &= \frac{NM}{2\pi\rho(z_s)} \int_0^x dx' \sum_{n,m} \gamma(x') e^{i(q_n-k_m)x'} \frac{\psi_n(z)}{2q_n} \\
&\quad \frac{\left[\Delta_m^{(1)}(q_n,k_m)\frac{\partial\psi_n}{\partial z}\mid_{z_i} + \Delta_m^{(2)}(q_n,k_m)\psi_n(z_i)\right]}{2k_m} e^{-iq_n x}
\end{aligned}
\tag{2.66}
$$

This equation is in the same form as the general result found earlier, demonstrating the equivalence of the the two approaches used. The one difference is in the factor of $\rho(z')$ missing here, which before came from the Green's function. Since the water density is generally set to unity this difference in definition is not important.

To find the backscattered field, the negative poles $q = -q_n$ are enclosed in the contour integration. The backscattered field at the source range is given by

$$
\begin{aligned}
s_b(0,z) &= \frac{NM}{2\pi\rho(z_s)} \int_{-\infty}^{\infty} dx' \sum_{n,m} \gamma(x') e^{-(\alpha_n+\alpha_m)|x'|} e^{i(-q_n-k_m)x'} \frac{\psi_n(z)}{-2q_n} \\
&\quad \frac{\left[\Delta_m^{(1)}(-q_n,k_m)\frac{\partial\psi_n}{\partial z}\mid_{z_i} + \Delta_m^{(2)}(-q_n,k_m)\psi_n(z_i)\right]}{2k_m}
\end{aligned}
\tag{2.67}
$$

2.4 Statistical measures of scattered field

The results presented in section 2.3.1 allow us to calculate the scattered field in the waveguide for a specific realization of the interface roughness. This can be extremely useful, for example in generating synthetic time series for comparison with data. No approximations other than the basic ones of small roughness height and slope have been made, so within the limits of the perturbation theory the results can be considered to be exact.

In this thesis we focus instead on calculating second-moment expectations of the scattered field, which can give quick insight into the scattering physics. To do so we describe the interface roughness in terms of a *power spectrum* P describing the amplitude distribution of roughness at different length scales. Several different types of spectra may be used to describe the roughness. Gaussian spectra are often used, largely because of their analytic simplicity, but for many surfaces power-law distributions such as the Goff-Jordan spectrum [25] seem to be more realistic as they include roughness on many length scales.

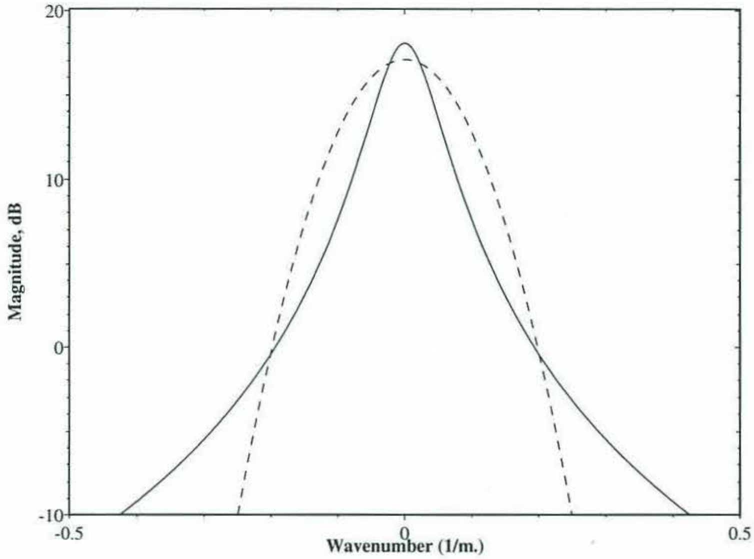

Figure 2-3: Goff-Jordan spectrum (solid line) and Gaussian spectrum (dashed) for 1 m RMS roughness, 20 m. correlation length

The Gaussian spectrum is defined as:

$$P(q) = \sqrt{2\pi} L e^{-(pL)^2} \tag{2.68}$$

while the Goff-Jordan spectrum is given by:

$$P(q) = \pi L \left[(pL)^2 + 1 \right]^{-1.5} \tag{2.69}$$

where L is the correlation length. Examples of both spectra, in a dB scale, are shown in Fig. 2.3 for a roughness correlation length(CL) of 20 m. The main difference is seen to be that the Goff-Jordan spectrum contains much more energy at large wavenumbers, corresponding to small-scale roughness.

To use the power spectrum, which is a wavenumber-domain description of the roughness, we must transform the spatial integrals over roughness $\gamma(x')$ in the scattering expressions to the wavenumber domain. In this section we show how this works for both the forward- and back-scattering cases. The results obtained are used to define other second-order statistics defined in the following sections.

In section 2.3.1 we showed that the equation for forward-scattering involved an integral over the rough boundary x'. Any second-moment statistics will involve a double integral over the rough surface. This double integral takes the general form:

$$I_2 \;=\; \int_0^{x_1}\int_0^{x_2} dx'dx'' < \gamma(x')\gamma(x'') > e^{i(q_n-k_m)x'}e^{-i(q_l-k_p)^*x''} \tag{2.70}$$

We next assume that the roughness is statistically stationary, so the correlation function $< \gamma(x')\gamma(x'') >$ depends only on the separation $y = x' - x''$. Changing variables to sum and difference coordinates, defined as

$$\begin{aligned} y &= x' - x'' \\ r &= \frac{x' + x''}{2}, \end{aligned} \tag{2.71}$$

the second-moment expectation can be split into two parts:

$$I_2 = \left(\int_{-x_2}^{x_1} dyN(y)e^{i\left[\frac{(q_n-k_m)+(q_l-k_p)^*}{2}\right]y}\right)\left(\int_0^{\frac{x_1+x_2}{2}} dre^{i[(q_n-k_m)-(q_l-k_p)^*]r}\right) \tag{2.72}$$

where N is the roughness correlation function. We examine each of these integrals separately.

In evaluating the integral over y several simplifying assumptions must be made. First, for almost all cases, x_1 and x_2 will be much larger than the correlation length. Thus we can extend the limits of integration over y to $\pm\infty$. Second, we note that as the modal attenuations become small, the integral over y approaches the Fourier transform of the roughness correlation function, as defined in Eq. 2.22. The difficulty in applying this definition is that the wavenumber argument to the power spectrum in Eq. 2.22 is real, while the exponential argument in Eq. 2.72 is complex. To work around this difficulty, we not that the correlation function gives its main contribution to the integral for separations y which are on the order of the correlation length or less. If the differences in mode attenuations are small enough that the exponential growth or decay is small over the distance of a correlation length, i.e.

$$e^{-[(\alpha_m-\alpha_n)+(\alpha_p-\alpha_l)]CL} \approx 1, \tag{2.73}$$

then the imaginary part of the wavenumbers can be neglected. The small slope approximation made in the perturbation theory ensures that each mode will scatter most strongly into the nearby modes. Since nearby modes will have comparable attenuations, the approximation above should be reasonable.

Carrying out the second integral, over r, gives the total second-order expectation as:

$$I_2 = 2\pi < \sigma^2 > P\left(\frac{(\bar{q_n} - \bar{k_m}) + (\bar{q_l} - \bar{k_p})}{2}\right) \frac{e^{i[(q_n-k_m)-(q_l-k_p)^*](x_1+x_2)/2} - 1}{i\,[(q_n - k_m) - (q_l - k_p)^*]} \tag{2.74}$$

For most combinations of modes, the oscillating exponential will reduce the contribution to the integral. The largest contributions are expected to come from the combinations ($n = m, l = p$ or $n = l, m = p$) for which the phase of the exponential is constant. These scattering paths give contributions on the order of x, accounting for the increase of the scattering surface with range.

Expressions for the back-scattered field in the waveguide were also found in section 2.3.1. Second-moment expectations for the backscattered field will also involve double integrals over space, and can be treated using the methods above. The backscattered field in a bistatic geometry was shown to include a spatial integral of the form:

$$I_1 = \int_x^\infty dx' \gamma(x') e^{i(-q_n-k_m)x'}. \tag{2.75}$$

The second-moment expectation can be shown to be

$$I_2 = -2\pi < \sigma^2 > P\left(\frac{(-\bar{q_n} - \bar{k_m}) + (-\bar{q_l} - \bar{q_p})}{2}\right) \frac{e^{i[(-q_n-k_m)+(q_l+k_p)^*](x_1+x_2)/2}}{i\,[(-q_n - k_m) + (q_l + k_p)^*]} \tag{2.76}$$

A monostatic scattering geometry is a special case of the result above, with both receivers located at $x = 0$. The scattered field is found as an integral over all space. The largest contributions again come from the modes $n = m, l = p$ and $n = l, m = p$. The second term above then becomes

$$\frac{1}{\alpha_n + \alpha_m + \alpha_l + \alpha_p} \tag{2.77}$$

This shows that the monostatic backscattered field will become infinite if there is no attenuation in the system, since scattering patches infinitely far away can contribute to the total energy. A similar result was found in modeling the ambient noise field generated by surface noise sources [38, Chap. 10].

The ability to perform the spatial integrals over x' and x'' analytically rather than numerically lies at the heart of the efficiency of the modal approach. The result is that the computation time for the modal formulation is independent of range. The computation time grows quadratically with range for the wavenumber integration implementation of Schmidt, as seen in Chapter 4.

In the next sections we define a number of different statistical measures of the scattered field which are helpful in understanding the scattering process and waveguide physics. Generally these can be lumped into estimates of the energy distribution and coherence among modes, and estimates of the energy distribution and coherence in space.

2.4.1 Cross-modal expectations and expected modal power

Here we calculate the second-moment expectations of mode amplitudes, for both the scattered and total fields. These are the most basic statistics to calculate, since nearly all other measures of the scattered field can be written in terms of the cross-modal amplitude expectations.

For the mean field the definition of the cross-modal expectation is quite simple. As seen in section 1, the mean pressure field with a unity strength source is given by

$$\begin{aligned} p(x,z) &= \frac{i}{\rho(z_s)} \sum_m \psi(z_s)\psi_m(z) e^{-ik_m x} \\ &= \sum_m d_m \psi_m(z) e^{-ik_m x} \end{aligned} \tag{2.78}$$

The cross expectation between modes n and l is simply $d_n d_l^*$.

The cross-modal expectations for the scattered field are found using the results obtained earlier. From Eq. 2.50 the forward-scattered mode amplitude is identified as

$$a_n(x) = \frac{1}{2\pi} \sum_m \int_0^x dx' \gamma(x') f_{nm} e^{i(q_n - k_m)x'}. \tag{2.79}$$

The results in section 2.4 are used to find the the cross-modal correlation for the forward-scattered modes:

$$\begin{aligned} < a_n(x) a_l^*(x) > &= \frac{<\gamma^2>}{2\pi} \sum_{m,p} P\left(\frac{(q_n - k_m) + (q_l - k_p)}{2}\right) \cdot \\ &\quad \frac{e^{i[(q_n-k_m)-(q_l-k_p)^*]x} - 1}{i[(q_n - k_m) - (q_l - k_p)^*]} f_{nm} f_{lp}^*. \end{aligned} \tag{2.80}$$

Results for the back-scattered modes can be found in a similar way. For example, the cross-modal expectations for the backscattered field at $x = 0$ are given by:

$$< a_n(0) a_l^*(0) > = \frac{<\gamma^2>}{2\pi} \sum_{m,p} P\left(\frac{(-q_n - k_m) + (-q_l - k_p)}{2}\right) \cdot$$

$$\frac{ib_{nm}(b_{lp})^*}{(-q_n - k_m) - (-q_l - k_p)^*} \tag{2.81}$$

For the case $n = l$ the modal amplitude expectation is simply the *expected modal power* for mode n. For long ranges almost all the contribution will come from the coherent terms $m = p$.

These expressions already give some insight into the scattering process. The roughness power spectrum $P(q)$ will have its maximum at $q = 0$, and the power spectrum width decreases as correlation length increases. For very short correlation lengths the power spectrum will be very broad, so the power spectrum is nearly constant over the range sampled. In this limit scattering will be basically isotropic and the forward and backscattered fields will be equally excited. As the correlation length increases, the scattering will become more forward directed. The difference argument to the power spectrum for the forward scattered field will be closer to zero than the wavenumber sum seen in the backscattered mode amplitude expression. As the correlation length becomes very large, the power spectrum will approach a delta function around the incident wavenumber. Each incident wave will then scatter only into angles very close to the incident angle. Physically the large correlation length means that energy will be coherently scattered from many ranges along the bottom, adding up according to the phase of the incident field.

2.4.2 Cross-modal coherence

Cross-modal coherence has proven to be a useful measure for describing modal fields. For example, Polcari [65] estimated coherence between modes from long-range Arctic transmission data taken from the FramIV experiment in 1982. The normalized cross-modal coherence between modes n and l is defined

$$T_{nl}(x) = \frac{|< a_n(x) a_l^*(x) >|}{\sqrt{<| a_n^2(x) |><| a_l^2(x) |>}} \tag{2.82}$$

The modal amplitudes calculated above are used. The normalization terms are equal to the expected modal powers.

It is more practically useful to find the cross-modal coherence for the *total* field, since this is more easily measured in experiments. The total forward traveling field is found by summing the mean field and forward scattered field:

$$p(x,z) = \sum_n \left[d_n - \frac{1}{2\pi} \sum_m \int_0^x dx' \gamma(x') e^{i(k_n - k_m)x'} f_{nm} \right] \psi_n(z) e^{-ik_n x} \tag{2.83}$$

(although the scattered wavenumber is usually denoted by q, k is used here to emphasize that the same modes are summed). Since the mean field and scattered field are incoherent, the total field cross-modal expectations are found by adding 2.80 to the mean-field expectation $(d_n d_l^*)$. If the scattered field is zero, the acoustic field is totally coherent and T_{nl} will be one for all n and l. In general the normalization insures that all diagonal elements will be one, meaning each mode is coherent with itself. The value of off-diagonal elements shows the loss of coherence in the field due to scattering.

2.4.3 Power spectral density

The power spectral density is a powerful measure which helps in understanding the distribution of scattered energy with wavenumber. It is defined as

$$PSD(q) = < \tilde{s}(q,z)\tilde{s}^*(q,z) >, \tag{2.84}$$

and is the expected level of energy scattered into each wavenumber q. It can be directly found from a second-moment expectation of Eq. 2.44.

First we calculate the power density for sound scattered from a single incident plane wave with wavenumber k_{inc}. The wavenumber integral over k then collapses to a single point. Calculations in Appendix A.5 show that the power spectral density is

$$PSD_{plane}(q) = \frac{< \gamma^2 >}{(2\pi)^3} \sum_{n,m} P(q - k_{inc}) \mid \psi_n(z) \frac{a_{nm}(q, k_{inc})}{(k_{inc}^2 - k_m^2)(q^2 - q_n^2)} \mid^2 \tag{2.85}$$

2.4.4 Spatial statistics and expected intensity

The sections above defined statistics useful for understanding the distribution of energy and coherence among modes. In this section statistical measures are defined which show the energy distribution and coherence in space.

The basic measure defined here is the spatial correlation of the scattered field. The spatial correlation is the second moment expected value of the scattered field, sampled at two receivers (x_1, z_1) and (x_2, z_2):

$$\begin{aligned} C_s(x_1, z_1, x_2, z_2) &= < s(x_1, z_1) s^*(x_2, z_2) > \\ &= \sum_{n,l} < a_n a_l^* > \psi_n(z_1) \psi_l^*(z_2) e^{-iq_n x_1} e^{iq_l^* x_2} \end{aligned} \tag{2.86}$$

The results above for the cross-modal amplitude expectation are used in calculations.

The spatial correlation of the *total* acoustic field is found from the cross-modal expectations for the total field. It can be shown to be (again writing the scattered wavenumber using k instead of q)

$$\begin{aligned} C_{tot}(x_1, z_1, x_2, z_2) &= \sum_{n,l} d_n d_l^* \psi_n(z_1)\psi_l(z_2) e^{-ik_n x_1} e^{ik_l^* x_2} \\ &+ \sum_{n,m}\sum_{l,p} < a_n a_l^* > \psi_n(z_1)\psi_l(z_2) e^{-ik_n x_1} e^{ik_l^* x_2} \end{aligned} \tag{2.87}$$

The spatial correlation can be used [68] to define several other measures for either the scattered or total fields, including the *normalized correlation*

$$C_{Sij} = \frac{Re[C_s(x_1, z_1, x_2, z_2)]}{\sqrt{C_s(x_1, z_1, x_1, z_1) C_s(x_2, z_2, x_2, z_2)}} \tag{2.88}$$

and the *spatial coherence*

$$\rho_{Sij} = \frac{\mid C_s(x_1, z_1, x_2, z_2) \mid^2}{C_s(x_1, z_1, x_1, z_1) C_s(x_2, z_2, x_2, z_2)} \tag{2.89}$$

Finally, the *expected intensity* is simply the spatial correlation with the two receivers placed at the same point:

$$< I(x, z) >= C_s(x, z, x, z) \tag{2.90}$$

2.5 Backscattered intensity *vs.* time

The calculations shown above have all assumed that the incident field is generated by a continuous wave, single-frequency source. Response to an incident pulse can be found by Fourier synthesis, but is computationally very intensive. To avoid this problem, several authors [88, 17] have developed approximate solutions for scattering, assuming the incident pulse is narrow-band but of reasonably short duration. A similar approach, starting from the scattering theory developed above, can be used to calculate backscattered energy from a narrow-band pulse as a function of time.

The scattering geometry is shown in Fig. 2-4. A sound source is located in a cylindrically symmetric ocean at $(r = 0, z = z_s)$. A vertical array at the source range measures backscatter. We assume a narrow-band pulse of duration τ is broadcast from the source. The energy in the outgoing mode m travels away from the source at c_m, the group velocity for the center frequency in the pulse. Sound scattering out of mode m into mode n at

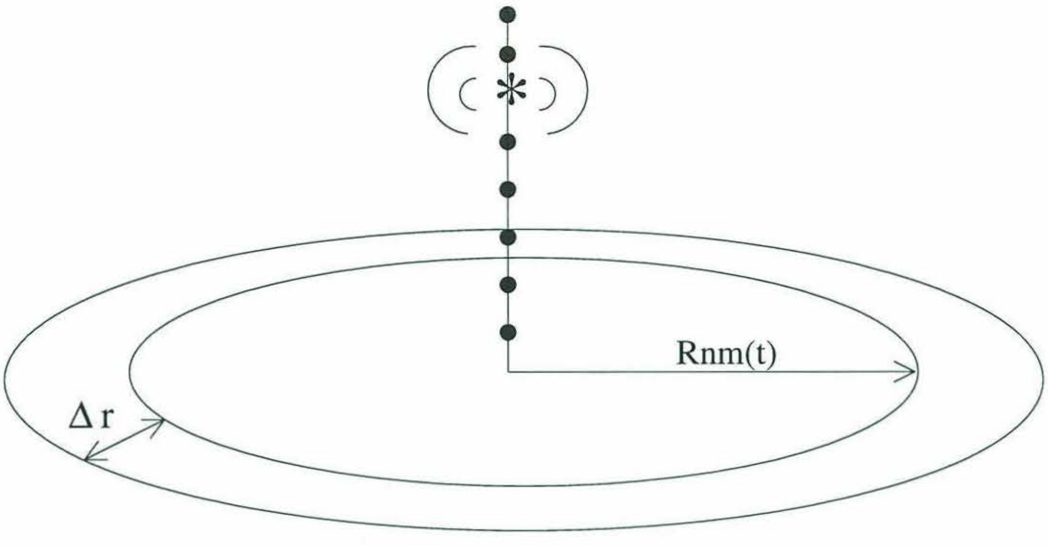

Figure 2-4: Modeled backscattering geometry. A narrow-band pulse is transmitted from a source, and backscattered energy is received on an array at the same range.

some range r' along the rough boundary will travel back to the source with group speed c_n. Relating travel time to distance through the modal group velocities, we can find the area along the bottom which contributes to backscatter as a function of time. At any given time, the received backscattered energy comes from a series of annuli centered around the source.

In this chapter the results obtained have been for two-dimensional environments. For cylindrically symmetric (r, z) environments the assumption made is that out-of-plane scattering can be neglected. The scattering scenario in Fig. 2-4 is three-dimensional, but the theory developed above can be applied if the roughness is assumed to be cylindrically symmetric. The change of variables discussed in Appendix A.7 is used to transform the problem to a 2D one. A solution for the two-dimensional problem is found (see Appendix A.6), and the change of variables is applied again to give the result for the cylindrically symmetric ocean.

For the $m \to n$ scattering path, the center of the insonified annulus at time t is

$$r_{nm}(t) = (t - \tau/2)\frac{c_n c_m}{c_n + c_m} \tag{2.91}$$

The limits of the annulus are given by $[r_1, r_2] = [r_{nm}(t) - \Delta r_{nm}, r_{nm}(t) + \Delta r_{nm}]$, where

$$\Delta r_{nm} = \frac{\tau}{2}\frac{c_n c_m}{c_n + c_m} \tag{2.92}$$

This relationship can be used to find the backscattering as a function of time. In section 2.3 the backscattered field generated by a continuous source was calculated for a plane geometry. Applying the scaling factor for the cylindrical ocean and integrating over the insonified area gives

$$s_b(z,t) \;=\; \sum_{n,m} \int_{-r_1}^{-r_2} dr' \sqrt{\frac{2}{\pi r'}}\,\gamma(r') e^{(\alpha_n+\alpha_m)r'} e^{i(-\bar{q}_n-\bar{q}_m)r'} \psi_n(z) b_{nm}. \qquad (2.93)$$

The backscattered intensity as a function of time is found from the second-moment expectation of this equation. The calculations involved are shown in Appendix A.6. In carrying out the calculations, several assumptions are made. First, only the coherent terms in the modal summation ($n = l$, $m = p$) are retained. The other, off-diagonal modal terms are not expected to influence the overall scattering energy much. Secondly, the pulse is assumed to be short enough that attenuation across the insonified area Δr_{nm} is small. If these assumptions are made, the expected intensity is given by:

$$\begin{aligned} < I_b(t,z) > \;&=\; < \gamma^2 > \sum_{n,m} P(-q_n - k_m) \Delta r_{nm} \frac{e^{-2(\alpha_n+\alpha_m)r_{nm}(t)}}{r_{nm}(t)} \cdot \\ & \quad \mid 4\psi_n(z) b_{nm} \mid^2 . \qquad (2.94) \end{aligned}$$

The backscattered intensity depends on the power spectrum and scattering amplitudes calculated previously. In addition, it is proportional to the width of the insonified area. Attenuation and cylindrical spreading of the wave as it travels to and from the insonified area at $r_{nm}(t)$ are taken into account. This result is very similar in form to the result derived by Ellis; the main difference is that the scattering amplitude b_{nm} above is found from the physical properties of the bottom, while Ellis uses an empirically determined coefficient in Lambert's law.

In comparing numerical results, it is convenient to normalize the energy in the pulse. This is done by setting the pulse amplitude to $1/\tau$.

2.6 Summary

The theoretical work in this chapter has shown how rough surface scattering theories can be combined with the integral theorem to calculate ocean reverberation. Excitations for the normal modes of the scattered field were found, and used to calculate the ensemble statistics of the scattered field. The important contributions of the chapter can be summarized in a few points. First, the elements of the modal transfer matrix are found from first principles. No empirical constants or phenomenological descriptions of the scattering were used. Second, using the KS theory to find the modal excitations allows us to deal with more complicated interfaces. The results presented here for scattering from a rough elastic bottom are, to the author's knowledge, the first time bottom elasticity has been included in a modal scattering theory. Third, the field is written as a coherent sum of modes, retaining phase information about the interference pattern of the scattered field. Lastly, expressing the ensemble statistics of the scattering in terms of modal sums rather than wavenumber integrals greatly reduces the computational work required.

Chapter 3

Volume scattering in ocean waveguides

The previous chapter has examined the scattering of sound by roughness at interfaces between different layers in the ocean. Sound is also scattered from inhomogeneities in the volume of the ocean. In the water column internal waves and other oceanographic processes perturb the ocean, giving rise to small fluctuations in the sound speed and density of the water. As discussed by Chernov [11] and others, the density fluctuations in the water are generally much less important acoustically than the sound speed fluctuations and can be neglected. The ocean seabed is also characterized by random fluctuations in density and sound speed; however in this case the density fluctuations cannot be ignored and are often dominant [86, 31]. Scattering from density fluctuations tends to greatly increase the backscattered energy, as is illustrated below. These effects can be especially important for low frequency shallow-water propagation, which tends to be dominated by bottom interaction.

In this chapter we develop new methods for modeling volume scattering in the ocean. In the first section, a new, self-consistent theory for scattering from random sound speed and density fluctuations in a three dimensional ocean is presented. This work allows calculation of the mean field attenuation due to volume scattering. The statistics of the scattered field in the waveguide are also found.

The next two sections concentrate on scattering of low-frequency sound from random layers in fluid sediment bottoms. First we model the scattering from a plane wave incident on the ocean bottom, without taking waveguide effects into account. Numerical examples are used to show the different effects of sound speed and density fluctuations over a range of parameter values. Although predicted qualitatively earlier by Chernov, the results shown help to develop a physical intuition about bottom scattering. They also show that out-of-plane scattering is quite important.

Next, propagation of normal modes in a shallow-water waveguide is studied. This study is broken into several stages. First, a perturbation method is developed and used to estimate mean field normal mode attenuation coefficients due to scattering. Comparison with earlier published work shows excellent agreement. The statistics of the scattered field are then studied, and expressions for the reverberant field in a 2D ocean are derived. Numerical results for the scattered field will be shown in the next chapter. In the final section, scattering by internal wave-induced sound speed fluctuations in the ocean is briefly discussed.

The scattering theory described here is analogous to the KS rough-surface scattering theory, and the results obtained are written in a form similar to the rough scattering results of the last chapter. This similarity aids comparison of the different scattering mechanisms.

3.1 Self-consistent volume scattering theory

The wave equation for inhomogeneous medium has been derived by several authors, including Chernov [11]. Assuming harmonic time dependence, we write the inhomogeneous Helmholtz equation:

$$[\nabla^2 + k^2(\vec{r}, z)]p(\vec{r}, z) - \frac{\nabla\rho(\vec{r}, z)}{\rho(\vec{r}, z)} \cdot \nabla p(\vec{r}, z) = S_\omega \delta(z - z_s)\delta(\vec{r}) \tag{3.1}$$

where the source is a point source of strength S_ω, and $\vec{r} = (x, y)$. We assume that there are small variations in both density and sound speed. If the background density is constant, we can write

$$\begin{aligned} \rho(\vec{r}, z) &= \rho_0 + \delta\rho(\vec{r}, z) \\ c(\vec{r}, z) &= c_0(z) + \delta c(\vec{r}, z) \end{aligned} \tag{3.2}$$

Expanding the Helmholtz equation to include first order-small terms in ρ and c gives

$$[\nabla^2 + k_0^2(z) - \frac{2\delta c(\vec{r}, z)k_0^2(z)}{c_0(z)}]p(\vec{r}, z) - \frac{\nabla(\delta\rho(\vec{r}, z))}{\rho_0} \cdot \nabla p(\vec{r}, z) = S_\omega \delta(z - z_s)\delta(\vec{r}) \tag{3.3}$$

Next we expand the pressure field in terms of a coherent, mean field and an incoherent diffusely scattered field:

$$p(\vec{r}, z) =< p(\vec{r}, z) > +s(\vec{r}, z) \tag{3.4}$$

Inserting this expansion in the equation above and averaging (remembering that sound speed and density fluctuations are zero mean) gives an equation for the coherent field:

$$\begin{aligned}[\nabla^2 + k_0^2(z)] < p(\vec{r}, z) > \; &- \; < \frac{2\delta c(\vec{r}, z) k_0^2(z)}{c_0(z)} s(\vec{r}, z) > \\ &- \; \frac{1}{\rho_0} < \nabla(\delta\rho(\vec{r}, z)) \cdot \nabla s(\vec{r}, z) >= S_\omega \delta(z - z_s)\delta(\vec{r})\end{aligned} \tag{3.5}$$

Subtracting this equation from the full unaveraged Helmholtz equation, we can get an expression for the scattered field:

$$[\nabla^2 + k_0^2(z)] s(\vec{r}, z) = \frac{2\delta c(\vec{r}, z) k_0^2(z)}{c_0(z)} < p(\vec{r}, z) > + \frac{1}{\rho_0} \nabla(\delta\rho(\vec{r}, z)) \cdot \nabla < p(\vec{r}, z) > \tag{3.6}$$

This equation is equivalent to Eq. 2 in Hines [31].

The two forcing terms on the RHS result from propagation of the mean field through the medium fluctuations. The first term accounts for scattering generated by sound speed fluctuations, and is monopole-like. The second term, which represents scattering from density fluctuations, depends on the derivatives of the acoustic field and the inhomogeneities. We therefore expect it to have a more complicated scattering pattern.

The problem can be simplified by assuming that variations in the sound speed and density are linked, since the sound speed is a function of density. Sound speed and density are then written in terms of some background variable. In the water column temperature is generally taken to be the background variable, as in Chernov. Hines, studying scattering from a random sediment bottom, expressed fluctuations in the sound speed and density as functions of the bottom *porosity* P [31]:

$$\begin{aligned}\delta c &= \frac{\partial c}{\partial P} \delta P(\vec{r}, z) \\ \delta\rho &= \frac{\partial\rho}{\partial P} \delta P(\vec{r}, z)\end{aligned} \tag{3.7}$$

where δP is the variation in the bottom porosity. Hines gives empirical values of the derivatives to be $\frac{\partial\rho}{\partial P} = -1.440\frac{g}{cm^3}$ and $\frac{\partial c}{\partial P} = -570\frac{m}{s}$. Here we follow Hines and consider the the material properties to be functions of porosity, remembering that very similar results are obtained if temperature is the fluctuating background variable.

We can rewrite the equations above, using the notation

$$\mu_c(z) \equiv \frac{2k_0^2(z)\frac{\partial c}{\partial P}}{c_0(z)}$$

$$\mu_\rho \equiv \frac{1}{\rho_0}\frac{\partial \rho}{\partial P} \tag{3.8}$$

to simplify the expressions. The mean field equation is rewritten as

$$\begin{aligned}
[\nabla^2 &+ k_0^2(z)] < p(\vec{r}, z) > -\mu_c(z) < \delta P(\vec{r}, z) s(\vec{r}, z) > \\
&- \mu_\rho < \nabla(\delta P(\vec{r}, z)) \cdot \nabla s(\vec{r}, z) >= S_\omega \delta(z - z_s)\delta(\vec{r})
\end{aligned} \tag{3.9}$$

and the scattered field equation becomes

$$[\nabla^2 + k_0^2(z)] s(\vec{r}, z) = \mu_c(z)\delta P(\vec{r}, z) < p(\vec{r}, z) > +\mu_\rho \nabla(\delta P(\vec{r}, z)) \cdot \nabla < p(\vec{r}, z) > \tag{3.10}$$

Our solution proceeds as follows: the equations above are Fourier transformed to yield expressions in the form of the depth-separated wave equation. We then find a solution for the transformed scattered field $\tilde{s}$ in terms of the coherent field. This solution is substituted into the transformed version of Eq. 3.9 to give a self-consistent equation for the coherent field. This equation will let us calculate the loss of coherent field energy due to scattering.

We begin by applying the 2-D wavenumber transform, Eq. 2.10. This yields (see App. B.3 for details):

$$\begin{aligned}
\left[\frac{\partial^2}{\partial z^2}\right. &+ \left. k_0^2(z) - \vec{q}^{\,2}\right] \tilde{s}(\vec{q}, z) = \\
&+ \frac{1}{2\pi}\int d^2\vec{k'} \left\{[\mu_c(z) - \mu_\rho(\vec{q} - \vec{k'}] \cdot \vec{k'})\delta\tilde{P}(\vec{q} - \vec{k'}, z) < \tilde{p}(\vec{k'}, z) >\right. \\
&+ \left. \mu_\rho \frac{\partial \delta\tilde{P}(\vec{q} - \vec{k'}, z)}{\partial z}\frac{\partial < \tilde{p}(\vec{k'}, z) >}{\partial z}\right\}
\end{aligned} \tag{3.11}$$

The horizontal derivatives in the density term have become algebraic factors of k and q. The RHS in the equation for the scattered field is seen to be a source term distributed over depth, and we can write the scattered field as [12, p. 42]

$$\begin{aligned}
\tilde{s}(\vec{q}, z) = -\int\int \quad dz_0 \quad d\vec{k'} G_\omega(\vec{q}, z, z_0) &\left[b_1(q, k')\delta\tilde{P}(\vec{q} - \vec{k'}, z) < \tilde{p}(\vec{k'}, z_0) > +\right. \\
&\left. \mu_\rho \frac{\partial \delta\tilde{P}(\vec{q} - \vec{k'}, z_0)}{\partial z_0}\frac{\partial < \tilde{p}(\vec{k'}, z_0) >}{\partial z_0}\right]
\end{aligned} \tag{3.12}$$

where

$$b_1(q, k) = \mu_c(z_0) - \mu_\rho(\vec{q} - \vec{k}) \cdot \vec{k} \tag{3.13}$$

Similarly we can transform the mean field equation, giving (see App. B)

$$
\begin{aligned}
[\frac{\partial^2}{\partial z^2} + k_0^2(z) \quad &- \quad \vec{k}^2] < \tilde{p}(\vec{k}, z) > - \frac{1}{2\pi} \int d^2\vec{q} \Big[(\mu_c(z) - \mu_\rho(\vec{k} - \vec{q}) \cdot \vec{q}) < \delta\tilde{P}(\vec{k} - \vec{q}, z) \tilde{s}(\vec{q}, z) > \\
&+ \quad \mu_\rho < \frac{\partial \delta\tilde{P}(\vec{k} - \vec{q}, z)}{\partial z} \frac{\partial \tilde{s}(\vec{q}, z)}{\partial z} > \Big] = S_\omega \delta(z - z_s) \delta(\vec{r})
\end{aligned}
\tag{3.14}
$$

Equations 3.12 and 3.14 are combined to eliminate the scattered field variable $\tilde{s}$, giving an equation only involving the coherent field $< \tilde{p} >$. This substitution results in several second-moment expectations of the porosity fluctuations and their z-derivatives. We model the fluctuation statistics as being described by a correlation function which is separable into horizontal and vertical components:

$$
< \delta P(\vec{r}, z) \delta P(\vec{r} + \vec{\rho}, z_0) > = < \sigma^2 > N(\vec{\rho}) M(z - z_0) \tag{3.15}
$$

This is rewritten in the wavenumber domain as

$$
< \delta\tilde{P}(\vec{k}, z) \delta\tilde{P}(\vec{q}, z_0) > = 2\pi < \sigma^2 > P_H(\vec{q}) \delta(\vec{k} + \vec{q}) M(z - z_0) \tag{3.16}
$$

where P_H is the power spectrum of horizontal fluctuations. Vertical derivatives of expectations involving δP translate into z-derivatives of M; for example

$$
< \delta\tilde{P}(\vec{k}, z) \frac{\partial \delta\tilde{P}(\vec{q}, z_0)}{\partial z_0} > = 2\pi < \sigma^2 > P_H(\vec{q}) \delta(\vec{k} + \vec{q}) \frac{\partial M(z - z_0)}{\partial z_0}. \tag{3.17}
$$

These $\frac{\partial M}{\partial z}$ and $\frac{\partial M}{\partial z_0}$ terms can be eliminated from the depth integrals using integration by parts, following the procedure developed by Chernov. The detailed calculations are quite messy and are shown in Appendix B.3. The only restrictions placed on M are that $M(z - z_0) \to 0$ and and $\frac{\partial M(z - z_0)}{\partial z} \to 0$ as the depth separation $z - z_0$ becomes large. These conditions are satisfied by a number of physically reasonable correlation functions, for example Gaussian or decaying exponential forms of $M(z - z_0)$.

After the integrations by parts, the final form of the mean field equation is:

$$
\begin{aligned}
[\frac{\partial^2}{\partial z^2} \quad &+ \quad k_0^2(z) - \vec{k}^2] < \tilde{p}(\vec{k}, z) > + < \sigma^2 > \int \int d^2\vec{q} dz_0 M(z - z_0) P_H(\vec{q} - \vec{k}) \\
&\Big[F_1(\vec{q}, \vec{k}, z_0) < \tilde{p}(\vec{k}, z_0) > + F_2(\vec{q}, \vec{k}, z_0) \frac{\partial < \tilde{p}(\vec{k}, z_0) >}{\partial z_0} \Big] = \frac{S_\omega}{2\pi} \delta(z - z_s)
\end{aligned}
\tag{3.18}
$$

The quantities in the correction term are

$$F_1(\vec{q},\vec{k},z_0) = a_1 a_2 G_\omega(\vec{q},z,z_0) + \mu_\rho(a_3 \frac{\partial^2 G_\omega(\vec{q},z,z_0)}{\partial z \partial z_0} - a_4 \frac{\partial G_\omega(\vec{q},z,z_0)}{\partial z}) \tag{3.19}$$

and

$$F_2(\vec{q},\vec{k},z_0) = \mu_\rho(a_3 - a_1)\frac{\partial G_\omega(\vec{q},z,z_0)}{\partial z_0} \tag{3.20}$$

where

$$\begin{aligned} a_1 &= \mu_c(z_0) - \mu_\rho(\vec{k}-\vec{q})\cdot\vec{q} \\ a_2 &= \mu_c(z_0) + \mu_\rho(k_0^2 - \vec{q}\cdot\vec{k}) \\ a_3 &= \mu_c(z_0) + \mu_\rho(2k_0^2 - \vec{k}\cdot(\vec{k}+\vec{q})) \\ a_4 &= \frac{2\mu_\rho k_0^2(z_0) + 3\mu_c(z_0)}{c_0(z_0)}\frac{\partial c_0}{\partial z_0} \end{aligned} \tag{3.21}$$

The complexity of this expression makes it difficult to interpret physically, but we can give some meaning to the terms. The integral term describes the loss of energy from the coherent field due to scattering. From the calculations shown in Appendix C, we also see that the algebraic terms involving $\vec{q}$, $\vec{k}$, and $k_0^2(z)$ multiplying the μ_ρ terms in a_1 - a_3 result from horizontal and vertical derivatives. All terms including z-derivatives of the pressure field or Green's function also involve only the density fluctuations. These terms all result from the spatial derivative term, $\frac{\Delta\rho(\vec{r},z)}{\rho(\vec{r},z)}$, in the inhomogeneous Helmholtz equation. The term a_4 takes account of any sound speed gradient.

This integro-differential equation is in general difficult to solve. However, if the vertical correlation length of the scatterers is small compared to a wavelength, a solution can be found. An example of this approach is shown later.

3.2 Plane-wave scattering from sediment bottoms: Power spectral density

Next we study plane wave scattering from a sediment bottom. A great deal of physical insight can be obtained by looking at the power spectral density, or power scattered into each wavenumber q. This is found as a special case of the cross-spectral density, the second-moment expectation of the transformed scattered field.

The expectation involves cross-terms involving expectations of M and its z-derivatives, which can be simplified using integration by parts. The detailed calculations are discussed in Appendix B.4, with the final result

$$\begin{aligned}
< \tilde{s}(\vec{q}_1, z_1) \quad \tilde{s}^*(\vec{q}_2, z_2) \quad &>= 2\pi < \sigma^2 > \int\int\int\int dz_0 dz' d\vec{k}_1 d\vec{k}_2 S(\vec{q}_1 - \vec{k}_m) \\
&M(z_0 - z')\delta(\vec{q}_1 - \vec{k}_1 - \vec{q}_2 + \vec{k}_2) \\
&\left[[\Delta^{(1)}(\vec{k}_1)\frac{\partial G_\omega(\vec{q}_1, z_1, z_0)}{\partial z_0} + \Delta^{(2)}(\vec{k}_1, \vec{q}_1)G_\omega(\vec{q}_1, z_1, z_0)\right] \\
&\left[[\Delta^{(1)}(\vec{k}_2)\frac{\partial G_\omega(\vec{q}_2, z_2, z')}{\partial z'} + \Delta^{(2)}(\vec{k}_2), \vec{q}_2)G_\omega(\vec{q}_2, z_2, z')\right]^* \quad (3.22)
\end{aligned}$$

where

$$\begin{aligned}
\Delta^{(1)}(\vec{k}, z) &= -\mu_\rho \frac{\partial < \tilde{p}(\vec{k}, z) >}{\partial z} \\
\Delta^{(2)}(\vec{q}, \vec{k}, z) &= [\mu_c(z) + \mu_\rho(k_0^2(z) - \vec{q} \cdot \vec{k})]\frac{\partial < \tilde{p}(\vec{k}, z) >}{\partial z} \quad (3.23)
\end{aligned}$$

To find the power spectral density, we consider a single wavenumber and single depth, or $q_1 = q_2 \equiv q$ and $z_1 = z_2 \equiv z$. The delta function then collapses to $k_1 = k_2$.

Experimental studies have shown that the vertical correlation lengths of fluctuations in sediment bottoms are usually quite short. Since we are considering low-frequency scattering from sediment bottoms, the vertical correlation length will be smaller than an acoustic wavelength. It is then reasonable to approximate the vertical correlation function as a delta function [75]:

$$M(z - z_0) \rightarrow \delta(z - z_0) \quad (3.24)$$

In the expression for the power spectral density removes one depth integral, giving $z = z_0$. The expected power spectral density is then given by

$$\begin{aligned}
< \tilde{s}(\vec{q}, z)\tilde{s}^*(\vec{q}, z) > &= 2\pi < \sigma^2 > \int dz_0 \int d\vec{k} P_H(\vec{q} - \vec{k}) \\
&\mid \Delta^{(1)} \frac{\partial G_\omega(\vec{q}, z, z_0)}{\partial z_0} + \Delta^{(2)} G_\omega(\vec{q}, z, z_0) \mid^2 \quad (3.25)
\end{aligned}$$

We consider the case of a single plane wave incident on the sediment from the water column, scattering into plane waves in the sediment. The incident field in the bottom is of the form

$$< \tilde{p}(\vec{k}, z_0) >= T_{12}(k)e^{-ik_{z2}z_0}. \quad (3.26)$$

where $T_{12}(k)$ is the transmission coefficient from the water into the sediment. We choose the Green's function to be the free-space Green's function. This means we can only evaluate the scattered field for receivers in the bottom medium. We will evaluate it at $z = 0$, the water-sediment interface. The depth-dependent Green's function is given by

$$G_\omega(\vec{q}, z, z_0) = -\frac{e^{-iq_{z2}|z-z_0|}}{4\pi i q_{z2}} \tag{3.27}$$

This expression has a square root singularity in the Green's function. This singularity is not physically meaningful and can be removed by changing the variables of integration [38], so it is not shown in the following plots.

The scattered field is strongly affected by the power spectrum chosen to represent the inhomogeneities. For these calculations both two-dimensional Gaussian and Goff-Jordan spectra are used. These spectra are simple generalizations of the 1D spectra defined in the last chapter:

$$\begin{aligned} P_{Gauss}(\vec{q}) &= \frac{L_x L_y}{2} e^{-\frac{(L_x q_x)^2 + (L_y q_y)^2}{4}} \\ P_{Goff-Jordan}(\vec{q}) &= L_x L_y \left[((L_x q_x)^2 + (L_y q_y)^2) + 1 \right]^{-2} \end{aligned} \tag{3.28}$$

where L_x and L_y are the correlation lengths in x and y respectively. The Goff-Jordan spectrum is more peaked near its maximum and contains much more energy at higher wavenumbers. This spectrum has been used in modeling rough surface scattering [47], and is chosen to reflect the idea that we expect variations in nature at many length scales. Also, it describes a power-law roll off at high wavenumbers like that measured by Yamamoto [85].

Figures 3-1 and 3-2 compare the effect of the choice of power spectrum. Results for correlation lengths of 10 m. and 1 m. are shown. A 10 m. correlation length was used by Tang in his modeling [75], and shorter horizontal correlation lengths were assumed by Hines[31]. For these plots scattering from sound speed fluctuations alone is included. The spectrum is plotted vs. horizontal wavenumbers in the x and y directions. A $100Hz$ plane wave is assumed to be incident on the bottom along the x-axis ($q_y = 0$), at a 10 degree vertical angle. The bottom properties are $\rho = 1.9g/cm^3$, $c_b = 1650m/s$, and $\frac{\delta c}{c_0} = 0.1$. For this combination of incident angle and bottom type the incident wave is evanescent in the bottom. Shown on the plot are the sediment wavenumber k_b (inner circle) and water wavenumber k_w (outer circle). Thus wavenumbers inside the $\mid k \mid = k_b$ circle correspond to the continuous spectrum, wavenumbers between the circles correspond to the discrete

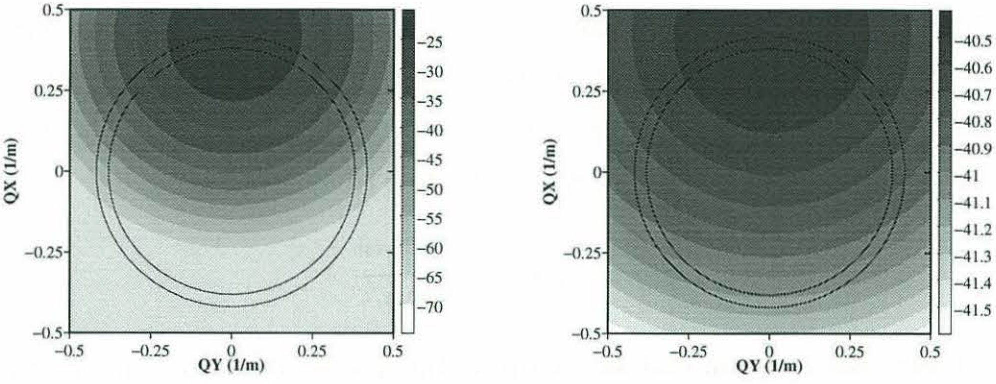

a. CL = 10 m.

b. CL = 1 m.

Figure 3-1: Plane-wave scattering from sound speed fluctuations. f = 100 Hz; Gaussian power spectrum, 10 degree incident wave.

spectrum, and wavenumbers outside the $\mid k \mid= k_w$ circle correspond to waves which are evanescent in both the water and sediment. Comparing the plots for 10 m. correlation lengths, the most striking difference is that the backscatter is greatly enhanced with the Goff-Jordan spectrum (Figure 3-2) due to the longer tails of the power spectrum. Strong out-of-plane scattering is seen with both spectra, though a peak is observed at angles close to in-plane. In both cases the scattering is basically forward-directed, with the peak in scattered energy centered around the specular direction. Decreasing the correlation length to 1 m. gives a much broader distribution of scattered energy. This is expected, since in the limit of small correlation length the inhomogeneities can be thought of as a random distribution of independent point scatterers. Each of these point scatterers radiates isotropically, so the overall scattering pattern is more diffuse. Decreasing the correlation length is also seen to reduce the peak scattered power considerably. This can be understood by remembering that sound will scatter most strongly from objects roughly the size of the wavelength or larger. Since the acoustic wavelength in this case is 16.5 m., most of the sound speed fluctuations for the 1 m. correlation length will have horizontal scales much less than a wavelength.

Figure 3-3 shows scattering from both sound speed and density fluctuations in the sediment bottom. For the 10 m. correlation length, the scattering intensity levels are only slightly higher than in the case without density fluctuations. Thus we conclude that, for long horizontal correlation lengths, scattering from sound speed fluctuations is dominant. When the correlation length is decreased to 1 m., the density scattering is dominant. The scattered field levels are increased over the 1 m. correlation length case with δc fluctuations only.

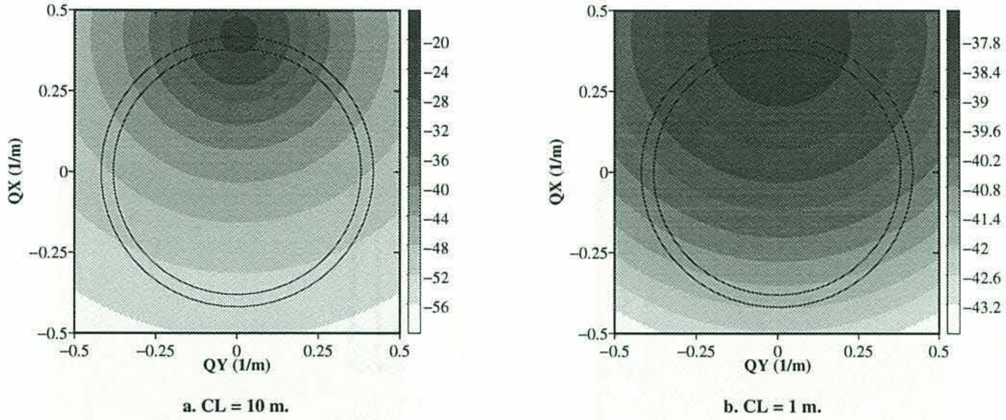

Figure 3-2: Plane-wave scattering from sound speed fluctuations. f = 100 Hz; Goff-Jordan power spectrum, 10 degree incident wave.

Most importantly, the maximum is now in the *backscattered* direction. This backscattering was predicted by Chernov [11] for 1-D scattering, and can be seen in the $\vec{q}-\vec{k}$ term in Eq. 3.12, which shows the density scattering contribution has a null in the forward direction. Since experimental data shows the short correlation length is perhaps more typical for most bottoms, this effect is quite important, especially when modeling monostatic experiments in shallow water.

The results so far have used Hines' empirically determined values of $\frac{\partial c}{\partial P}$ and $\frac{\partial \rho}{\partial P}$. These values were determined from a limited dataset, and we can expect variations depending on the particular sediment bottom. Hines' values predict that the normalized density fluctuations $\frac{\delta\rho}{\rho_0}$ are about twice the normalized sound speed fluctuations $\frac{\delta c}{c_0}$. In Fig. 3-4results are shown in which $\frac{\delta\rho}{\rho_0}$ is adjusted so the normalized density fluctuations are equal to ($K = 1$) and half of ($K = 0.5$) the normalized sound speed fluctuations. The density scattering is still seen to have a very strong effect, though now the scattering is almost entirely into the continuous spectrum. Interestingly these plots would be reasonably well described by Lambert's law, which predicts the maximum scattered field in the vertical direction.

We can also use this approach to study scattering from a bottom with an anisotropic power spectrum. Fig. 3-5 shows scattering of plane waves on a bottom with a correlation length of 2 m. in x and 10 m. in y. Increasing the correlation length in y gives a power spectrum with much less width in q_y. In Fig. 3-5 we let a plane wave be incident on the bottom at a vertical angle of 10 degrees, and horizontal angles of 0 (along the x axis), 45 degrees, and 90 degrees (along the y axis). From observing the plots we see that the anisotropy causes the scattered field to be skewed away from the incident angle for incident

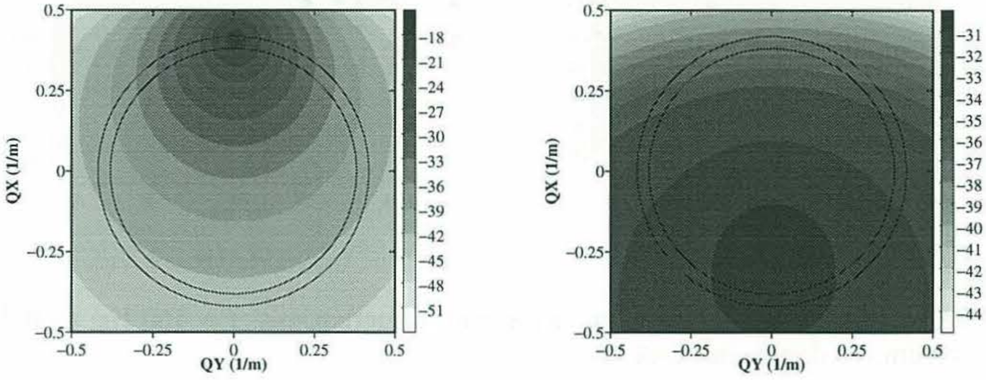

a. CL = 10 m.

b. CL = 1 m.

Figure 3-3: Plane-wave scattering from sound speed and density fluctuations. f = 100 Hz; Goff-Jordan power spectrum, 10 degree incident wave.

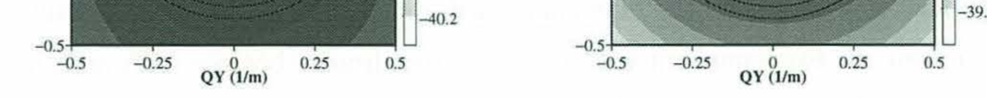

a. K = 1

b. K = 0.5

Figure 3-4: Plane-wave scattering from sound speed and density fluctuations. Same as above, but ratio K of normalized sound speed and density fluctuations is varied; equal for K = 1, normalized density fluctuations halved for K = 0.5

angles not lined up with the axes of the bottom. Comparing the 0 and 90 degree cases, we see the shorter correlation length in x causes increased scattering into the continuous spectrum for the 0 degree incident wave, vs. increased out-of-plane scattering for a wave incident along along the y axis.

3.3 Modal scattering from random sediment bottoms

In shallow water at low frequencies the acoustic field is often well described as a sum of a reasonably small number of normal modes. This leads us to specialize the theory developed above to consider scattering of a modal sound field from inhomogeneities in fluid sediment bottoms. In doing so we will make a number of simplifying assumptions. The most useful of these, discussed above, is that the vertical correlation function can be approximated as a delta function. The second major simplification made is that the sound speed is constant in the layer where volume fluctuations are present. This assumption is limiting, but will still allow us to examine the basic scattering physics. The main advantage of studying isovelocity layers is that the incident field can be written in terms of up- and down-going plane waves. This allows the depth integrals in the scattered field expressions to found analytically. The integrals over the incident field modes and their derivatives must otherwise be performed numerically, making the calculations much slower and less accurate.

KRAKEN or any other normal mode code can used to find the mode shapes and eigenvalues for the waveguide. The continuous spectrum contribution is included by introducing a *false bottom*, a pressure-release boundary sufficiently deep in the sediment that attenuation will kill off unphysical reflections from the fictitious interface. The modal problem is then converted to a proper Sturm-Liouville problem and all modes are proper modes. Since there are both up- and down-going plane waves in the scattering layer, we write the mode shape as

$$\psi_n(z) = \left[\begin{array}{ll} \zeta_n(z), & z < z_1 \\ A_n e^{-ik_{zn}(z-z_1)} + B_n e^{ik_{zn}(z-z_1)}, & z > z_1 \end{array} \right. \tag{3.29}$$

where $\zeta_n(z)$ are the mode shapes found by the normal mode program, and z_1 is the top of the volume scattering layer. These plane waves propagate in the bottom at angles found from

$$k_{zn} = \sqrt{k_b^2 - Re(k_n)^2} \tag{3.30}$$

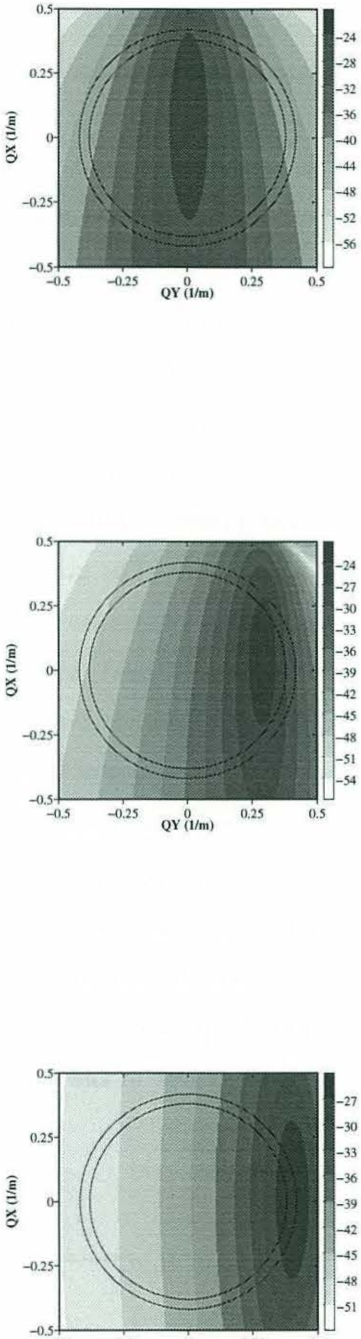

Figure 3-5: Plane-wave scattering from anisotropic sound speed and density fluctuations, for incident angles of 0, 45, and 90 degrees. f = 100 Hz; Goff-Jordan power spectrum; CLx = 2 m, CLy = 10 m.

where k_b is the bottom wavenumber. From the boundary conditions of continuity of pressure and normal velocity we find

$$A_n = \frac{1}{2}\left(\zeta_n(z_1) - \frac{\rho_2}{\rho_1 \alpha_n}\zeta'(z_1)\right) \tag{3.31}$$

$$B_n = \frac{1}{2}\left(\zeta_n(z_1) + \frac{\rho_2}{\rho_1 \alpha_n}\zeta'(z_1)\right) \tag{3.32}$$

One problem which arises is that of dealing with the effects of *attenuation* in the bottom. The modal attenuations calculated by a normal mode program such as KRAKEN represent an integrated attenuation over the full mode shape, and cannot be easily related to plane wave attenuations. Instead, the sediment attenuation is included by introducing an imaginary part of the bottom wavenumber:

$$\tilde{k_b} = k_b(1 - i\delta) \tag{3.33}$$

If the sediment attenuation is given in units of dB/λ, the imaginary part δ is given by [38, Chap 2]

$$\delta \approx \frac{\alpha}{54.58} \tag{3.34}$$

This suggests the following approach: first, the eigenvalues and mode shapes at the water-sediment interface are found numerically. Next, the *real* parts of the eigenvalues and mode shapes are used to estimate the amplitudes of the plane waves in the scattering layer. Finally, the vertical wavenuber α_b is found using the complex bottom wavenumber, which accounts for attenuation in the bottom.

3.3.1 Mode attenuation coefficients

In this section the mean field equation is solved to find mean-field modal attenuations. First we must rearrange the mean field equation slightly. If we restrict ourselves to calculating attenuations for the propagating modes of the waveguide only, we can take advantage of the fact that these modes are exponentially decaying in the bottom to write

$$\frac{\partial < \tilde{p}(\vec{k}, z) >}{\partial z} = -\alpha_b < \tilde{p}(\vec{k}, z) > \tag{3.35}$$

where $\alpha_b = \sqrt{\vec{k}^2 - k_b^2}$. This lets us write the homogeneous mean field equation (3.18) in the form

$$[\frac{\partial^2}{\partial z^2} + k_b^2 - \vec{k}^2] < \tilde{p}(\vec{k}, z) > + < \sigma^2 > f(\vec{k}, z) < \tilde{p}(\vec{k}, z) >= 0 \tag{3.36}$$

where $f(\vec{k}, z)$ comes from combining the F_1 and F_2 terms. It is clear that the last term is a $O(\sigma^2)$ perturbation to the mean field. Since the scattering theory retains terms only up to order $O(\sigma^2)$, it is consistent to use the unperturbed eigenvalues and eigenfunctions when calculating $f(\vec{k}_n, z)$; i.e. $f(\vec{k}_n, z) \approx f(\vec{k}_{n_0}, z)$. This argument was made by Kuperman [43] in his original paper on rough surface scattering.

We next substitute the modal forms of the Green's function (as a sum over modes m) into the mean-field equation, and switch to polar coordinates: $\int d^2\vec{q} = \int\int q dq d\theta$. Integrating over q exposes poles at $q = q_m$, leaving the integration over θ. Physically, this means that the scattered field will travel in the modes of the waveguide, but can be scattered into any horizontal angle. The correction term above becomes

$$\begin{aligned} f(\vec{k}, z) &= \frac{iz_{CL}}{2\rho(z)} \int d\theta \sum_{m=1}^{M} P_H(\vec{q}_m - \vec{k})[a_1 a_2 \psi_m^2(z) + \mu_\rho a_3 (\psi_m'(z))^2 - \\ & \quad \mu_\rho(a_4 - \alpha_b(z)(a_1 - a_2 + \mu_\rho[q_m^2 - k_0^2(z)]))\psi_m(z)\psi_m'(z)] \end{aligned} \tag{3.37}$$

Here we have left implicit the dependence of the a_i terms:

$$a_i = a_i(\vec{q}_m, \vec{k}, z) \tag{3.38}$$

where $\vec{q} = (q_m cos\theta, q_m sin\theta)$.

This equation can be rewritten in the form of an eigenvalue perturbation problem, giving

$$[\frac{\partial^2}{\partial z^2} + k_0^2(z)]\psi_n = k_n^2\psi_n - < \sigma^2 > f(\vec{k}_n, z)\psi_n \tag{3.39}$$

The new eigenvalue can then be found using perturbation theory, as described by Bender and Orzag [5]. Appendix B shows the first-order correction for the eigenvalue is:

$$\Delta k_n = \frac{< \sigma^2 >}{2k_{n0}} \int_0^D \frac{f(\vec{k}_{n_0}, z)\psi_n^2(z)}{\rho(z)} dz \tag{3.40}$$

The imaginary part of Δk_n is the mode attenuation coefficient.

To validate our approach, we compare our method to results obtained by D. Tang [75], who studied scattering from a bottom containing sound speed fluctuations only. Tang's code REF was used to calculate mean field plane-wave reflection coefficients for the sediment bottom. These reflection coefficients were used as a boundary condition for the normal mode code KRAKEN, which calculated the modified eigenvalues. The resulting change in the mode attenuation was taken to be Tang's prediction for scattering loss.

KRAKEN was then used to find the eigenvalues and mode shapes for the unperturbed scenario. These were used in Eq. 3.40 to calculate the mode attenuations using our method.

A simple scenario, shown in Fig. 3-6, was used for comparison. A 50 m. deep isovelocity water layer overlays a sediment halfspace, the upper 50 m. of which contains sound speed inhomogeneities. The inhomogeneities are assumed to have a 2D isotropic Gaussian correlation function in the horizontal and to be delta-correlated in the vertical. Attenuation in the water and sediment is neglected, so any attenuation is purely due to scattering.

Figure 3-7 shows the plane wave reflection coefficient for correlation function parameters which are used by Tang in his thesis: $\delta c_{rms}/c_0 = 0.1$, horizontal correlation length $l_0 = 10$ m., and vertical correlation length $z_{CL} = 1$ m.

When comparing the modal results with Tang's attenuation coefficients, a factor of two difference was found. In Figure 3-8, the results found by the modal approach were divided by two, giving the excellent agreement shown. Unfortunately the source of this difference has not been located yet, but likely is a result of an algebraic error in one of the two methods.

Figure 3-8 shows the modal attenuation coefficients for $f = 200Hz$, with the factor of two difference removed. When only scattering into the proper modes is allowed, the direct calculation significantly underestimates the actual modal attenuation. The continuous spectrum is then included numerically by introducing a false bottom at 400 m. depth (note we can allow a false bottom without any bottom attenuation only because we are interested here in scattering *into* the continuous spectrum; when calculating statistics of the scattered field we must always include bottom attenuation so the continuous spectrum modes will decay quickly with range). When these extra modes are included the estimates from the two methods agree quite well.

Next the fluid bottom, shallow water waveguide shown in Fig. 3-9 is considered. Both sound speed and density fluctuations are included. For notational convenience, we define a parameter σ, which is set equal to the normalized sound speed fluctuation $\delta c/c_0$. For a given σ the density fluctuations are found from the relationship between density and sound speed fluctuations given by Hines' constants. We again examine horizontal correlation lengths of 1

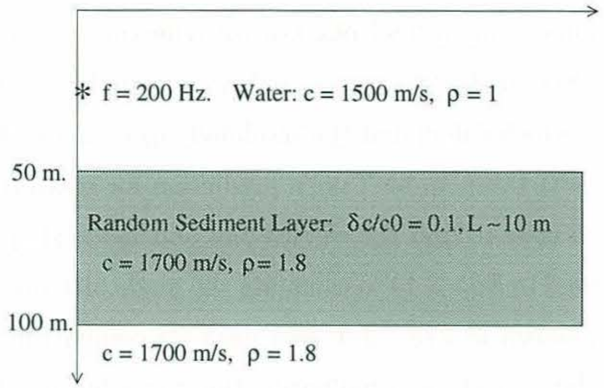

Figure 3-6: Scenario for comparison with Tang's results. f = 200 Hz; Gaussian spectrum, 10 m. correlation length, $\delta c/c_0 = 0.1$.

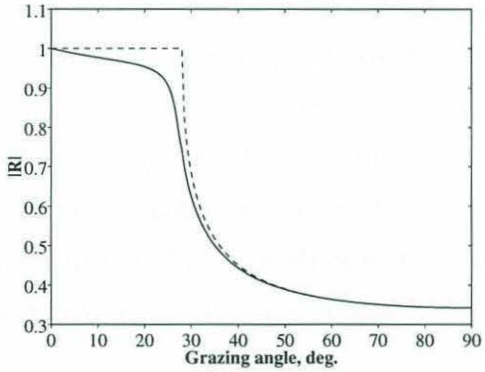

Figure 3-7: Reflection coefficients for scenario. Dashed line is for nonrandom bottom; solid line is for bottom with random layer.

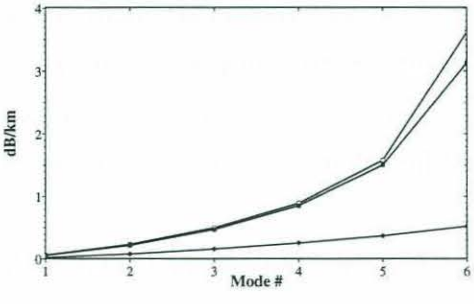

Figure 3-8: Comparison with Tang's results. Open boxes are from Tang; diamonds are modal solution including continuous spectrum modes; filled boxes are modal solution, proper modes only.

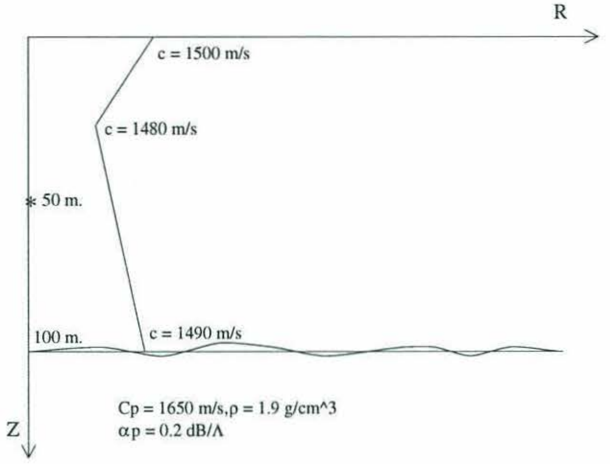

Figure 3-9: Shallow water scattering scenario.

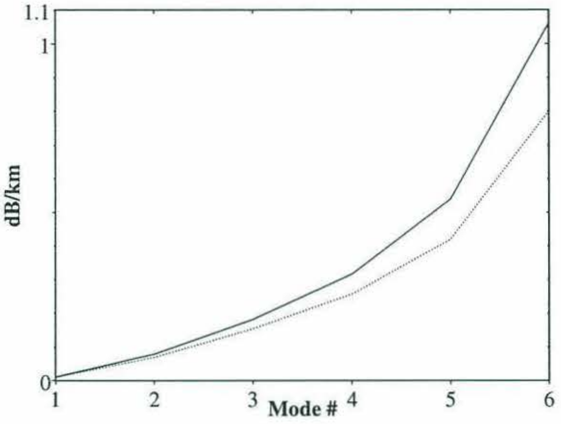

Figure 3-10: Mode attenuations for shallow water example. f = 100 Hz; Goff-Jordan spectrum, 10 m. correlation length, $\sigma = 0.1$. Solid line includes effect of both sound speed and density fluctuations, dotted line includes sound speed fluctuations only.

and 10 m. The random scattering layer is assumed to be between 100 and 150 m. depth. For the 10 m. correlation length, seen in Fig. 3-10, we see including density scattering causes only a slight increase in mode attenuation, while density fluctuations are the predominant cause of loss for the shorter 1 m. correlation length case (Fig. 3-11). This is in agreement with the earlier discussion. Finally, the full scattering loss with the 1 m. correlation length is shown in Figure 3-12 to be of roughly the same order of magnitude as the loss caused by a bottom attenuation of $0.1dB/\lambda$. Whether or not attenuation due to volume scattering is a significant attenuation mechanism will depend on the environment considered. However, we will see in the next chapter that the coherent field loss always affects the correlation statistics of the total field.

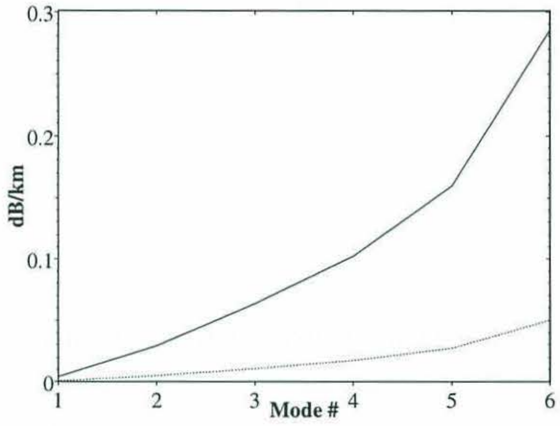

Figure 3-11: Mode attenuations for shallow water example. f = 100 Hz; Goff-Jordan spectrum, 1 m. correlation length, $\sigma = 0.1$. Solid line includes effect of both sound speed and density fluctuations, dotted line includes sound speed fluctuations only.

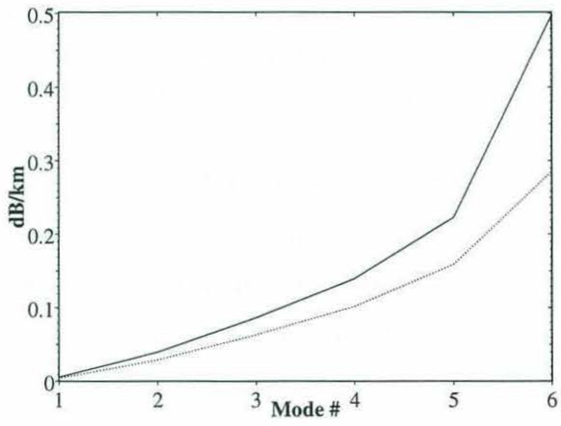

Figure 3-12: Mode attenuations for shallow water example. f = 100Hz; Goff-Jordan spectrum, 1 m. correlation length, $\sigma = 0.1$. Dotted line includes effect of both sound speed and density fluctuations, solid line shows attenuation due to volume absorption of 0.1 dB/λ.

3.3.2 Reverberant field statistics: 2D ocean

Perhaps the most useful application of this volume scattering theory is in calculating statistics of the reverberant and total field in ocean waveguides. Here we examine scattering in two-dimensional (x, z) or (r, z) waveguides. The results above have clearly demonstrated the importance of out-of-plane and three dimensional effects, so the scattered field statistics generated here cannot be expected to be fully realistic. However, the 2D simplification allows us to examine the interaction of scattering and waveguide physics with a greatly reduced computational load.

As was seen when studying rough surface scattering, the range-wavenumber transforms are defined so that similar expressions are obtained in the wavenumber domain whether the scenario is two- or three-dimensional in space. We can therefore write the 2D analog of Eq. 3.12, the transformed scattered field.

$$\begin{aligned}\tilde{s}(q,z) = -\int_{z_1}^{z_2} dz_0 \int \; dk \quad & G_\omega(q,z,z_0)\Big[b_1(q,k)\delta\tilde{P}(q-k,z) < \tilde{p}(k,z_0) > + \\ & \mu_\rho \frac{\partial \delta\tilde{P}(q-k,z_0)}{\partial z_0}\frac{\partial < \tilde{p}(k,z_0) >}{\partial z_0}\Big]\end{aligned} \tag{3.41}$$

where

$$b_1(q,k) = \mu_c(z_0) - \mu_\rho(q-k)k \tag{3.42}$$

and the scatterers are assumed to be in the layer bounded by $[z1, z2]$. As for rough surface scattering, the mean field and Green's function can be expressed in terms of modes. Since we are interested in finding the scattered field in the spatial domain, the porosity fluctuations are written in the spatial domain, using the Fourier transform. The scattered field is then found from the inverse transform:

$$\begin{aligned}s(x,z) &= -\frac{1}{2\pi}\int_{z_1}^{z_2} dz_0 \int dx' \int dq \int dk G_\omega(q,z,z_0)\left[b_1(q,k)\delta P(x',z) < \tilde{p}(k,z_0) > + \right. \\ & \left. \mu_\rho \frac{\partial \delta P(x',z_0)}{\partial z_0}\frac{\partial < \tilde{p}(k,z_0) >}{\partial z_0}\right] e^{-ikx'} e^{-iq(x-x')}\end{aligned} \tag{3.43}$$

The approach to calculating the second moments of the scattered field is the same as in the rough surface case, with the one difference being that vertical derivatives of the porosity are handled using integration by parts. The details of the calculation are shown in App. A.6. Numerical results for the scattered field are seen in the next Chapter.

3.4 Scattering from internal waves

The scattering theory developed in section 3.1 has so far only been used to estimate the effects of random variations in the sediment bottom. Inhomogeneities in the water column caused by oceanographic disturbances are also important scatterers, as is well known. In this section we address scattering from internal wave- induced variability in shallow water.

The theoretical development so far has included scattering from both sound speed and density inhomogeneities. As mentioned above, density fluctuations can be neglected when modeling fluctuations in the water column due to internal waves and other oceanographic disturbances. There are several reasons why this is so. First, experimental data reported by Beranek (cited by Chernov) for typical conditions in seawater show that

$$\begin{aligned} \frac{1}{c_0}(\frac{\partial c}{\partial T}) |_{p_0} &\sim 2 \times 10^{-3} \\ \frac{1}{\rho_0}(\frac{\partial \rho}{\partial T}) |_{p_0} &\sim 2.6 \times 10^{-4} \end{aligned} \tag{3.44}$$

i.e. velocity fluctuations are an order of magnitude larger than density fluctuations. Secondly, internal waves cover a very large range of length scales, with much of the energy concentrated at lower (near-tidal) frequencies with horizontal wavelengths measured in kilometers. As we saw above, when correlation lengths are long the scattering tends to be dominated by sound speed fluctuations.

The equations for the mean and scattered fields become much simpler when density fluctuations are neglected. Setting $\mu_\rho = 0$, the mean field equation is:

$$\begin{aligned} [\frac{\partial^2}{\partial z^2} + k_0^2(z) &- \vec{k}^2] < \tilde{p}(\vec{k}, z) > + < \sigma^2 > \int\int d^2\vec{q} dz_0 M(z - z_0) S(\vec{q} - \vec{k}) \\ & \mu_c^2(z_0) G_\omega(\vec{q}, z, z_0) < \tilde{p}(\vec{k}, z_0) > = \frac{S_\omega}{2\pi} \delta(z - z_s). \end{aligned} \tag{3.45}$$

The scattered field equation becomes

$$\tilde{s}(\vec{q}, z) = - \int\int dz_0 d\vec{k'} G_\omega(\vec{q}, z, z_0) \mu_c(z_0) \delta\tilde{T}(\vec{q} - \vec{k'}, z_0) < \tilde{p}(\vec{k'}, z_0) > \tag{3.46}$$

where the ocean temperature fluctuations are given by δT.

The types of internal wave motions possible are controlled by the density gradient profile in the ocean. The hydrodynamic equations of motion, together with the boundary conditions at the surface and seabed, form a boundary value problem which can be solved to find internal wave modes. In shallow water, current meter data has been explained by decomposition into a fairly small number of internal wave modes [18]. In the open ocean there are a large number of internal wave modes, which can be regarded as forming a continuum. The energy distribution versus frequency and wavenumber is surprisingly constant in the deep ocean and has been empirically described by the well-known Garrett-Munk internal wave spectrum [20]. In general, internal wave motions are correlated over large depths, which poses a problem for the acoustic theory presented in section 3.2. While the derivation makes no assumption about the vertical correlation structure of the sound speed fluctuations, it is not possible to find a perturbation solution of the mean field equation unless the fluctuations are delta-correlated.

There is one scenario of practical interest for which we *can* assume the fluctuations to be delta-correlated in depth. In shallow water there is often a strong density contrast, the thermocline, between the well-mixed warm surface water and colder deeper water. To first order this is modeled as a two-density ocean, and the hydrodynamic equations of motion can be solved to find the dispersion relations for internal waves traveling on the density interface. Wave motions on the thermocline have been studied in Massachusetts Bay [29] as well as in the South China Sea, where soliton waves were observed. Since these interface waves have no vertical structure it should be possible to model scattering from them using the theory presented above.

3.5 Summary

In this chapter a new self-consistent theory describing scattering from volume fluctuations in the ocean has been developed. This theory advances the state of the art because it includes scattering from both sound speed and density fluctuations, and allows calculation of coherent field attenuation due to scattering. Previous modeling including both sound speed and density fluctuations has been based on the Born approximation, and does not give coherent field scattering loss. The effects of including density fluctuations in a 3D ocean were examined in some detail. Density scattering was seen to increase backscattered energy. When the horizontal correlation length of scatterers is small, density scattering significantly changes the overall scattering pattern. The effects of out-of-plane scattering and anisotropic fluctuation statistics were illustrated as well. The theory was extended to find modal attenuations due to scattering, showing agreement with previous work for scenarios involving sound speed fluctuations only. For scenarios involving both sound speed and density fluctuations, modal scattering losses were shown to be comparable in magnitude to the effects of bottom attenuation. The theory can also be used to model reverberation in a 2D ocean, for comparison with the surface scattering results in the last chapter.

Chapter 4

Numerical results for ocean reverberation

In this chapter the theoretical tools developed above are used to study reverberation in 2D ocean environments. The reformulated KS rough scattering theory discussed in Chapter 2 and the volume scattering theory shown in Chapter 3 are implemented in a reverberation code (NMSCAT). This program can be used as a numerical laboratory to identify the important parameters of the scattering problem.

In the first section the rough surface scattering results are validated by comparing them with Schmidt & Kuperman's [68] wavenumber integration implementation (OASS). The two approaches are shown to agree quite well for both fluid and elastic bottoms, with the differences in predicted intensity generally being less than $1dB$. The reduction in computation time required for the modal approach is also quantified. The computation time for OASS is shown to grow quadratically with range, while the NMSCAT computation time is independent of range. As a result, the modal approach may be several orders of magnitude faster for long-range reverberation problems.

The model is then used to study surface and volume scattering for a number of different cases. The effects of the scatterer statistics, the scattering mechanism, and the waveguide are examined in detail. The statistical description of the roughness and/or fluctuations is seen to have a strong effect on the scattering process. Surface and volume scattering are compared, and the role of density fluctuations in increasing backscatter is shown. The effects of locating the scattering in a waveguide are quite fundamental and are demonstrated by a number of examples. An elastic bottom example demonstrating strong scattering into the Scholte interface wave is used to highlight the importance of taking bottom elasticity into account.

The statistics of the total field are calculated for several different examples, and are seen to depend strongly on bottom type. For low contrast bottoms the scattered field is mostly lost into the bottom, so the total field coherence can actually increase with range. The cross-modal coherences are plotted, and used to see the loss of coherence in the field with range. At longer ranges the cross-modal coherence matrix is nearly diagonal, meaning the modes are incoherent.

Finally, some time-domain results for scattering from a narrow-band pulse are shown. This is accomplished by using the modal group velocities to find which sections of the bottom are generating the scattering received at any given time, a concept which has been developed by several authors [88, 17]. The time-domain results make the role of the continuous spectrum modes and elastic interface waves clear.

4.1 Rough surface scattering and model validation

Here we present results for three different shallow water environments, and compare the results to Schmidt and Kuperman's OASS model. In Appendix A numerical results for NMSCAT and OASS were shown to agree for the simple case of an ideal waveguide. In this section we consider more realistic scenarios. The three rough bottoms considered, in order of increasing bottom impedance, are a sand (fluid) bottom, a limestone bottom, and a basalt bottom. Variations on these environments will be used later in the chapter to demonstrate different reverberation effects.

4.1.1 Fast fluid bottom

The fluid bottom example considered is shown in Fig. 4-1. The example is a shallow (100 m.) ocean with a bilinear sound speed profile. The bottom is represented as a fluid half-space with properties typical for a sand bottom. A 70 Hz source is located at a depth of 50 m. in the water column.

In this example the impedance contrast at the bottom is fairly low. For the frequency and water depth shown there are 4 proper modes. The continuous spectrum contribution can either be included by using KRAKEN to find leaky modes, or by introducing a false bottom deep in the sediment to convert the problem to a Sturm-Liouville form. When modeling volume scattering from within the sediment the false-bottom approach is used, since the leaky modes diverge in the bottom. For rough surface scattering the leaky mode

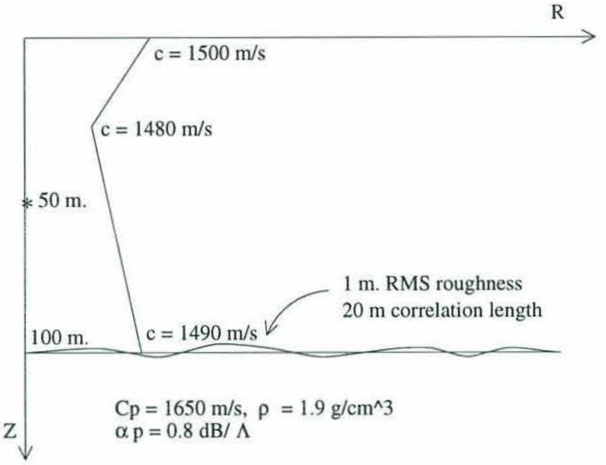

Figure 4-1: Fluid bottom reverberation scenario

sum is preferable because it is more compact, resulting in faster computation times. Table 4.1 shows proper and leaky pole locations as found by KRAKEN; 6 continuous spectrum modes are found (many more are found using a false bottom).

Mode	*real(k_n)*	*imag(k_n)*
1	0.2950478	-1.2735956E-05
2	0.2907900	-6.4778695E-05
3	0.2836920	-1.3358952E-04
4	0.2734942	-2.6635826E-04
5	0.2596908	-1.2600222E-03
6	0.2401055	-2.6681011E-03
7	0.2140755	-4.1656587E-03
8	0.1790221	-6.2538525E-03
9	0.1278224	-1.0457729E-02
10	0.0309523	-4.9936121E-02

Table 4.1: Eigenvalues for fast fluid bottom, f = 70 Hz. First 4 modes are proper, last 6 are leaky modes

Figures 4-2 and 4-3 show the expected scattered field intensity for a receiver at a depth of 50 m. as a function of range. Figure 4-2 compares the two solutions for an (x, z) geometry, while Figure 4-3 assumes a cylindrically symmetric (r, z) geometry. The dark line is the intensity found by the OASS code, while the dashed line is the NMSCAT result. The agreement is seen to be good, with the modal solution capturing the interference

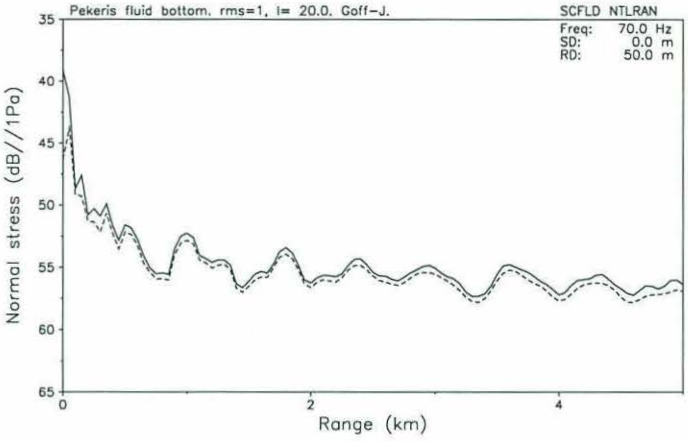

Figure 4-2: Expected scattered field intensity, fluid bottom case, (x, z) geometry. Solid line is OASS result, dashed line is NMSCAT result. Note the overall agreement.

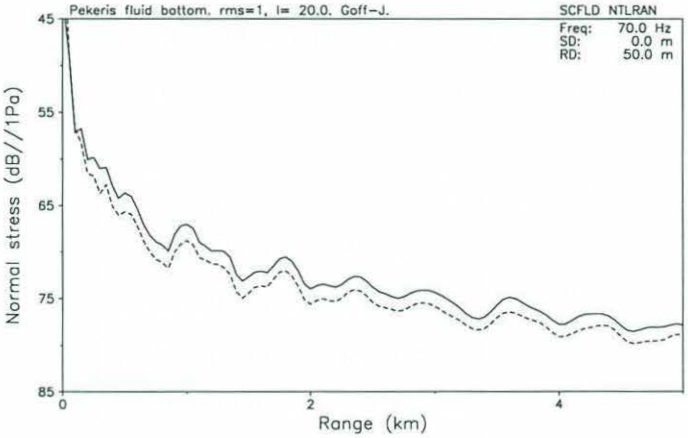

Figure 4-3: Expected scattered field intensity, fluid bottom case, (r, z) geometry. Solid line is OASS result, dashed line is NMSCAT result.

pattern almost exactly. The modal result is somewhat sensitive to the method used to calculate the derivative of the mode shape at the surface. The error involved in calculating the derivative is believed to be responsible for the discrepancy between the results. The cylindrical geometry is taken care of by a simple transformation of variables (see Appendix A.7). It has the effect of increasing the range of scattered field levels, magnifying the disagreement between the two results.

For this problem the continuous spectrum has an especially strong contribution, due to the penetrable nature of the ocean bottom. Figure 4-4 illustrates the effect of scattering into the continuous spectrum. The effect is strongest at shorter ranges, as expected, since the leaky modes in the incident field have not attenuated away yet. However, the continuous

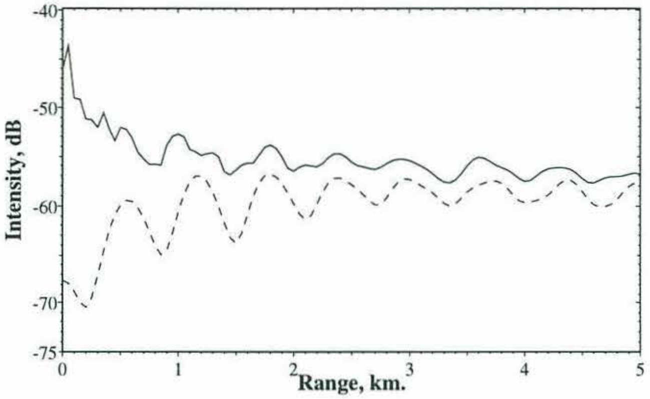

Figure 4-4: Effect of scattering into leaky modes. Plane geometry, scenario above; solid: all modes, dashed: proper modes only

spectrum contribution is noticeable at longer ranges also, indicating that scattering from the proper modes into leaky modes is important. The single-mode excitation results shown later in the chapter can be used to study these effects in more detail.

As stated in the introduction, one of the motivations of this thesis was to develop a more numerically efficient reverberation code. The efficiency of the modal approach is shown in Figure 4-5. Scattered field intensity is calculated at a single receiver depth on 101 receivers spaced between the source and the maximum range. The computation time for the modal approach is a function of the number of modes, and is independent of range. The computation time for OASS, in contrast, is quadratic with maximum range. The reason for this is that the number of wavenumber samples required for Fourier synthesis of the field in OASS increases linearly with range, and the scattering calculations involve wavenumber convolutions. Thus at long range the modal approach is much more efficient.

4.1.2 Limestone example

Next we consider a scattering scenario with a rough limestone bottom, shown in Fig. 4-6. For this example the water column is assumed to be isovelocity. The shear and compressional wave speeds in the bottom are fairly high, presenting a large impedance contrast to the bottom. Because the water sound speed and shear sound speeds are so close, we can expect strong coupling between compressional waves in the water and bottom shear waves.

Figure 4-7 shows the mode shapes found by KRAKEN for this waveguide. Mode 1 corresponds to the Scholte wave, an interface wave on the fluid-elastic interface which is evanescent in the water. For this example the Scholte wave decays fairly slowly in the

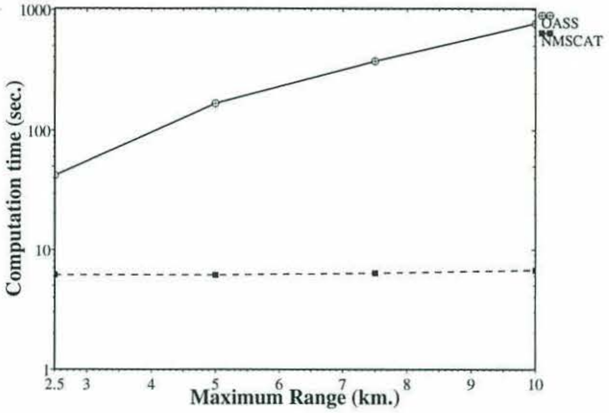

Figure 4-5: Computation times on Alpha 700 for OASS and NMSCAT compared. Rough surface: 1 m. rms, 10 m. CL. 1 receiver depth (50 m.), 101 receiver ranges from [0, Rmax], Modal approach is much more efficient for large Rmax

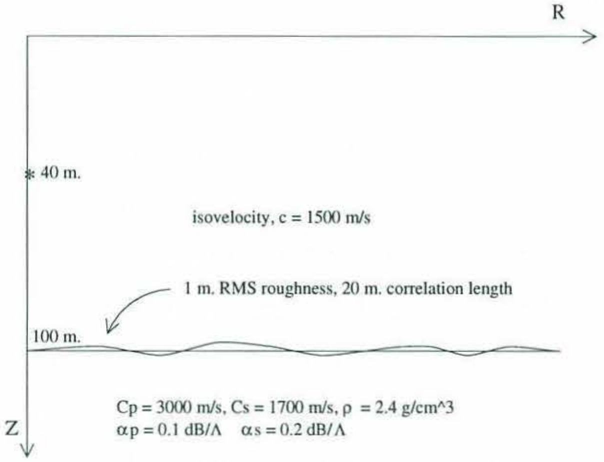

Figure 4-6: Scattering scenario with rough limestone bottom; source frequency 50 Hz.

water. The other modes are seen to be lightly damped. Modes 5-7 radiate into the bottom in shear, so can be considered continuous spectrum modes. None of the modes radiates into the bottom in compression.

At this point we begin applying the scattering theory developed above. First we plot the power spectral density of energy scattered from a plane wave incident on the bottom at a grazing angle of 9.3 degrees (phase speed $1520 m/s$). The predicted PSD is shown in Figure 4-8 along with the result from Schmidt's OASS code. The OASS result is tapered to remove the evanescent spectrum, and it also calculates scattering into the continuous spectrum ($| q | < 0.1$) which is neglected in the modal calculation. The forward-scattered field is seen to be about 15 dB higher than backscatter. The disagreement in the predicted

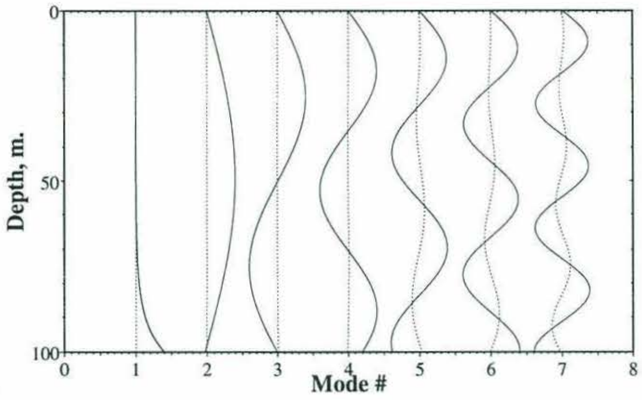

Figure 4-7: Mode shapes for limestone scenario. Mode 1 is Scholte wave mode, evanescent in both water and bottom.

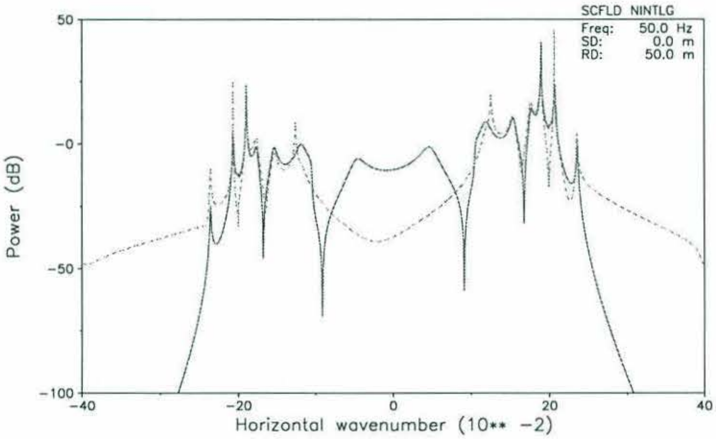

Figure 4-8: Power spectral density for plane wave incident at 9.3 degrees. Solid line is OASS result, dashed line is NMSCAT; agreement indicates the elastic solution is correct.

amplitude for mode 2 shown in the plot indicate that OASES and KRAKEN found slightly different mode locations; this type of plot, while very informative, is quite sensitive to the sampling of the modal peaks.

The more conclusive test of agreement comes in comparing the OASS and NMSCAT intensity predictions vs. range, as for the fluid bottom case. This comparison is shown in Figure 4-9. Two different results for the modal approach are shown; one in which 7 modes are used, and another in which an additional leaky mode is included. These results are seen to bracket the OASS result at short ranges. The mode 8 eigenvalue has a large complex part, so it is possible this mode was not found accurately by the complex root finder used. This example demonstrates that accuracy at short ranges depends on the ability to model the

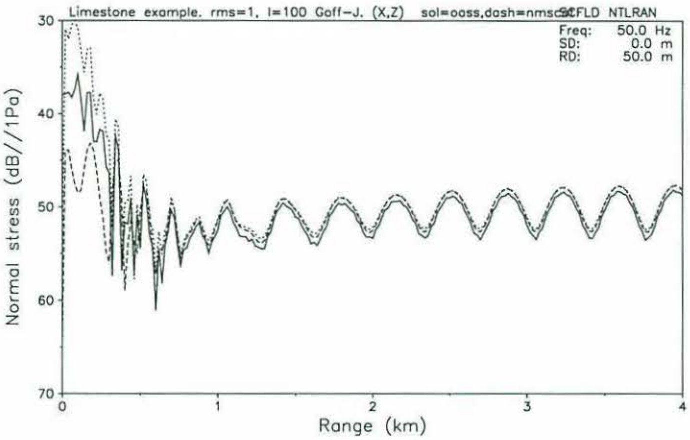

Figure 4-9: Expected scattered field intensity, limestone bottom. Solid line is OASS result, dashed line is NMSCAT result with 7 modes, dotted line is NMSCAT result with 8 modes.

continuous spectrum well, which can be difficult using modes. However, at ranges beyond half a kilometer the agreement between NMSCAT and OASS is quite good.

4.1.3 Basalt bottom example

The last environment we consider is a shallow ocean with a rough basalt bottom, shown in Fig. 4-10. A downward-refracting sound speed profile is assumed, and a 50 Hz source is located at 50 m. depth. This bottom presents an extremely high impedance contrast to the incident sound field. Only mode 7 radiates into shear waves in the bottom; all other modes are totally trapped in the water column. Figure 4-11 shows NMSCAT results for bottom roughness of 1 m. RMS and correlation length 50 m. Since little energy is lost into the bottom the scattered field energy is seen to grow noticeably with range, satisfying energy conservation. The consequences of this for total field coherence will be examined below.

4.2 Effect of scatterer statistics

The reverberation problem is very complicated as there are strong interactions between the random variations of ocean properties, the propagation environment, and the scattering mechanism. For this reason it is difficult to come up with a set of "rules" which will describe reverberation in all different environments. It *is* possible to highlight effects which may be important in particular cases, to begin to build up an intuition about reverberation. The following sections present a number of such examples.

We begin by examining the influence of the roughness and/or fluctuation statistics on

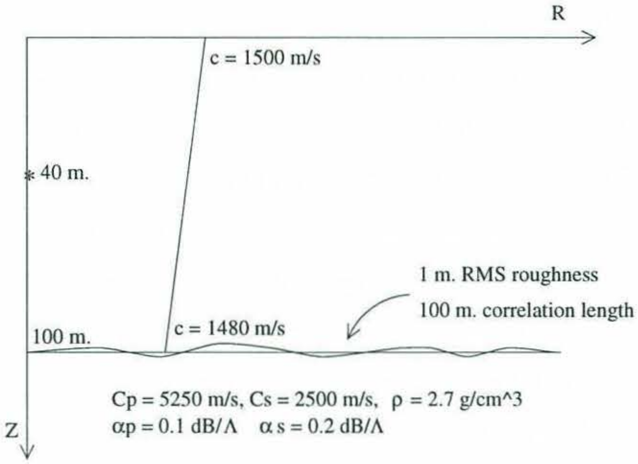

Figure 4-10: Basalt bottom reverberation scenario; source frequency 50 Hz

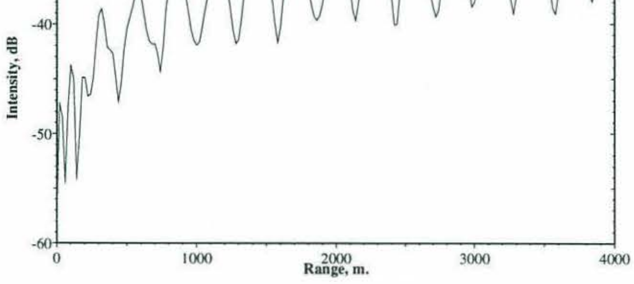

Figure 4-11: Expected scattered field intensity, basalt bottom. Solid line is NMSCAT result.

the scattered field excitation. The effect of the power spectrum on the scattering process was discussed in Chapter 2. Briefly, we expect that the directivity of the scattering will depend on the correlation length of the random scatterers. If the correlation length is larger than an acoustic wavelength, sound is scattered in a more directional way. Each section of the random seafloor can be considered to be a virtual source for the scattered field. The longer correlation length means that these virtual sources form a "virtual array" which has some radiation pattern. The phase of each "virtual element" in the array is a combination of the incident field phase and a random component. Since the random phase components are zero-mean we expect most of the energy to be forward-scattered.

If the correlation length is less than a wavelength, the picture is very different. The scatterer dimensions are small compared to an acoustic wavelength, so they will radiate as isotropic point sources. Backscattering will become as strong as forward scattering.

These trends are seen in Fig. 4-12 - Fig. 4-15 for scattering in the fluid bottom example described in section 4.1. The first two plots show the power spectral density of the scattered field generated by a plane wave incident on the bottom at the same angle as mode 1. In Figure 4-12 sound is scattered from bottom roughness with an RMS roughness height of 1 m, while in Fig. 4-13 scattering is from a layer of volume scatterers in the first 20 m. of the seabed. In the volume scattering layer $\sigma = 0.05$ (from Chapter 3, we remember this means the normalized sound speed fluctuations $\frac{\delta c}{c_0}$ are set to 0.05, and the normalized density fluctuations, found from Hines, are roughly twice that). In both cases the correlation length of the scatterers is varied from $20m.$ (solid line) to $5m.$ (dashed line). For the longer correlation length the Goff-Jordan spectrum used contains significant energy at length scales longer than the acoustic wavelength (roughly 20 m.), and the resulting scattered field is strongly forward-directed. When the correlation length is decreased, the level of backscattered energy is increased for both surface and volume scattering. In addition, higher levels of scattering into the forward-scattered continuous spectrum modes are observed.

These trends are also seen in spatial-domain results. Figures 4-14 and 4-15 show scattered field intensities on receiver arrays, for rough surface and volume scattering respectively. Vertical receiver arrays are located at the source range, to measure backscattering, and 2 km. away. Decreasing the correlation length increases the backscattering greatly, as predicted. For the longer correlation length, the forward scattered field is seen to be dominated by the proper modes. At this range the continuous spectrum modes have been stripped from the incident field. Because the correlation lengths are long the remaining proper modes are scattering with a fairly narrow angular spread, exciting mainly proper

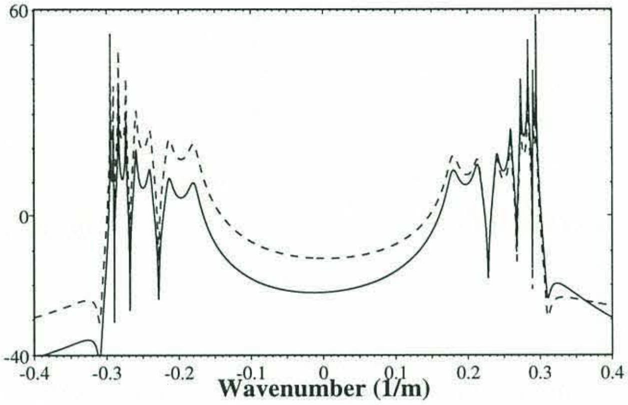

Figure 4-12: Scattered field power spectral density; energy scattered from mode 1. Rough fluid bottom: 1 m. RMS height, Solid = 20 m. CL, Dash = 5 m. CL

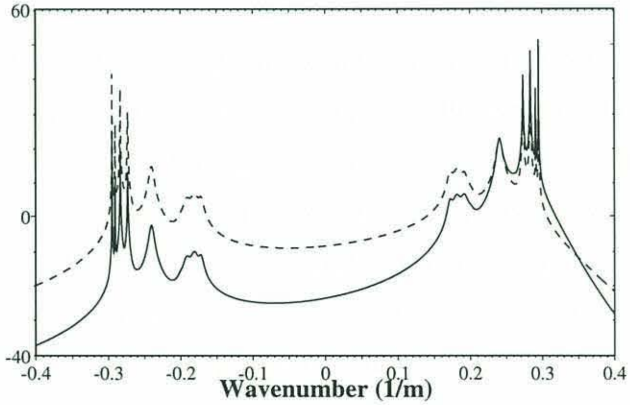

Figure 4-13: Scattered field power spectral density; energy scattered from mode 1. Fluid bottom: random layer between [100 m., 120 m.]; $\sigma = .05$. Solid = 20 m. CL, Dash = 5 m. CL

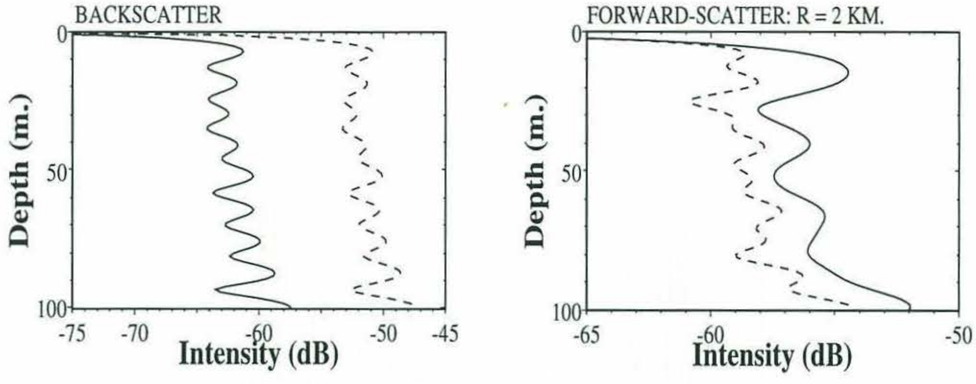

Figure 4-14: Back- and forward-scattered intensities on vertical arrays, rough fluid bottom. First plot at the source range, the second 2 km. away. 1 m. RMS height, Solid = 20 m. CL, Dash = 5 m. CL. Note more isotropic scattering for shorter correlation length.

modes in the scattered field. This effect is similar to the idea of 'nearest neighbor' mode coupling often invoked in mode coupling theory. As the correlation length is decreased, the proper modes scatter into a broader angular spectrum, exciting more continuous spectrum modes in the scattered field. The effect of these higher modes is more clearly seen in the rough surface case than with the volume scattering layer.

The effects of correlation length on the directionality of the scattered field have been discussed by a number of authors [11, 68]. What is new here is that the effect is shown for a modal propagation environment, and that the effects of changing correlation length on surface and volume scattering can be compared side by side. While there are differences in the scattered field levels, the overall trends are seen to be similar for both mechanisms.

The examples so far have all assumed the roughness/fluctuation statistics are described by the Goff-Jordan power spectrum. This spectrum is believed to be realistic in that it describes a distribution of energy on many different length scales. In the scattering literature the Gaussian power spectrum has often been used because of its analytical simplicity, so it is interesting to see what difference the choice of power spectrum makes. Figure 4-16 compares the Goff-Jordan and Gaussian spectra for a correlation length of 20 m. The most striking difference is that the Gaussian spectrum contains much less energy at large wavenumbers, i.e. is much smoother on small length scales. The power spectral density for scattering from a rough surface using the two spectra is shown in Fig. 4-17. The predicted levels are similar for forward scatter, but a huge difference is seen in backscattered levels. The Goff-Jordan levels are much higher, due to the higher levels assumed in the spectrum

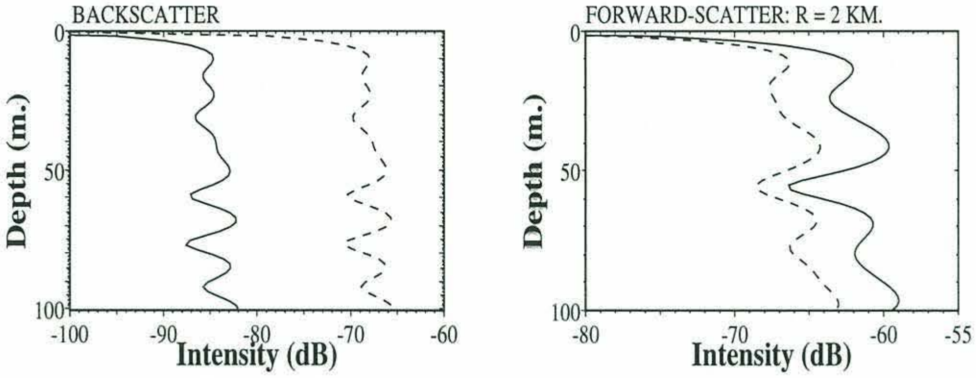

Figure 4-15: Back- and forward-scattered intensities on vertical arrays, volume scattering layer. The first is at the source range, the second 2 km. away. Scattering layer between [100 m., 120 m.] $\sigma = .05$. Effects of correlation length are similar to rough bottom case.

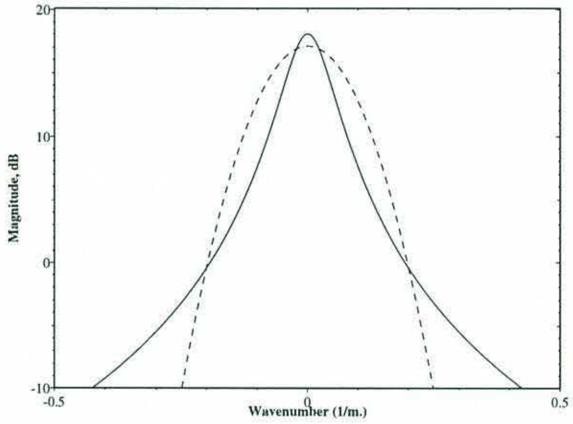

Figure 4-16: Goff-Jordan (solid) and Gaussian (dashed) spectra for a correlation length of 20 m., shown on a dB scale. Note the large differences for higher wavenumbers.

for large wavenumbers. This difference is less dramatic for shorter correlation lengths - for example, for a correlation length of 10 m. the difference in backscattered energy levels is on the order of 12 dB.

From these examples, it is clear that the directionality of the scattered field depends strongly on the correlation function and characteristic length scales of the scatterers.

4.3 Effect of scattering mechanism

The approach developed in this thesis allows us to directly compare the effects of surface and volume scattering from ocean bottoms. In this section the different scattering mechanisms

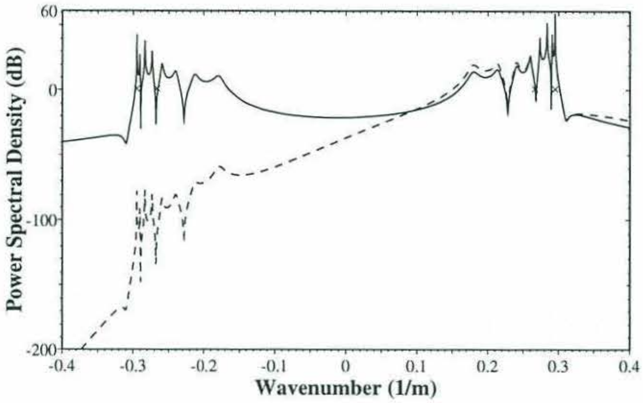

Figure 4-17: Power spectral density for scattering from mode 1 incident on a rough bottom, for the fluid-bottom scenario. Results for Goff-Jordan (solid) and Gaussian (dashed) spectra are shown. RMS roughness height is 1 m. and correlation length is 20 m. The choice of power spectrum has a strong effect on backscattering predicted levels.

are compared, and the role played by density fluctuations in volume scattering is illustrated.

4.3.1 Comparison of surface and volume scattering

When comparing surface and volume bottom scattering, two basic questions can be asked. The first is: what is the relative importance of the two scattering mechanisms? Secondly, is there a basic difference between rough surface and volume scattering? The discussion in Chapter 1 concluded that, in many cases, rough surface scattering can be described in terms of volume scattering, or vice versa. This equivalence is tested below.

The relative importance of seabed roughness *vs.* seabed volume inhomogeneities depends on the situation considered. In some environments rough surface scattering may dominate reverberation, while in others, for example when the bottom is fairly flat, volume scattering will be more important. The comparison must be made on a case-by-case basis. Figure 4-18 compares volume and surface scattering for the fluid bottom scenario from section 4.1. A volume scattering layer is located in the top 10 m. of the sediment, with $\sigma = 0.05$ and a 5 m. correlation length. Interface scattering of the same order of magnitude is generated by setting RMS bottom roughness to $0.4m.$, for the same correlation length. For larger roughnesses interface scattering will dominate, and for smaller roughness volume scattering will be more important.

Next we examine the second question, of whether there is a fundamental difference between surface and volume scattering. In the introduction, the problem of scattering from

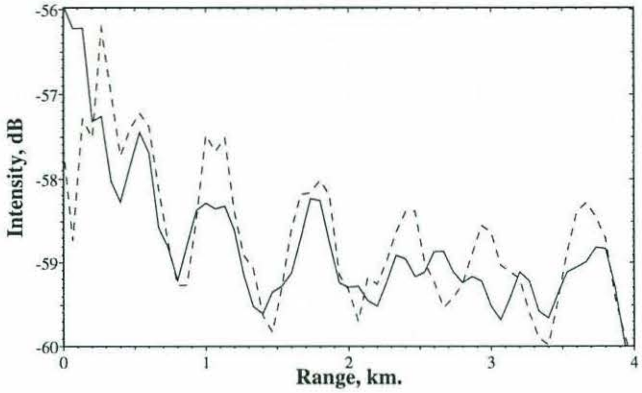

Figure 4-18: Comparison of scattered field intensity from a water-sediment rough interface, with RMS roughness 0.4 m., with scattered field from a 10 m. thick volume scattering layer (dashed line) with $\sigma = 0.05$. Correlation length is 5 m. for both cases; fluid bottom scenario

a stack of rough sediment layers was examined (see Fig. 1-4). The sediment is deposited in layers, so randomness in the seabed can be viewed either as roughness between layer interfaces or as volume fluctuations. Tang [77] has recently shown theoretically that the two descriptions are equivalent.

We can use the code developed to check this prediction numerically, for scattering in the fluid bottom environment above. This requires that statistics for the volume scattering and rough surface stack be related. To do so, we use the ideas developed in Tang's work. The rough surface scattering theory is rewritten in terms of the sound speed and density differences across the interface, giving a form comparable to the volume scattering theory. The scattered field from a stack is given as a summation of the fields from all rough layers (assumed uncorrelated here, though not in Tang's work). This summation is converted into a depth integral, under the assumption that the separation between layers is small compared to a wavelength. The volume and surface scattering expressions can then be directly related. Tang shows that the relationship between the surface and volume parameters is given by:

$$\begin{aligned} \delta c_{RMS}(x,z) &\equiv \gamma(x,z_i)\frac{\Delta c(z_i)}{\Delta z} \\ \delta \rho_{RMS}(x,z) &\equiv \gamma(x,z_i)\frac{\Delta \rho(z_i)}{\Delta z} \end{aligned} \tag{4.1}$$

where δc_{RMS} and $\delta \rho_{RMS}$ are the volume fluctuations, $\gamma(x, z_i)$ is the surface roughness at the ith rough interface in the stack, Δc and $\Delta \rho$ are the differences in sound speed and density on either side of the rough interface, and Δz is the separation between rough interface

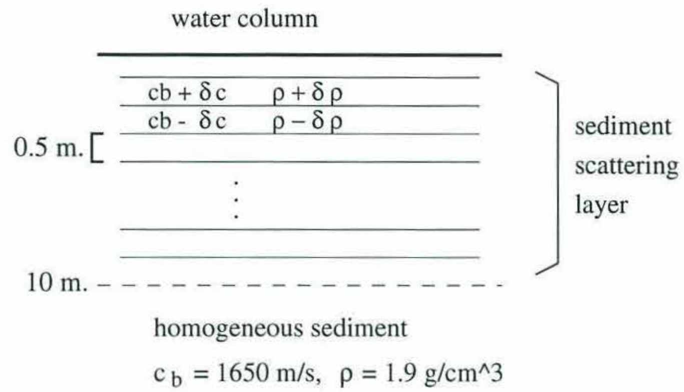

Figure 4-19: Sediment scattering layer modeled as a stack of rough interfaces. Sound speed and densities in the layers alternate as discussed in the text. RMS interface roughness is 0.5 m., correlation length 5 m.

depths.

In the example below, sediment fluctuations are assumed to be located in the upper 10 m. of the seabed. The fluctuation correlation length is assumed to be 5 m., and all other environmental parameters are as described in Figure 4-13. An equivalent stack of rough surfaces is modeled as shown in Fig. 4-19. The upper 10 m. of the seabed are divided into 20 layers, spaced 0.5 m. apart. The sound speed and density of each layer alternates around the average bottom properties. The water-sediment interface is smooth, but all of the sediment-sediment interfaces are rough, with a 5 m. correlation length. The sound speed and density changes between the rough layers are then set from the formula above. Unfortunately it is not totally clear how to choose the RMS roughness height; for the numerical example it is chosen to be half a meter as well. Scattering from all the rough interfaces are added up incoherently, and are compared to scattering from the volume layer in Fig. 4-20. The scattered field levels are seen to agree within an error of about 1 dB, which is reasonable given the approximate way in which the rough stack parameters were assigned. More importantly, the interference patterns in the two fields agree almost exactly. This shows that the relative scattered mode excitations generated by the two different mechanisms are the same, indicating that the underlying scattering physics are equivalent.

4.3.2 Sound speed *vs.* density fluctuations in volume scattering

In Chapter 3 the effect of including scattering from density variations as well as sound speed variations was examined. Density fluctuations were shown to generate scattering mainly in the backwards direction. The plots below show this conclusion remains true when waveguide effects are taken into account. Fig. 4-21 shows the expected increase in backscatter in both

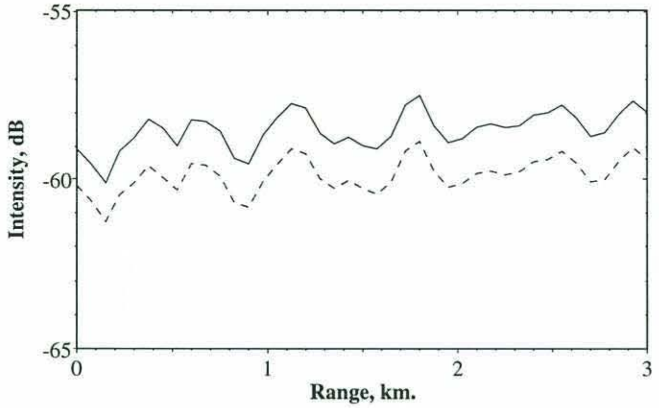

Figure 4-20: Comparison of scattered field intensity from a 10 m. thick thick stack of rough sediment layers (solid line) and a 10 m. thick volume scattering layer (dashed).

the wavenumber and spatial domains. Including density fluctuations is seen in Fig. 4-22 to increase backscattered intensity on an array by more than 10 dB for the example chosen. This shows the importance of using the more complete scattering model.

4.4 Waveguide and propagation effects

From the results presented so far it is clear that locating the scatterers in a waveguide has a strong effect on both the scattered field excitation and the propagation of scattered energy. In this section these effects are examined in more detail.

4.4.1 Scattered field excitation

First we present a number of examples demonstrating the effect of the background sound speed profile on excitation of the scattered field. The first scenario, shown in Fig. 4-23 compares scattering for the isovelocity limestone bottom example above with scattering when the sound speed profile is downward-refracting. The downward refraction causes the incident field to interact more strongly with the rough seafloor. Fig. 4-24 shows this has the expected effect of increasing the reverberant energy levels.

The *location* the scattering elements in the waveguide also has a strong influence on the field generated. Here this point is illustrated by examining the result of changing the depth of a volume scattering layer in the seabed. At short ranges both proper and continuous spectrum modes are important in the incident field, while at longer ranges the continuous-spectrum modes are stripped away. Since the proper modes have only limited penetration

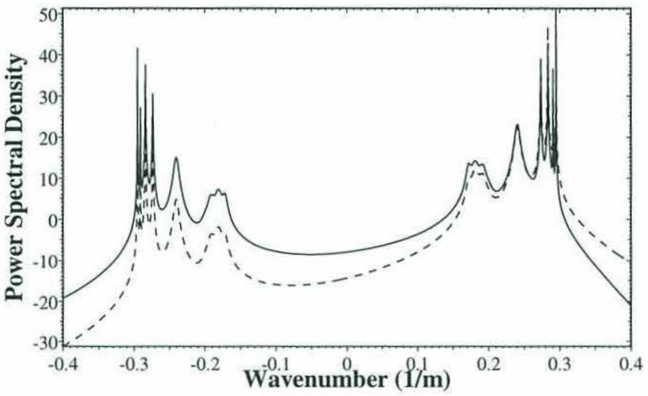

Figure 4-21: Power spectral density for field scattered from incident plane wave at angle of mode 1. Random layer between [100 m., 120 m.] depth; $\sigma = .05$, CL = 5 m. Solid line shows scattering from both δc and $\delta\rho$, dashed line from δc only. Including density fluctuations is seen to strongly increase backscatter.

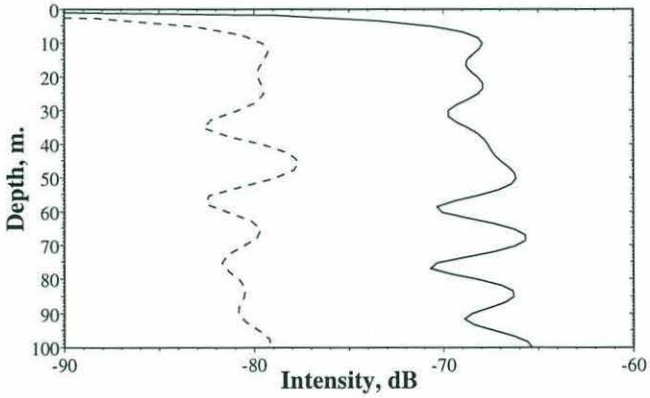

Figure 4-22: Backscattered field intensity for same scenario as above.

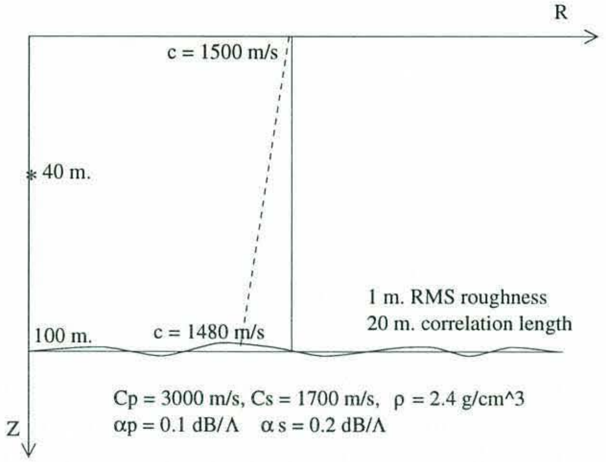

Figure 4-23: Limestone bottom scenario, with isovelocity sound speed profile (solid line) and downward-refracting sound speed profile (dashed line). Bottom is rough with 1 m. RMS roughness and 20 m. correlation length

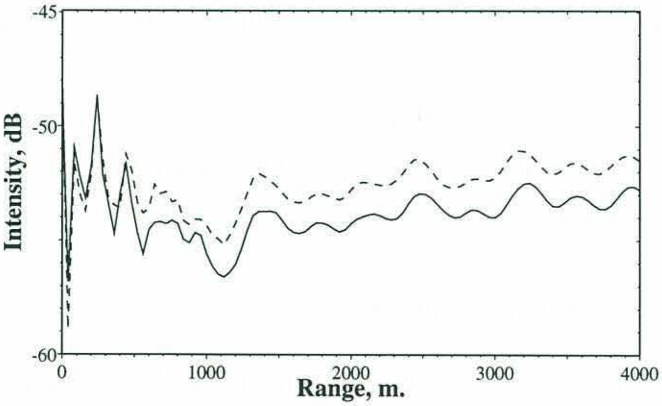

Figure 4-24: Effect of sound speed profile gradient on scattered field intensity at 40 m. receiver depth. Downward refraction increases scattering.

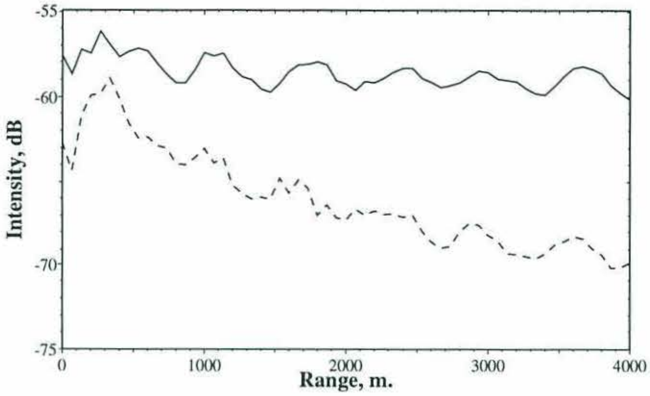

Figure 4-25: Effect of volume scattering layer depth on scattered field excitation; receiver depth 50 m. Fluid bottom scenario; in scattering layer $\sigma = .05$, and correlation length is 5 m. Solid line shows scattered field intensity for scattering layer between [100 m., 120 m.]; dashed line shows intensity for layer between [110 m., 130 m.]

into the bottom, they will not sense volume fluctuations deep in the seabed. *This suggests that scatterers beneath the proper mode penetration depths contribute only weakly to long-range reverberation.* Apparently this idea has been discussed previously by Dr. Weston, but this author has been unable to locate a reference.

The effect of scatterer depth is illustrated numerically in Figure 4-25. We consider once again the fluid-bottom (sand) scenario from section 4.1. A volume scattering layer is first located in the upper 20 m. of the seabed, then is shifted down by 10 m. At short ranges, where the bottom-penetrating higher modes are important in the incident field, the effect of changing the layer depth is not too large. At longer ranges, however, only the proper modes are present in the incident field. Of these modes only mode 4 will penetrate very far into the lower scattering layer. As a result the scattered field levels observed at longer ranges drop substantially for the deeper scattering layer.

4.4.2 Propagation of scattered field

Once the scattered field is generated, it travels in the modes of the waveguide. As a result the scattered field contains as much or more information about the underlying modes of the waveguide as it does about the scattering process. We emphasize this point by examining the spatial correlation statistics of the scattered field.

Scattering from seabed roughness in the fluid bottom example above is modeled first. An interface roughness of 1 m. RMS and correlation lengths of 5, 20 and 80 m. are assumed.

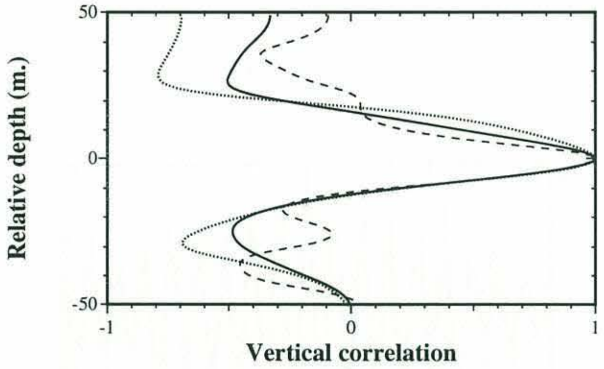

Figure 4-26: Normalized vertical correlation, range = 2 km. First receiver fixed at 50 m. depth, second is varying over water column. Correlation lengths of 5 m. (dashed line), 20 m. (solid line) and 80 m. (dotted line) are shown. The vertical correlation is dominated by mode shapes.

Figure 4-26 shows the vertical correlation of the scattered field at a range of 2 km. One receiver is fixed at a depth of 50 m., while the depth of the second is moved from the top to the bottom of the water column. The correlation structure is dominated by the mode shapes. For a correlation length of 5 m., some higher-order modes are present in the scattered field, as shown above. The vertical correlation has some added "wiggles" coming from the higher-order mode shapes. For correlation lengths of 20 or 80 m. the scattered field consists almost entirely of proper modes, so the vertical correlation length is almost unchanged.

Figure 4-27 and Figure 4-28 show the horizontal correlation and coherence of the scattered field. One receiver is fixed at a range of 2 km., while the range of the second is varied; both receivers are at 50 m. depth. The correlation basically displays the modal structure of the field; both the small- and large- scale oscillations in Fig. 4-27 correspond to modal interference lengths. The coherence, in Fig. 4-28, basically picks out the envelope of the correlation. For the shortest correlation length higher-order modes are excited, giving a shorter length scale in the interference pattern. When the interference pattern is increased to 20 m. these higher modes have have little effect. The coherence is in general higher but the main lobe of the coherence has roughly the same width. For the extremely long correlation length of 80 m. the coherence is in general much higher. *Thus the roughness correlation length has a larger effect on horizontal coherence than vertical coherence, but the horizontal statistics are clearly shaped by modal interference lengths.*

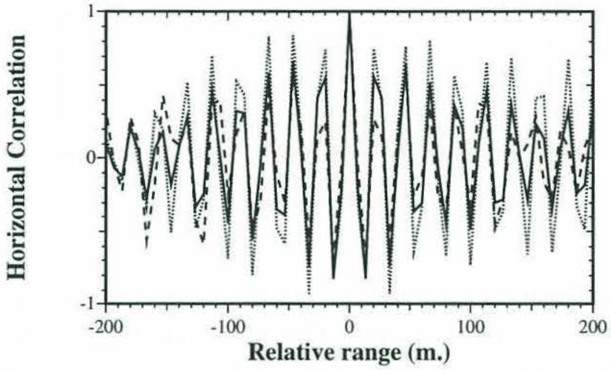

Figure 4-27: Normalized horizontal correlation for 20 m. CL; receiver depths are 40 m. One receiver is fixed at 2 km range, second is moved in range

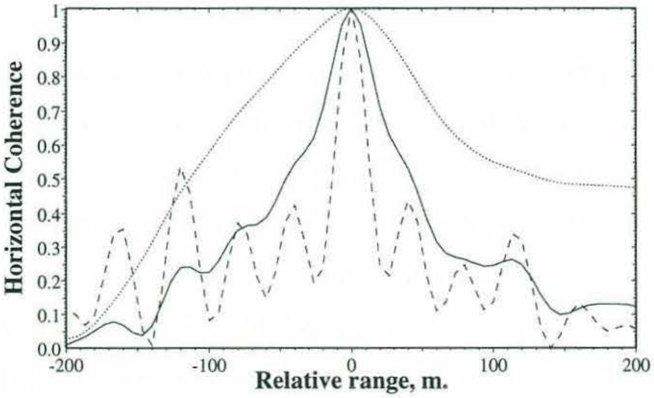

Figure 4-28: Horizontal coherence for situation above, but varying correlation lengths. Solid line for CL = 5 m., dotted line for CL = 20 m., dash-dot for CL 100 m. Note that changes are fairly small.

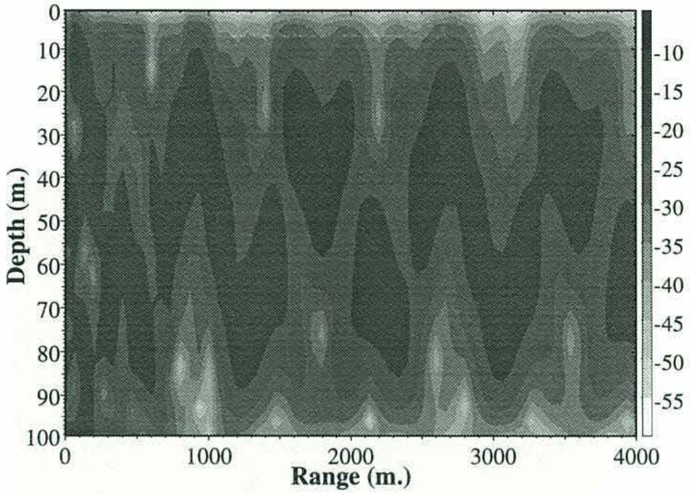

Figure 4-29: Mean field transmission loss, limestone scenario: (x, z) ocean. Source frequency is 50 Hz., source depth 40 m.

4.4.3 Scholte wave excitation

One of the main effects of bottom elasticity is the existence of an interface wave on the fluid- elastic boundary. This interface wave will not be present in the mean field unless the source is located very close to the bottom, but may be important or even dominant in the scattered field.

To illustrate this point, the limestone bottom scenario above is used. The seafloor is assumed rough with a correlation length of 20 m. and RMS roughness of 1 m. The mean field (assuming an (x, z) scenario) is shown in Fig. 4-29 The proper modes interfere, giving a beam-like propagation pattern at longer ranges. The interface wave is not excited, as the source is far from the rough bottom.

Figs. 4-30 shows the expected scattered field intensity in the water column, without including mode 1 (the Scholte wave) in the modal summation. Thus the result is close to what we would expect if the bottom was represented as a fluid. Roughness at ranges when the mean field hitting the bottom is strong (for example, at about 1.2 km.) give rise to higher levels of scattering. Fig. 4-31 shows the same plot, but with the interface wave included. *This suggests that excitation of the interface mode can be the dominant feature of the scattered field near the bottom.*

4.5 Scattering from a single incident mode

In recent years researchers at Woods Hole Oceanographic have been developing techniques for using a vertical array to excite a single mode for shallow water experiments [8]. Single-

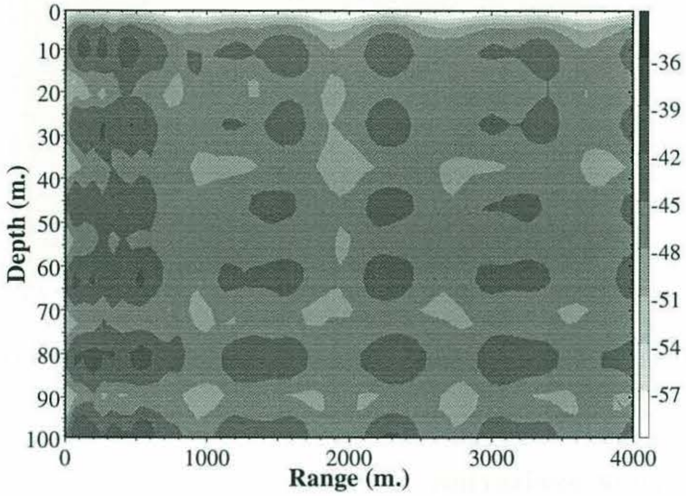

Figure 4-30: Scattered field intensities for limestone bottom scenario, CL = 20 m., without including Scholte wave

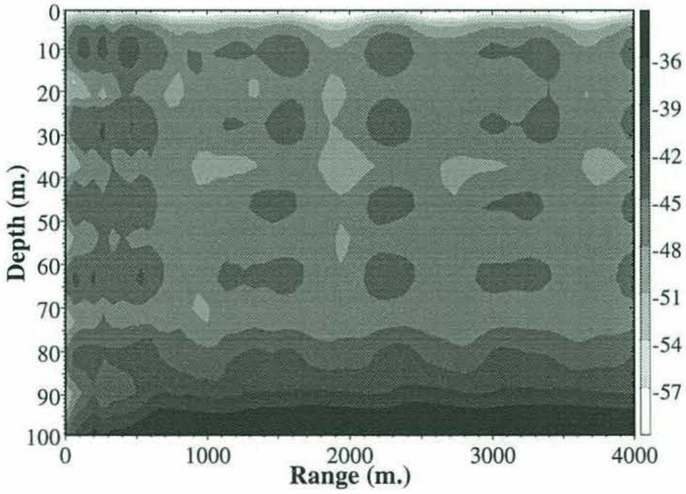

Figure 4-31: Scattered field intensities for limestone bottom scenario, CL = 20 m., Scholte wave included in modal sum. Note dominance of Scholte mode near the bottom

mode excitation would allow more detailed experimental study of modal scattering, as individual mode-to-mode scattering paths could be separated out. Such scattering experiments can be modeled using NMSCAT. The results, shown below, also demonstrate that nearest-neighbor mode coupling is often weaker than coupling between more widely separated modes.

We first consider scattering from the rough fluid bottom example above. Figs. 4-32 and 4-33 show scattered field modal powers *vs.* range for incident modes 1 and 6, respectively. The modal composition of the scattered fields are clearly quite different.

In Fig. 4-32, mode 1 scatters most strongly into the other propagating modes. Since mode 1 decays very slowly, it continues to excite the scattered modes at ranges far from the source. The other proper modes are also lightly damped, so the scattered energy in these modes grows with range. Interestingly, mode 1 scatters most strongly into mode 4. The reason for this can be seen by examining the expressions for the scattering kernels given in Chapter 2. The strength of the scattering depends on the values of the incident and scattered modes and their derivatives at the rough interface, modulated by the power spectrum at the wavenumber difference: $P(q_n - k_m)$. In this example the Goff-Jordan power spectrum is broad enough that mode 4, which has a larger slope at the rough interface, is more strongly excited than modes closer to the incident mode.

Figure 4-33 shows scattering out of an incident mode 6. The incident mode is leaky, and does not survive to very long ranges. Mode 6 scatters predominantly into nearby leaky modes, which are also quickly damped. These modes are very strongly excited, however. At longer ranges the strongest scattered field energy is in mode 4. This mode is only weakly excited near the source, but the energy trapped in mode 4 is attenuated much more slowly.

It can be argued that scattering and/or coupling between neighboring modes should be dominant, since the power spectrum gives the highest values for small wavenumber differences. The examples above show this argument is valid in a rough sense, as higher-order modes scatter preferentially into other high-order modes and low-order modes scatter into other low-order modes. However, the exact distribution of energy is more complicated. In general there is a tendency for modes to scatter more strongly into higher modes.

To illustrate this point we consider several more examples. Figure 4-34 again shows scattering from incident mode 1, but with a correlation length of 100 m. The power spectrum is much narrower, and as a result scattering from mode 1 into mode 2 is strongest. Scattering from mode 1 into itself is still low, due to the small values of mode 1 and it's slope at the interface. This example suggests that nearest-neighbor mode coupling might be expected to

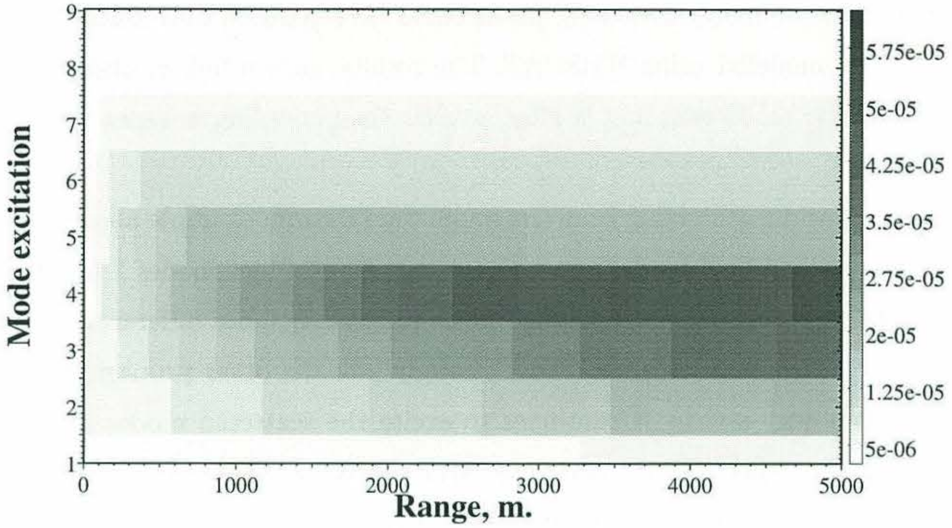

Figure 4-32: Scattered mode powers *vs.* range for incident mode 1; fast fluid bottom scenario, 1 m. RMS roughness height, 20 m. correlation length.

be dominant when scatterer correlation lengths are long. Figure 4-35 shows the scattered field mode powers for mode 4 incident, with a roughness correlation length of 20 m. At short ranges mode 4, the highest propagating mode, is seen to scatter most strongly into itself and its neighbors. At short ranges mode 5 is strongly excited, but the energy in this leaky mode decays due to radiation into the bottom. In contrast mode 3 is more weakly excited at short ranges, but contains more energy at longer ranges as the energy in mode 3 is trapped in the waveguide. Thus we see that the distribution of energy among modes depends on the roughness statistics, modal attenuations and propagation, and scattering mechanism.

Figure 4-36 shows the total expected scattered field intensity generated by a single incident mode. Scattering from mode 1 (solid line) is compared with scattering out of mode 6 (dashed line) for a plane geometry. The scattered field generated by mode 1 consists primarily of proper modes, as seen above. The scattered energy is trapped within the water column, so the intensity grows with range. In contrast, mode 6 scatters mainly into continuous spectrum modes, which lose energy rapidly in the bottom. Thus the scattering from mode 6 is dominant at short ranges but decays rapidly. In general we can expect that scattering out of continuous spectrum modes may dominate the scattered field at short ranges, but scattering from proper modes will be dominant at long ranges.

In previous sections we have noted that scattered fields generated by rough surfaces

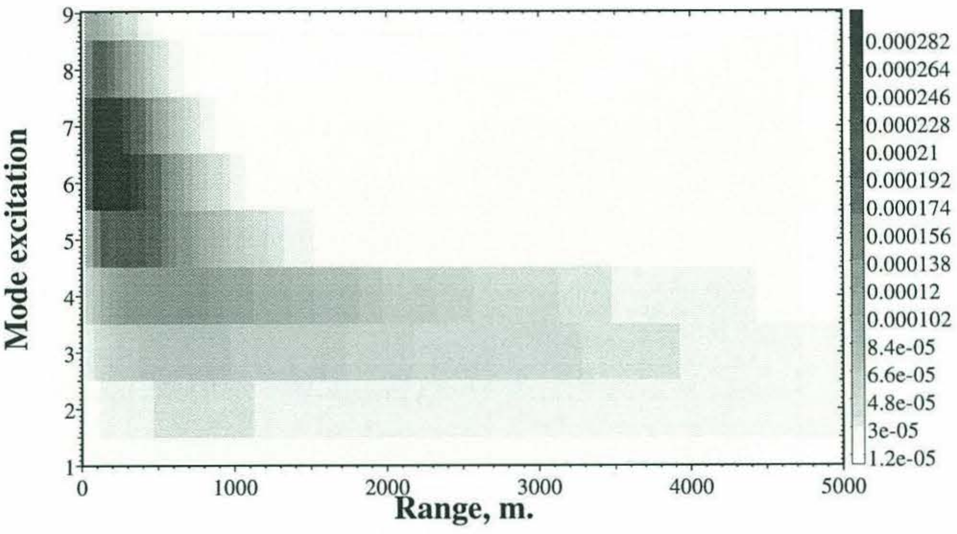

Figure 4-33: Scattered mode powers *vs.* range for incident mode 6; same scenario as above. Note higher modes are strongly excited, but die out quickly

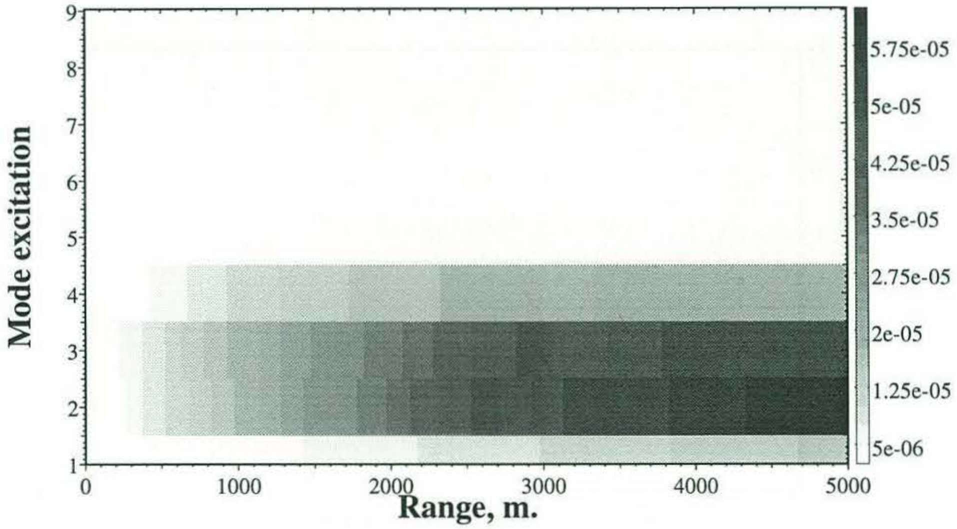

Figure 4-34: Scattered mode powers *vs.* range for incident mode 1; 100 m. roughness correlation length, otherwise same scenario as above. Nearest-neighbor mode coupling is a better approximation for this case.

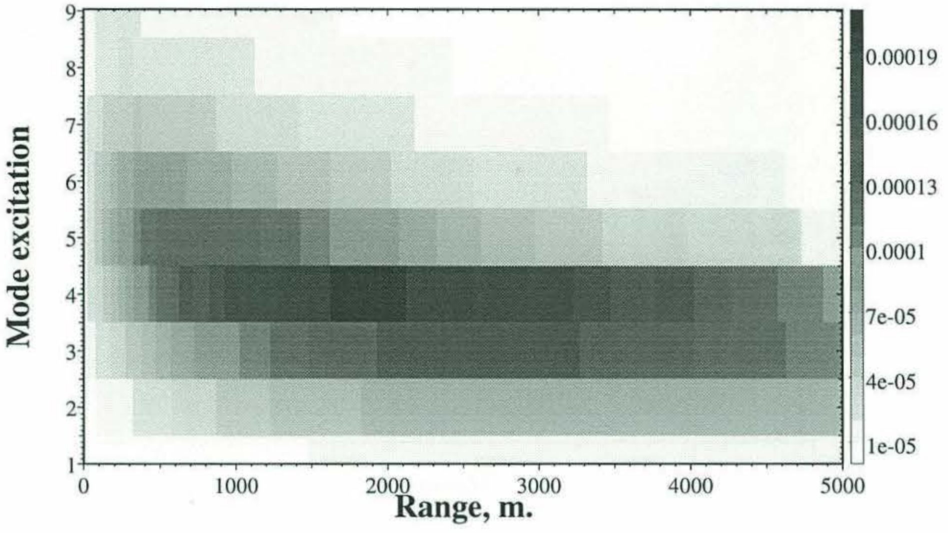

Figure 4-35: Scattered mode powers *vs.* range for incident mode 4; 20 m. roughness correlation length, otherwise same scenario as above.

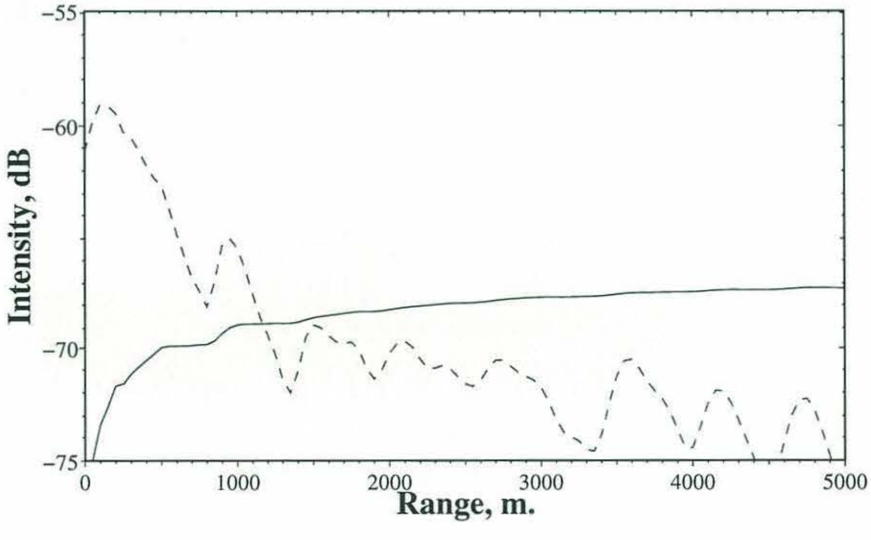

Figure 4-36: Scattered field intensity for single incident mode; solid line shows scattering from incident mode 1, dashed line shows scattering from incident mode 6.

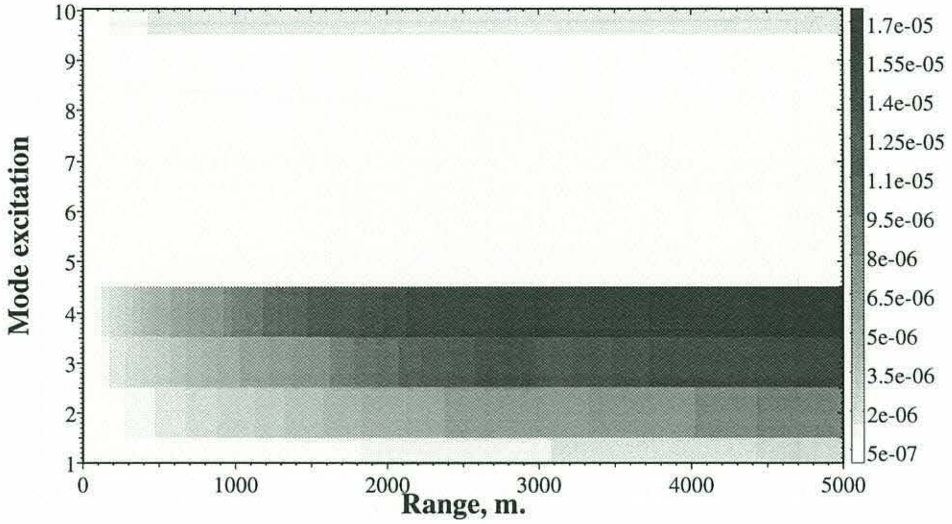

Figure 4-37: Volume scattering: mode power *vs.* range for incident mode 1; fast fluid bottom scenario, random sediment layer between [100 m., 120 m.]. Fluctuation correlation length is 20 m., $\sigma = 0.05$. Note similarity to mode excitation by rough surface scattering.

and volume inhomogeneities are similar in nature. In Chapter 1 it was argued that the distinction between rough surface and volume scattering is often unclear, as the scattering physics for many problems can be described in either framework. This similarity is clearly seen when comparing Figure 4-37, which shows mode power for scattering from mode 1 incident on a bottom containing volume inhomogeneities, with Fig. 4-32 above. For both cases the correlation length of the scatterers is set to 20 meters. The powers of the proper modes (1-4) are seen to be qualitatively quite similar. In the sediment scattering case the continuous spectrum is represented by a sum of false-bottom modes, rather than leaky modes. Thus it is difficult to compare mode excitations for the continuous spectrum modes, as many more false bottom modes are present.

Figure 4-38 shows the scattered field intensity for energy scattered out of mode 1 by the scattering layer. The shape of the curve is quite similar to that seen in Figure 4-36 for rough surface scattering, though the levels are lower.

4.6 Total field statistics

So far results for the scattered field alone have been presented. In experimental measurements the *total* acoustic field is measured, and scattered field statistics are inferred indirectly. In this section results for the total field energy and coherence are presented. This allows

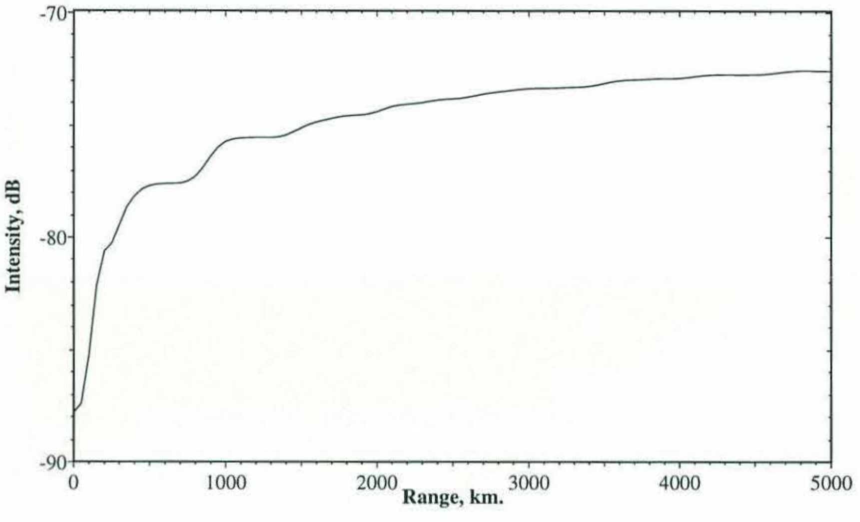

Figure 4-38: Volume scattering: intensity of field scattered from incident mode 1; same scenario as previous plot.

us to see in what situations scattering has the largest effect in terms of causing a loss of coherence of the acoustic field. *The main conclusion is that the effects of scattering depend strongly on the bottom type.*

In order to find total field statistics we must find the scattering loss experienced by the mean field. For volume scattering a 2D version of the eigenvalue perturbation method described in Chapter 3 is used. To find scattering loss due to interfacial roughness, OASES is used to find mean field reflection coefficients including scattering loss. These reflection coefficients can be input to KRAKEN as a boundary condition. The resulting mode attenuations are subtracted from those found by KRAKEN for the unperturbed case, giving the modal scattering loss.

As mentioned above, the effects of scattering are found to depend on the bottom type. To illustrate this for rough surface scattering we compare the highest-impedance example above, the basalt bottom, with the much lower-impedance sand bottom. Figures 4-39 and 4-40 show the mean field intensity, with and without scattering loss, and the scattered field intensity for the basalt and sand bottoms respectively. The effects of the mean field scattering loss are seen by comparing the unperturbed (Born approximation) mean field (dotted line) with the self-consistent mean field calculation (solid line). For both scenarios the scattering loss has a noticeable effect. In the basalt case the scattering loss is seen to strip all but the lowest two modes, changing the mean field interference pattern as well as

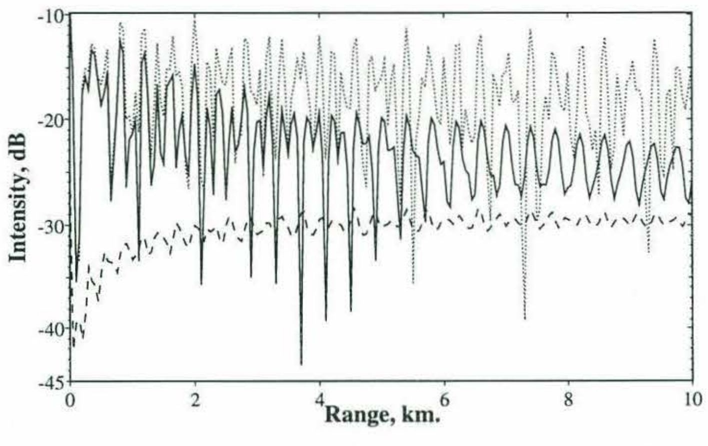

Figure 4-39: Basalt bottom scenario: mean field intensity from the Born (dotted) and self-consistent (solid) calculations, and scattered field intensity (dashed line). Receiver depth is 75 m., RMS bottom roughness is 2 m., and correlation length is 50 m. Note that the influence of the scattered energy grows with range

its amplitude.

The more interesting difference is seen for the scattered field intensities (dashed line). In the basalt bottom case there is little radiation into the bottom, so nearly all scattered energy is trapped in the water column. The scattered field grows with range as more and more scattering area is added, eventually becoming comparable in strength to the mean field. For the fluid bottom case, in contrast, much of the scattering is into continuous spectrum modes which transmit energy out of the water column into the ocean bottom. As a result the scattered field actually decays faster than the mean field, and always remains much weaker than the mean field.

This difference in bottom type results in very different changes for the total field coherence *vs.* range. For the basalt bottom, the scattered and total field vertical coherences are shown in Fig. 4-41 and 4-42 for ranges of 1 and 4 km. respectively. If there were no scattering the total field coherence would be unity at all depths. Instead, the total field coherence is strongly affected by the scattered field coherence, and becomes closer to it with increasing range. As the scattered field strength grows with range the total field coherence drops, with a pattern determined by the mode shapes of the scattered field.

Figures 4-43 and 4-44 show the total field vertical coherence alone at the same ranges. Since the scattered field is much weaker compared to the mean field, the coherence is much higher. Moreover, since the scattered field decays more rapidly than the mean field, total field coherence is seen to actually *grow* with range. This phenomenon has been discussed by Dozier [15] in relation to shallow-water data.

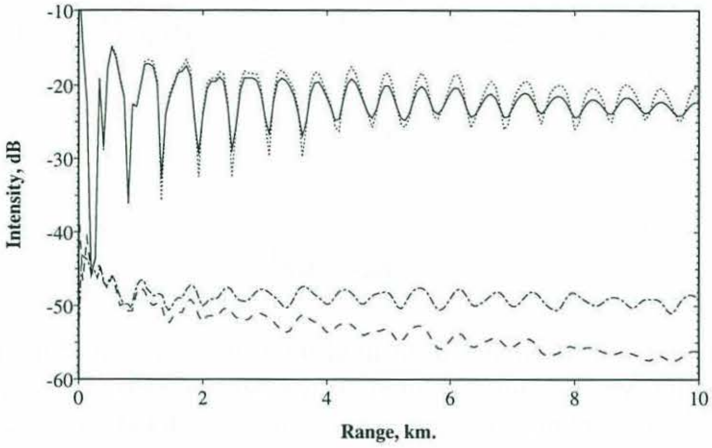

Figure 4-40: Sand bottom scenario: mean field intensity from the Born (dotted) and self-consistent (solid) calculations, and scattered field intensity (dashed line). Receiver depth is 50 m., RMS bottom roughness is 2 m., and correlation length is 20 m. Scattered field decays faster than mean field

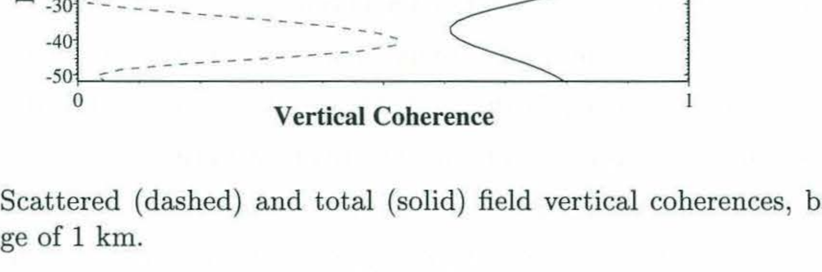

Figure 4-41: Scattered (dashed) and total (solid) field vertical coherences, basalt bottom case, at a range of 1 km.

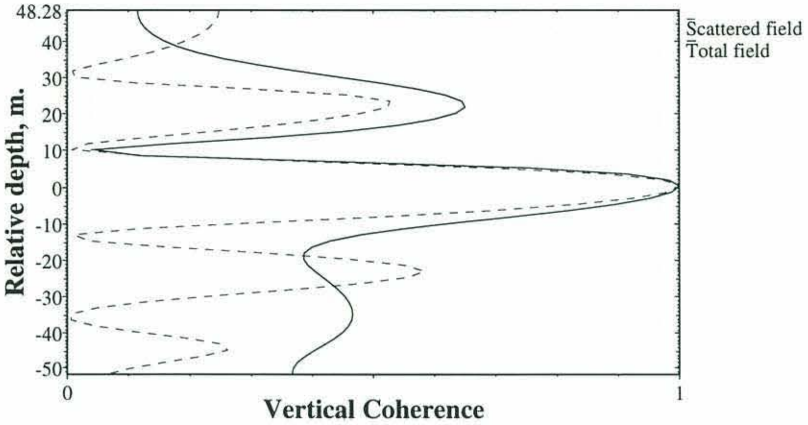

Figure 4-42: Scattered (dashed) and total (solid) field vertical coherences, basalt bottom case, at a range of 4 km. Total field coherence decreases with range

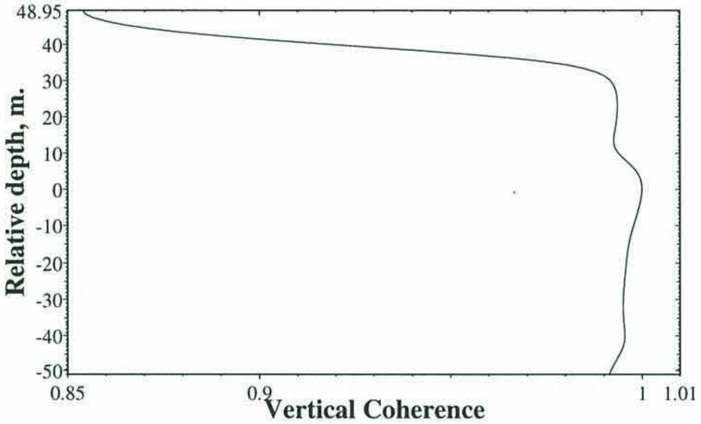

Figure 4-43: Total field vertical coherence, fluid bottom case, at a range of 1 km.

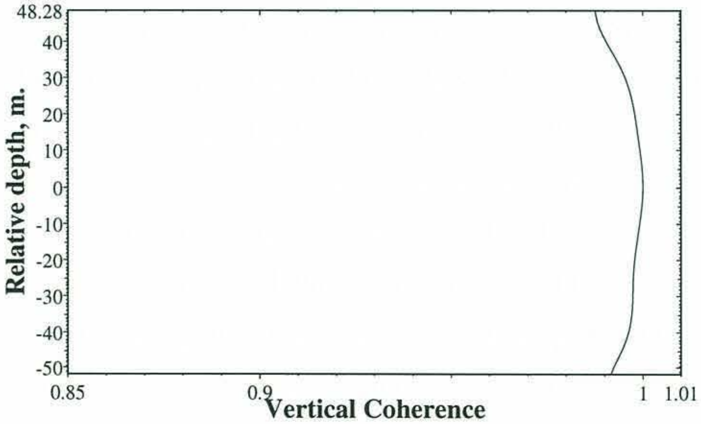

Figure 4-44: Total field vertical coherence, fluid bottom case, at a range of 4 km. Coherence *grows* with range.

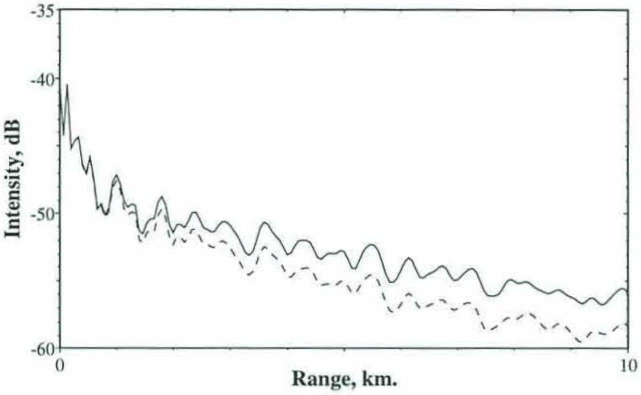

Figure 4-45: Effect of re-scattering loss on scattered field: fluid bottom scenario, higher loss bottom. Solid: first order scattered field; Dashed: scattered field with scattering loss to higher order scattered fields

4.6.1 Importance of multiple scattering

The scattered field energy will re-scatter as it travels in the waveguide. This re-scattering will change the energy distribution among scattered field modes. In addition, since there is a general tendency for lower-order modes to scatter more strongly into the more strongly attenuated higher modes, the total scattered field energy in the waveguide will be decreased somewhat.

These effects cannot be captured using the present single-scatter theory. However, we can use the tools developed to identify situations in which multiple scattering should be important. Physically, we expect the scattering loss from the first-order scattered field to occur at roughly the same rate as the scattering loss from the mean field into the first-order scattered field. This scattering loss can be included from the mean field attenuation coefficients found earlier. Figs. 4-45 and 4-46 show the scattered field intensity, with and without this "re-scattering loss", for the fluid and basalt bottom scenarios discussed above. In some sense the two curves can be considered to be upper and lower bounds for the scattered field. More generally, the difference between the curves is indicative of the importance of multiple scattering. From the figures below we see that the effect of re-scattering is fairly weak for the fluid bottom, but much stronger for the basalt bottom. In the fluid bottom case, the higher bottom attenuation prevents the scattered field generated at any point from traveling too far, so multiple scattering is less signifigant. For the basalt bottom nearly all scattered energy is trapped in the bottom, and is available to re-scatter.

It is important to stress that the existence of multiple scattering does *not* fundamentally

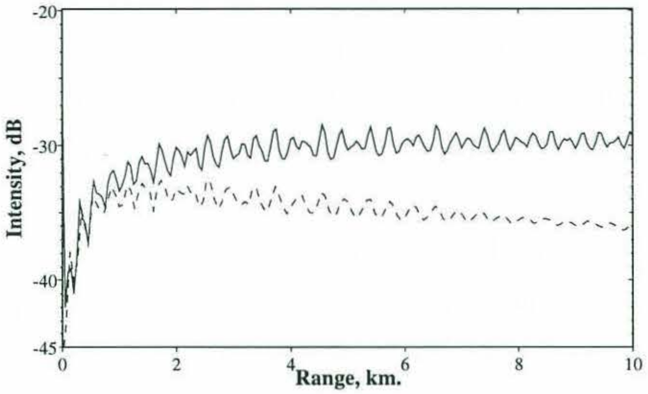

Figure 4-46: Effect of re-scattering loss on scattered field: basalt bottom scenario. Solid: first order scattered field; Dashed: scattered field with scattering loss to higher order scattered fields

change the discussion above about the importance of bottom type. For the basalt bottom case, re-scattered energy will be trapped in the water column just as the scattered field is, and will be attenuated only lightly. The total scattered energy in the water column (both single- and multiple-scattered sound) will grow with range. This results from the fact that this is nearly a conservative system, so from energy conservation the total scattered energy must increase with range to account for scattering loss from the mean field. A prediction from multiple-scattering theory should thus lie much closer to the upper curve in Fig. 4-46 than the lower curve. The main result of re-scattering for this example will be a redistribution of energy, with higher modes having larger amplitudes than predicted by the single scatter theory.

For the fluid bottom case, re-scattering will again direct more energy into the higher modes. Since these modes are very highly attenuated in this example (most are leaky) the total scattered field intensity will be reduced, and will lie somewhere between the two curves.

4.6.2 Cross-modal coherences

The cross-modal coherences defined in Chapter 2 give a more systematic way of looking at field coherence. Cross-modal coherences, as a function of range, for each of the three bottom scenarios are shown below and discussed.

Fig. 4-47 shows the normalized forward-scattered and total field cross-modal coherences for the fluid bottom scenario at ranges of 0.5, 5, and 20 km. The information in these pictures helps us understand the evolution of the field with range. At the shortest range the forward-scattered field is very weak, and continuous spectrum modes have not yet been stripped from the incident field. As a result the coherence of all modes, including the leaky modes, is quite high. By 4 km. most of the higher-mode energy in the incident field has been attenuated away. The cross-modal coherences of the higher modes for the total field resemble those for the scattered field, showing that only scattered field energy is in these modes. At 20 km. the same pattern is seen, though now only the four proper modes remain in the mean field. However, the cross-coherence of the proper modes is nearly one, indicating that, for these modes, the mean field is much stronger than the scattered field. This agrees with our discussion above, which showed the mean field was dominant when the spatial correlations of the field were calculated.

Since the cross-modal coherences are non-negligible even at 20 km., a fairly long range for such a shallow ocean, the question arises as to whether the mode coherences *ever* totally decay. Figure 4-48, which shows the cross-modal coherences at a range of 50 km., shows that the modes become incoherent at long ranges. This may at first seem puzzling, since the scattered field is so much weaker than the incident field for this case. From Fig. 4-49, we see that at ranges beyond 20 km. only mode 1 remains in the mode field, as all higher modes have attenuated away. Any energy in modes higher than 1 is thus in the scattered field, so cross-modal coherences are low. However, the scattered field is so much weaker than the mean field that the total field statistics will effectively be set by the single mean field mode.

Figure 4-50 shows the same plots for the limestone bottom scenario, again for ranges of 0.5, 5, and 20 km. The longer spacing is chosen because the field is changing more slowly. At the short range total field coherence is shown to be high, except for mode 1. Mode 1 in this example is the Scholte wave, which is present only in the scattered field. At the longer ranges the higher mean field modes are being attenuated away, and most of the energy in these modes is scattered field energy. This is seen in the fact that the total field cross-modal coherences for the higher modes have the same pattern as the scattered field modes. For this example KRAKEN did not find any continuous spectrum modes, so all 7 modes are proper. The increasing loss of total field coherence between 5 and 20 km shows that the scattering is having a significant effect. This is to be expected , since the limestone bottom is fairly hard. From the discussion above, most of the scattered field energy is trapped within the water column rather than radiated into the bottom. By 20 km. the cross-modal coherence matrix is nearly diagonal, meaning all modes are incoherent. Several mode coupling theories, such

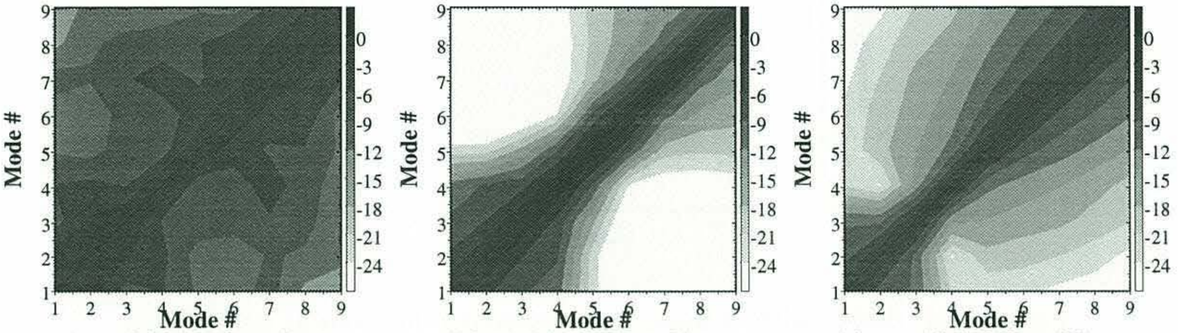

a) Scattered field XMC, r = .5 km. b) Scattered field XMC, r = 5 km. c) Scattered field XMC, r = 20 km.

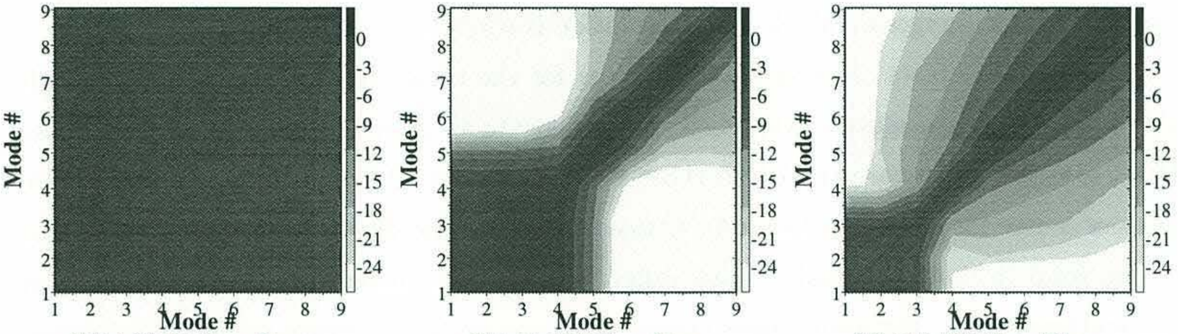

c) Total field XMC, r = .5 km. e) Total field XMC, r = 5 km. f) Total field XMC, r = 20 km.

Figure 4-47: Cross-modal expectations (XMC) for fluid bottom scenario

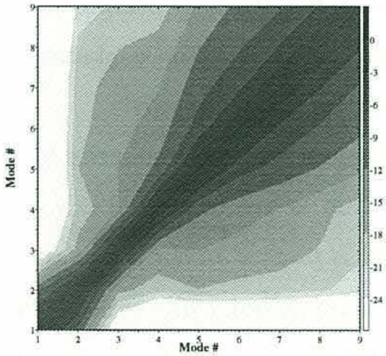

Figure 4-48: Cross-modal expectations for fluid bottom scenario, at 50 km.

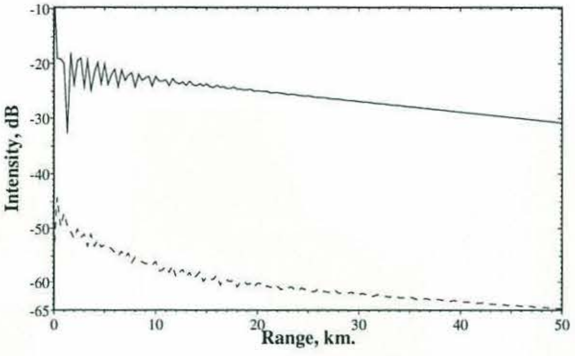

Figure 4-49: Self-consistent mean and scattered field levels at long ranges

as that of Dozier and Tappert [16], assume the modes to be incoherent. NMSCAT can be used to find the ranges at which this assumption is correct.

Figure 4-51 shows cross-modal coherences for the basalt bottom scenario. Although the basalt bottom is elastic, KRAKEN did not locate an interface wave for this example. Otherwise the results are similar to those for the limestone bottom, although the harder bottom causes the coherence loss to be noticeable even at the shortest range. The coherence of the total field drops steadily with range, showing the increasing relative strength of the scattered field. For even longer ranges the cross-modal coherence matrix will become effectively diagonal.

4.7 Backscattered intensity from transmitted pulse

In Chapter 2 results were derived for expected backscattered intensity as a function of time. The calculation neglected out-of-phase contributions, giving a smoothed result similar to the use of an incoherent modal summation in finding transmission loss. This smoothed time record captures the overall envelope of the backscattered time series, and helps give physical insight into the back-scattering process.

Figures 4-52 and 4-53 show backscattered time series for the fast fluid bottom waveguide modeled above. The ocean bottom is at $100m$. in both cases; backscattered energy on a receiver array at the source range is plotted in the water column and the upper 30 m. of the bottom. The ocean is assumed to be cylindrically symmetric, with a bottom attenuation of $0.2dB/\lambda$ and inhomogeneity correlation length of $5m$. All other parameters are as in section 4.1. In Fig. 4-52 backscattering from a rough fluid bottom with $1m$. RMS roughness is shown. A pulse of 0.5 sec. duration and a center frequency of 70 Hz. is broadcast. The

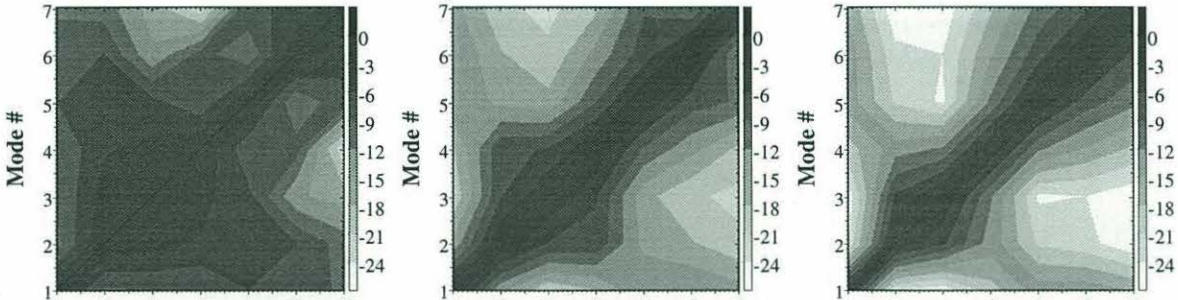

a) Scattered field XMC, r = .5 km. b) Scattered field XMC, r = 5 km. c) Scattered field XMC, r = 20 km.

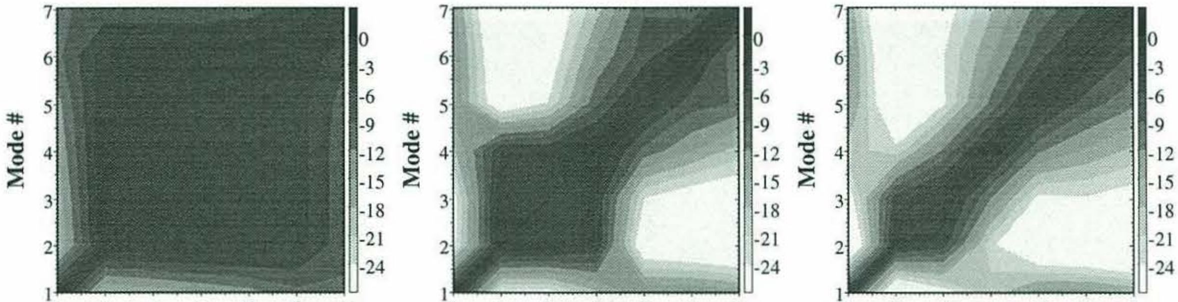

d) Total field XMC, r = .5 km. e) Total field XMC, r = 5 km. f) Total field XMC, r = 20 km.

Figure 4-50: Cross-modal expectations (XMC) for limestone bottom scenario

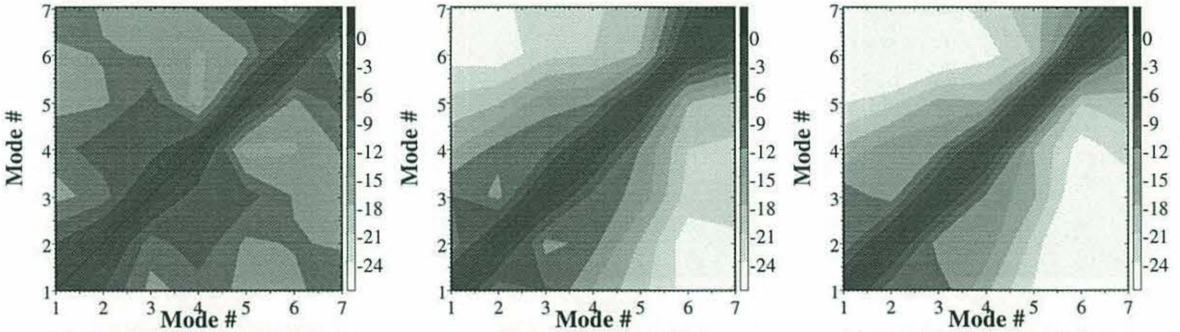

a) Scattered field XMC, r = 0.5 km.

b) Scattered field XMC, r = 5 km.

c) Scattered field XMC, r = 20 km.

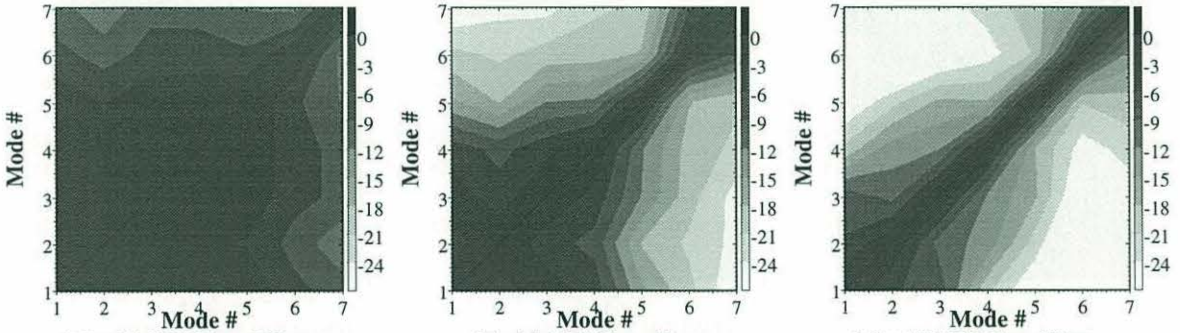

d) Total field XMC, r = 0.5 km.

e) Total field XMC, r = 5 km.

f) Total field XMC, r = 20 km.

Figure 4-51: Cross-modal expectations (XMC) for basalt bottom scenario expected backscattered intensity is plotted, starting immediately after the pulse has been transmitted. The highest levels are received in the first second or so, and is contained in the continuous spectrum modes. After a few seconds the received energy is contained almost entirely in the proper modes; mode 4 is the highest proper mode present, and is seen to be dominant in the time series. Reverberation at these longer times is generated at regions farther from the source, and only the proper modes have low enough attenuation to propagate to and from the scattering site without being stripped. This phenomenon has been described by Urick [83, p. 281] in discussing experimental shallow-water reverberation data.

Figure 4-53 shows scattering in the same waveguide, but for volume scattering from a random layer in the upper 20 m. of the sediment bottom (between 100 m. and 120 m. depth). The correlation length is again $5m.$, and $\sigma = 0.05$. At short times the reverberation is again dominated by the high-angle continuous spectrum modes. The energy in these modes is predominantly in the bottom, indicating that the high-angle scattered energy is not coupling into the water column well. At longer times the evanescent decay of the proper modes in the bottom is observed. Comparing these two plots, the scattered field generated by the volume scattering is seen to fall off more quickly with range. This reflects the fact that the proper modes, dominant at longer times, do not penetrate into the bottom well.

Figure 4-54 shows backscattered energy from a rough limestone bottom, the same scenario shown in section 4.2.1. Roughness correlation length is again $5m.$, and the RMS roughness height is $1m.$Receivers are located in the water column only. The main features of the plot are similar, with continuous spectrum energy dominating the early arrivals and the proper modes (mode 3 is the highest proper mode) dominating later arrivals. However, between 2 and 4 seconds, higher backscattering levels are visible on the hydrophones between 80-100 m. This corresponds to energy scattered into the Scholte wave which exists on the fluid-elastic interface. For this example KRAKEN finds the Scholte mode to have an attenuation in between that of the proper and continuous spectrum modes, explaining its decay rate in time.

The figures above were plotted using the Born approximation; attenuation of the outgoing mean field due to scattering was ignored. In Fig. 4-55 the self-consistent correction is included, and its effect is seen to be fairly small. For the sediment scattering case shown above the effect is even smaller. In other cases, however, the added attenuation may be significant.

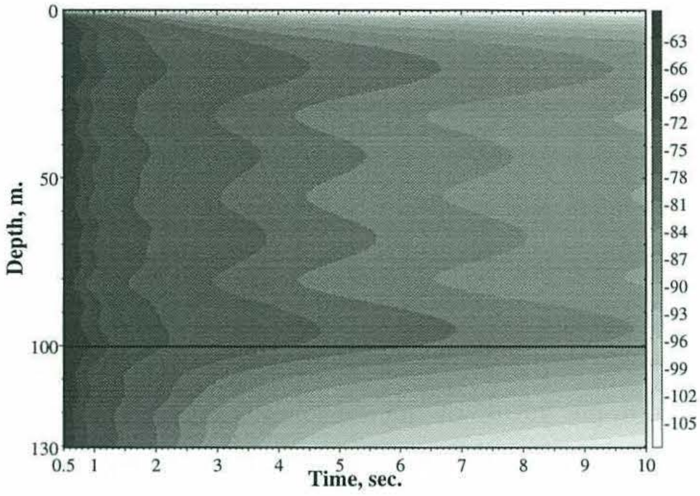

Figure 4-52: Backscattered intensity *vs.* time for rough fluid bottom. Pulse duration is 0.5 sec, center frequency 70 Hz.; RMS roughness = 1 m., 5 m. correlation length. Proper modes dominate at longer times.

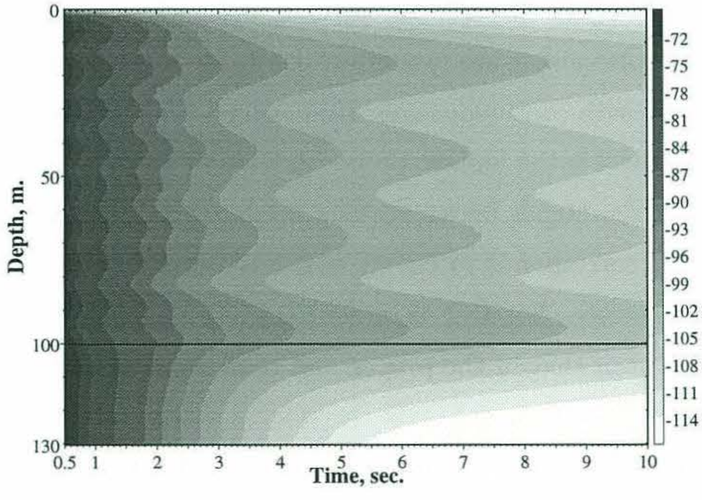

Figure 4-53: Backscattered intensity *vs.* time for fluid bottom with random layer in upper 20 m. of bottom [100-120 m.]. 0.5 sec pulse centered at 70 Hz.; σ = 0.05, CL = 5 m. Received intensity plotted also in the sediment bottom; note early continuous- spectrum energy is largely trapped in bottom.

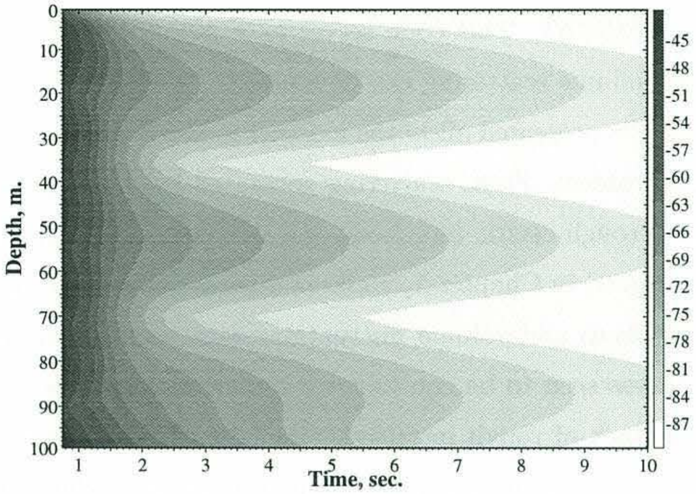

Figure 4-54: Backscattered intensity *vs.* time for rough limestone bottom. 0.75 sec pulse centered at 50 Hz.; RMS roughness = 1 m., CL = 5 m. Scholte mode energy can be seen in first 5 sec.

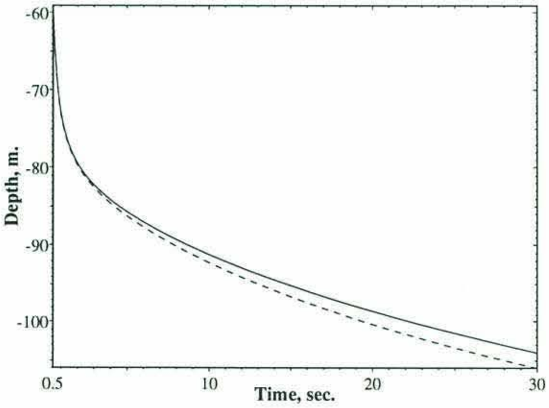

Figure 4-55: Self-consistent *vs.* Born calculations for backscattered intensity. Rough fluid bottom, (r, z) geometry, 50 m. receiver depth, other parameters as before. Mean-field mode attenuation due to scattering has only a small effect on backscattering levels.

4.8 Summary

The scattering theories developed in Chapters 2 and 3 have been implemented in a modal reverberation code, NMSCAT. This code serves as a numerical laboratory in which the effects of surface and volume scattering can be studied.

The numerical results presented allow the modeler to study a number of different factors in the reverberation problem. First, scattering generated by different types of scatterers - rough fluid interfaces, rough elastic interfaces, and volume fluctuations in a fluid bottom - were compared. As argued in Chapter 1, no large differences in the character of scattering from fluid rough interfaces and volume fluctuations were seen. Scattering from randomness in the sediment was seen to be equivalent whether described as volume scattering or as scattering from a stack of rough interfaces. Including bottom elasticity was shown to potentially give large changes in field predictions, due to scattering into the fluid-elastic interface wave. Second, the effect of roughness and/or fluctuation statistics was examined. The directionality of the scattered field was seen to depend strongly on the choice of power spectrum as well as the horizontal correlation length. Finally, waveguide propagation effects were shown to be extremely important. The total field coherence in the ocean appears to depend strongly on bottom type. Time domain results allowed further understanding of the roles played by different types of modes - proper, continuous spectrum, and Scholte modes - in backscattering.

Chapter 5

Long-range Arctic propagation

Recently an international effort has begun to test the feasibility of acoustically monitoring the climate of the Arctic Ocean. The permanent ice cover in the central Arctic makes it difficult to obtain oceanographic data, and as a result the Arctic is much less well understood than the temperate oceans. Acoustic tomography is attractive as it provides a possible means for synoptic measurements of Arctic Ocean properties. Monitoring of the Arctic is of special interest since many global climate models predict that the Arctic should be especially sensitive to any global warming [56]. The reason for this is that the total volume of the ice cover is much less than that of the ocean it covers. Thus even a relatively small warming of the Arctic, which would likely come as a result of an influx of warmer water from the Atlantic, could have a large effect on the ice cover. A substantial melting of the ice cover would in turn affect the global climate, as the presence of the ice changes the albedo of the polar regions, as well as damping ocean/atmosphere exchange [28].

Earlier studies [56, 22, 21] show that at low frequencies the acoustic phase and travel time are relatively insensitive to changes in the ice cover, while amplitude attenuation is strongly affected by changes in ice thickness and roughness. These results are re-confirmed below. Previous analysis also indicates that internal wave levels in the Arctic are low enough not to cause large travel time fluctuations [56]. Thus it might be possible to use travel time information to invert for water mass temperatures, and modal attenuations to estimate the parameters of the ice cover.

Acoustic monitoring of Arctic climate was proposed in 1991 by a group at Science Applications International Corp (SAIC) [56]. This led to a trans-Arctic propagation (TAP) feasibility experiment involving US, Canadian, and Russian research groups. From April 17-22 1994, CW and coded maximal length sequence (MLS) transmissions were broadcast

Figure 5-1: April '94 feasibility test source was at Turpan camp (83 30.0' N, 26 0.0' E, north of Svalbard); receiver camps were Narwhal (83 52.5' N, 62 52.9' W, Lincoln Sea) and Simi (72 59.9' N, 149 35.8' W , Beaufort Sea)

from the Russian ice camp 'Turpan' (see Fig. 5.1) and received on a vertical array the US/Canadian ice camp 'Narwhal' (900 km. range) and on vertical and horizontal arrays at the MIT/WHOI ice camp 'Simi' (2600 km range). Most transmissions were centered around 19.6 Hz and had a duration of one hour. Results so far show the phase along the 2600 km. path was quite stable, giving excellent travel time resolution.

In this chapter we focus on developing modeling tools to help understand the results of this and future trans-Arctic experiments. The Arctic Ocean is acoustically distinctive because the sound speed increases monotonically with depth. This causes sound to be refracted upward, interacting with the rough ice cover. This scattering problem must be well understood in order to model long-range propagation. The KS perturbation scattering theory described earlier has been extended by LePage & Schmidt [47] to consider scattering from a three-dimensional rough ice sheet. This work showed the importance of scattering into the flexural wave of the ice sheet and was used to show good agreement with previous data for long-range transmission loss in the Arctic. In this chapter LePage's work is extended slightly and is used to study the effects of a changing ice cover on trans-Arctic propagation. After a discussion of the acoustical environment in the Arctic, a parameter study is presented which shows the sensitivity of modal group speeds and attenuations to ice parameters. Time series simulations are then made and compared to TAP data. It is shown that use of historical sound speed data gives travel time predictions which are slower than those observed. However, there is recent evidence of warming in the eastern Arctic, and simulations including this effect should agree more closely with the data. Finally, we compare predictions of the LePage/Schmidt ice scattering model with those obtained with the impedance scattering theory of Kudryashov *et al.* [42]. Earlier comparisons of the two theories had shown very close agreement, giving the impression that the scattering process was well understood. A closer examination shows that the agreement seems to be coincidental, and that actually the two theories are modeling slightly different physical scenarios.

5.1 Acoustical environment in the Arctic

In this section we describe the environment in more detail, concentrating first on the oceanography and second on typical properties of the ice cover. Overviews of Arctic circulation and water masses can be found in Pickard and Emery [63] and Carmack [10, p.171-222], and an excellent discussion of ice in the Arctic is given by Gow and Tucker [28, p.47-122].

5.1.1 Arctic oceanography

From Figure 5.1 we can see that the main channel which connects the Arctic to the other oceans is through the Fram Strait, between Svalbard and Greenland. The West Spitzbergen Current (WSC), which passes through this strait, is the main inflow of water into the Arctic. Relatively warm and salty Atlantic water flows into the Arctic in this current. Yearly variations in the inflow of Atlantic water can be fairly large [21]. On entering the Arctic the Atlantic water cools rapidly but remains warmer than most Arctic water. In the central Arctic the WSC appears to split into several branches. The main outflow from the Arctic is in the East Greenland current (EGC), which also flows through the Fram Strait. The EGC carries water at all depths. In the region of the Fram Strait there appears to be some recirculation of the Atlantic water, with some portion of the Atlantic water which has circulated through the Arctic mixed back in, while the rest exits in the EGC.

The water masses in the Arctic can be divided into three layers. The first 200 m. or so in depth are known as the *surface* layer. This water is quite cold, close to the freezing point, and is strongly influenced in salinity by river runoff and by the melting and freezing of the ice cover. The *Atlantic* water is roughly between 200-800 meters, and is carried into the Arctic by the WSC. The lower *deep* water makes up about 60% of the Arctic Ocean by

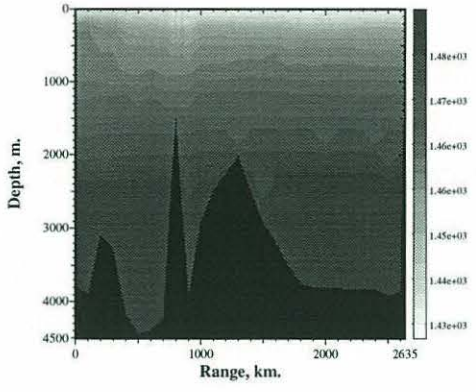

Figure 5-2: GDEM sound speed database. Sounds speeds plotted from source (left) to receiver(right)

volume. It is divided into several water masses by bathymetry.

These different water types are seen in Fig. 5.2, which shows sound speed data along the TAP propagation path taken from the Generalized Digital Environment Model (GDEM) [79]. The bathymetry along the path is also shown. Near 800 km. the path intersects the Lomonsov ridge, which divides the Arctic into the Eurasian basin (source side) and the Canadian basin (receiver side). The cooling of the Atlantic water as it travels into the Arctic can be seen in the early part of the path. The Atlantic water loses more energy to the surface, which is colder than the deep water below it, causing the temperature maximum to become deeper. A front has been observed near the Lomonosov ridge, as seen on the plot. In the Canadian basin the deep water is somewhat warmer, giving a higher sound speed. This effect is more easily seen in Fig. 5.3, which shows individual sound speed profiles at the source and the receiver. We can also see that the cooling of the Atlantic water has caused the near-surface acoustic duct to become thicker but less clearly defined.

Recent icebreaker [9] and submarine data has shown that the front near the Lomonsov ridge has recently shifted towards the Canadian basin, and that the Atlantic water in the Eurasian basin is warmer than shown in the GDEM data. Pawlowicz [61] has explained these changes by arguing that the recirculation of Atlantic water in the Fram Strait area is partly controlled by the location of the front near the Lomonosov ridge. A shift in the frontal location could cause more Atlantic water to be recirculated, causing an overall warming trend in the Eurasian basin water.

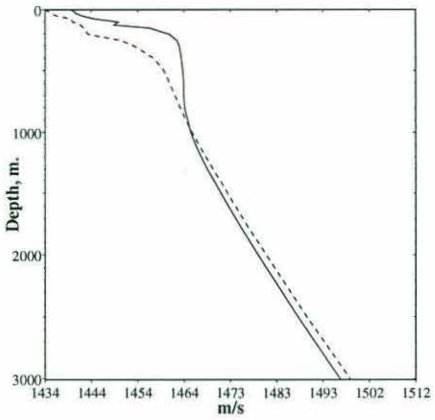

Figure 5-3: Source and receiver sound speed profiles. Source profile = solid, receiver profile = dashed

5.1.2 Ice cover model

In the central Arctic the ice covers around 99% of the ocean during the winter and $80-90\%$ in the summer. This ice can be divided by age into first-year and multi-year ice. First-year ice is generally about 1 meter in thickness. As several years pass the ice becomes thicker and stronger, with the mean thickness for multi-year ice being around 3-4 meters. The ice forms into large sections, or *floes*, whose circulation is driven by currents and wind. Substantial variations in ice thickness can be found in any given area. These differences can develop as gaps, or *leads*, between adjoining ice sheets open up and then freeze over. Adjacent floes may also be of different ages and have different thicknesses. Small scale roughness is introduced by fractures in the ice and by dendritic growths on the bottom of the ice resulting from rejection of salt as the water freezes. Larger scale features such as *ridges* may result when floes are driven up against each other, deforming the ice sheets. Ridges with thicknesses up of to 10 meters have been observed. Histograms of ice thickness show all these types of ice. A small peak in ice thickness at around 1 meter is observed, corresponding to first year ice. Most ice measured is at around 3-4 m. thickness, but there is a long tail to the histogram corresponding to deformed ice with very large thickness.

The model for the ice sheet used for these calculations is shown in Fig. 5.4. The nominal ice thickness is taken to be 4 meters. The compressional and shear wave speeds and attenuations in the ice are typical of those found in experimental studies [84, 57]. We note that these ice attenuations are much larger than those measured in laboratory studies of wave propagation in ice. The increase in *in situ* attenuation is believed to come from friction at small-scale fractures of the ice sheet. The roughness on the top and bottom of the

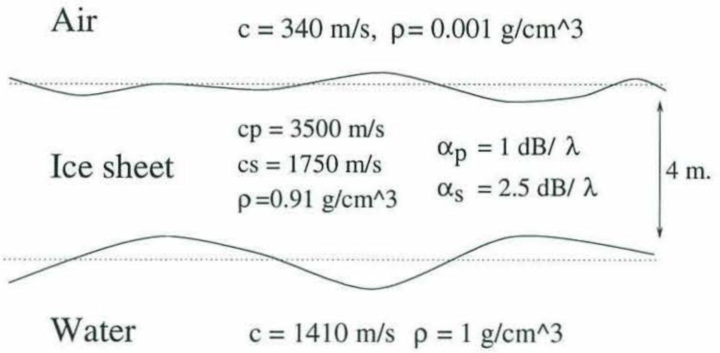

Figure 5-4: Nominal ice parameter values

ice sheet is described by a Goff-Jordan power law spectrum. The RMS roughness is taken to change with ice thickness according to the empirical relation $\sigma_{RMS} = 0.65H$ [22]. The top and bottom roughnesses are assumed to be uncorrelated, with the rms top roughness being one-quarter that of the bottom. In actual fact the top and bottom roughnesses will be somewhat correlated, but assuming the correlation is zero greatly simplifies the calculations involved.

5.2 Sensitivity of coherent field propagation

LePage and Schmidt's model can be used to study the sensitivity of modal attenuations and group speeds on parameters of the ice cover. Kevin LePage's SELFCON code was used with the nominal ice parameters above to calculate the coherent field reflection coefficient, which is used as a boundary condition input to the normal mode code KRAKEN. LePage's code was modified slightly to include the effects of attenuation in the ice sheet and different top and bottom roughness heights.

Figure 5.3 showed the existence of a strong Arctic surface duct. The low order modes are trapped in the duct, while higher-order modes interfere to form a convergence zone pattern. Due to this constant interaction we expect the lowest modes to be stripped by scattering from the rough ice sheet. The sensitivity of coherent field propagation to variations in sound speed and ice parameters is examined below.

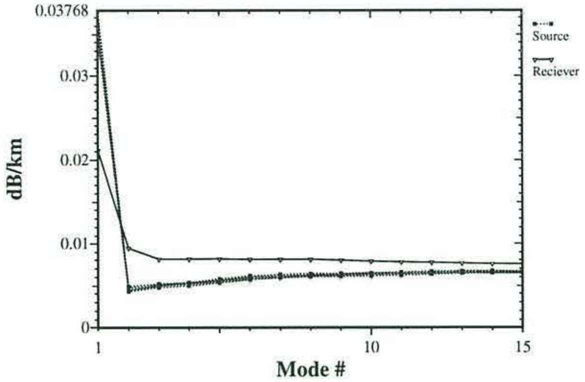

Figure 5-5: Dependence of mode attenuation on sound speed profile. Solid line uses receiver SSP; 5 dotted lines from 5 days of measured SSP at Turpan source camp

5.2.1 Sensitivity to sound speed profile variation

Sound speed profiles at the source were measured during the five days transmissions were carried out. We can use these data to get some idea of the effect of short-term variations in the sound velocity profile. The plots below show mode attenuations and group velocities for the nominal ice parameters. The five sound speed profiles at the source are used and compared to a sound speed profile at the receiver. Daily variability at the Turpan camp during the experiment is seen to give only small changes in propagation. On the other hand, the effect of the different water masses at the source and receiver is quite strong. Near the source only mode 1 is trapped in the surface duct, while near the receiver modes 1 and 2 are in the duct, meaning mode 2 experiences more ice interaction and as a result is attenuated more rapidly.

5.2.2 Sensitivity to ice parameters

Ice parameters were varied around the nominal values shown above. Historical sound speed data for the source location are used to model acoustic propagation. Order of magnitude results (see Table 5.1) show that modal attenuations $\Delta\beta_n$ and group speeds Δc_g are far more sensitive to roughness parameters than to wave speeds or attenuation in the ice. These results seem to be qualitatively similar to the results of a parameter study done using the impedance scattering theory [21], but we predict a greater sensitivity to thickness.

Figures 5.7 and 5.8 show mode attenuations and group speeds as thickness and roughness correlation lengths are varied. As mentioned above ice roughness is assumed to be

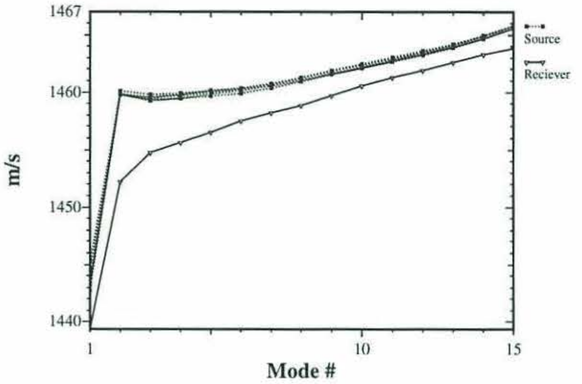

Figure 5-6: Dependence of modal group speeds on sound speed profile. same profiles as above

proportional to ice thickness. This increasing roughness is mostly responsible for increases in mode attenuation seen for increasing thickness, while changes in group speed are due to thickness change directly. The largest changes are seen for very large ice thicknesses and for short correlation lengths. The changes in modal group velocities are fairly small when compared to the differences due to the different water masses at the source and receiver.

Figures 5.9 - 5.12 show representative plots of the effect of changing the wave speeds and attenuations in the ice. These results are summarized in Table 5.1.

Parameter	*Range*	$\Delta\beta_n$ (dB/km)	Δc_g (m/s)
H	2 - 6 m.	2e-2	.6
CL	11-44 m.	2e-2	.5
α_s	1.5 - 3 dB/λ	5e-3	.05
α_p	0.5 - 1.5 dB/λ	5e-5	1e-3
c_p	3000-4000 m/s	2e-4	4e-3
c_s	1600-1900 m/s	2e-5	4e-4

Table 5.1: Order-of-Magnitude changes in modal attenuation and group speed over range of ice parameter variation; changes in thickness (H), correlation length (CL), compressional and shear wave speeds c and attenuations α are considered.

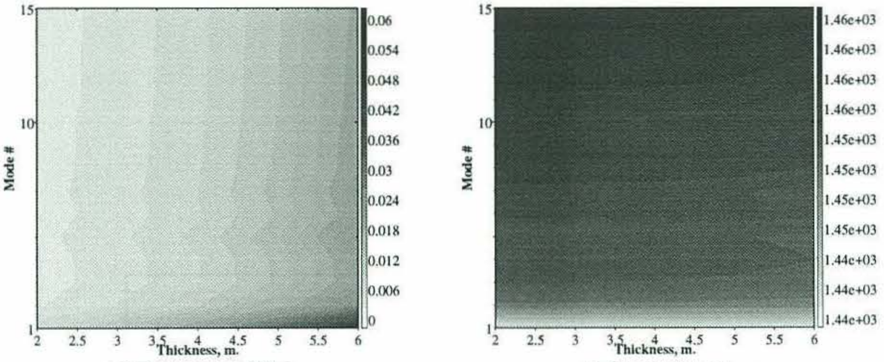

a. Mode attenuation, dB/km.

b. Group Speeds, m/s.

Figure 5-7: Effect of changing ice thickness on modal attenuation and group speeds

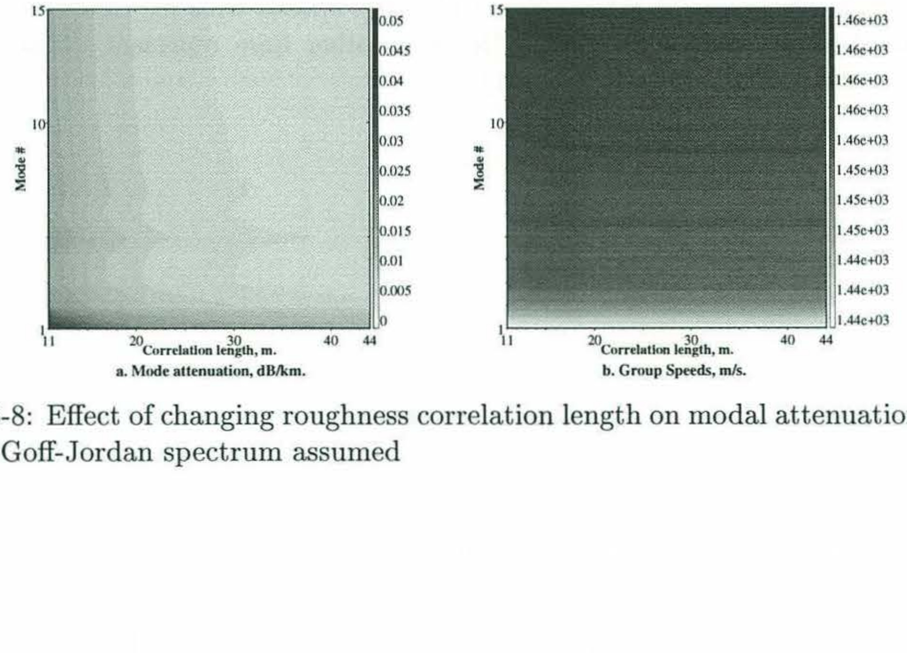

a. Mode attenuation, dB/km.

b. Group Speeds, m/s.

Figure 5-8: Effect of changing roughness correlation length on modal attenuation and group speeds. Goff-Jordan spectrum assumed

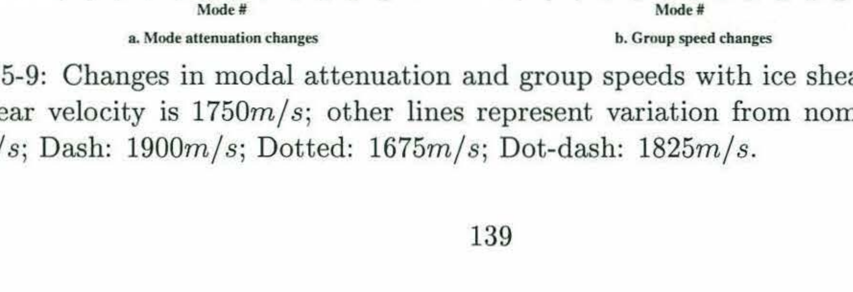

a. Mode attenuation changes

b. Group speed changes

Figure 5-9: Changes in modal attenuation and group speeds with ice shear velocity. Nominal shear velocity is $1750m/s$; other lines represent variation from nominal case. Solid: $1600m/s$; Dash: $1900m/s$; Dotted: $1675m/s$; Dot-dash: $1825m/s$.

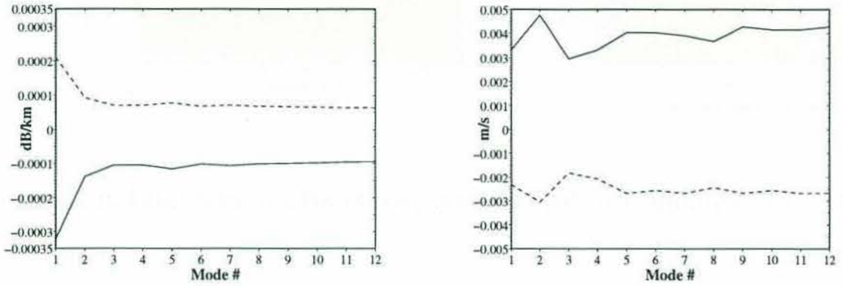

a. Mode attenuation changes

b. Group speed changes

Figure 5-10: Changes in modal attenuation and group speeds with ice compressional velocity. Nominal compressional velocity is $3500m/s$; other lines represent variation from nominal case. Solid: $3000m/s$; Dash: $4000m/s$.

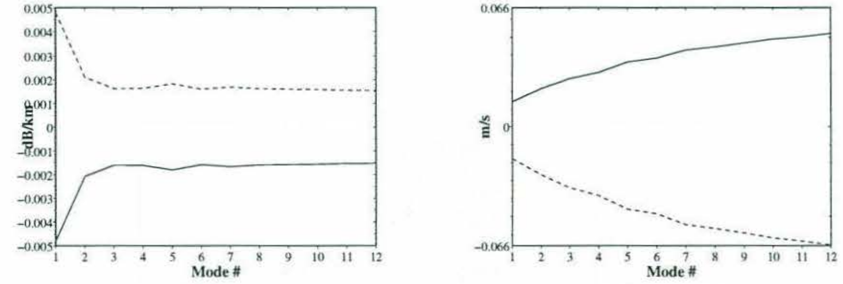

a. Mode attenuation changes

b. Group speed changes

Figure 5-11: Changes in modal attenuation and group speeds with ice shear attenuation. Nominal shear attenuation is $2dB/\lambda$; other lines represent variation from nominal case. Solid: $1.5dB/\lambda$; Dash: $3.5dB/\lambda$

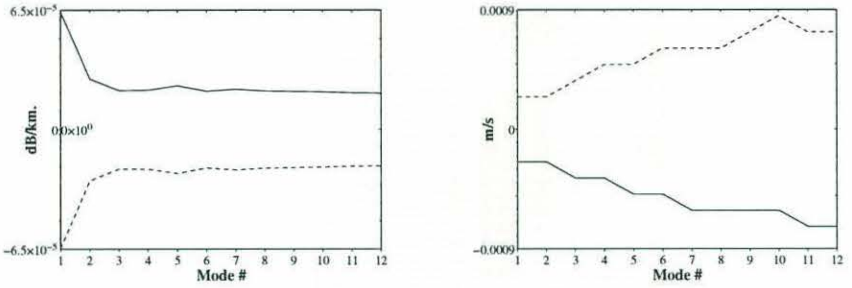

a. Mode attenuation changes

b. Group speed changes

Figure 5-12: Changes in modal attenuation and group speeds with ice compressional attenuation. Nominal compressional attenuation is $1dB/\lambda$; other lines represent variation from nominal case. Solid: $0.5dB/\lambda$; Dash: $1.5dB/\lambda$

5.3 Comparison of modeled and received time series

Coded MLS transmissions from the April '94 TAP experiment have been matched-filtered and coherently averaged to provide travel time data. MLS receptions on the Simi vertical line array for Julian day 110 are shown below. Mode shapes 2-4 have zero-crossings near 200 m, in the middle of the plot. Mode 1 is highly attenuated and difficult to identify in the data.

To help in interpretation of the data, time series simulations have been generated using KRAKEN, with LePage's SELFCON code used to specify the boundary condition at the ice. Historical sound speed profiles from the GDEM atlas were used for the modeling. A Gaussian pulse with a bandwidth similar to that of the M-sequence transmissions was propagated through the ocean. The ocean was modeled in 34 range segments, chosen to capture the largest changes in sound speed and bathymetry along the path.

Coupled-mode simulations of the TAP experiment are shown in Fig. 5.14. The Gaussian pulse used for simulation has much larger dispersion than the actual TAP signal, but the results can help identify modal arrivals. Modes > 7 are sharply attenuated due to coupling at the Lomonosov ridge. This stripping appears to be consistent with what is seen in the data. Mode 1 is seen to be heavily attenuated. The mode 2 - mode 3 delay is larger than observed in the data. The higher order modes are fastest, and are seen in both the simulation and the data to have overlapping arrivals.

We can explain differences in the relative modal arrival times by assuming that the Atlantic water was warmer and penetrated deeper into the Arctic during the experiment

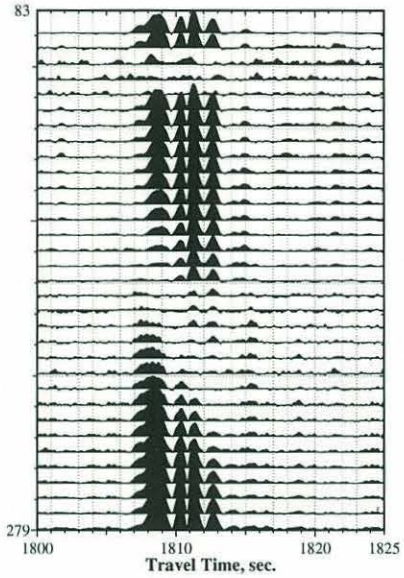

Figure 5-13: Processed time series on vertical array. (processing done by E. Scheer, Woods Hole Oceanographic)

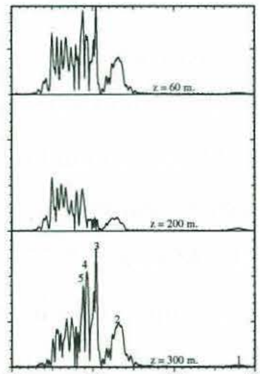

Figure 5-14: Coupled mode simulated TAP time series for three different depths

than is shown in the GDEM data. As mentioned earlier icebreaker observations by Carmack *et al.* indicate that this is the case.

5.4 Comparison of impedance and boundary operator scattering theories

Scattering theories developed by LePage & Schmidt [47] and Kudryashov *et al.* have been used to predict long-range transmission loss in the Arctic. Kudryashov's method is based on perturbing an impedance boundary condition at the interface, while LePage & Schmidt's method uses the KS boundary operator approach to perturb all boundary conditions at the rough interface. Earlier comparisons showed very close agreement between the approaches [22]. This apparent agreement was deceptive, both because the MIT group had not included the effects of attenuation in the ice and because the models for ice statistics used were quite different. When attenuation is included and the same ice model is used, the boundary operator approach yields much higher mode attenuations.

A detailed comparison of the boundary operator and impedance scattering theories is given in Appendix C, and the results are summarized here. The reason for the disagreement between the two theories can be understood by considering scattering from a rough fluid-fluid interface. The boundary operator approach ensures that both the mean and scattered fields satisfy the two boundary conditions at the rough interface. The impedance boundary condition, however, is only a single boundary condition based on the unperturbed reflection coefficient. Kudryashov's method is based on a Taylor expansion of the boundary impedance, using the interface roughness as the small parameter. Thus the expression for the scattered field derived comes from perturbing a *single* boundary condition, the impedance boundary condition, and cannot satisfy the *two* boundary conditions at a rough fluid-fluid interface. The impedance scattering theory gives exact agreement with the KS theory for inherently one-sided boundaries, such as a pressure-release or rigid surfaces, and can be expected to give a good approximation for boundaries with high impedance contrast. In the other limit, as the impedance contrast goes to zero, the impedance method incorrectly predicts that a scattered field will still exist.

The important question for Arctic modeling is whether the ice plate impedance is high enough that the two scattering theories will be in reasonable agreement. Fig. 5.15 shows mode attenuation coefficients for scattering from the ice sheet calculated using the two methods. The sound speed profile is taken from historical data for the TAP source location

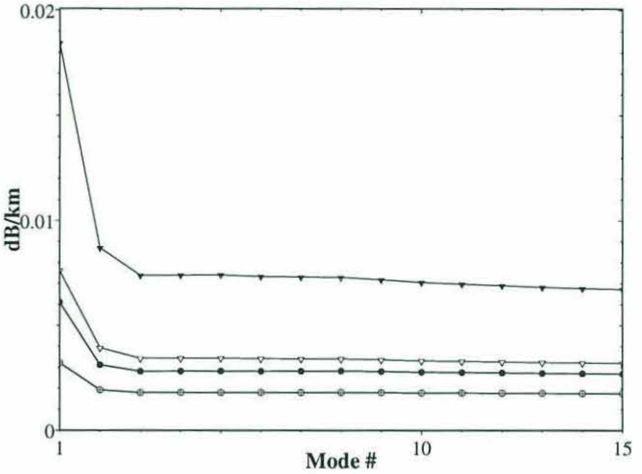

Figure 5-15: Mode attenuation caused by scattering from rough ice plate: f = 20 Hz; Goff-Jordan power spectrum. Closed triangle is LePage result, including ice attenuation; open triangle is Lepage, no attenuation; Closed circle is Kudryashov result, K12 = 0.7; Open circle is Kudryashov, K12 = 0

and typical ice parameters (shown on plot) are used. The top and bottom roughnesses of the ice sheet are assumed to be perfectly correlated. We see the impedance method results (including ice attenuation) are quite close to the LePage/Schmidt results with attenuation in the ice set to zero. Much higher attenuations (and proportionally larger losses for mode 1) are predicted when attenuation in the ice is included.

We stress that the mode attenuations presented by Gavrilov, Kudryashov *et al.* in their reports [22, 21] are higher than those shown in Fig. 5.15, and in fact agree well with the mode attenuations found using the modified SELFCON (including attenuation in the ice) and KRAKEN. The difference in the results comes from the fact that the Russian group have assumed a different model for ice roughness. The ice roughness is described using a bimodal distribution which is probably more realistic than the Goff-Jordan spectrum used in generating Fig. 5.15. Perhaps more importantly, correlation between roughnesses on the top and bottom of the ice is taken into account. As mentioned earlier, this correlation is difficult to model using the KS scattering theory. Thus the main conclusion of this section is that further work remains to be done in understanding scattering from the Arctic ice cover, combining the realistic ice model used by Gavrilov and Kudrashov with a more generally applicable scattering theory.

5.5 Summary

While earlier chapters concentrated mainly on scattering in shallow water, this chapter examined the effect of scattering from the rough ice cover on long-range Arctic propagation. The primary modeling tool was the ice plate scattering model of LePage & Schmidt. This model was modified slightly and used to carry out a parameter study of the effect of different ice parameters on Arctic propagation. Modal scattering losses and group speeds were calculated, and shown to depend most strongly on ice thickness and roughness parameters. Simulated time series were generated and compared to results from the April '94 TAP experiment. Modeling showed that the modal amplitudes could be explained in a satisfactory way using the scattering model if shear wave attenuation in the ice was taken into account. Comparison of simulations with data showed that Arctic water was warmer than indicated in historical databases. More recent oceanographic measurements also show warmer water in the Arctic. Simulations using the measured oceanography are expected to show better agreement with the data. This and other modeling work indicates that tomographic modeling of Arctic ocean temperature is practical.

Chapter 6

Conclusions and future directions

In this thesis an attempt has been made to understand and model the extremely complicated scattering processes which take place in real ocean waveguides. While the work presented here is helpful in understanding some of the physics involved, much fundamental work remains to be done. In this final chapter we attempt to draw general conclusions from what has been learned, and use the insights gained to suggest directions for continuing research.

6.1 Summary of results

First we consider the shallow water reverberation problem. The results of the thesis can be summarized under several headings:

Sensitivity to propagation environment:

For the low frequency reverberation scenarios considered in this thesis, propagation and waveguide effects were seen to be extremely important. For virtually all cases considered, the spatial statistics calculated for the reverberant field were dominated by the modal interference pattern. Bottom sound speeds and sound speed gradients in the water were also shown to have a large impact on bottom scattering levels. Bottom impedance was seen to be an important factor for determining whether or not scattering has a large effect on total field statistics.

This sensitivity has several practical implications. First, it shows that modelers need to represent the deterministic background properties of the ocean as accurately as possible. In the chapters above, results were derived in several cases for very idealized ocean environments - for example, random sediment layers were assumed to be isovelocity, and only isovelocity elastic halfspaces were considered. These kinds of idealized results are important and useful tools, since they allow us to isolate the different effects in scattering. However, models based on these simplifications may fall short when compared to experimental data.

For experimentalists, correct interpretation of scattering data may depend on accurate measurements of the water and bottom properties. Good measurements of bottom properties are of course difficult to make, and are one of the main reasons shallow-water propagation is difficult to predict in the first place. Hopefully modelers can make a contribution to better experiment design by predicting, given a rough description of the experimental site, which environmental parameters are the most important to measure correctly.

The dominant role played by the waveguide in shaping the scattered field means that inversion for scattering mechanisms from low-frequency reverberation data would be extremely difficult. The numerical results in Chapter 4 showed few obvious means for telling whether reverberation was caused by rough fluid interfaces, rough elastic interfaces, or volume inhomogeneities in the bottom. This can be contrasted to Tang's work [75], which showed theoretically that correlation lengths of sediment inhomogeneities could be inverted from bottom scattering data. In his scenario the receiving array was quite close to the bottom, so waveguide effects were not important.

As a final note, it might be possible for a model which handles the propagation effects well to obtain a good match with data even if only a very simplistic scattering model is used. For example, Ellis [17] has shown good agreement to data with a normal-mode reverberation model. The scattering theory used, Lambert's law, almost certainly does not model the physics realistically.

Sensitivity to roughness and/or volume fluctuation statistics:
The numerical results in Chapters 3 and 4 showed clearly that the nature of the scattered field depends strongly on the statistical distribution of the random scatterers. Both the characteristic length scales and the power spectrum descriptions of the scatterers had large effects on the directionality of the scattered field. This shows that work such as that done by Goff and Jordan [25] in describing bottom roughness and Yamamoto [86] in describing volume fluctuations in sediments is critical. Any effort put into better understanding and parameterizing the variations of the ocean's properties can be expected to have a large payoff in terms of more realistic scattering models.

Modeling of different scattering mechanisms:
One of the main thrusts of this thesis has been to include several different scattering mechanisms into the reverberation model. The numerical results supported the idea, introduced in Chapter 1, that volume and surface scattering can be considered to be physically similar. More dramatic differences were seen when bottom elasticity was included, due to

the presence of interface waves. In general, however, we reach the somewhat surprising conclusion that the actual scattering mechanism is often less important than either the roughness/fluctuation statistics or the environment in which the scattering occurs.

In Chapter 5 modeling results in support of the trans-Arctic propagation experiments were detailed. A number of results of that modeling can be briefly stated:

- Modal attenuations and group speeds are most sensitive to ice thickness and roughness, rather than other ice parameters.
- Observed modal amplitudes can be matched reasonably well using the modified LePage-Schmidt ice scattering model.
- Inversion for water temperatures from long-range acoustic transmission data seems to be possible.
- More work is needed in developing ice scattering models.

6.2 Directions for future modeling efforts

There are a number of ways in which the models proposed in this thesis can be improved on and extended. The most obvious steps would be to relax some of the simplifying assumptions made. As one example, the effect of a sound speed gradient in sediment volume scattering layers has been neglected. An isogradient layer could be taken into account by representing the waves in the layer in terms of Airy functions, rather than plane waves.

The work presented above models volume scattering in fluid media only, and cannot account for the presence of gradients or multiple layers in elastic bottoms. The modal reverberation model would be more useful if it could treat more realistic elastic layers (including the ice cover in the Arctic), and could describe volume scattering in elastic media. These more realistic elastic scattering formulations would need to be based on a better understanding of the fluid/elastic reciprocity relationship.

Probably the most useful extensions to the models proposed above would be to consider range-dependence and three-dimensional scattering. Mild range dependence could be handled using adiabatic modes, using only slight modifications to the present theory. Stronger range dependence would be more difficult to treat, as it would require using coupled-mode theory. In principle three-dimensional scattering could be treated using the approach developed in Chapter 2. The speed advantage of the modal formulation would be especially important for 3D calculations.

Finally, single-scattering theories are almost certainly inaccurate for extremely long-range propagation. Over long ranges the scattered field will have many opportunities to re-scatter, redistributing energy among scattered field modes (note that a single-scatter theory should be accurate for finding coherent field scattering loss, as in Chapter 5, since scattered energy can never re-scatter back into the coherent field). An approach could be developed in which the ocean is divided up into segments, each of which is short enough that single-scatter reverberation theory should be accurate. The cross-modal coherences could then propagated through the different single-scatter segments. Such an approach could be used to calculate scattered field statistics for future TAP experiments.

Appendix A

Derivations for rough surface scattering theory

A.1 Wavenumber transform of Helmholtz theorum

As previously discussed, the scattered field in the water column can be written in terms of boundary conditions along the rough surface using the Helmholtz integral theorum. This theorum can be transformed into the wavenumber domain as follows. The integral theorum along a rough surface (x', z') is given by:

$$s(x,z) = \int dx^{'} [s(x',z') \frac{\partial G_\omega(x,z \mid x',z')}{\partial z'} - \frac{\partial s(x',z')}{\partial z'} G_\omega(x,z \mid x',z')] \tag{A.1}$$

To simplify the explanation here we consider transforming only the first term:

$$s(x,z) = \int dx^{'} s(x',z') \frac{\partial G_\omega(x,z \mid x',z')}{\partial z'} \tag{A.2}$$

Applying the 2-D (x, z) wavenumber transform as defined in Chapter 2 gives:

$$\tilde{s}(q,z) = \frac{1}{2\pi} \int dx \int dx^{'} s(x',z') \frac{\partial G_\omega(x,z \mid x',z')}{\partial z'} e^{iqx} \tag{A.3}$$

We can then substitute expressions for $s(x', z')$ and the Green's function:

$$\begin{aligned} s(x',z') &= \int dq_1 \tilde{s}(q_1,z') e^{-iqx'} \\ \frac{\partial G(x,z \mid x',z')}{\partial z'} &= \int dq_2 \frac{\partial G(q_2,z,z')}{\partial z'} e^{-iq_2(x-x')} \end{aligned} \tag{A.4}$$

This gives a four-fold integral:

$$\tilde{s}(q,z) = \int\int\int\int dxdx^{'}dq_1dq_2\tilde{s}(q_1,z')\frac{\partial G_\omega(q_2,z,z')}{\partial z'}e^{i(q_2-q_1)x'}e^{i(q-q_2)x} \tag{A.5}$$

The exponential terms are eliminated using the definition of the delta function:

$$\delta(q-q_2) = \frac{1}{2\pi}\int_{-\infty}^{\infty} dxe^{(q-q_2)x}, \tag{A.6}$$

etc. The final result is

$$\tilde{s}(q,z) = 2\pi\tilde{s}(q,z')\frac{\partial G(q,z,z')}{\partial z'} \tag{A.7}$$

The other terms are evaluated in the same manner to give the result quoted in Chapter 2. It is also easy to find the equivalent result for an (x,y,z) geometry.

A.2 Spatial domain approach to rough surface scattering

In this section we briefly show a spatial-domain approach to the scattering problem. This work seems to show that representing the roughness in terms of its Fourier transform is only valid for a full modal solution when the mode attenuations are zero.

The spatial domain Helmholtz equation is shown in section 2.3. The KS theory shows that the scattered field boundary conditions on the rough surface are given by

$$Bs(x',z') = \gamma(x')\frac{\partial B}{\partial z} < p(x',z') > -\frac{\partial \gamma}{\partial x'}b < p(x',z') > \tag{A.8}$$

The appropriate boundary operator matrices are used.

A.2.1 Rough pressure-release surface

First we consider the simple case of scattering from a pressure-release surface. The KS equations then give

$$s(x',z') = -\gamma(x')\frac{\partial < p(x',z') >}{\partial z'} \tag{A.9}$$

Inserting this in the Helmholtz integral equation, we have

$$s(x,z) = -\int_{-\infty}^{\infty} dx'\gamma(x')\frac{\partial < p(x',z') >}{\partial z'}\frac{\partial G_\omega(x,z \mid x',z')}{\partial z'} \tag{A.10}$$

In the Born approximation the mean field is given by

$$\frac{\partial < p(x',z') >}{\partial z'} = \frac{iNM}{\rho(z_s)} \sum_m \frac{\psi_m(z_s)\frac{\partial \psi_m(z')}{\partial z'}}{2k_m} e^{-ik_m x'} \tag{A.11}$$

where NM is the normalization factor to the field at 1 meter, and the Green's function is

$$G_\omega(x,z \mid x',z') = \frac{i}{\rho(z')} \sum_n \frac{\psi_n(z')\psi_n(z)}{2q_n} e^{-iq_n|x-x'|} \tag{A.12}$$

where the absolute value sign ensures that the scattered field travels away from the scattering patch. Inserting these expressions into the Helmholtz equation and simplifying gives

$$s(x,z) = \frac{NM}{\rho(z_s)\rho(z')} \int_{-\infty}^{\infty} dx' \gamma(x') \sum_{n,m} \frac{\psi_m(z_s)\frac{\partial \psi_m(z')}{\partial z'}}{2k_m} \frac{\psi_n(z)\frac{\partial \psi_n(z')}{\partial z'}}{2q_n} e^{-iq_n|x-x'|} e^{-ik_m x'} \tag{A.13}$$

If we make the forward scattering approximation, then $x - x'$ will always be positive, and the forward-scattered field is:

$$s(x,z) = \frac{NM}{\rho(z_s)\rho(z')} \int_0^x dx' \gamma(x') e^{i(q_n-k_m)x'} \sum_{n,m} \frac{\psi_m(z_s)\frac{\partial \psi_m(z')}{\partial z'}}{2k_m} \frac{\psi_n(z)\frac{\partial \psi_n(z')}{\partial z'}}{2q_n} e^{-iq_n x} \tag{A.14}$$

which agrees with the results given in section 2.3.

A.2.2 Rough rigid surface

Now we look at scattering from a rigid surface. The Kuperman/ Schmidt equations give the boundary condition for the scattered field on the boundary (x',z') as:

$$\frac{\partial}{\partial z} s(x',z') = \gamma(x') \frac{\partial^2}{\partial z^2} < p(x',z') > - \frac{\partial \gamma(x')}{\partial x'} \frac{\partial < p(x',z') >}{\partial x'} \tag{A.15}$$

From the Helmholtz integral, the scattered field in the water is given by

$$s(x,z) = \int_{-\infty}^{\infty} \frac{\partial s(x',z')}{\partial z'} G(x,z \mid x',z'). \tag{A.16}$$

In carrying out this integral we will split up the two terms first and then recombine them later. The first term, inserting the expressions for the pressure and Green's function given above, is

$$T_1 \quad = \quad \frac{NM}{\rho(z_s)\rho(z')} \int_{-\infty}^{\infty} dx' \sum_{m,n} \gamma(x') e^{ik_m x'} (k_0^2(z) - k_m^2) \frac{\psi_m(z_s)\psi_m(z')}{2k_m}$$

$$\frac{\psi_n(z')\psi_n(z)}{2q_n}e^{-iq_n|x-x'|} \tag{A.17}$$

where the $(k_0^2(z) - k_m^2)$ term is the second derivative rewritten using the depth-separated wave equation. If we once again make the forward scatter approximation, the first term is

$$T_1 = \frac{NM}{\rho(z_s)\rho(z')}\int_0^x \sum_{m,n}\gamma(x')e^{-ik_m x}(k_0^2(z) - k_m^2)\frac{\psi_m(z_s)\psi_m(z')}{2k_m}\frac{\psi_n(z')\psi_n(z)}{2q_n}e^{-iq_n(x-x')} \tag{A.18}$$

Now we look at the second term. With the forward-scattering approximation it becomes

$$T_2 = \frac{-iNM}{\rho(z_s)\rho(z')}\int_o^x dx' \sum_{m,n}\frac{\partial\gamma(x')}{\partial x'}k_m e^{-ik_m x'}\frac{\psi_m(z_s)\psi_m(z')}{2k_m}\frac{\psi_n(z')\psi_n(z)}{2q_n}e^{-iq_n(x-x')} \tag{A.19}$$

Inserting the Fourier transform of the roughness derivative:

$$\frac{\partial\gamma(x')}{\partial x'} = \int_{-\infty}^{\infty}\tilde{\gamma}(q)(-iq)e^{-iqx'}dq \tag{A.20}$$

gives for the integral over x':

$$I_1 = \int_0^x dx' \int_{-\infty}^{\infty} dq\tilde{\gamma}(q)(-iq)e^{i((q_n-k_m)-q)x'}. \tag{A.21}$$

The dominant contribution to the integral will come for $q = (q_n - k_m)$; at other wavenumbers the contribution will be reduced due to the rapidly oscillating phase (Note that if the integral were over all x', it could be written as a delta function in q. The delta function would be exactly satisfied only for $(q_n - k_m)$ real, in other words if the mode attenuations are neglected. Neglect of the mode attenuations was discussed in section 2.4) The second scattering term is then well approximated by

$$T_2 = \frac{-NM}{\rho(z_s)\rho(z')}\sum_{m,n}\int_0^x dx'\gamma(x')e^{-ik_m x'}k_m(q_n - k_m)\frac{\psi_m(z_s)\psi_m(z')}{2k_m}\frac{\psi_n(z')\psi_n(z)}{2q_n}e^{-iq_n x} \tag{A.22}$$

Adding the terms together and simplifying, the scattered field generated by a rough rigid boundary at z' is

$$\begin{aligned} s(x,z) &= \frac{NM}{\rho(z_s)\rho(z')}\sum_{m,n}\int_0^x dx'\gamma(x')e^{-ik_m x'}[k_0^2(z') - k_m q_n]\frac{\psi_m(z_s)\psi_m(z')}{2k_m} \\ &\quad \frac{\psi_n(z')\psi_n(z)}{2q_n}e^{-iq_n(x-x')} \end{aligned} \tag{A.23}$$

A.2.3 Results for idealized waveguides

If the waveguide is isovelocity, the mode shapes and eigenvalues can be found analytically. The scattering formulas above then take on simple forms.

For the rough pressure-release bottom, the simplest case is that of the ideal waveguide. The water column is assumed isovelcity and is of depth D, bounded by pressure-release surface on top and bottom. The mode shapes are given by

$$\psi_m(z) = \sqrt{\frac{2\rho}{D}} \sin\left(k_{zn} z\right) \tag{A.24}$$

where

$$k_{zn} = \frac{n\pi}{D}. \tag{A.25}$$

The scattered field is then given by

$$s(x, z) = 2\pi NM \sum_{n,m} \tilde{\gamma}(q_n - k_m) \frac{k_{zm} \sin\left(k_{zm} z_s\right)}{k_m D} \frac{k_{zn} \sin\left(k_{zn} z\right)}{k_n D} e^{-iq_n x} \tag{A.26}$$

For a rough rigid bottom, the simplest waveguide where we can apply the result above is an isovelocity ocean with a pressure release top and rough rigid bottom at depth D. The mode shapes are then given by

$$\psi_m(z) = \sqrt{\frac{2\rho}{D}} \sin\left(k_{zn} z\right) \tag{A.27}$$

where

$$k_{zn} = \frac{(n - 1/2)\pi}{D}. \tag{A.28}$$

Using these values in the equation above gives an expression which is easy to evaluate.

A.3 Equivalence to boundary operator approach

In this section we analytically evaluate the normal mode reverberation model derived above for the simple example of an ideal waveguide, and show it agrees *exactly* with the Kuperman/Schmidt result for the same problem. The ideal waveguide is chosen because its simplicity makes analytical evaluation possible. The global boundary opertator $\tilde{B}(q)$ is a 2x2 matrix which can be inverted analytically, while more complicated scenarios must be solved numerically.

The ideal waveguide consists of an isovelocity fluid layer of depth D bounded above and below by pressure release surfaces. An acoustic source of unit amplitude is located at depth z_s. It is easy to show that the mode shapes for this scenario are given by

$$\phi_n(z) = \sqrt{\frac{2\rho}{D}} \sin\left(k_{zn} z\right) \tag{A.29}$$

where the eigenvalues are given by

$$k_{zn} = \frac{n\pi}{D} \tag{A.30}$$

We now assume that the upper interface $z = 0$ is rough. When looking at the special case of scattering from rough pressure-release surfaces earlier we found

$$\tilde{s}(q, z) = \frac{-i}{\rho} \sum_{n,m} \tilde{\gamma}(q - k_m) \frac{\psi_m(s_z)\psi_m^{'}(0)}{2k_m} \frac{\psi_n(z)\psi_n^{'}(0)}{q^2 - q_n^2} \tag{A.31}$$

Inserting the forms for the mode shapes, noting that $\psi_n^{'}(0) = \sqrt{\frac{2\rho}{D}} q_{zn}$, and carrying out the simple contour integral, we find

$$s(x, z) = 2\pi \sum_{n,m} \tilde{\gamma}(q_n - k_m) \frac{\sin\left(k_{zm} z_s\right) k_{zm}}{k_m D} \frac{\sin\left(q_{zn} z\right) q_{zn}}{q_n D} e^{-i q_n x} \tag{A.32}$$

Next we use a wavenumber integration for this problem and demonstrate exact agreement. First we must find the solution for the mean field in the waveguide. The equation to be solved is the depth separated wave equation with a unit strength source term,

$$\frac{\partial^2 \tilde{\chi}}{\partial z^2} + (k_0(z)^2 - k^2)\tilde{\chi} = -\frac{\delta(z - z_s)}{2\pi} \tag{A.33}$$

The solution for $\chi\tilde{(k)}$ can be written as a sum of the solutions to the homogeneous equation and a particular solution [38, Chap. 2]

$$G_\omega(k, z, z_s) = g_\omega(k, z, z_s) + H_\omega(k, z) \tag{A.34}$$

The homogeneous equation has two solutions, which can be written as up- and down-going plane waves:

$$H_\omega(k, z) = \tilde{\chi}^- e^{-i k_z z} + \tilde{\chi}^+ e^{i k_z z} \tag{A.35}$$

The particular solution is simply the free-space Green's function. It can be shown to be [38, Chap. 2]

$$g_\omega(k, z, z_s) = -\frac{e^{ik_z|z-z_s|}}{4\pi i k_z} \tag{A.36}$$

The amplitudes of the up- and down-going plane waves are found by applying the boundary conditions of $p = 0$ at $z = 0, D$. The boundary conditions can be written in the matrix form:

$$\begin{bmatrix} 1 & 1 \\ e^{-ik_zD} & e^{ik_zD} \end{bmatrix} \tilde{\chi} = \frac{1}{4\pi i k_z} \begin{bmatrix} e^{ik_z z_s} \\ e^{-ik_z z_s} \end{bmatrix}, \tag{A.37}$$

where the source terms come from the particular solution, and the plane wave amplitude vector is

$$\tilde{\chi}(k) = \begin{bmatrix} \tilde{\chi}^- \\ \tilde{\chi}^+ \end{bmatrix}. \tag{A.38}$$

This $2x2$ system is easily solved, giving

$$\begin{aligned} \chi(k,z) &= \tilde{\chi}^-(k)e^{-ik_z z} + \tilde{\chi}^+(k)e^{ik_z z} - \frac{e^{-k_z|z-z_z|}}{4\pi i k_z} \\ &= -\frac{1}{4\pi} \left[\begin{array}{ll} \frac{\sin k_z z \sin k_z(D-z_s)}{k_z \sin k_z D}, & z < z_s \\ \frac{\sin k_z z_s \sin k_z(D-z)}{k_z \sin k_z D}, & z > z_s \end{array} \right. \end{aligned} \tag{A.39}$$

This expression has simple poles at $k_zD = m\pi$, corresponding to the modes of the ideal waveguide. We note that this is the same eigenvalue condition as was found using the normal mode approach. Carrying out the inverse transform shows that the unperturbed mean field in the waveguide is given by

$$\chi(x,z) = \frac{i}{D} \sum_m \frac{\sin(k_{zm}z)\sin(k_{zm}z_s)}{k_m} e^{-ik_m x} \tag{A.40}$$

where $k_m = \sqrt{k_0^2 - k_{zm}^2}$ is the horizontal wavenumber. This expression is identical to the result for the unperturbed field obtained from the normal mode method.

Now we are ready to evaluate the scattered field in the waveguide using the KS result. Under the Born approximation, the mean-field vector $< \tilde{\chi}(k) >$ is the same as the unperturbed plane-wave amplitude vector $\tilde{\chi}(k)$. The global boundary operator B on the left-hand side is the same as that used to calculate the unperturbed field. To evaluate the RHS we need use only the *local* boundary operator for the upper surface, given by

$$\tilde{B}(q) = \begin{bmatrix} 1 & 1 \end{bmatrix} \tag{A.41}$$

For the pressure-release surface the rotation operator $\tilde{b} = 0$. The forcing term can be rewritten using contour integration to pull out the modal terms from the integral over k, giving

$$\tilde{B}(q)\tilde{s}(q) = \begin{bmatrix} -i \sum_m \tilde{\gamma}(q - k_m) \frac{k_{zm} \sin k_{zm} z_s}{k_m D} \\ 0 \end{bmatrix} \tag{A.42}$$

This system of equations is solved algebraically for the transformed scattered field, $\tilde{s}(q) = \tilde{s}^- e^{-iq_z z} + \tilde{s}^+ e^{iq_z z}$, giving

$$\tilde{s}(q, z) = -i \sum_m \tilde{\gamma}(q - k_m) \frac{\sin(k_{zm} z_s) k_{zm}}{k_m D} \frac{\sin(q_z(D - z))}{\sin(q_z D)} \tag{A.43}$$

The next step is to transform back to the spatial domain. First we write the roughness in the spatial domain:

$$\tilde{\gamma}(q_n - k_m) = \frac{1}{2\pi} \int dx' \gamma(x') e^{i(q_n - k_m)x'} \tag{A.44}$$

Carrying out the inverse transform, selecting the forward-scattered poles, and expanding out $\sin q_{zn}(D - z)$, the final result is

$$s(x, z) = \sum_{n,m} \int dx' \gamma(x') e^{-ik_m x'} \frac{\sin(k_{zm} z_s) k_{zm}}{k_m D} \frac{\sin(q_{zn} z) q_{zn}}{q_n D} e^{-iq_n(x - x')} \tag{A.45}$$

which is the same result as found from the normal mode reverbation method.

Numerical results from NMSCAT (the normal mode reverberation code developed in this thesis) and Schmidt's OASS code are compared in Figs. A-1 and A-2 for the ideal waveguide case. The waveguide bottom is assumed to be rough, with a 1 m. rms roughness and 20 m. correlation length. The statistics are described by a Goff-Jordan spectrum. Agreement is seen to be excellent for both geometries at all but the shortest ranges.

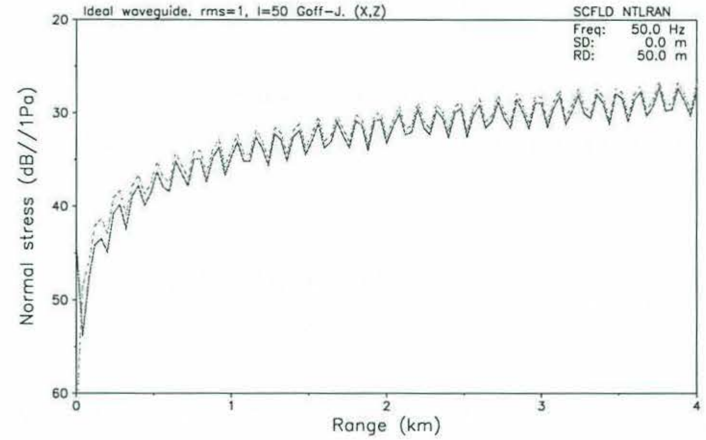

Figure A-1: Expected scattered field intensity, fluid bottom case, (x, z) geometry. Solid line is OASS result, dashed line is NMSCAT result. Note the overall agreement.

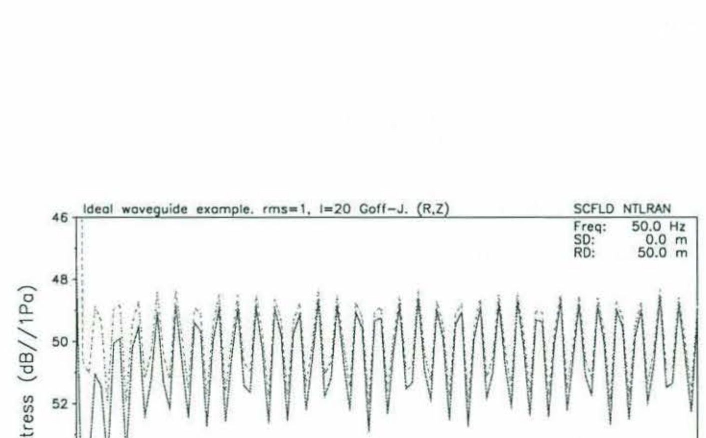

Figure A-2: Expected scattered field intensity, fluid bottom case, (r, z) geometry. Solid line is OASS result, dashed line is NMSCAT result.

A.4 Scattering from rough elastic interface

To set up the boundary conditions for scattering from an elastic halfspace we first need the equations of motion for the elastic medium. Newton's law can be written as [14, p. 158]

$$\sum_j \frac{\partial \sigma_{ij}}{\partial x_j} + \rho f_i = \rho \frac{\partial^2 u_i}{\partial t^2} \tag{A.46}$$

where σ_{ij} is the stress tensor, $\vec{f}$ is the body force, and $\vec{u}$ is the displacement vector. The strain ϵ is related to the displacement by

$$\epsilon_{ij} = \frac{1}{2}(\frac{\partial u_i}{\partial x_j} + \frac{\partial u_j}{\partial x_i}) \tag{A.47}$$

where $\vec{u} = (u, v, w)$ is the displacement vector. and finally the elastic Hooke's law for an isotropic homogeneous elastic medium is:

$$\sigma_{ij} = 2\mu\epsilon_{ij} + \lambda \sum_k \epsilon_{kk}.\delta_{ij} \tag{A.48}$$

These three equations can be combined into a set of three coupled equations. To decouple the equations, we express the displacement using the Helmholtz decomposition:

$$\vec{u} = \nabla\phi + \vec{\nabla} x \vec{\psi}. \tag{A.49}$$

When considering the 2D case we make two further simplifying assumptions; first all strain is in-plane:

$$\frac{\partial}{\partial y} = 0, \tag{A.50}$$

and second that there is no out-of-plane motion:

$$v = 0. \tag{A.51}$$

Then the displacements in the solid are given by

$$\begin{aligned} u &= \frac{\partial \phi}{\partial x} - \frac{\partial \psi}{\partial z} \\ v &= 0 \\ w &= \frac{\partial \phi}{\partial z} + \frac{\partial \psi}{\partial x} \end{aligned} \tag{A.52}$$

Under plane strain and using the Helmholtz decomposition, the equations of motion decouple into two equations, one for the compressional potential:

$$(\nabla^2 + k_p^2)\phi = 0, \tag{A.53}$$

where $k_p = \frac{\omega}{c_p}$ and $c_p^2 = \frac{\lambda+2\mu}{\rho_2}$, and the other for the shear potential

$$(\nabla^2 + k_s^2)\psi = 0 \tag{A.54}$$

where $k_s = \frac{\omega}{c_s}$ and $c_s^2 = \frac{\mu}{\rho_2}$.

As there is no source in the elastic halfspace, there are only down-going waves. If the fluid-elastic interface is at z_i, the compressional potential is

$$\phi(x, z) = \int dk\tilde{\phi}(k, z)e^{-ikx} \tag{A.55}$$

where

$$\tilde{\phi}(k, z) = Ce^{-\gamma_p(z-z_i)} \tag{A.56}$$

and $\gamma_p = \sqrt{k^2 - k_p^2}$. Likewise the shear wave potential is given by

$$\psi(x, z) = \int dk\tilde{\psi}(k, z)e^{-ikx} \tag{A.57}$$

where

$$\tilde{\psi}(k, z) = De^{-\gamma_s(z-z_i)} \tag{A.58}$$

and $\gamma_s = \sqrt{k^2 - k_s^2}$.

At the fluid-elastic interface three boundary conditions must be satisfied. First is the continuity of normal stress. Since pressure is just the negative of normal stress, we have

$$\sigma_{zz} = -p, \tag{A.59}$$

where p is the pressure in the water column. The second condition is continuity of displacement. We can relate pressure and displacement through Newton's law, $F = ma$. Ifthe motion is harmonic, the boundary condition becomes

$$\omega^2 w = \frac{1}{\rho_0}\frac{\partial p}{\partial z} \tag{A.60}$$

The third boundary condition is that the tangential shear σ_{xz} be zero at the interface.

To set up these boundary conditions we must write the stresses and displacements in the elastic bottom in terms of the velocity potentials. From Hooke's law and the stress-strain relation σ_{zz} and σ_{xz} are found:

$$\begin{aligned} \sigma_{zz} &= 2\mu(\frac{\partial^2\phi}{\partial z^2} + \frac{\partial^2\psi}{\partial x\partial z}) + \lambda\nabla^2\phi \\ \sigma_{xz} &= \mu(\nabla^2\psi + 2[\frac{\partial^2\phi}{\partial x\partial z} - \frac{\partial^2\psi}{\partial z^2}]) \end{aligned} \tag{A.61}$$

In terms of the compressional and shear velocity potentials defined in section 2.3.3, these quantities are

$$\begin{aligned} \sigma_{zz} &= \mu[(2k^2 - k_s^2)Ce^{-\gamma_p z} + 2ik\gamma_s De^{-\gamma_s z}] \\ \sigma_{xz} &= \mu[2ik\gamma_p Ce^{-\gamma_p z} - (2k^2 - k_s^2)De^{-\gamma_s z}] \end{aligned} \tag{A.62}$$

In addition, for the rotation term in the scattering expression we will need the quantity

$$\begin{aligned} -\sigma_{zz} + \sigma_{xx} &= -2\mu(\frac{\partial^2\phi}{\partial z^2} - \frac{\partial^2\phi}{\partial x^2} + 2\frac{\partial^2\psi}{\partial x\partial z}) \\ &= -2\mu[(2k^2 - k_p^2)Ce^{-\gamma_p z} + 2ik\gamma_s De^{-\gamma_s z}] \end{aligned} \tag{A.63}$$

the boundary conditions collected together in matrix form are

$$\tilde{B}\begin{bmatrix} p \\ C \\ D \end{bmatrix} = 0 \tag{A.64}$$

where

$$\tilde{B} = \begin{bmatrix} 1 & \mu(2k^2 - k_s^2) & \mu 2ik\gamma_s \\ \frac{1}{\rho_1}\frac{\partial}{\partial z} & \omega^2\gamma_p & ik\omega^2 \\ 0 & \mu 2ik\gamma_p & -\mu(2k^2 - k_s^2) \end{bmatrix} \tag{A.65}$$

The pressure field can be written in terms of normal modes, as indicated in section 2.3.3.

The plane wave coefficients C_m and D_m corresponding to mode m can then be found algebraically. Since calculating ψ_n' introduces some numerical error, we solve for the unknowns using the first and third equations, giving

$$\begin{aligned} C_m &= -\frac{2k_m^2 - k_s^2}{\mu[(2k_m^2 - k_s^2)^2 - 4k_m^2\gamma_{pm}\gamma_{sm}]}\psi_m(z_i) \\ D_m &= -\frac{2ik_m\gamma_{pm}}{\mu[(2k_m^2 - k_s^2)^2 - 4k_m^2\gamma_{pm}\gamma_{sm}]}\psi_m(z_i), \end{aligned} \tag{A.66}$$

where $\psi_m(z_i)$ is the value of mode m evaluated at the fluid-elastic interface.

Now we begin the scattered field calculation. The boundary operator B was defined above. From it we calculate

$$\frac{\partial \tilde{B}(k)}{\partial z} = \begin{bmatrix} \frac{\partial}{\partial z} & -\mu\gamma_p(2k^2 - k_s^2) & -\mu 2ik\gamma_s^2 \\ \frac{(k^2-k_w^2)}{\rho_1} & -\omega^2\gamma_p^2 & -ik\omega^2\gamma_s \\ 0 & -2ik\mu\gamma_p^2 & \mu\gamma_s(2k^2 - k_s^2) \end{bmatrix} \tag{A.67}$$

By expanding the boundary conditions one can calculate the rotation operator $\tilde{b}$:

$$\tilde{b}(k) = \begin{bmatrix} 0 & \mu 4ik\gamma_p & -2\mu(2k^2 - k_s^2) \\ \frac{ik}{\rho_1} & -ik\omega^2 & \gamma_s\omega^2 \\ 0 & -2\mu(2k^2 - k_p^2) & -4\mu ik\gamma_s \end{bmatrix} \tag{A.68}$$

These quantities are used in the KS equation to find the scattered field. The incident (mean) field is written as a sum over modes m, where the mode shape ψ_m is found in terms of the plane wave amplitudes in the halfspace. Simplifying gives

$$\begin{aligned} \tilde{B}(q)\tilde{s}(q) &= \frac{-NM}{(2\pi)^2\rho(z_s)}\int_0^\infty dk \sum_m \tilde{\gamma}(q-k)\frac{\psi_m(z_s)}{k^2 - k_m^2}[\frac{\partial \tilde{B}(k)}{\partial z} - i(q-k)\tilde{b}(k)] \begin{bmatrix} \psi_m(z_i) \\ C_m \\ D_m \end{bmatrix} \\ &\equiv \frac{-NM}{(2\pi)^2\rho(z_s)}\int_0^\infty dk \sum_m \tilde{\gamma}(q-k) \begin{bmatrix} a_m^{(1)}(q,k) \\ a_m^{(2)}(q,k) \\ a_m^{(3)}(q,k) \end{bmatrix} \end{aligned} \tag{A.69}$$

where C_m and D_m are the scattered field plane wave amplitudes in the bottom.

The scattered field equation equation consists of three coupled equations. After some tedious algebra, these equations can be manipulated into an impedance form, given by

$$\tilde{s}(q, z_i) - Z_0(q)\frac{\partial \tilde{s}(q, z_i)}{\partial z} = G_s(q). \tag{A.70}$$

Here $\tilde{s}(q, z_i)$ is the scattered field at the rough z_i, the boundary impedance Z is given by

$$Z_0(q) = -\frac{\mu}{\rho_1 \omega^2}\frac{(2q^2 - k_s^2)^2 - 4q^2\gamma_s(q)\gamma_p(q)}{\gamma_p(q)k_s^2}, \tag{A.71}$$

and the forcing term for the scattered field is

$$G_s(q) = \frac{-NM}{(2\pi)^2\rho(z_s)}\int_0^\infty dk \sum_m \tilde{\gamma}(q-k)\frac{\Delta_m^{(1)}(q,k) + \Delta_m^{(2)}(q,k)Z_0(q)}{k^2 - k_m^2} \tag{A.72}$$

where

$$\begin{aligned} \Delta_m^{(1)}(q,k) &\equiv a_m^{(1)}(q,k) + \frac{iqa_m^{(3)}(q,k)}{\gamma_p(q)k_s^2}(2q^2 - k_s^2 - 2\gamma_p(q)\gamma_s(q)) \\ \Delta_m^{(2)}(q,k) &\equiv -\rho_1 a_m^{(2)}(q,k) \end{aligned} \tag{A.73}$$

The wavenumber-domain solution for this equation is given by Eq. 2.64. When transformed back to the spatial domain, the residues for the forward-scattering poles $q = q_n$ are

$$\begin{aligned} Res(q - q_n) &= \frac{Kernal(q)\mid_{qn}}{\frac{\partial \pi}{\partial q}\mid_{qn}} \\ &= 2q_n\frac{Kernal(q_n)Z_0(q_n)}{\psi_n(z_i)} \end{aligned} \tag{A.74}$$

The results can be further simpified by rewriting the impedance in terms of mode shapes:

$$Z_0(q_n) = \frac{p}{p_z} = \frac{\psi_n(z)}{\psi_n'(z)}, \tag{A.75}$$

giving the result shown in Eq. 2.66. Similar calculations are carried out for the backscattered field.

A.5 Power spectral density

In section 2.3.2 an expression for the scattered field in the wavenumber domain was found:

$$\tilde{s}(q,z) = \frac{1}{(2\pi)^2}\int_{-\infty}^{\infty} dk \sum_{n,m} \tilde{\gamma}(q-k)\psi_n(z)\frac{a_{nm}(q,k)}{(k^2-k_m^2)(q^2-q_n^2)} \tag{A.76}$$

where

$$a_{nm}(q,k) = \frac{-NM}{\rho(z')\rho(z_s)}\left[\Delta_m^{(1)}(q,k)\frac{\partial\psi_n(z')}{\partial z'} + \Delta_m^{(2)}(q,k)\psi_n(z')\right] \tag{A.77}$$

If only a single plane wave is incident on the rough surface with some wavenumber k_{inc}, the scattered field is given by

$$\tilde{s}(q,z) = \frac{1}{(2\pi)^2}\sum_{n,m}\tilde{\gamma}(q-k_{inc})\psi_n(z)\frac{a_{nm}(q,k_{inc})}{(k_{inc}^2-k_m^2)(q^2-q_n^2)} \tag{A.78}$$

The second moment of this quantity is the power spectral density of the scattered field. Kuperman & Schmidt [45] have shown the second-moment of the transformed roughness can be written in terms of the power spectrum:

$$<\tilde{\gamma}(q-k)\tilde{\gamma}^*(q-k')>= 2\pi <\gamma^2> P(q-k)\delta(k-k'). \tag{A.79}$$

The power spectral density can then be written as

$$PSD(q)_{plane} = \frac{1}{(2\pi)^3}\sum_{n,m}P(q-k_{inc}) \mid \psi_n(z)\frac{a_{nm}(q,k_{inc})}{(k_{inc}^2-k_m^2)(q^2-q_n^2)} \mid^2 \tag{A.80}$$

In general the incident field will consist of many modes, rather than a simple plane wave. The contour integral over k is then carried out, enclosing the positive k_m poles which are propagating away from the source. The transformed scattered field is then given by

$$\tilde{s}(q,z) = \frac{i}{2\pi}\sum_{n,m}\tilde{\gamma}(q-k_m)\psi_n(z)\frac{a_{nm}(q,k_m)}{2k_m(q^2-q_n^2)}. \tag{A.81}$$

Following the same steps as before, the total power spectral density is given by

$$PSD(q) = \frac{\gamma^2}{2\pi}\sum_{n,m}P(q-k_m) \mid \psi_n(z)\frac{a_{nm}(q,k_m)}{2k_m(q^2-q_n^2)} \mid^2 \tag{A.82}$$

A.6 Backscattered intensity *vs.* time

In section 2.5, the backscattered signal from a narrowband pulse was found as a function of time. The derivations for finding backscattered intensity are shown in this appendix. First, the backscattered intensity *vs.* for a plane geometry is found. The transformation of variables shown in Appendix A.7 is then used to find the result for the cylindrically symmetric ocean.

In section 2.3 the backscattered intensity, for a plane geometry, is shown to be

$$s_b(z) = \sum_{n,m} \int_{-\infty}^{\infty} \left[\gamma(x') e^{-(\alpha_n+\alpha_m)|x'|} e^{i(-\bar{q}_n-\bar{k}_m)x'} \right] \psi_n(z) b_{nm} \tag{A.83}$$

The modal group velocities can be used to relate the travel time to the insonified area. For the $m \rightarrow n$ scattering path, the center of the insonified region at some time t is

$$x_{nm}(t) = (t - \tau/2) \frac{c_n c_m}{c_n + c_m}. \tag{A.84}$$

The insonfied region is given by $[x_1(t), x_2(t)] = [x_{nm} - \Delta x_{nm}, x_{nm} + \Delta x_{nm}]$, where

$$\Delta x_{nm} = \frac{\tau}{2} \frac{c_n c_m}{c_n + c_m}. \tag{A.85}$$

At some time t, all backscattering will come from the insonified region $[x_1(t), x_2(t)]$. The backscattered energy from the right-going wave is

$$s_b(z,t) = \sum_{n,m} \int_{x_1(t)}^{x_2(t)} \left[\gamma(x') e^{-(\alpha_n+\alpha_m)|x'|} e^{i(-\bar{q}_n-\bar{k}_m)x'} \right] \psi_n(z) b_{nm} \tag{A.86}$$

The backscattered intensity is then found from a second-moment expectation of this equation:

$$\begin{aligned} < I_b(z,t) > \; &= \; 2 \sum_{n,m} \sum_{l,p} \int_{x'_1}^{x'_2} dx' \int_{x''_1}^{x''_2} dx'' < \gamma(x') \gamma^*(x'') > \\ & \quad e^{-(\alpha_n+\alpha_m)x'} e^{-(\alpha_l+\alpha_p)x''} e^{i(-\bar{q}_n-\bar{q}_m)x'} e^{-i(-\bar{q}_l-\bar{q}_p)x''} \\ & \quad (\psi_n(z) b_{nm})(\psi_l(z) b_{lp})^* \end{aligned} \tag{A.87}$$

where the integration limits depend on mode numbers and time, as discussed above. The factor of 2 accounts for the fact that scattering is recieved from both the right and left sides of the source.

Next we switch to sum and difference coordinates, defined by:

$$\begin{aligned} y &= x' - x'' \\ r &= \frac{x' + x''}{2} \end{aligned} \tag{A.88}$$

The expected intensity is then

$$\begin{aligned} < I_b(t,z) > &= \sum_{n,m,l,p} \int_{y-}^{y+} dy N(y) e^{i(-q_n - q_m - q_l - q_p)y/2} \\ & \int_{r-}^{r+} dr e^{i(-q_n - q_m + q_l^* + q_p^*)r} \psi_n(z) \psi_l^*(z) \frac{b_{nm} b_{lp}^*}{r - y/2} \end{aligned} \tag{A.89}$$

The limits on y are $y\pm = y_d \pm \Delta r$, where

$$y_d = r_{lp}(t) - r_{nm}(t) \tag{A.90}$$

is the distance between the centers of the insonified regions and

$$\Delta r = \Delta r_{lp} + \Delta r_{nm} \tag{A.91}$$

is their combined width. Similarly the limits on r are $r\pm = r_c \pm \Delta r/2$, where

$$r_c = (r_{nm} + r_{lp})/2 \tag{A.92}$$

At this point we can argue, as many authors do, that we keep only the coherent terms, i.e. $n = l$ and $m = p$. The off-diagonal elements can be expected to give a smaller contribution because of phase oscillations in the integrals. Also, the nm and lp insonification regions move at different speeds, so at longer times the correlation $N(y)$ decreases. Ellis [17] has demonstrated that this assumption gives a smoothed answer which captures the overall energy levels of the full answer.

If the annulus width is not too large, the cylindrical spreading term is well approximated as:

$$\frac{1}{r - y/2} \approx \frac{1}{r_{nm}(t)} \tag{A.93}$$

so the intensity becomes

$$
\begin{aligned}
< I_b(t,z) > \quad \approx \quad & 2\sum_{n,m}\int_{-2\Delta x_{nm}}^{2\Delta x_{nm}} dyN(y)e^{i(-q_n-q_m)y} \\
& \int_{r^-}^{r^+} dre^{-2(\alpha_n+\alpha_m)r}\frac{\mid \psi_n(z)b_{nm}\mid^2}{r_{nm}(t)}
\end{aligned}
\tag{A.94}
$$

where

$$
r^{\pm} = r_{nm}(t) \pm 2\Delta r_{nm}. \tag{A.95}
$$

The first integral can be written as a convolution of the power spectrum with a window accounting for the finite pulse length:

$$
I_1 = 2\pi < \gamma^2 > P(-q_n - k_m) * (\frac{1}{2\pi}\frac{\sin(2(-q_n-k_m)\Delta r)}{(-q_n-k_m)/2}) \tag{A.96}
$$

Numerical tests show this factor has an effect only for extremely short pulse durations (which violate the narrowband assumption) or extremely long correlation lengths, so the convolution is dropped in the following.

The integral over r, assuming the attenuation over the insonification area is small, is

$$
I_2 = 2\Delta r_{nm}e^{-2(\alpha_n+\alpha_m)r_{nm}(t)} \tag{A.97}
$$

so the expected intensity is given by:

$$
\begin{aligned}
< I_b(t,z) > \quad = \quad & 8\pi < \gamma^2 > \sum_{n,m} P(-q_n-k_m)\Delta r_{nm}\frac{e^{-2(\alpha_n+\alpha_m)r_{nm}(t)}}{r_{nm}(t)} \cdot \\
& \mid \psi_n(z)b_{nm}\mid^2
\end{aligned}
\tag{A.98}
$$

In comparing numerical results it is convenient to normalize the energy in the pulse. If the pulse is uniform and of duration τ, then it follows that the amplitude is set to $1/\tau$. Multiplying by this amplitude gives the normalized intensity:

$$
\begin{aligned}
< I_b(t,z) > \quad = \quad & 8\pi < \gamma^2 > \sum_{n,m} P(-q_n-k_m)(\frac{c_n c_m}{c_n+c_m})\frac{e^{-2(\alpha_n+\alpha_m)r_{nm}(t)}}{r_{nm}(t)} \cdot \\
& \mid \psi_n(z)b_{nm}\mid^2 .
\end{aligned}
\tag{A.99}
$$

To find intensity for a cylindrically symmetric ocean, the spreading correction factor of

$2/\pi r$ is applied, as discussed below.

A.7 Cylindrically symmetric geometry

The Helmholtz equation in a cylindrical geometry is given by

$$\frac{1}{r}\frac{\partial}{\partial r}\left(r\frac{\partial \Phi}{\partial r}\right) + \frac{\partial^2 \Phi}{\partial z^2} + k_0^2(z)\Phi = 0. \tag{A.100}$$

Using a change of variables defined as

$$\phi(r,z) = \sqrt{\frac{\pi r}{2}}\Phi(r,z) \tag{A.101}$$

the Helmholtz equation becomes

$$\frac{\partial^2 \phi}{\partial r^2} + \frac{1}{4r^2}\phi + \frac{\partial^2 \phi}{\partial z^2} + k_0^2(z)\phi = 0. \tag{A.102}$$

The $1/r^2$ term decays very quickly away from the source, so we can neglect it. This will limit the accuracy of our answer somewhat. However, near the source the modal answer is approximate in any case since very high-angle continuous spectrum energy is neglected. If the second term is neglected, the Helmholtz equation has the same form as in the (x, z) geometry. Thus the effects of the cylindrical 2D ocean can be taken into account by multiplying the Cartesian result by a factor of $\sqrt{2/\pi r}$.

Appendix B

Derivations for volume scattering theory

B.1 Perturbation theory for eigenvalue correction

Consider the form of the eigenvalue problem above:

$$[\frac{\partial^2}{\partial z^2} + k_0^2(z)]\psi_n = k_n^2\psi_n - < \sigma^2 > f(\vec{k}_{n_0}, z)\psi_n \tag{B.1}$$

Since this is the equation for the mean field, all quantities above are averaged, though this is not shown explicitly. The equation can be rewritten in the form

$$H\psi_n = E_n\psi_n - < \sigma^2 > f(\vec{k}_{n_0}, z)\psi_n \tag{B.2}$$

Expanding the perturbed quantities to second order:

$$\begin{aligned} \psi_n &= \psi_n^{(0)} + \sigma\psi_n^{(1)} + \sigma^2\psi_n^{(2)} + \cdots \\ E_n &= E_n^{(0)} + \sigma E_n^{(1)} + \sigma^2 E_n^{(2)} + \cdots \end{aligned} \tag{B.3}$$

Since we are interested in calculating the mean field we average the equations above. Since σ is zero-mean we get the equations:

$$\begin{aligned} < \psi_n > &= \psi_n^{(0)} + < \sigma^2 > \psi_n^{(2)} + \cdots \\ < E_n > &= E_n^{(0)} + < \sigma^2 > E_n^{(2)} + \cdots \end{aligned} \tag{B.4}$$

where all quantities are averaged even if not explicity written so. Substituting these above and equating terms of like order gives the following equations.

$$O(1): \qquad \qquad \text{(B.5)}$$
$$H^{(0)}\psi_n^{(0)} = E_n^{(0)}\psi_n^{(0)}$$

This is just the unperturbed equation. The $O(\sigma)$ terms are zero, by inspection. Finally,

$$O(\sigma^2): \qquad \qquad \text{(B.6)}$$
$$H^{(0)}\psi_n^{(2)} = E_n^{(0)}\psi_n^{(2)} + E_n^{(2)}\psi_n^{(0)} - <\sigma^2> f(\vec{k}_{n_0}, z)\psi_n^{(0)}$$

The first two terms are eliminated using the first-order solution. Operating on the remaining terms with

$$\int \frac{\psi_n^{(0)}}{\rho(z)}(\cdot)dz \qquad \text{(B.7)}$$

and using the normalization condition gives the result:

$$E_n^{(2)} = <\sigma^2> \int \frac{(\psi_n^{(0)})^2 f(\vec{k}_{n_0}, z)}{\rho(z)}dz \qquad \text{(B.8)}$$

We relate this to the eigenvalue perturbation Δk_n by noting that

$$\begin{aligned} k_n^2 &= (k_{n0} + \Delta k_n)^2 \\ &= k_{n0}^2 + 2\Delta k_n k_{n0} + O(\sigma^4) + \cdots \end{aligned} \qquad \text{(B.9)}$$

Then the final expression, quoted in section 3.3.1, is

$$\begin{aligned} \Delta k_n &= \frac{1}{2k_{n0}} E_n^{(2)} \\ &= \frac{<\sigma^2>}{2k_{n0}} \int_0^D \frac{f(\vec{k}_{n_0}, z)\psi_n^2(z)}{\rho(z)}dz \end{aligned} \qquad \text{(B.10)}$$

B.2 Model of inhomogeneities in sediment bottoms

The discussion in the chapter developed a statistical model in terms of porosity fluctuations. In practice it is easier to specify the strength of the fluctuations in terms of the normalized sound speed fluctuations. The density fluctuations are then found from Hines' coefficients.

The sound speed fluctuations are given by

$$\delta c = \frac{\partial c}{\partial P}\delta P \tag{B.11}$$

so it is easy to see that the normalized RMS sound speed fluctuation can be written as

$$\frac{\delta c}{c_0}_{RMS} = \frac{\frac{\partial c}{\partial P}}{c_0}\delta P_{RMS} \tag{B.12}$$

In Chapter 3 the mean-squared porosity fluctuation was written as $< \mu^2 >$. From the equation above,

$$< \mu^2 >= (\frac{c_0}{\frac{\partial c}{\partial P}}\frac{\delta c}{c_0}_{RMS})^2 \tag{B.13}$$

This conversion is used to compare with Tang's results.

B.3 Scattering Integrals and Mean field equation

In this appendix the details of several calculations refered to above are shown. Before beginning we state several facts which will be of use. From the definition of the wavenumber transform we have

$$\delta P(\vec{r}, z) = \frac{1}{2\pi}\int_{-\infty}^{\infty} d^2\vec{k}\tilde{\delta P}(\vec{k}, z)e^{-i\vec{k}\cdot\vec{r}} \tag{B.14}$$

$$< p(\vec{r}, z) >= \frac{1}{2\pi}\int_{-\infty}^{\infty} d^2\vec{k} < \tilde{p}(\vec{k}, z) > e^{-i\vec{k}\cdot\vec{r}} \tag{B.15}$$

$$s(\vec{r}, z) = \frac{1}{2\pi}\int_{-\infty}^{\infty} d^2\vec{k}\,\tilde{s}(\vec{k}, z)e^{-i\vec{k}\cdot\vec{r}} \tag{B.16}$$

Horizontal derivatives can be written easily; for example

$$\frac{\partial\delta P(\vec{r}, z)}{\partial\vec{r}} = \frac{1}{2\pi}\int_{-\infty}^{\infty} d^2\vec{k}(-i\vec{k})\tilde{\delta P}(\vec{k}, z)e^{-i\vec{k}\cdot\vec{r}} \tag{B.17}$$

We use also the following property of the delta function:

$$\frac{1}{(2\pi)^2}\int_{-\infty}^{\infty} d^2\vec{r}e^{i\vec{k}\cdot\vec{r}} = \delta(\vec{k}) \tag{B.18}$$

First we evaluate the wavenumber transform of the scattered field equation. From the results in section 3.1, the transformed scattered field is given by

$$\begin{aligned}[\frac{\partial^2}{\partial z^2} + k_0^2(z) - \vec{q}^{\,2}]\tilde{s}(\vec{q}, z) &= \frac{\mu_c(z)}{2\pi} \int \delta P(\vec{r}, z) < p(\vec{r}, z) > e^{i\vec{q}\cdot\vec{r}} d^2\vec{r} \\ &+ \frac{\mu_\rho}{2\pi} \int \nabla \delta P(\vec{r}, z) \cdot \nabla < p(\vec{r}, z) > e^{i\vec{q}\cdot\vec{r}} d^2\vec{r} \qquad \text{(B.19)}\end{aligned}$$

The work to be done is in evaluating the RHS. We begin by looking at the simpler first term, which involves only μ_c. Inserting the appropriate definitions from above gives

$$RHS1 = \frac{\mu_c(z)}{(2\pi)^3} \int\int\int d^2\vec{k}_1\, d^2\vec{k}_2\, d^2\vec{r}\, \delta\tilde{P}(\vec{k}_1, z) < \tilde{p}(\vec{k}_2, z) > e^{i[\vec{q}-(\vec{k}_1+\vec{k}_2)]\vec{r}} \qquad \text{(B.20)}$$

Using the delta function property, we integrate over $\vec{r}$:

$$RHS1 = \frac{1}{2\pi} \int\int d^2\vec{k}_1 d^2\vec{k}_2\, \delta\tilde{P}(\vec{k}_1, z) < \tilde{p}(\vec{k}_2, z) > \delta[\vec{q} - (\vec{k}_1 + \vec{k}_2)] \qquad \text{(B.21)}$$

The delta function pulls out $\vec{k}_1 = \vec{q} - \vec{k}_2$. Renaming $\vec{k}_2 \equiv \vec{k}'$ we have

$$RHS1 = \frac{\mu_c(z)}{2\pi} \int d^2\vec{k}'\, \delta\tilde{P}(\vec{q} - \vec{k}', z) < \tilde{p}(\vec{k}', z) > \qquad \text{(B.22)}$$

We next examine the second term, which involves spatial derivatives of $\rho(\vec{r}, z)$. We expand the derivative terms in the kernel as:

$$\nabla \delta P(\vec{r}, z) \cdot \nabla < p(\vec{r}, z) >= \frac{\partial \delta P(\vec{r}, z)}{\partial \vec{r}} \frac{\partial < p(\vec{r}, z) >}{\partial \vec{r}} + \frac{\partial \delta P(\vec{r}, z)}{\partial z} \frac{\partial < p(\vec{r}, z) >}{\partial z} \qquad \text{(B.23)}$$

Rewriting in terms of the transformed variables and integrating over $\vec{r}$ and $\vec{k_1}$ as above, we can find

$$\begin{aligned}RHS2 &= \frac{\mu_\rho}{2\pi} \int d^2\vec{k}' [-(\vec{q} - \vec{k}') \cdot \vec{k}'\, \delta\tilde{P}(\vec{q} - \vec{k}', z) < \tilde{p}(\vec{k}', z) > \\ &+ \frac{\partial \delta\tilde{P}(\vec{q} - \vec{k}')}{\partial z} \frac{\partial < \tilde{p}(\vec{k}', z) >}{\partial z}] \qquad \text{(B.24)}\end{aligned}$$

Adding these results together gives the combined RHS for the scattered field equation:

$$\begin{aligned}RHS &= \frac{1}{2\pi} \int d^2\vec{k}([\mu_c(z) - \mu_\rho(\vec{q} - \vec{k}) \cdot \vec{k}]\, \delta\tilde{P}(\vec{q} - \vec{k}, z) < \tilde{p}(\vec{k}, z) > \\ &+ \mu_\rho \frac{\partial \delta\tilde{P}(\vec{q} - \vec{k})}{\partial z} \frac{\partial < \tilde{p}(\vec{k}, z) >}{\partial z}) \qquad \text{(B.25)}\end{aligned}$$

The second result we show is the transformation of the mean field equation, Eq. 3.9. Again we break the equation into two terms, and look at the simpler one multiplying μ_c first. This term is

$$I1 = -\frac{\mu_c(z)}{2\pi}\int_{-\infty}^{\infty} < \delta P(\vec{r}, z) s(\vec{r}, z) > e^{i\vec{k}\cdot\vec{r}} d^2\vec{r} \tag{B.26}$$

The calculation begins as above, by substituting in the expressions for $s(\vec{r}, z)$ and $\delta P(\vec{r}, z)$.

$$I1 = -\frac{\mu_c(z)}{(2\pi)^3}\int\int\int d^2\vec{r} d^2\vec{k}_1 d^2\vec{q} < \delta\tilde{P}(\vec{k}_1, z)\tilde{s}(\vec{q}, z) > e^{i(\vec{k}-(\vec{k}_1+\vec{q}))\vec{r}} d\vec{r} \tag{B.27}$$

Integrating over $\vec{r}$ again gives a delta function $\delta[\vec{k} - (\vec{k}_1 + \vec{q})]$; this is used to eliminate the integral over $\vec{k}_1$ using $\vec{k}_1 = \vec{k} - \vec{q}$. This gives the result

$$I1 = -\frac{\mu_c(z)}{2\pi}\int d\vec{q} < \delta\tilde{P}(\vec{k} - \vec{q}, z)\tilde{s}(\vec{q}, z) > \tag{B.28}$$

Next we look at the remaining terms, given by

$$\begin{aligned} I2 &= -\frac{\mu_\rho}{2\pi}\int d^2\vec{r} < \frac{\partial\delta P(\vec{r}, z)}{\partial\vec{r}} \cdot \frac{\partial s(\vec{r}, z)}{\partial\vec{r}} > e^{i\vec{k}\cdot\vec{r}} \\ &- \frac{\mu_\rho}{2\pi}\int d^2\vec{r} < \frac{\partial\delta P(\vec{r}, z)}{\partial z} \cdot \frac{\partial s(\vec{r}, z)}{\partial z} > e^{i\vec{k}\cdot\vec{r}} \end{aligned} \tag{B.29}$$

Carrying out substitutions and integrations exactly as done above gives the result

$$\begin{aligned} I2 &= -\frac{\mu_\rho}{2\pi}\int d^2\vec{q}\left\{-(\vec{k} - \vec{q}) \cdot \vec{q} < \delta\tilde{P}(\vec{k} - \vec{q}, z)\tilde{s}(\vec{q}, z) > \right. \\ &+ \left. < \frac{\partial\delta\tilde{P}(\vec{k} - \vec{q})}{\partial z}\frac{\partial < \tilde{p}(\vec{q}, z) >}{\partial z} > \right\} \end{aligned} \tag{B.30}$$

These two terms are added to give the intermediate result shown in Eq. 3.14.

We proceed by evaluating the expectation terms above. This calculation is straightforward but long, so we will not show all details here. We first look at the first expectation in Eq. B.28:

$$E_1 = < \delta\tilde{P}(\vec{k} - \vec{q}, z)\tilde{s}(\vec{q}, z) > \tag{B.31}$$

Substituting in the expression for $\tilde{s}(q, z)$ from Eq. 3.12 we can write

$$E_1 = -\int\int dz_0 d\vec{k'} G_\omega(\vec{q}, z, z_0)\left[\mu_c(z_0) - \mu_\rho(\vec{q} - \vec{k'} \cdot \vec{k'}\right] \cdot$$

$$\begin{aligned} & < \tilde{\delta P}(\vec{k}-\vec{q},z)\tilde{\delta P}(\vec{q}-\vec{k}',z_0) >< \tilde{p}(\vec{k}',z_0) > \\ - \quad & \mu_\rho \int\int dz_0 d\vec{k}' G_\omega(\vec{q},z,z_0) < \tilde{\delta P}(\vec{k}-\vec{q},z)\frac{\partial \tilde{\delta P}(\vec{q}-\vec{k}',z_0)}{\partial z_0} > \cdot \\ & \frac{\partial < \tilde{p}(\vec{k}',z_0) >}{\partial z_0} \end{aligned} \tag{B.32}$$

Using the definition of the power spectrum, we can write

$$\begin{aligned} < \tilde{\delta P}(\vec{k}-\vec{q},z)\tilde{\delta P}(\vec{q}-\vec{k}',z_0) > &= 2\pi < \sigma^2 > P_H(\vec{q}-\vec{k})\delta(\vec{k}-\vec{k}')M(z-z_0) \\ < \tilde{\delta P}(\vec{k}-\vec{q},z)\frac{\partial \tilde{\delta P}(\vec{q}-\vec{k}',z_0)}{\partial z_0} > &= 2\pi < \sigma^2 > P_H(\vec{q}-\vec{k})\delta(\vec{k}-\vec{k}') \cdot \\ & \quad \frac{\partial M(z-z_0)}{\partial z_0} \end{aligned} \tag{B.33}$$

Our assumption that the vertical correlation length $z_{CL} >> \lambda$ lets us approximate M with a delta function; i.e.

$$M(z-z_0) = z_{CL}\delta(z-z_0) \tag{B.34}$$

where z_{CL}, the vertical correlation length, is the small range over which M is nonzero. The first integral above is then trivial, and gives

$$E_{11} = -2\pi < \sigma^2 > z_{CL}P_H(\vec{q}-\vec{k})G_\omega(\vec{q},z,z_0)(\mu_c(z) - \mu_\rho(\vec{q}-\vec{k}) \cdot \vec{k} < \tilde{p}(\vec{k},z) > \tag{B.35}$$

The second integral, rewritten

$$E_{12} = -2\pi < \sigma^2 > P_H(\vec{q}-\vec{k}) \int dz_0 G_\omega(\vec{q},z,z_0)\frac{\partial M(z-z_0)}{\partial z_0}\frac{\partial < \tilde{p}(\vec{k},z_0) >}{\partial z_0} \tag{B.36}$$

can be found using integration by parts, following Chernov [11]. Dropping the constants for a moment, we have

$$\begin{aligned} E_{12} \quad \sim \quad & -G_\omega \frac{\partial < \tilde{p} >}{\partial z_0} M \,|_{-\infty}^{\infty} \\ + \quad & \int dz_0 \, M(z-z_0)\left[G_\omega(\vec{q},z,z_0)\frac{\partial^2 < \tilde{p}(\vec{k},z_0) >}{\partial {z_0}^2} + \frac{\partial G_\omega(\vec{q},z,z_0)}{\partial z_0}\frac{\partial < \tilde{p}(\vec{k},z_0) >}{\partial z_0}\right] \\ = \quad & z_{CL}\left[G_\omega(\vec{q},z,z)\frac{\partial^2 < \tilde{p}(\vec{k},z_0) >}{\partial {z_0}^2} \,|_z + \frac{\partial G_\omega(\vec{q},z,z_0)}{\partial z_0} \,|_z \, \frac{\partial \tilde{p}(\vec{k},z_0)}{\partial z_0} \,|_z\right] \end{aligned} \tag{B.37}$$

The first term drops out as $M \to 0$ for large $(z - z_0)$. We can simplify the second derivative using the Helmholtz equation:

$$\frac{\partial^2 < \tilde{p}(\vec{k}, z_0) >}{\partial {z_0}^2} = -[k_0^2(z) - \vec{k}^2] < \tilde{p}(\vec{k}, z_0) > \tag{B.38}$$

Putting all this together, we obtain for the first expectation

$$\begin{aligned} E_1 &= -2\pi z_{CL} P_H(\vec{q} - \vec{k}) \Big\{ a_2 G_\omega(\vec{q}, z, z) < \tilde{p}(\vec{k}, z_0) > \\ &- \mu_\rho \frac{\partial G_\omega(\vec{q}, z, z_0)}{\partial z_0} |_z \frac{\partial < \tilde{p}(\vec{k}, z_0) >}{\partial z_0} |_z \Big\} \end{aligned} \tag{B.39}$$

where a_2 is as defined in section 3.1.

The calculation for the second expection,

$$E_2 = < \frac{\partial \delta \tilde{P}(\vec{k} - \vec{q}, z)}{\partial z} \frac{\partial \tilde{s}(\vec{q}, z)}{\partial z} > \tag{B.40}$$

is similar but much more complicated, so we only indicate the steps involved. Substituting in the scattered field expression again gives two expectations,

$$\begin{aligned} < \frac{\partial \delta \tilde{P}(\vec{k} - \vec{q}), z}{\partial z} \delta \tilde{P}(\vec{q} - \vec{k}', z_0) > &= 2\pi < \sigma^2 > P_H(\vec{q} - \vec{k}') \delta(\vec{k} - \vec{k}') \frac{\partial M(z - z_0)}{\partial z} \\ < \frac{\partial \delta \tilde{P}(\vec{k} - \vec{q}), z}{\partial z} \frac{\partial \delta \tilde{P}(\vec{q} - \vec{k}', z_0)}{\partial z_0} > &= 2\pi < \sigma^2 > P_H(\vec{q} - \vec{k}') \delta(\vec{k} - \vec{k}') \\ & \frac{\partial^2 M(z - z_0)}{\partial z^2} \end{aligned} \tag{B.41}$$

Using a change of variables argument [11], it is easy to show that $\frac{\partial M}{\partial z} = -\frac{\partial M}{\partial z_0}$, giving two integrals which involve derivatives with respect to z_0. We again use integration by parts, using the assumption that $\frac{\partial M(z - z_0}{\partial z_0} \to 0$ as $z - z_0$ becomes large to simplify the integral involving $\frac{\partial^2 M}{\partial {z_0}^2}$. Using the Helmholtz equation to eliminate second- and third-derivatives as appropriate, we get the final result

$$\begin{aligned} E_2 &= -2\pi z_{CL} P_H(\vec{q} - \vec{k}) \Bigg\{ a_2 \frac{\partial G_\omega(\vec{q}, z, z)}{\partial z} \frac{\partial < \tilde{p}(\vec{k}, z_0) >}{\partial z_0} + a_3 \frac{\partial^2 G_\omega(\vec{q}, z, z_0)}{\partial z \partial z_0} |_z < \tilde{p}(\vec{k}, z) > \\ &- a_4 \frac{\partial G_\omega(\vec{q}, z, z)}{\partial z} < \tilde{p}(\vec{k}, z) >) - \mu_\rho \frac{\partial^3 G_\omega(\vec{q}, z, z_0)}{\partial z \partial z_0^2} \Bigg\} \end{aligned} \tag{B.42}$$

where $a1 - a4$ are defined in section 3.1 E_1 and E_2 are then combined to give the self-consistent equation for the mean field quoted in Equation 3.18.

B.4 Scattered field cross-spectral density

The cross-spectral density is

$$\begin{aligned}
< \tilde{s}(\vec{q}_1, z_1)\tilde{s}^*(\vec{q}_2, z_2) >= & \int\int\int\int dz_0 d\vec{k}_1 dz' d\vec{k}_2 G_\omega(\vec{q}_1, z_1, z_0) G^*_\omega(\vec{q}_2, z_2, z') \cdot \\
& [b_1(\vec{q}_1, \vec{k}_1)\delta\tilde{P}(\vec{q}_1 - \vec{k}_1, z_0) < \tilde{p}(\vec{k}_1, z_0) > \\
+ & \mu_\rho \frac{\partial \delta\tilde{P}(\vec{q}_1 - \vec{k}_1, z_0)}{\partial z_0} \frac{\partial < \tilde{p}(\vec{k}_1, z_0) >}{\partial z_0}][b_1(\vec{q}_2, \vec{k}_2)\delta\tilde{P}(\vec{q}_2 - \vec{k}_2, z') < \tilde{p}(\vec{k}_2, z') > \\
+ & \mu_\rho \frac{\partial \delta\tilde{P}(\vec{q}_2 - \vec{k}_2, z')}{\partial z'} \frac{\partial < \tilde{p}(\vec{k}_2, z') >}{\partial z'}]^* \qquad \text{(B.43)}
\end{aligned}$$

We proceed by looking at the cross terms: from the definition of the 2-D porosity fluctuation spectrum,

$$< \delta\tilde{P}(\vec{q}, z)\delta\tilde{P}(\vec{k}, z') >= 2\pi < \sigma^2 > P_H(\vec{q})\delta(\vec{q} - \vec{k})M(z - z') \qquad \text{(B.44)}$$

we find

$$\begin{aligned}
T_1 = & 2\pi < \sigma^2 > P_H(\vec{q}_1 - \vec{k}_1)\delta(\vec{q}_1 - \vec{k}_1 - \vec{q}_2 + \vec{k}_2) b_1(\vec{q}_1, \vec{k}_1) b_1^*(\vec{q}_2, \vec{k}_2) M(z_0 - z') \cdot \\
& < \tilde{p}(\vec{k}_1, z_0) >< \tilde{p}^*(\vec{k}_2, z') > \qquad \text{(B.45)}
\end{aligned}$$

The z derivatives of δP are handled by noting that they will only affect the vertical correlation function $M(z - z')$. The other three cross terms are then given by

$$\begin{aligned}
T_2 = & 2\pi < \sigma^2 > P_H(\vec{q}_1 - \vec{k}_1)\delta(\vec{q}_1 - \vec{k}_1 - \vec{q}_2 + \vec{k}_2)\mu_\rho b_1(\vec{q}_1, \vec{k}_1) \cdot \\
& \frac{\partial M(z_0 - z')}{\partial z'} < \tilde{p}(\vec{k}_1, z_0) > \frac{\partial < \tilde{p}^*(\vec{k}_2, z') >}{\partial z'} \qquad \text{(B.46)}
\end{aligned}$$

$$\begin{aligned}
T_3 = & 2\pi < \sigma^2 > P_H(\vec{q}_1 - \vec{k}_1)\delta(\vec{q}_1 - \vec{k}_1 - \vec{q}_2 + \vec{k}_2)\mu_\rho b_1^*(\vec{q}_2, \vec{k}_2) \cdot \\
& \frac{\partial M(z_0 - z')}{\partial z_0} \frac{\partial < \tilde{p}(\vec{k}_1, z_0) >}{\partial z_0} < \tilde{p}^*(\vec{k}_2, z') > \qquad \text{(B.47)}
\end{aligned}$$

and

$$\begin{aligned}
T_4 = & 2\pi < \sigma^2 > P_H(\vec{q}_1 - \vec{k}_1)\delta(\vec{q}_1 - \vec{k}_1 - \vec{q}_2 + \vec{k}_2)\mu_\rho^2 \cdot \\
& \frac{\partial^2 M(z_0 - z')}{\partial z_0 \partial z'} \frac{\partial < \tilde{p}(\vec{k}_1, z_0) >}{\partial z_0} \frac{\partial < \tilde{p}^*(\vec{k}_2, z') >}{\partial z'} \qquad \text{(B.48)}
\end{aligned}$$

so the expectation can be written as

$$
\begin{aligned}
< \tilde{s}(\vec{q}_1, z_1) \quad & \tilde{s}^*(\vec{q}_2, z_2) >= 2\pi < \sigma^2 > \int\int d\vec{k}_1 d\vec{k}_2 P_H(\vec{q}_1 - \vec{k}_1) \cdot \\
& \delta(\vec{q}_1 - \vec{k}_1 - \vec{q}_2 + \vec{k}_2) \cdot \\
& \int\int dz_0 dz' \Big[b_1(\vec{q}_1, \vec{k}_1) b_1^*(\vec{q}_2, \vec{k}_2) M(z_0 - z') < \tilde{p}(\vec{k}_1, z_0) >< \tilde{p}^*(\vec{k}_2, z') >] \\
+ \quad & \mu_\rho b_1(\vec{q}_1, \vec{k}_1) \frac{\partial M(z_0 - z')}{\partial z'} < \tilde{p}(\vec{k}_1, z_0) > \frac{\partial < \tilde{p}^*(\vec{k}_2, z') >}{\partial z'} \\
+ \quad & \mu_\rho b_1^*(\vec{q}_2, \vec{k}_2) \frac{\partial M(z_0 - z')}{\partial z_0} \frac{\partial < \tilde{p}(\vec{k}_1, z_0) >}{\partial z_0} < \tilde{p}^*(\vec{k}_2, z') > \\
+ \quad & \mu_\rho^2 \frac{M(z_0 - z')^2}{z_0 z'} \frac{\partial < \tilde{p}(\vec{k}_1, z_0) >}{\partial z_0} \frac{\partial < \tilde{p}^*(\vec{k}_2, z') >}{\partial z'} \Big] \cdot \\
& G_\omega(\vec{q}_1, z_1, z_0) G_\omega^*(\vec{q}_2, z_2, z')
\end{aligned} \tag{B.49}
$$

Next the double integral over depth is considered, separate from the wavenumber integration. The integral of the first term is simply

$$
\begin{aligned}
I_1 \quad = \quad & \int\int dz' dz_0 M(z_0 - z') b_1(\vec{q}_1, \vec{k}_1, z_0) b_1^*(\vec{q}_2, \vec{k}_2, z') < \tilde{p}(\vec{k}_1, z_0) >< \tilde{p}^*(\vec{k}_2, z') > \\
& G_\omega(\vec{q}_1, z_1, z_0) G_\omega^*(\vec{q}_2, z_2, z')
\end{aligned} \tag{B.50}
$$

In integrating the second term we encounter the derivative $\frac{\partial M(z_0 - z')}{\partial z'}$. This term is evaluated using integration by parts. We assume the vertical correlation length is limited, so the first term resulting from integration by parts, proportional to M, will vanish at the endpoints of the integral, i.e. where $(z - z_0)$ is large. The result is

$$
\begin{aligned}
I_2 \quad = \quad & \mu_\rho \int\int dz_0 dz' M(z_0 - z') b_1(\vec{q}_1, \vec{k}_1, z_0) G_\omega(\vec{q}_1, z_1, z_0) < \tilde{p}(\vec{k}_1, z_0) > \\
& \Big[(k_0^2(z') - \vec{k}_2^2) < \tilde{p}(\vec{k}_2, z') > G_\omega(\vec{q}_2, z_2, z') \cdot \\
- \quad & \frac{\partial < \tilde{p}(\vec{k}_2, z') >}{\partial z'} \frac{\partial G_\omega(\vec{q}_2, z_2, z')}{\partial z'} \Big]^*
\end{aligned} \tag{B.51}
$$

where the Helmholtz equation was used to simplify a second derivative. The third and fourth terms are integrated similarly, though the fourth term involves two integration by parts and requires assuming that $\frac{\partial M}{\partial z} \to 0$ for large $z_0 - z$, as was done in finding the mean field equation. The results are

$$
\begin{aligned}
I_3 \quad = \quad & \mu_\rho \int\int dz' dz_0 M(z_0 - z') b_1^*(\vec{q}_2, \vec{k}_2, z') G_\omega^*(\vec{q}_2, z_2, z') < \tilde{p}^*(\vec{k}_2, z') > \cdot \\
& \Big[(k_0^2(z_0) - \vec{k}_1^2) < \tilde{p}(\vec{k}_1, z_0) > G_\omega(\vec{q}_1, z_1, z_0)
\end{aligned}
$$

$$
- \left. \frac{\partial< \tilde{p}(\vec{k}_1, z_0) >}{\partial z_0} \frac{\partial G_\omega(\vec{q}_2, z_2, z_0)}{\partial z_0} \right] \tag{B.52}
$$

and

$$
\begin{aligned}
I_4 &= \mu_\rho^2 \int\int dz' dz_0 M(z_0 - z') \cdot \\
&\left[\frac{\partial< \tilde{p}(\vec{k}_1, z_0) >}{\partial z_0} \frac{\partial G_\omega(\vec{q}_1, z_1, z_0)}{\partial z_0} - (k_0^2(z_0) - \vec{k}_1^2) G_\omega(\vec{q}_1, z_1, z_0) < \tilde{p}(\vec{k}_1, z_0) > \right] \cdot \\
&\left[\frac{\partial< \tilde{p}(\vec{k}_2, z') >}{\partial z'} \frac{\partial G_\omega(\vec{q}_2, z_2, z')}{\partial z'} \right. \\
&- \left. (k_0^2(z') - \vec{k}_2^2) G_\omega(\vec{q}_2, z_2, z') < \tilde{p}(\vec{k}_2, z') > \right]^* \qquad (B.53)
\end{aligned}
$$

These terms are clearly symmetric, and the symmetry can be used to simplify the expressions. Defining the terms

$$
\begin{aligned}
\Delta^{(1)}(\vec{k}, z) &= -\mu_\rho \frac{\partial< \tilde{p}(\vec{k}, z) >}{\partial z} \\
\Delta^{(2)}(\vec{q}, \vec{k}, z) &= [\mu_c(z) + \mu_\rho(k_0^2(z) - \vec{q} \cdot \vec{k})] < \tilde{p}(\vec{k}, z) > \qquad (B.54)
\end{aligned}
$$

then the cross-spectral power density is given by

$$
\begin{aligned}
< \tilde{s}(\vec{q}_1, z_1) \tilde{s}^*(\vec{q}_2, z_2) > &= 2\pi < \sigma^2 > \int\int\int\int dz_0 dz' d\vec{k}_1 d\vec{k}_2 P_H(\vec{q}_1 - \vec{k}_m) \cdot \\
&M(z_0 - z') \delta(\vec{q}_1 - \vec{k}_1 - \vec{q}_2 + \vec{k}_2) \cdot \\
&\left[\Delta^{(1)}(\vec{k}_1, z_0) \frac{\partial G_\omega(\vec{q}_1, z_1, z_0)}{\partial z_0} + \Delta^{(2)}(\vec{k}_1, \vec{q}_1, z_0) G_\omega(\vec{q}_1, z_1, z_0) \right] \cdot \\
&\left[\Delta^{(1)}(\vec{k}_2, z') \frac{\partial G_\omega(\vec{q}_2, z_2, z')}{\partial z'} \right. \\
&+ \left. \Delta^{(2)}(\vec{k}_2, \vec{q}_2, z') G_\omega(\vec{q}_2, z_2, z') \right]^* \qquad (B.55)
\end{aligned}
$$

B.5 Reverberant field statistics in a 2D ocean

Here the steps involved in calculating the second-moment statistics of the reverberant field for volume scattering in a 2D ocean are outlined. Most of the algebra is similar to that shown in other parts of the thesis, so only the main steps are outlined.

We have seen above that the wavenumber-domain results take a similar form whether the 2D or 3D wavenumber transform is used. By analogy with the results in the section above, a 2D cross-spectral density can be written down. First, however, we note that a different expression for the second-moment of the porosity fluctuations is needed. The goal of section B.4 was to find the cross-spectral density - a wavenumber domain result. The porosity statistics were therefore written in the wavenumber domain. The 2D equivalent would be

$$< \tilde{\delta P}(q,z)\tilde{\delta P}^{*}(k,z_0) >= 2\pi < \sigma^2 > P_H(q)\delta(q-k)M(z-z_0) \tag{B.56}$$

In this section we are interested in finding spatial statistics in the ocean. We therefore write the porosity statistics in the spatial domain, as was done in section 2.3.1 when studying rough surface scattering. The second moment is found from the Fourier transforms:

$$< \tilde{\delta P}(q,z)\tilde{\delta P}^{*}(k,z_0) >= \frac{1}{(2\pi)^2}\int dr' \int dr'' < \delta P(r',z_1)\delta P(r'',z_2) > e^{iqr'}e^{-ikr''} \tag{B.57}$$

Using the 2D version of the results from section B.4, and replacing the wavenumber-domain expression of the porosity fluctuation statistics with the spatial-domain expression, we find:

$$\begin{aligned}
< \tilde{s}(q_1,z_1)\tilde{s}^{*}(q_2,z_2) > \;=\; & \frac{1}{(2\pi)^2}\int_{z_1}^{z_2} dz_0 \int_{z_1}^{z_2} dz' \int\int dk_1 dk_2 \cdot \\
& \left\{\int dr' \int dr'' < \delta P(r',z_1)\delta P(r'',z_2) > e^{i(q_1-k_1)r'}e^{-i(q_2-k_2)r''}\right\} \cdot \\
& \left[\Delta^{(1)}(k_1)\frac{\partial G_\omega(q_1,z_1,z_0)}{\partial z_0} + \Delta^{(2)}(q_1,k_1)G_\omega(q_1,z_1,z_0)\right] \cdot \\
& \left[\Delta^{(1)}(k_2)\frac{\partial G_\omega(q_2,z_2,z^{'})}{\partial z^{'}} + \Delta^{(2)}(q_2,k_2)G_\omega(q_2,z_2,z^{'})\right]^{*}
\end{aligned} \tag{B.58}$$

The next step is to convert the integrals to modal sums and carry out contour integrals over k_1 and k_2, picking the positive poles which travel out from the source. The cross-spectral density is then given by

$$\begin{aligned}
< \tilde{s}(\vec{q_1},z_1)\tilde{s}^{*}(\vec{q_2},z_2) > \;=\; & \frac{\mid NM \mid^2}{(2\pi)^4\rho^2(z_s)}\int_{z_1}^{z_2} dz_0 \int_{z_1}^{z_2} dz' \sum_{n,m,l,p}\frac{1}{\rho^2(z_0)} \cdot \\
& \left\{\int dr' \int dr'' < \delta P(r',z_1)\delta P(r'',z_2) > e^{i(q_1-k_1)r'}e^{-i(q_2-k_2)r''}\right\} \cdot \\
& \left[\psi_n(z_1)\frac{\Delta_m^{(1)}\frac{\partial\psi_n(z_0)}{\partial z_0} + \Delta_m^{(2)}(q_1)\psi_n(z_0)}{2k_m(q_1^2-q_n^2)}\right] \cdot \\
& \left[\psi_l(z_2)\frac{\Delta_p^{(1)}\frac{\partial\psi_l(z')}{\partial z'} + \Delta_p^{(2)}(q_2)\psi_l(z')}{2k_p(q_2^2-q_l^2)}\right]^{*}
\end{aligned} \tag{B.59}$$

where m and p are sums over the incident fields k_1 and k_2, and

$$\begin{aligned} \Delta_m^{(1)} &= -\mu_\rho \psi_m(z_s)\psi_m(z_0) \\ \Delta_m^{(2)}(q_1) &= \psi_m(z_s)\psi_m(z_0)\left[\mu_c(z_0) + \mu_\rho(k_b^2 - q_1 k_m)\right] \end{aligned} \tag{B.60}$$

with $\Delta_p^{(1)}$, $\Delta_p^{(2)}$ having the same form.

In Chapter 2 we saw that most of the scattered field statistics can be found from the cross-modal amplitude expectations, so we calculate those here. To begin, we note the spatial correlation of the scattered field is defined as

$$< s(x_1, z_1)s^*(x_2, z_2) >= \int\int dq_1 dq_2 < \tilde{s}(q_1, z_1)\tilde{s}^*(q_2, z_2) > e^{-iq_1 x_1} e^{iq_2^* x_2} \tag{B.61}$$

First we find the statistics of the forward-scattered field. All forward scattering received at some point x_1 will come from ranges r' between $[0, x_1]$, and the forward scattered field received at at x_2 comes from ranges r'' between $[0, x_2]$, limiting the range of the spatial integrals. As in section 2.4 we define sum and difference coordinates:

$$\begin{aligned} y &= r' - r'' \\ r &= (r' + r'')/2. \end{aligned} \tag{B.62}$$

In the new coordinate system, the terms in the curly braces above can be simplified. They become, using Eqn. 3.15

$$\begin{aligned} Braces &= 2\pi < \sigma^2 > P_H(\frac{(q_1 - k_1) + (q_2 - k_2)}{2})M(z - z_0) \\ &\quad \int_0^{\frac{x_1 + x_2}{2}} dr e^{i[(q_1 - k_1) - (q_2 - k_2)^*]r} \\ &= 2\pi < \sigma^2 > P_H(\frac{(q_1 - k_1) + (q_2 - k_2)}{2})M(z - z_0) \\ &\quad \frac{e^{i[(q_1 - k_1) - (q_2 - k_2)^*]\frac{x_1 + x_2}{2}}}{i[(q_1 - k_1) - (q_2 - k_2)^*]} \end{aligned} \tag{B.63}$$

If the vertical correlation function M is approximated by a delta function, only one depth integral remains in Eq. B.61. Next we carry out the contour integrals over q_1 and q_2, choosing the positive (forward-scattered) poles. Combining all these results, the forward-scattered field correlation is found to be

$$
\begin{aligned}
< s(x_1, z_1) s^*(x_2, z_2) > \; = \; & \frac{< \sigma^2 >}{2\pi} \sum_{n,m,l,p} \int_{z_1}^{z_2} dz_0 P_H\left(\frac{(q_n - k_m) + (q_l - k_p)}{2}\right) \cdot \\
& \left\{ \frac{e^{i[(q_1 - k_1) - (q_2 - k_2)^*] \frac{x_1 + x_2}{2}}}{i[(q_1 - k_1) - (q_2 - k_2)^*]} \right\} \cdot \\
& \psi_n(z_1) \psi_l^*(z_2) a_{nm}(z_0) a_{lp}^*(z_0) e^{-iq_n x_1} e^{iq_l^* x_2}
\end{aligned}
\tag{B.64}
$$

where

$$
a_{nm}(z_0) = \frac{1}{\rho(z_s)\rho(z_0)} \left(\frac{\Delta_m^{(1)}(k_m)\psi_n'(z_0) + \Delta_m^{(2)}(q_n, k_m)\psi_n(z_0)}{4k_m q_n} \right)
\tag{B.65}
$$

and a_{lp} is similar.

This procedure is similar to that used in section 2.4, and the results are similar to those for rough surface scattering, with the addition of a depth integral. The same procedure can be used to find the spatial covariance of the backscattered field. If both receivers are at the source range, the result is:

$$
\begin{aligned}
< s(0, z_1) s^*(0, z_2) > \; = \; & \frac{< \sigma^2 >}{2\pi} \sum_{n,m,l,p} \int_{z_1}^{z_2} dz_0 P_H\left(\frac{(-q_n - k_m) + (-q_l - k_p)}{2}\right) \cdot \\
& \left\{ \frac{1}{i[(-q_n - k_m) + (-q_l - k_p)^*]} \right\} \cdot \\
& \psi_n(z_1) \psi_l^*(z_2) b_{nm}(z_0) b_{lp}^*(z_0)
\end{aligned}
\tag{B.66}
$$

where

$$
b_{nm}(z_0) = \frac{1}{\rho(z_s)\rho(z_0)} \left(\frac{\Delta_m^{(1)}(k_m)\psi_n'(z_0) + \Delta_m^{(2)}(-q_n, k_m)\psi_n(z_0)}{-4k_m q_n} \right)
\tag{B.67}
$$

Now the modal cross-coherences can be defined. Writing the pressure field as

$$
s(x, z) = \sum_n a_n \psi_n(z) e^{-iq_n x}
\tag{B.68}
$$

helps to identify the cross-modal expectations:

$$
< a_n(x_1) a_l^*(x_2) > \; = \; \frac{< \sigma^2 >}{2\pi} \sum_{m,p} \int_{z_1}^{z_2} dz_0 P_H\left(\frac{(-q_n - k_m) + (-q_l - k_p)}{2}\right) \cdot
$$

$$\left\{ \frac{e^{i[(q_1-k_1)-(q_2-k_2)^*]\frac{x_1+x_2}{2}}}{i[(q_1-k_1)-(q_2-k_2)^*]} \right\} a_{nm}(z_0)a_{lp}^*(z_0) \tag{B.69}$$

A similar result for the backscattered mode amplitudes can be written:

$$\begin{aligned} < b_n(0)b_l^*(0) > &= \frac{<\sigma^2>}{2\pi}\sum_{m,p}\int_{z_1}^{z_2} dz_0 P_H(\frac{(-q_n-k_m)+(-q_l-k_p)}{2})\cdot \\ & \left\{ \frac{1}{i[(-q_n-k_m)+(-q_l-k_p)^*]} \right\} b_{nm}(z_0)b_{lp}^*(z_0) \end{aligned} \tag{B.70}$$

These expressions are used to generate the numerical results shown in Chapter 4.

Appendix C

Examination of impedance scattering theory

This appendix compares two approaches to studying scattering from rough surfaces. The aim is to calculate attenuation of the coherent sound field and statistics of the scattered field.

We first examine the simple case of scattering from a fluid-fluid boundary. Previous work by Kryazhev and Kudryashov [40] and Kudryashov [42] (refered to as K1 and K2 from now on) is rewritten slightly and compared to results from the two-sided scattering theory developed by Kuperman [43] and Kuperman and Schmidt [45]. The comparison shows that the two approaches agree in two limiting cases; first, as the correlation length of the roughness increases and the roughness power spectrum approaches a delta function; and second, as the impedance contrast between the two fluids increases.

The differences seen in other cases can be understood by remembering that *both* the mean and scattered fields must satisfy the two boundary conditions at the interface. The boundary impedance is found by satisfying the boundary conditions for the mean field, but it is only a single boundary condition, containing information about the reflection coefficient at the boundary. A perturbation method based on expanding the impedance boundary condition does not have enough information to satisfy the *two* boundary conditions for the scattered field. In contrast the two-sided approach uses both the reflection and transmission coefficients. In the limit of large impedance contrasts (Dirichlet or Neuman boundary conditions) there is only one boundary condition, and the two results agree exactly.

The reason for agreement in the limit of large correlation length can also be understood. As the correlation length increases, the roughness power spectrum approaches a delta function around the incident wavenumber. Sound is not scattered into wavenumbers other than the incident wavenumber, just as mean-field energy isn't scattered to wavenumbers other than incident. Thus the scattering problem is identical to the mean-field reflection problem. Since the impedance was found by satisfying the boundary conditions for the mean-field, it will also satisfy the boundary conditions for the scattered field in this limit.

Both of these approaches have been applied to the important problem of calculating the reflection coefficient of the rough Arctic ice sheet. The impedance method is computationally much faster, so if it is accurate it should be used. The question then becomes: does the ice sheet present a high enough impedance contrast to an incident wave for the impedance method to be accurate? In the last section we compare reflection coefficients for the rough ice plate calculated by both methods to answer this question.

C.1 Theory

The scattering theory developed by Kydryashov and Kryashev is outlined here. This theory has been described in a number of publications [40, 42], but is restated here for clarity. We consider scattering from an interface between two half-spaces separated by a rough boundary centered around $z = 0$, with z defined positive downwards. The rough boundary depth is given by $\alpha(\vec{r})$. A time dependence of $e^{i\omega t}$ is assumed, so the waves propagating outward from the boundary are of the form $e^{-ik_{z2}z}$ for $z > 0$ (region 2) and $e^{ik_{z1}z}$ for $z < 0$ (region 1). A wave is incident on the boundary from region 1. Since the boundary condition is given in terms of an impedance relation, we write

$$p(\vec{r}, \alpha(\vec{r})) - \gamma[\frac{\partial p(\vec{r}, z)}{\partial n}]_{z=\alpha(\vec{r})} = 0 \tag{C.1}$$

Here p is the acoustic pressure in medium 1 and $\frac{\partial}{\partial n}$ is the normal derivative. Assuming the interface slopes are small we write

$$\frac{\partial}{\partial n} = \frac{\partial}{\partial z} - \nabla_{\perp}\alpha(\vec{r}) \cdot \nabla_{\perp} \tag{C.2}$$

Assuming the height of the rough surface is small we expand the pressure in a Taylor series about $z = 0$. In K1 and K2 the expansion is done to first order, while in Kuperman's paper it is done to second order. Keeping terms to second order correction:

$$p(\vec{r}, \alpha(\vec{r})) = p(\vec{r}, 0) + \alpha(\vec{r})\frac{\partial p(\vec{r}, 0)}{\partial z} + \frac{\alpha^2(\vec{r})}{2}\frac{\partial^2 p(\vec{r}, 0)}{\partial z^2} \tag{C.3}$$

When considering scattering from a plate we will also expand the plate impedance in terms of the roughnesses α_1 and α_2 at the top and bottom of the plate:

$$\gamma = \gamma_0(h_0) + \alpha_1 \frac{\partial \gamma_0}{\partial h} + \alpha_2 \frac{\partial \gamma_0}{\partial h} + O(\alpha^2) \tag{C.4}$$

where γ_0 is the impedance for the nominal plate height h_0. For the case of two halfspaces, however, $\gamma = \gamma_0$.

We insert the expansions above into the impedance relation. We also write the acoustic field as the sum of a coherent (mean) part and a diffusely scattered part:

$$p(\vec{r}, z) =< p(\vec{r}, z) > +s(\vec{r}, z) \tag{C.5}$$

Taking the average of the resulting expression, remembering that both $s(\vec{r}, z)$ and $\alpha(\vec{r})$ are zero-mean, gives the coherent field boundary condition:

$$< p(\vec{r}, 0) > -\gamma_0 \frac{\partial < p(\vec{r}, 0) >}{\partial z} =< G(\vec{r}) > \tag{C.6}$$

where

$$\begin{aligned} < G(\vec{r}) > \ &= \ - < \alpha(\vec{r}) \frac{\partial s(\vec{r}, 0)}{\partial z} > - \frac{< \alpha^2 >}{2} \frac{\partial^2 < p(\vec{r}, 0) >}{\partial z^2} + \gamma_0 < \alpha(\vec{r}) \frac{\partial^2 s(\vec{r}, 0)}{\partial z^2} > \\ &\quad + \gamma_0 \frac{< \alpha^2 >}{2} \frac{\partial^3 < p(\vec{r}, 0) >}{\partial z^3} - \gamma_0 < \nabla_\perp \alpha(\vec{r}) \nabla_\perp s(\vec{r}, 0) > \end{aligned} \tag{C.7}$$

The first order terms agree with the mean field equation found in Eq. 4 of K1. Numerical work has shown the second order terms to have almost no impact on the answer.

A boundary condition for the scattered field can be found by subtracting the mean-field boundary condition from the boundary condition for the total field. When doing so we will keep only first-order terms. From the expression for $< G(\vec{r}) >$ we see that the scattered field terms are always multiplied by $\alpha(\vec{r})$, so the mean-field equation will still be second-order accurate. The subtraction yields the boundary condition

$$s(\vec{r}, 0) - \gamma_0 \frac{\partial s(\vec{r}, 0)}{\partial z} = G_s(\vec{r}) \tag{C.8}$$

where

$$G_s(\vec{r}) = -\alpha(\vec{r}) \frac{\partial < p(\vec{r}, 0) >}{\partial z} + \gamma_0 \alpha(\vec{r}) \frac{\partial^2 < p(\vec{r}, 0) >}{\partial z^2} - \gamma_0 \nabla_\perp \alpha(\vec{r}) \cdot \nabla_\perp < p(\vec{r}, 0) > \tag{C.9}$$

So far we have followed K1 and K2 almost exactly, with the exception of retaining second-order terms in the mean field boundary condition. At this point we diverge slightly and transform the boundary conditions obtained above, using the the 2-D wavenumber transform [45]

$$\begin{aligned} f(x,y,z) &= \frac{1}{2\pi}\int_{-\infty}^{\infty} F(\vec{q},z)e^{-i\vec{q}\cdot\vec{r}}d^2\vec{q} \\ F(\vec{q},z) &= \frac{1}{2\pi}\int_{-\infty}^{\infty} f(x,y,z)e^{i\vec{q}\cdot\vec{r}}d^2\vec{r} \end{aligned} \tag{C.10}$$

where $\vec{q}$ is the horizontal wavenumber. The transformed mean field boundary condition is

$$< \tilde{p}(\vec{k},0) > -\gamma_0(\vec{k})\frac{\partial < \tilde{p}(\vec{k},0) >}{\partial z} = < \tilde{G}(\vec{k}) > \tag{C.11}$$

where

$$\begin{aligned} < \tilde{G}(\vec{r}) > &= -\frac{1}{2\pi}\int d^2\tilde{q} < \tilde{\alpha}(\vec{k}-\vec{q})\frac{\partial\tilde{s}(\vec{q},0)}{\partial z} > -\frac{< \alpha^2 >}{2}\frac{\partial^2 < \tilde{p}(\vec{k},0) >}{\partial z^2} \\ &+\frac{\gamma_0(\vec{k})}{2\pi}\int d^2\tilde{q} < \tilde{\alpha}(\vec{k}-\vec{q})\frac{\partial^2\tilde{s}(\vec{q},0)}{\partial z^2} > +\gamma_0(\vec{k})\frac{< \alpha^2 >}{2}\frac{\partial^3 < \tilde{p}(\vec{k},0) >}{\partial z^3} \\ &+\frac{\gamma_0(\vec{k})}{2\pi}\int d^2\tilde{q}\vec{q}\cdot(\vec{k}-\vec{q}) < \tilde{\alpha}(\vec{k}-\vec{q})\tilde{s}(\vec{q},0) > \end{aligned} \tag{C.12}$$

The transformed equation for the scattered field is

$$\tilde{s}(\vec{q},0) - \gamma_0(\vec{q})\frac{\partial\tilde{s}(\vec{q},0)}{\partial z} = \tilde{G}_s(\vec{q}) \tag{C.13}$$

where the forcing term becomes

$$\tilde{G}_s(\vec{q}) = \frac{1}{2\pi}\int d^2\vec{k}'\,\tilde{\alpha}(\vec{q}-\vec{k})[-\frac{\partial}{\partial z} + \gamma_0(\vec{q})\frac{\partial^2}{\partial z^2} + \gamma_0(\vec{q})\vec{k}\cdot(\vec{q}-\vec{k})] < \tilde{p}(\vec{k},0) > \tag{C.14}$$

By inspection, we can write down a solution for the scattered field which is the same as Eq. 6 in K1:

$$\tilde{s}(\vec{q},z) = \tilde{G}_s(\vec{q})\frac{Z(z,\vec{q})}{\pi(\vec{q})} \tag{C.15}$$

where

$$\pi(\vec{q}) = Z(0,\vec{q}) - \gamma_0(\vec{q})\frac{\partial Z(0,\vec{q})}{\partial z} \tag{C.16}$$

Here $Z(z, \vec{q})$ is chosen so it solves the Helmholtz equation in medium 1 and the radiation condition as $z \to -\infty$. For waveguide propagation Z is also required to satisfy the boundary conditions at other (smooth) interfaces, and $\pi(\vec{q})$ gives rise to poles at the modal eigenvalues q_n of the unperturbed waveguide. The solutions $Z(z, q_n)$ will then correspond to the unperturbed normal modes.

The angle-dependent impedance can be written in terms of the plane-wave reflection coefficient. For a fluid-fluid boundary with the sign conventions defined above the impedance for medium 2 is

$$\gamma_0(\theta) = \frac{p}{p_z} = \frac{1 + R(\theta)}{ik_1 sin\theta(R(\theta) - 1)} \tag{C.17}$$

or, replacing θ by $\vec{k}$,

$$\gamma_0(\vec{k}) = \frac{1 + R(\vec{k})}{ik_{z1}(R(\vec{k}) - 1)} \tag{C.18}$$

This sign convention holds for reflection for the bottom; we will switch it for reflection from the surface.

C.2 Comparison of approaches for fluid-fluid rough boundary

In this section we compare the expressions for scattering from a rough fluid-fluid interface obtained from impedance and two-sided approaches. First we continue looking at the impedance method. We can use the expressions above to find the scattered field and mean field reflection coefficient for a rough fluid-fluid surface, expressing the acoustic field in terms of plane waves. First we will look at the scattered field.

We can write down forms for the quantities above:

$$Z(z, \vec{q}) = e^{iq_{z1}z} \tag{C.19}$$

satisfies the Helmholtz equation and radiation conditions, so

$$\pi(\vec{q}) = 1 - iq_{z1}\gamma_0(\vec{q}) \tag{C.20}$$

The incident field is given by

$$< \tilde{p}(\vec{k}, z) >= e^{-ik_{z1}z} + R(\vec{k})e^{ik_{z1}z} \tag{C.21}$$

so we can write down:

$$\begin{aligned} < \tilde{p}(\vec{k}, 0) > &= 1 + R(\vec{k}) \\ \frac{\partial < \tilde{p}(\vec{k}, 0) >}{\partial z} &= ik_{z1}(R(\vec{k}) - 1) \\ \frac{\partial^2 < \tilde{p}(\vec{k}, 0) >}{\partial z^2} &= -k_{z1}^2(1 + R(\vec{k})) \end{aligned} \tag{C.22}$$

The expression for γ_0 is as given above, and the plane-wave reflection coefficient is given by

$$R(q) = \frac{\rho_2 q_{z1} - \rho_1 q_{z2}}{\rho_2 q_{z1} + \rho_1 q_{z2}} \tag{C.23}$$

With some algebra we can reduce the form given for $\tilde{s}$ above to

$$\tilde{s}(\vec{q}, z) = \frac{e^{iq_{z1}z}}{2\pi} \int d^2\vec{k}\tilde{\alpha}(\vec{q} - \vec{k}) \frac{\rho_1 q_{z2} k_{z1}(R(k) - 1) + \rho_2(1 + R(k))[k_{z1}^2 - \vec{k} \cdot (\vec{q} - \vec{k})]}{i(\rho_1 q_{z2} + \rho_2 q_{z1})} \tag{C.24}$$

Here we have eliminated the $R(\vec{q})$ terms coming from $\gamma_0(q)$ since these do not appear in the Kuperman/Schmidt expressions, using the definition of the reflection coefficient.

The scattered field expression is next substituted into the the coherent field boundary condition. This equation can be used to find a corrected coherent field impedance $< \gamma >$. This expression is not given here, but is identical to Eq. 2 of K2 with the $\frac{\partial \gamma}{\partial h}$ terms set to zero, with the addition of second-order correction terms not included in K2. The mean-field impedance can be used to find a corrected mean-field reflection coefficient $< R >$, shown in plots below. The correction terms are not very important through most of the angles.

These formulas can be compared to those from the articles by Kuperman and Schmidt. From Eq. 10 of Kuperman and Schmidt, using boundary operators for pressure waves interacting with a fluid-fluid boundary, we find

$$\begin{aligned} \tilde{s}(\vec{q}, z) &= \frac{e^{iq_{z1}z}}{2\pi} \int d^2\vec{k}\tilde{\alpha}(\vec{q} - \vec{k}) \frac{\rho_1 q_{z2}[k_{z1}(R(k) - 1) + k_{z2}T(k)]}{i(\rho_1 q_{z2} + \rho_2 q_{z1})} \\ &\quad + \frac{(\rho_2[k_{z1}^2 - \vec{k} \cdot (\vec{q} - \vec{k})])(1 + R(k)) - (\rho_1[k_{z2}^2 - \vec{k} \cdot (\vec{q} - \vec{k})])T(k)}{i(\rho_1 q_{z2} + \rho_2 q_{z1})} \end{aligned} \tag{C.25}$$

This expression has two terms which are identical to those found using the impedance method, but has two additional terms (multiplied by the transmission coefficient $T(k)$) coming from the two-sided nature of the boundary conditions. These terms can be rewritten using $T(k) = 1 + R(k)$, but do not cancel out.

Kuperman also gives an expression for the coherent field reflection coefficient. Plots of this are shown below.

By comparing the two expressions for the scattered field, we can see when the two approaches will agree. As the correlation length of the roughness becomes very long, the power spectrum approaches a delta function, so the integrals only pick out $q = k$. The terms corresponding to the roughness slopes (i.e. $\vec{k} \cdot (\vec{q} - \vec{k})]))$ disappear, and the remaining "extra" terms in the Kuperman/Schmidt expression cancel each other out.

The approaches also agree for inherently one-sided boundary conditions, such as pressure-release surfaces or rigid bottoms. Plots of the reflection coefficients show that the agreement is better for large impedance contrasts at the interface, and worse for lesser contrasts. In the limit as the impedances are equal ($\rho_1 \rightarrow \rho_2, c_1 \rightarrow c_2$, the impedance method incorrectly predicts there will still be a scattered field, while the Kuperman results shows no scattered field. The impedance method also predicts a non-zero mean field $< R >$ in this limit. This problem seems to be recognized in K2.

It is fairly clear why the two results don't agree in general. At a fluid-fluid interface two boundary conditions must be satisfied. The boundary conditions can be rewritten in terms of two quantities, the reflection coefficient and the transmission coefficient. An impedance boundary condition based on the reflection coefficient alone is "missing" some information, and cannot satisfy two boundary conditions. For inherently one-sided boundary conditions (rigid or pressure-release) the impedance approach will give exact agreement, and it will give good agreement as the impedance contrast across the boundary becomes quite large.

Results for mean-field reflection coefficients for different rough fluid-fluid interfaces are shown in Figs. 1 and 2. For all cases, medium 1 has $c_1 = 1500 m/s$,$\rho_1 = 1 g/cm^3$, and the roughness is described by an isotropic Gaussian spectrum. Figure 1 shows scattering at $20Hz$ from a fluid bottom, with $c_2 = 1800m/s$, $\rho_2 = 1.8$, and $\sigma = 2m$. Agreement is seen to be good for when the correlation length is long, but poor for a more realistic correlation length. Figure 2 shows the agreement is better for a bottom with a larger impedance difference (c_2 = 3500 m/s, ρ_2= 0.91) for the same roughness correlation length, and is excellent for scattering from a rough air-water interface.

In other cases the impedance method in general predicts more scattering loss than Kuperman's result. Since the impedance method predicts a non-zero scattered field as

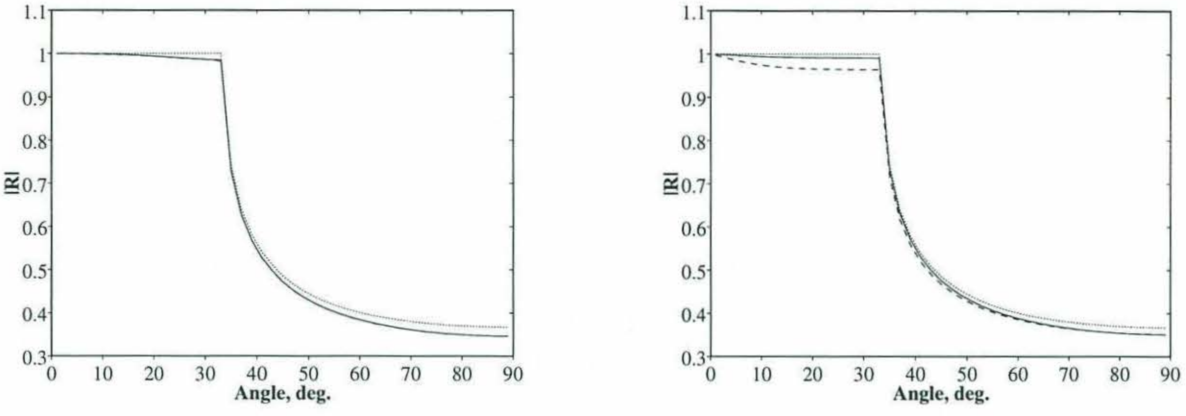

Figure C-1: Effect of changing correlation length. f = 20 Hz; Gaussian power spectrum, c_2 = 1800 m/s, ρ_2 = 1.8, σ = 2 m. Dotted line is R for smooth interface; solid is Kuperman result; dashed is Kudryashov result

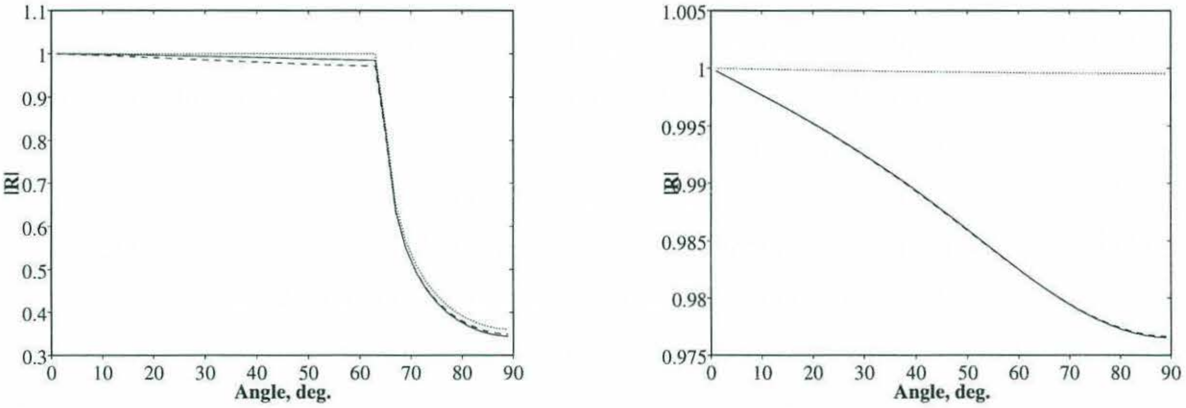

Figure C-2: Effect of changing medium 2 impedance. f = 20 Hz; Gaussian power spectrum; Dotted line is R for smooth interface; solid is Kuperman result; dashed is Kudryashov result

the impedance contrast between the halfspaces disappears, we expect to see it overpredict scattering loss for a small impedance-contrast like Figure 1b).

C.3 Numerical results: Rough ice plate

In this section we look at reflection from a rough ice plate. Expressions from K2 for the mean field reflection coefficient were coded, and the results are compared to LePage's SELF-CON code [47] (which implements the Kuperman/Schmidt theory). Although Kudryashov's expressions are used, we use different sound speed profiles, ice parameters, and statistical models for the ice roughness, so the results are different from those shown in the AcoustIn-

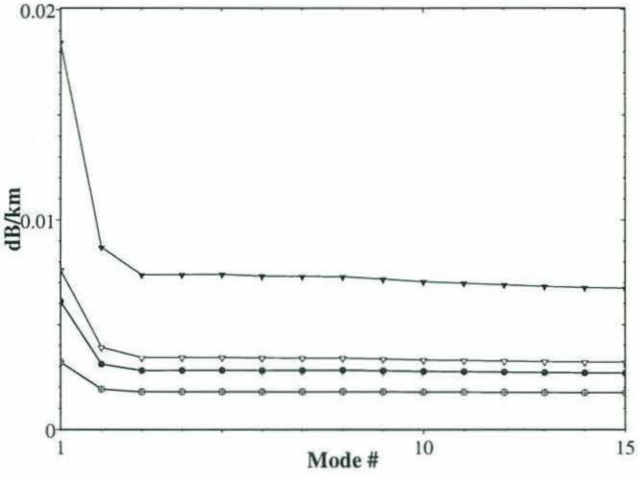

Figure C-3: Mode attenuation caused by scattering from rough ice plate. f = 20 Hz; Goff-Jordan power spectrum; Closed triangle is LePage result, including ice attenuation; open triangle is Lepage, no attenuation; Closed circle is Kudryashov result, K12 = 0.7; Open circle is Kudryashov, K12 = 0

form reports [22, 21]. However, we note the code we have written from Kudryashov's expressions gives modal attenuations which are roughly the same as those shown in Fig. 17 of [22].

Here we model reflection from an Arctic ice plate with the parameters: $c_p = 3500$ m/s, $c_s = 1750$ m/s, ice density = 0.91, $c_w = 1431$ m/s, H = 4 m., $\sigma = 2$ m., CL = 22 m., $\alpha_p = 2.5$ dB/λ, $\alpha_s = 1.0$ dB/λ. Figure 3 shows Kevin LePage's results, with and without attenuation in the ice plate, and results from Kudryashov's formula, for $K12 = 0$ and $K12 = 0.7$. $K12$ is a parameter Kudryashov uses to measure the correlation between roughness at the upper and lower boundaries of the ice plate; $K12 = 1$ denotes total correlation, while $K12 = 0$ means zero correlation. In LePage's code the roughnesses are assumed to be totally uncorrelated. Earlier, close agreement was shown between LePage's results and Kudryashov's with $K12 = 0.7$ (though different statistical models for ice roughness were used for the comparison) [22]. As is seen in Fig. 3, LePage's results without ice attenuation agree reasonable well with the impedance model with $K12 = 0.7$. However, when ice attenuation is included (meaning the scattering theories model the same physical scenario) LePage's code is seen to give much larger modal attenuations.

Bibliography

[1] K. Attenborough and S. Taherzadeh. Propagation from a point source over a rough finite impedance boundary. *J. Acoust. Soc. Am.*, 98(3):1717–1722, Sept. 1995.

[2] F.G. Bass and I.M. Fuks. *Waves scattered from Statistically Rough Surfaces.* Pergamon, Oxford, 1979.

[3] L. Baxter and M.H. Orr. Fluctuations in sound transmission through internal waves associated with the thermocline. *J. Acoust. Soc. Am.*, 71(1):61–66, Jan. 1982.

[4] A. Bellis and F.D. Tappert. Coupled mode analysis of multiple rough surface scattering. *J. Acoust. Soc. Am.*, 66(3):811–826, Sept. 1979.

[5] C. Bender and S. Orszag. *Applied Mathematical Methods for Scientists and Engineers.* McGraw-Hill, New York, 1978.

[6] M.J. Beran and S. Frankenthal. Volume scattering in a shallow channel. *J. Acoust. Soc. Am.*, 91(2):3203–3211, June 1992.

[7] C.A. Boyles. Coupled mode solution for a cylindrically symmetric oceanic waveguide with a range and depth dependent refractive index and a time varying rough sea surface. *J. Acoust. Soc. Am.*, 73(3):800–805, March 1983.

[8] J.R. Buck, J.C. Preisig, M. Johnson, and J. Catipovic. Monochromatic single-mode excitation in shallow water using feedback control. *Proceedings of the International Conference on Acoustics, Speech, and Signal Processing*, Detroit, MI, May 1995.

[9] E. Carmack, R.Macdonald, and R. Perkin. Anomalous warm water in the canadian basin of the Arctic ocean. *Geophys. Res. Lett.*, (in press) 1995.

[10] E.C. Carmack. Large-scale physical oceanography of polar oceans. In Jr. W.O. Smith, editor, *Polar Oceanography: Part A, Physical Science.* Academic Press, Inc., 1990.

[11] L. A. Chernov. *Wave Propagation in a Random Medium.* McGraw-Hill, New York, 1960.

[12] J.A. DeSanto. *Scalar Wave Theory.* Springer-Verlag, Berlin, Heidelberg, New York, 1992.

[13] M.E. Dougherty and R.A. Stephen. Seismo/acoustic propagation through rough seafloors. *J. Acoust. Soc. Am.*, 90:2637–2651, 1991.

[14] J.F. Doyle. *Wave propagation in structures.* Springer-Verlag, Berlin, Heidelberg, New York, 1989.

[15] L.B. Dozier. Spatial coherence in shallow water. *Science Application International Corp. report SAIC-85/1035*, February 1985.

[16] L.B. Dozier and F.D. Tappert. Statistics of normal mode amplitudes in a random ocean: Theory. *J. Acoust. Soc. Am.*, 63(2):352–365, February 1977.

[17] D.D. Ellis. A shallow-water normal-mode reverberation model. *J. Acoust. Soc. Am.*, 97(5):2804–2814, May 1995.

[18] H. Essen, F. Schirmer, and S. Sirkes. Acoustic remote sensing of internal waves in shallow water. *Int. J. Remote Sensing*, 4(1):33–47, 1983.

[19] H. Fan. *Wave theory modeling of three-dimensional seismo-acoustic reverberation in ocean waveguides.* PhD thesis, Massachusetts Institute of Technology, Sept. 1995.

[20] C. Garrett and W. Munk. Internal waves in the ocean. *Ann. Rev. Fluid Mech.*, 11:339–369, 1979.

[21] A.N. Gavrilov. Acoustic monitoring of Arctic ocean climate: feasibility research and modeling. *AcoustInform Ltd.*, Aug. 1994.

[22] A.N. Gavrilov and V.N. Kudryashov. Numerical monitoring of low-frequency sound propagation in horizontally stratified Arctic waveguide. *AcoustInform Ltd.*, March 1994.

[23] P. Gerstoft and H. Schmidt. A boundary element approach to seismo-acoustic facet reverberation. *J. Acoust. Soc. Am.*, 89:1629–1642, 1991.

[24] K. Gilbert. A stochastic model for scattering from the near- surface oceanic bubble layer. *J. Acoust. Soc. Am.*, 94(6):3325–3334, December 1993.

[25] J. Goff and T. Jordan. Stochastic modeling of seafloor morphology: Inversion of sea beam data for second order statistics. *J. Geophys. Res.*, 93:13589–13608, 1993.

[26] N.S. Gorskaya and M.A. Raevskii. Acoustic mode conversion on a rough surface. *Sov. Phys. Acoust.*, 31(2):99–102, March-April 1985.

[27] N.S. Gorskaya and M.A. Raevskii. Low-frequency sound field in an ocean waveguide with an irregular bottom. *Sov. Phys. Acoust.*, 36(3):231–234, May-June 1990.

[28] A.J. Gow and W.B. Tucker III. Sea ice in the polar regions. In Jr. W.O. Smith, editor, *Polar Oceanography: Part A, Physical Science.* Academic Press, Inc., 1990.

[29] D. Halpern. Observations on short-period internal waves in Massachusetts Bay. *Ann. Rev. Fluid Mech.*, 11:339–369, 1979.

[30] E.Y. Harper and F.M. Labianca. Perturbation theory for scattering of sound from a point source by a moving rough surface in the presence of refraction. *J. Acoust. Soc. Am.*, 57(5):1044–1051, May 1975.

[31] P. Hines. Theoretical model of acoustic backscatter from a smooth seabed. *J. Acoust. Soc. Am.*, 88(1):324–334, July 1990.

[32] F. Ingenito. Scattering from an object in a stratified medium. *J. Acoust. Soc. Am.*, 82(6):2051–2059, Dec. 1987.

[33] A. Ishimaru. *Wave propagation and scattering in random media.* Academic Press, New York, 1978.

[34] A.N. Ivakin. A unified perturbation approach to volume and roughness scattering. *130th meeting, Acoustical Society of America*, December 1995.

[35] A.N. Ivakin and Y.P. Lysanov. Theory of underwater sound scattering by volume inhomogeneities of the bottom. *Sov. Physics Acoust.*, 27, Jan.-Feb. 1981.

[36] A.N. Ivakin and Y.P. Lysanov. Underwater sound scattering by volume inhomogeneities of a bottom bounded by a rough surface. *Sov. Physics Acoust.*, 27:212–215, 1981.

[37] D. Jackson, D. Winebrenner, and A. Ishimaru. Application of the composite roughness model to high-frequency bottom backscattering. *J. Acoust. Soc. Am.*, 79(5):1410–1422, May 1986.

[38] F.B. Jensen, W.A. Kuperman, M.B. Porter, and H. Schmidt. *Computational Ocean Acoustics.* American Institute of Physics, Woodbury, New York, 1994.

[39] B.L.N. Kennett. Guided wave propagation in laterally varying media - i. theoretical development. *Geophys. J. R. astr. Soc.*, 79:225–255, 1984.

[40] F.I. Kryazhev and V.M. Kudrashov. Sound field in a waveguide with a statistically rough admittance boundary. *Sov. Phys. Acoust.*, 30(5):391–393, Sept.-Oct. 1984.

[41] F.I. Kryazhev, V.M. Kudrashov, and N.A. Petrov. Propagation of low-frequency sound waves in a waveguide with irregular boundaries. *Sov. Phys. Acoust.*, 22(3):211–216, May-June 1976.

[42] V.M. Kudrashov. Influence of shear elasticity on the scattering of sound by a plate with statistically rough boundaries. *Sov. Phys. Acoust.*, 33(6):625–627, Nov.-Dec. 1988.

[43] W.A. Kuperman. Coherent component of specular reflection and transmission at a randomly rough two-fluid interface. *J. Acoust. Soc. Am.*, 58:365–370, 1975.

[44] W.A. Kuperman and H. Schmidt. Rough surface elastic wave scattering in a horizontally stratified ocean. *J. Acoust. Soc. Am.*, 79:1767–1777, 1986.

[45] W.A. Kuperman and H. Schmidt. Self-consistent perturbation approach to rough surface scattering in stratified elastic media. *J. Acoust. Soc. Am.*, 86(4):1511–1522, October 1989.

[46] K.D. LePage. *Elastic Scattering in Ocean Waveguides.* PhD thesis, Massachusetts Institute of Technology, September 1992.

[47] K.D. LePage and H. Schmidt. Modeling of low frequency transmission loss in the central Arctic. *J. Acoust. Soc. Am.*, 96:1783–1795, 1994.

[48] D. Li. Low-frequency bottom backscattering data analysis using multiple constraints beamforming. Master's thesis, Massachusetts Institute of Technology and Woods Hole Oceanographic Institution, May 1994.

[49] V. Lupien and R. Fricke. Coregistration of received signals with bathymetry using artist. *128th meeting, Acoustical Society of America*, December 1994.

[50] J. Lynch, A. Newhall, C. Chiu, and J. Miller. Three-dimensional ray acoustics in a realistic ocean. In A. Robinson and D. Lee, editors, *Oceanography and Acoustics: Prediction and Propagation Models.* AIP Press, New York, 1994.

[51] D. Marcuse. *Theory of dielectric optical waveguides.* Academic Press, New York, second edition, 1993.

[52] S.T. McDaniel. Calculation of mode conversion rates. *J. Acoust. Soc. Am.*, 63(5):1372–1374, May 1978.

[53] S.T. McDaniel. Mode conversion in shallow-water sound propagation. *J. Acoust. Soc. Am.*, 62(2):320–325, May 1978.

[54] S.T. McDaniel. Comparison of coupled-mode theory with the small-waveheight approximation for sea-surface scattering. *J. Acoust. Soc. Am.*, 70(2):535–540, Aug. 1981.

[55] S.T. McDaniel and D.F. McCammon. Mode coupling and the environmental sensitivity of shallow-water propagation loss predictions. *J. Acoust. Soc. Am.*, 82(1):217–223, May 1987.

[56] P. Mikhalevsky, R. Muench, and F. DiNapoli. Acoustic measurement of Arctic ocean warming. *Science Applications International Corporation*, March 1991.

[57] B. Miller and H. Schmidt. Observation and inversion of seismo-acoustic waves in a complex Arctic ice environment. *J. Acoust. Soc. Am.*, 89(4):1668–1685, April 1991.

[58] J. Miller. *Estimation of Sea Surface Wave Spectra Using Acoustic Tomography.* PhD thesis, Woods Hole Oceanographic Institution and the Massachusetts Institute of Technology, September 1987.

[59] J.A. Ogilvy. Wave scattering from rough surfaces. *Rep. Prog. Phys.*, 50:1553–1608, 1987.

[60] D. Palmer, M. Brown, F. Tappert, and H. Bezdek. Classical chaos in nonseparable wave propagation problems. *Geophys. Res. Letters*, 15(6):569–572, June 1988.

[61] R. Pawlowicz. On temperature changes in the western eurasian basin. *Deep Sea Research*, (submitted) 1995.

[62] D. Peregrym. An investigation of shallow water mode coupling effects during single mode transmission. Master's thesis, Massachusetts Institute of Technology and Woods Hole Oceanographic Institution, Sept. 1994.

[63] G. Pickard and W. Emery. *Descriptive Physical Oceanography, 5th Ed.* Pergamon Press, Oxford, New York, 1993.

[64] A.D. Pierce. Extension of the method of normal modes to sound propagation in an almost stratified medium. *J. Acoust. Soc. Am.*, 37:19–27, 1965.

[65] J. J. Polcari. *Acoustic mode coherence in the Arctic ocean.* PhD thesis, Massachusetts Institute of Technology and Woods Hole Oceanographic Institution, May 1986.

[66] Michael B. Porter. *The KRAKEN Normal Mode Program.* unpublished.

[67] E. Scheer and A.B. Baggeroer. Modal leakage in range dependent environments. *WHOI internal memo*, 1993.

[68] H. Schmidt and W.A. Kuperman. Spectral representations of rough interface reverberation in stratified ocean waveguides. *J. Acoust. Soc. Am.*, 97(4):2199–2209, April 1995.

[69] H. Schmidt, W. Seong, and J.T. Goh. Spectral super-element approach to range-dependant ocean acoustic modeling. *J. Acoust. Soc. Am.*, 98(1):465–472, July 1995.

[70] H.G. Schneider. Excess sound propagation loss in a stochastic environment. *J. Acoust. Soc. Am.*, 62:871–877, 1977.

[71] E.C. Shang. Some new challenges in shallow water acoustics. In H.M. Merklinger, editor, *Progress in Underwater Acoustics.* Plenum, New York, 1987.

[72] J.H. Stockhausen. Scattering from the volume of an inhomogeneous halfspace. *NRE report*, 63/9, 1963.

[73] G.R. Sutton and J.J. McCoy. Scattering of acoustic signals by inhomogeneities in a waveguide - a single-scatter treatment. *J. Acoust. Soc. Am.*, 60(4):833–839, October 1976.

[74] G.R. Sutton and J.J. McCoy. Spatial coherence of acoustic signals in randomly inhomogeneous waveguides - a multiple-scatter theory. *J. Math. Phys.*, 18(5):1052–1057, May 1977.

[75] D. Tang. *Acoustic Wave Scattering from a Random Ocean Bottom.* PhD thesis, Massachusetts Institute of Technology and Woods Hole Oceanographic Institution, June 1991.

[76] D. Tang. Backscattering by sediment volumetric inhomogeneities. *personal communication*, 1995.

[77] D. Tang. A note on scattering by a stack of rough surfaces. *J. Acoust. Soc. Am.*, accepted for publication, 1996.

[78] D. Tang and G.V. Frisk. Plane-wave reflection from a random fluid half-space. *J. Acoust. Soc. Am.*, 90(5):2751–2756, Nov. 1991.

[79] W. Teague, M. Carron, and P. Hogan. A comparison between the generalized digital environment model and levitus climatologies. *J. Geoph. Res.*, 95(C5), May 1990.

[80] E.I. Thoros and D.R. Jackson. The validity of the perturbation approximation for rough surface scattering using a Gaussian roughness spectrum. *J. Acoust. Soc. Am.*, 86(1):261–277, July 1989.

[81] I. Tolstoy. Coherent acoustic scatter at a rough interface between two fluids. *J. Acoust. Soc. Am.*, 68(1):258–268, July 1980.

[82] V. Twersky. On scattering and reflection of sound by rough surfaces. *J. Acoust. Soc. Am.*, 29:209–255, 1957.

[83] R. J. Urick. *Principles of Underwater Sound.* McGraw-Hill, New York, third edition, 1983.

[84] Q. Wang. *Wavelet-based inversion of seismo-acoustic waves in Arctic ice.* PhD thesis, Massachusetts Institute of Technology, Sept. 1995.

[85] T. Yamamoto. Velocity variabilities and other physical properties of marine sediments measured by crosswell acoustic tomography. *J. Acoust. Soc. Am.*, 98(4):2235–2248, Oct. 1995.

[86] Tokuo Yamamoto. Acoustic scattering from velocity and density fluctuations in the sediment. *Acoustical Society of America meeting, Austin, TX*, November 1994.

[87] T.C. Yang. Scattering from boundary protuberances and reverberation imaging. *J. Acoust. Soc. Am.*, 93(1):231–242, Jan. 1993.

[88] R. Zhang and G. Jin. Normal-mode theory of average reverberation intensity in shallow water. *J. Sound and Vibration*, 119(2):215–223, 1987.